The Low Temperature Fracture Behaviour of the Super Duplex Stainless Steel Zeron 100

by

Alan Owen Humphreys

A thesis submitted to the Faculty of Engineering

of the University of Birmingham

for the degree of

DOCTOR OF PHILOSOPHY

IRC in Materials for High Performance Applications,

School of Metallurgy and Materials,

The University of Birmingham,

Edgbaston, Birmingham.

B15 2TT

September 1997

ABSTRACT

The micromechanisms of fracture in an austenitic/ferritic super-duplex stainless steel (Zeron 100) have been studied for a range of product forms, including cross-rolled plate, conventional (ingot) route and powder route extruded pipe, hot isostatically pressed (HIP'd) powder, and weldments produced using both tungsten inert gas (TIG) and manual metal arc (MMA) techniques. The rolled plate material was also investigated after heat treatments at temperatures of 425 and 850°C, which were known to embrittle the material.

The as-received microstructures were characterised using optical, scanning electron microscopy (SEM) and transmission electron microscopy (TEM) techniques, including energy dispersive X-ray (EDX) analysis. Macro-residual stresses and crystallographic textures have also been measured. Both impact and fracture toughness tests were carried out over a range of test temperatures between ambient and -196°C using a variety of notch orientations for all product forms. Fracture analysis was performed using both optical and SEM analysis, including electron backscattered pattern (EBSP) methods.

Failure at test temperatures of greater than -80°C was characterised by ductile crack growth and plastic collapse of the specimen. Reduction of the test temperature to below -100°C resulted in cleavage of the ferrite phase for the as-received product forms, although the weld metals were found to cleave at test temperatures as high as -50°C. Crack formation, which occurred in the ferrite, was found to be nucleated by microcracks resulting from intersecting deformation twins. The origin of this cleavage was particularly associated with a highly strained region close to the interphase boundary. This region was identified by decorating dislocations with nitride particles using a heat treatment at a temperature of 550°C for 5 hours.

In some product forms and testpiece orientations, extensive transverse crack growth occurred following crack bifurcation and splitting, and this resulted in an increase in toughness values. The fracture behaviour was more dependent upon the phase morphology than on other microstructural characteristics such as crystallographic texture and grain size. The crack path was found to have a larger effect upon the toughness values than the amount of microductility on the fracture surface. An empirical correlation between crack opening displacement (COD) and Charpy values has also been derived.

The toughness values of the MMA weldments were much less than those of the TIG form, as a result of the lower inclusion content of the latter. However, the fracture toughness values for TIG weldments were also low, due to pop-in failures caused by local embrittlement of the root weld bead.

Heat treatment of the as-received rolled plate material at temperatures of 425 and 850°C produced a large reduction in toughness after ageing times of 6000 and 10 minutes, due to the formation of alpha prime and sigma phase respectively.

ACKNOWLEDGEMENTS

The work carried out in this thesis has been with the support of Weir Materials Ltd., Manchester, and I am very grateful both to of them and to the School of Metallurgy and Materials for providing financial support. I would like to thank Professor I.R.Harris and Professor M.H.Loretto for the provision of research facilities in the school of Metallurgy and Materials and within the IRC respectively.

I am indebted to my supervisor Professor P.Bowen for his support, encouragement and most importantly patience during the course of this work. Thanks are also due to Dr M.Strangwood with all his guidance with microstructural parts of the project, Mrs X.Li for lending me some of her TEM foils for analysis, Dr P.Bate for help with the texture measurements, Ian Brough at UMIST for assisting me with the EBSP equipment there and Dr J.Marrow for helpful discussions. I am also eternally grateful to all the technical staff in this department, particularly Pete Mullane for machining my specimens, Dave Price for help with mechanical testing, John Knight for his services to the metallographic community and Chris Cooper for teaching me the delights of the FEG SEM.

There are many other dubious individuals that I must thank for making my PhD in Birmingham a vaguely enjoyable experience. The lads at Weir Materials were great, particularly Mark and Tim, and my visits there were always a great cultural experience. Thanks to the huge international community of the fracture and fatigue group for a laugh, particularly my 'practical partner' Lisa and erstwhile training chum Steve. Also to the BUCCC boys for some great times, all my housemates over the last four years for putting up with my idiosyncratic behaviour, Escoffier and co. for providing great culinary distractions during the writing period, Katie for her continued love and support, my family for putting up with me, and last and most Helen for helping me out in the dark room (and other places). Cheers to you all...

KEY

a	Half crack length	U_0	Elastic energy
a_0	Lattice parameter	U_a	Crack growth energy release
a_{max}	Critical flaw size	U_p	Crack potential energy
Δa_n	Dugdale plastic zone size	U_γ	Total surface energy
B	Specimen width	V_p	Plastic displacement
C_o	Carbide film thickness	W	Specimen depth
d	Grain diameter	Y	Gauge length
D_0	Hole diameter	Z	Hole depth
E	Young's modulus	z	Knife edge thickness
$f(a/W)$	Geometrical function	β	Cottrell constant
F	Applied force	δ	Crack opening displacement
G	Elastic energy release rate	δ_c	Critical COD value (no SCG)
G_C	Critical value of G	δ_i	Crack initiation COD value
J	EPFM parameter	δ_m	Maximum load COD value
J_C	Critical value of J	δ_u	Critical COD value (some SCG)
k_y	Hall-Petch constant	ε	Applied strain
K	Stress intensity factor	ε_f	Failure strain
K_C	Critical value of K	ε_{ys}	Yield strain
K_{IC}	Plane strain critical K	Φ	Normalised COD
ΔK	Amplitude of K (fatigue)	Γ	Contour for calculation of J
m	COD scaling constant	γ_e	Surface energy term
M_S	Martensite start temperature	γ_p	Plastic energy term
P	Applied load	γ_{gb}	Grain boundary plastic energy
PREN	Pitting resistance equivalent no.	μ	Shear modulus
P_{max}	Maximum load	ν	Poisson's ratio
P_Q	Critical load	σ	Applied stress
r	Rotational factor (COD)	σ_c	Critical stress
r_c	Critical carbide diameter	σ_f	Fracture stress
r_y	Cylindrical plastic zone size	σ_m	Mean stress
r^*	Critical distance (RKR model)	σ_{tot}	Total stress
R	Resistance to crack growth	σ_{ys}	Yield stress
t_i	Traction vector	τ_{eff}	Effective shear stress
T^*	Critical temperature	τ_i	Friction stress
U	Total energy of system	τ_y	Shear stress at yield

CONTENTS

LIST OF TABLES

LIST OF FIGURES

1 - INTRODUCTION

Duplex stainless steels are alloys based upon a two phase austenite-ferrite structure, where both components are stainless (defined as having a solution composition of chromium greater then 12 wt.%). Generally they contain equal volume fractions of austenite and ferrite to ensure optimum properties[1]. These steels combine the high strength and stress corrosion cracking resistance of ferritic stainless steels with the high fracture toughness of austenitic grades, and have been developed[2] for use in corrosive environments between temperatures of -100 and 250°C. Initially, duplex stainless steels had a relatively low alloy content (typically 22wt.%Cr, 5wt.%Ni, 3wt.%Mo, 0.1wt.%N), ensuring their cost effectiveness compared to other stainless steels.

Recently, due to industrial demands for materials with higher strength, pitting and stress-corrosion cracking resistance (especially in marine environments where chloride corrosion is a particular problem), more highly alloyed grades known as 'super' duplex stainless steels have been developed[3]. Zeron 100 (UNS S32760) developed by Weir Materials in 1991 (25wt.%Cr, 7wt.%Ni, 3.5wt.%Mo, 0.25wt.%N), was one of the first alloys of this type to become available and is produced in a number of product forms, namely extruded billet, extruded powder, hot isostatically pressed powder and rolled plate. It has been employed in many highly corrosive environments, especially pipelines and reaction vessels for sour well applications with regard to the offshore oil industry[4,5].

The good low temperature fracture toughness of Zeron 100 has resulted in its use in various Arctic and North Sea applications. In this industry, toughness evaluation is still achieved using Charpy impact testing, as opposed to the use of fracture mechanics techniques. There have been several cases where intermittent low impact

toughness values have been recorded for which no satisfactory explanation can be deduced from microstructural analysis[6,7,8]. Additional problems have arisen as the highly alloyed microstructure is more susceptible to rapid phase transformations than less alloyed grades[9] (particularly during welding) and these precipitates can be highly deleterious to the material's fracture toughness. Hence, it is necessary to determine the micromechanisms of fracture and relate these to composition, processing route and heat treatment via microstructural variables.

In addition, as the alloy has only recently been developed, there is a lack of low temperature fracture toughness data for structural applications. It is natural that as such steels have a large ferrite content, acceptability criteria were based originally upon those developed for fully ferritic steels to ensure their toughness values lay in the 'upper shelf' region. However, it is now becoming clear that the presence of austenite greatly alters the micromechanisms of fracture, enhancing the fracture toughness and reducing the propensity to catastrophic cleavage at low temperatures. Therefore to encourage increased use of the alloy, new design criteria need to be formulated which require well-characterised, reliable low temperature fracture toughness data. As a fracture mechanics approach is often costly and time consuming, it would be of great benefit to establish criteria based on impact toughness values alone, by establishing a quantitative relationship between impact and fracture toughness data.

Thus, the project undertaken was to analyse the fracture behaviour of Zeron 100 in its different product forms including weldments, using a variety of notch orientations. In addition, a limited number of heat treatments would be performed upon these to determine the effects of various precipitates upon fracture. The micromechanisms of fracture at low temperatures were to be elucidated, and related to microstructural characteristics in order to determine the critical parameters to achieve adequate fracture toughness. Extensive impact and fracture toughness ductile to brittle

transition curves were to be obtained, in order to attempt to elucidate an empirical relationship between the different test values..

References:-

[1]BAESLACK W.A. & LIPPOLD J.C., 'Phase transformation behaviour in duplex stainless steel weldments', Metal Construction, 20, p26-31, 1988.

[2]CHARLES J, 'Super duplex stainless steels - structure and properties', Proc.conf."Duplex Stainless Steels'91", Beaune, France, pub.Editions de Physique, p3-47, 1991.

[3]BERNHARDSSON S., 'The corrosion resistance of duplex stainless steels', Proc.conf."Duplex Stainless Steels'91", Beaune, France, pub.Editions de Physique, p185-210, 1991.

[4]SPENCE M.A. & WARBURTON G.R., 'An investigation into the effects of reeling and straightening on the mechanical properties and corrosion resistance of Zeron 100 super duplex stainless steel for use in sub-sea flow applications', proc.conf."Duplex stainless steels '94", Glasgow, pub.T.W.I., Cambridge, U.K., paper 23, 1994.

[5]BYRNE G., SPENCE M.A., OLSEN B., HOUGHTON P.J. & McMAHON J., 'Advantages of HIP production routes for process manifolds', proc.conf."Duplex stainless steels '94", Glasgow, U.K., pub.TWI, paper 19, 1994.

[6]Weir Technical Report TN615, 'Investigation into low impact values on Zeron 100 shaft material', Weir Materials, Manchester, 1991.

[7]Weir Technical Report TN1005, 'Investigation into low impact toughness of the parent material on batch testing of 6" and 8" 0.25" WT welded pipe at butting', Weir Materials, Manchester, 1993.

[8]Weir Technical Report TN592, 'Investigation into low impact toughness values on a HIP disc and slab in UNS S32760', Weir Materials, Manchester, 1991.

[9]NILSSON J.O., 'Overview: super duplex stainless steels', Mat.Sci.Tech., 8, p685-700, 1992.

2 - DUPLEX STAINLESS STEELS

2.1 STAINLESS STEELS

Stainless steels are defined as iron-based alloys with a chromium content of greater than 12wt.%. This ensures the presence of a thin passivating film of chromium oxide, that provides both protection against corrosion in aqueous corrosive environments and resistance to oxidation at high temperatures. They are a very diverse range of steels, in terms of composition, microstructure and properties, and have been extensively reviewed[1,2,3,4].

2.1.1 The Fe-Cr-Ni System

The most simple stainless steel is an iron-chromium alloy, which is a binary system (figure 2.1) containing three separate phases. A body-centred cubic (bcc) ferrite phase is continuous across the whole system, and incorporates both the α and δ iron allotropes (hence it is generally referred to as δ ferrite). The ferrite field completely encloses a face-centred cubic (fcc) austenite phase (the gamma loop) which is thus unstable at room temperature. A third phase, sigma, exists at a chromium concentration of around 50 wt.% at elevated temperatures. Note that additionally, the metastable martensite phase can be produced upon austenite transformation, and this is used to produce an important group of stainless steels.

The gamma loop can be stabilised at higher chromium concentrations and lower temperatures by the addition of nickel (figure 2.2). Thus by varying the composition of the Fe-Cr-Ni system, stainless steel microstructures can be produced that are either fully ferritic, fully austenitic, or a combination of both (duplex). Although chromium and nickel are the principal alloying elements, other elements can be added to improve the material's properties, and these have an additional effect upon the stability of the

phases. The principal austenite forming elements (in order of decreasing effect) are N, C, Ni, Co, Cu, Mn whereas the ferrite stabilising elements are Al, V, Cr, Mo, Si, W.

2.1.2 Austenitic Stainless Steels

The composition of austenitic stainless steels is generally 18-30wt.%Cr and 8-20wt.%Ni with a low C content (≤0.03wt.%). Typical alloys are listed in table 2.1. These have an excellent corrosion resistance, which can be further improved by increasing the nickel and chromium content, or adding molybdenum. Their low temperature toughness is excellent (as the fcc structure is not susceptible to a ductile to brittle transition). The oxide film gives good oxidation protection at elevated temperatures of up to 700°C (above which sigma and other intermetallic phase precipitation occurs), thus they have a wide range of service temperatures. Although austenitic alloys have a low yield strength, this can be improved by interstitial (principally with N) and precipitation (via Ni_3(Al/Ti deposition)) hardening. However, austenitic alloys are susceptible to intergranular stress corrosion cracking (SCC), particularly in the presence of chloride ions, which act to destabilise the passive film. This limits their use in marine environments.

Although, the material is generally easy to weld, problems can arise due to sensitisation and solidification cracking. Sensitisation, or weld decay[5] can occur during cooling of the weld when chromium rich $M_{23}C_6$ carbides are precipitated along grain boundaries, depleting the surrounding region of chromium. This results in the transformed regions becoming susceptible to intergranular corrosion. The addition of Ti and Nb to the microstructure, which form preferential carbides to that of chromium, can be used to minimise the problem. Solidification (hot) cracking[6] occurs due to the large thermal expansivity of austenite. During cooling, contraction of solidified dendrites which are still surrounded by a liquid film can pull the dendrite arms apart, resulting in inter-granular cracking. The problem can be alleviated by using welding consumables with a slightly lower alloy content to that of the parent alloy, resulting in a small amount

(5vol.%) of ferrite being formed. The deposited ferrite is strong enough to hold the dendrite arms together.

2.1.3 Ferritic Stainless Steels

Ferritic stainless steels are generally cheaper than austenitic alloys due to their low nickel composition (an austenite stabilising element). They have a large (15-30wt.%) chromium content, which ensures an excellent resistance to corrosion, including stress corrosion cracking. Typical alloys are listed in table 2.1. The addition of 1-2wt.% molybdenum, particularly in high chromium alloys, can further stabilise the passive film. Ferritic alloys generally have a high yield strength, although their low ductility results in their being less formable than austenitic steels.

The bcc ferrite structure is particularly prone to embrittlement, due to the ductile to brittle transition which occurs at lower temperatures. The lack of a phase transformation upon cooling makes it difficult to refine the microstructure and hence the transition temperature is relatively high (-20 to +80°C). Thus, the alloys are not suitable for low temperature use, and various embrittling phase transformations above 250°C further limit suitable service temperatures. In addition, the alloys are prone to embrittlement from interstitial elements, particularly hydrogen, carbon and nitrogen, although modern steelmaking methods (argon-oxygen refining, electron beam vacuum melting) can limit their presence.

Ferritic stainless steels are generally less weldable than austenitic alloys, as rapid grain growth can occur within the heat affected zone, thus weakening the structure. Although the low thermal expansivity of ferrite ensures that solidification cracking is not a problem in ferritic steels, sensitisation can occur during slow cooling of the weld. However, the high diffusivity of elements within ferrite (compared to austenite) minimises chromium depletion around the grain boundary. The bcc structure

is particularly susceptible to hydrogen embrittlement, so the choice of shielding gas during welding is critical.

2.1.4 Martensitic Stainless Steels

A subgroup of ferritic stainless steels are the martensitic alloys (as listed in table 2.1). These occur when the martensitic transformation temperature is above that of room temperature, and thus transform upon cooling (via a diffusionless shear transformation). The transformation temperature can be calculated using empirical equations, such as[7]:

$M_S(^\circ C)$= 1305 - 61.1(%Ni) - 41.7(%Cr) - 33.3(%Mn) - 27.8(%Si) - 1667(%C+%N)

(compositions in wt.%) .....(2.1)

Note that the transformation temperature may be raised if the microstructure is severely deformed. The material is hot-worked in the austenite phase, and transformed upon cooling to produce very high strength, corrosion and oxidation resistant alloys. They are difficult to machine, and possess poor toughness, although this may be improved by subsequent tempering. Martensitic alloys are straightforward to weld, although they are susceptible to hydrogen embrittlement.

A further group of martensitic alloys are the controlled transformation stainless steels. These have been developed to produce components with the high strength properties of a martensitic steel, but with improved machinability. By rigorously controlling the alloy content, the martensitic transformation temperature may be set at just below room temperature. Thus, the alloy may be machined as an austenitic steel, and the finished component transformed to a martensitic steel. This can be achieved by refrigeration treatment, or heat treatment to precipitate chromium carbides, thus decreasing the matrix alloy content and raising the transformation temperature above that of ambient. The latter process requires a dispersion of δ ferrite within the matrix to act as nucleation sites for such precipitation to occur.

2.1.5 Stainless Steel Applications

Austenitic alloys are the most common group of stainless steels. Their high corrosion resistance and good mechanical properties ensures a wide range of applications, from domestic and architectural use to petrochemical and chemical processing pipes and vessels. Ferritic alloys have the advantage of being resistant to chloride corrosion, and thus can be employed within marine environments. However, their applications are limited by poor mechanical properties. High strength martensitic steels are used to create blades, compressors and discs for hydroelectric and gas turbines. The tight alloy compositional requirements for the production of controlled transformation steels limit their use to specialised military applications, such as missile casings and aircraft fuselages.

Although the above alloys enjoy many applications, there has been a necessity to develop a marine corrosion resistant alloy (stable to chloride ions), with high strength, toughness, and good weldability. This resulted in the development of duplex, and subsequently super duplex stainless steels.

2.2 DEVELOPMENT OF DUPLEX STAINLESS STEELS

The development of duplex stainless steels during the 20th Century has been well documented[8,9,10,11]. Their existence was reported as early as 1927[12] and they became commercially available within 10 years. The original alloys, which were based upon an austenite matrix containing 20-30vol.% ferrite, were found to match the corrosion resistance of austenitic alloys, with improved mechanical properties. However, due to the limitations of steelmaking at the time, it was not possible to accurately reproduce the narrow composition ranges necessary to manufacture a good duplex grade, and very low levels of sulphur, oxygen and carbon could not be

achieved. This resulted in poor workability and solidification cracking of the cast microstructure, thus limiting the material to specialist applications.

More modern duplex stainless steels were developed during the early 1970's, due to a world-wide shortage of nickel, and the expansion of the offshore industry (particularly in North Sea and Arctic applications). The low nickel content of duplex grades compared to that of other stainless steels offered considerable economic advantage[13]. It was also discovered that duplex steels were resistant to stress corrosion cracking and hence suitable for marine applications. Improved refinement treatments (vacuum/argon oxygen degassing) ensured that lower residual contents of interstitial elements (S, P, C, N, O) could be achieved, resulting in improved workability of the material.

A major advance in the development of duplex stainless steels was the discovery that the addition of nitrogen could be used to stabilise the austenite structure. This allowed a reduction of the nickel composition, resulting in a more cost-effective material. The higher nitrogen content increased the austenite reformation rate during welding, thus increasing possible welding speeds and reducing the material's susceptibility to solidification cracking. Nitrogen additions were also found to raise the yield stress of the material without significant degradation of toughness.

Recently, due to demands from the chemical and petro-chemical industries for alloys with still higher strength, chloride corrosion resistance and improved weldability, more highly alloyed materials (25wt.% Cr) known as 'super'-duplex stainless steels have been developed. These are defined as having a pitting resistance equivalent number[14] (PREN) greater than 40, where

$$\text{PREN} = \text{wt\%Cr} + 3.3(\text{wt\%Mo}) + 16(\text{wt\%N}) \qquad \text{.....(2.2)}$$

Typical grades of duplex and super-duplex stainless steels are listed in table 2.1. In general it is found that the optimum combination of properties are achieved with a

ferrite matrix and a 50vol.% austenite content[15]. A variety of alloys has been developed for specific applications, as well as standard grades, and are available in cast, wrought, and hot-isostatically pressed (HIP'd) forms. Zeron 100 (nominal composition of (Fe-25wt.%Cr-7wt.%Ni-3.5wt.%Mo-0.25wt.%N-0.7wt.%Cu-0.7wt.%W-<0.03wt.%C, PREN 40.6) is an example of the new generation of super DSS's and is the subject of research within this thesis.

2.3 MICROSTRUCTURE AND ALLOY CHEMISTRY

The microstructure of modern duplex stainless steels are usually based upon a ferritic matrix, containing austenite colonies which are oriented with respect to the parent phase via a Kurjumov-Sachs type relationship[16]. The alloys are only metastable at ambient temperature, being developed at temperatures of between 1050 and 1200°C to achieve the required phase balance, and subsequently water-quenched. The phase balance is difficult to predict, due to the large number of alloying elements present. Before the advent of computer modelling, Schaeffler diagrams and their derivatives[17,18] were used to represent the equilibrium microstructure (figure 2.3), although alloys were invariably developed using an empirical approach. Recently, computer simulations have been used to achieve more accurate predictions of phase balance[19]. However, it should be noted that due to elemental partitioning between phases and the slow diffusivity of non-interstitial elements, equilibrium conditions are rarely achieved.

A number of alloying elements are used to influence factors such as corrosion resistance, mechanical properties, formability, weldability and stability to heat treatment. However, these can also have a detrimental effect upon material behaviour, and the effect of alloying additions must be carefully analysed.

Chromium forms a stable Cr_2O_3 surface film on the steel, thus providing passivity to both general corrosion and chloride pitting. The passivation potential increases with the level of chromium content. However, chromium is a reactive element, and thus high concentrations can promote the formation of σ and other phases (M_2X, $M_{23}C_6$, χ). It has been reported[20] that very high chromium levels (27wt.%) can promote stress corrosion cracking, possibly due to ferrite embrittlement.

Molybdenum additions further extend the passive potential range of duplex stainless steels, although the exact mechanism for this is not understood[21]. Additions of 3wt.% have been shown to stabilise the oxide film to chloride ion attack, thus protecting the material against crevice corrosion in seawater[22]. However, higher molybdenum additions are not possible, as this extends the σ phase field to high temperatures, resulting in embrittlement of thick sections during casting.

Nitrogen levels of 0.2-0.3wt.% stabilise the austenite phase and provide interstitial strengthening. The corrosion resistance is also improved, as nitrogen modifies the passive film, as well as enhancing equi-partitioning of chromium between the two phases, thus protecting austenite from preferential attack[8]. Its high diffusivity increases the rate of austenite formation, thus improving the weldability of the steel[23].

Nickel is the principal austenite stabilising element, used to balance against the ferrite stabilising elements to provide the optimum 50:50 phase balance. It has the advantage of having no particular effects on the microstructural properties, although levels of 4-8wt.% have been reported to increase the pitting corrosion resistance[24]. It is however an expensive alloying element, hence it is desirable to limit its additions to a minimum.

Silicon improves the fluidity of the liquid steel, thus aiding casting. In some solutions such as boiling $MgCl_2$, silicon additions have been shown to increase the

stress corrosion cracking resistance, but in others such as a standard NACE (3.5vol.% aqueous NaCl) solution, it can have a deleterious effect on corrosion[25], as silicon is prone to attacked by chloride ions. Silicon additions of greater than 1wt.% can increase the rate of σ phase formation[8].

Tungsten behaves in a similar manner to molybdenum, and increases the corrosion resistance, particularly with respect to chloride ions. Hence, recent interest has centred on the partial replacement of molybdenum with tungsten[26], as the former element stabilises brittle intermetallic phases. However, high tungsten additions accelerate the kinetics of sigma phase formation[27], although there is evidence that bulk (as opposed to intergranular) precipitation is induced, thus providing more uniform strength and limiting the degradation of toughness[28].

Copper improves the resistance to oxidation by acids such as H_2SO_4 and H_2PO_4 by forming a layer on the steel surface during active dissolution. Some workers[29] have reported the precipitation of copper particles in the ferrite matrix. These can refine the microstructure during heat treatment, as they have a similar orientation to the matrix as austenite (Kurjumov-Sachs relationship), thus providing low-energy nucleation sites for austenite precipitates[30]. They also subsequently pin interphase boundaries, preventing significant grain growth. High copper levels (>2wt.%) are found to be detrimental to the hot workability of the steel and can promote precipitation hardening[31].

Manganese increases the solubility of nitrogen in stainless steels[32]. However, only small additions can be tolerated as MnS inclusions can be formed which provide ideal nucleation sites for pitting corrosion[10].

Carbon is generally restricted to a maximum of 0.03wt.% in wrought duplex stainless steels to ensure good workability of the structure. These low levels also

suppress carbide precipitation during welding, which can lead to sensitisation. However, a small amount of carbon is desirable to provide interstitial strengthening of the matrix.

Sulphur and **Phosphorus** both form precipitates that can nucleate pitting corrosion in the material, as well as embrittling the matrix and so their levels are kept to an absolute minimum.

2.4 PHASE TRANSFORMATIONS

Due to their highly alloyed nature, a large number of phases can be produced during heat treatment of duplex stainless steels, which are mostly deleterious to material toughness, as well as providing nucleation sites for pitting corrosion. These phase transformations have been extensively reviewed[33,34,35] and are summarised in figure 2.4. The crystallography of each phase is listed in table 2.2.

2.4.1 Alpha Prime Formation

It is well known that long term ageing of a duplex stainless steel between temperatures of 280 and 550°C results in the formation of α' phase[36]. The transformation, which is responsible for the so-called '475°C embrittlement' effect, involves the formation of chromium-rich bcc platelets oriented on {100} planes. This can occur by nucleation and growth, or spinodal decomposition, depending on composition and temperature. Spinodal decomposition, or 'uphill diffusion' can occur if the composition of the ferrite lies between the two points of inflection on the free energy-composition curve, thus allowing the free energy of the system to be decreased by a small change in composition. Phase separation then occurs by the formation of compositional waves in the matrix, which become concentrated to form α' precipitates.

Nucleation and growth, which generally occurs at higher temperatures to that of spinodal decomposition, results from the homogenous nucleation of α' precipitates throughout the matrix.

Although it possible to detect large α' precipitates using conventional techniques, iron and chromium have very similar X-ray and electron scattering factors, thus resolution of compositional modulation during spinodal decomposition is difficult to achieve. A faint contrast is sometimes observed during TEM analysis, due to surface effects (probably preferential oxidation) resulting from foil preparation and storage[37,38]. More accurate measurements of the modulation amplitude and wavelength have been achieved using atom probe field ion microscopy (FIM)[39] and small angle neutron scattering (SANS)[40]. Decomposition may also be detected using Mössbauer spectroscopy[41,42], as the α' precipitates are paramagnetic domains. However, these methods are complex and not widely available, so it is often impossible to positively identify the presence of spinodally decomposed α'.

As spinodal decomposition is particularly hard to detect, it can cause problems during the manufacture of duplex steels. There is no energy barrier to decomposition and thus it can occur spontaneously with no incubation period, although there is a small activation barrier associated with the diffusional process[43]. Its presence can dramatically raise the ferrite yield stress, resulting in low fracture toughness values. The strain field between ferrite and α' is not sufficient to explain the strengthening mechanism through conventional dislocation theories, and an accepted model for α' strengthening has yet to be produced (though it is thought to be due to a decrease in dislocation mobility[44]).

The kinetics of formation are solely controlled by diffusional processes, principally chromium, and so are strongly affected by alloy composition. Additions of chromium, molybdenum and copper have been shown to increase the rate of

decomposition[11], whereas nickel increases the temperature limit of the spinodal region. Strain fields around local precipitates in the matrix may also promote spinodal decomposition[45].

2.4.2 Sigma Phase Formation

Sigma phases are a series of binary or ternary compounds that form in transition metal systems such as Fe-Cr, Fe-V and Co-Cr. In duplex stainless steels they are usually Fe-Cr based compounds, formed at temperatures between 650 and 900°C and are enriched with Mo, Si and W[46]. Sigma phase has a complex structure, based on an ordered tetragonal unit cell[47]. Formation is via the eutectoidal decomposition of the ferrite phase resulting in sigma phase and secondary austenite.

$$\alpha \rightarrow \sigma + \gamma_2 \qquad .....(2.3)$$

Although it is well documented that sigma phase is precipitated at ferrite/ferrite grain boundaries and phase interfaces, its mode of nucleation is uncertain. Some authors[35] suggests that its formation is promoted by the presence of $M_{23}C_6$ carbides although other authors argue that the nucleation process is independent of other phases[48]. Precipitation of sigma phase has also been shown to be accelerated by a deformed microstructure[49].

Sigma phase formation is detrimental to the fracture properties of the matrix as it is a highly brittle phase and thus only a small volume fraction is needed to produce a large reduction in toughness[50]. The phase is chromium-rich, thus it denudes the surrounding matrix leading to an associated reduction in corrosion resistance. Sigma phase formation is a particular problem in super duplex stainless steels, as high levels of chromium, molybdenum and tungsten accelerate its nucleation. Thus, the heat treatment temperature can affect the kinetics of formation, as the ferrite is diluted of these elements at higher temperatures. Several quantitative models have been formulated to calculate the kinetics of formation and thus the critical cooling rate from heat treatment to avoid precipitation[51]. Unlike α' phase, sigma can be readily identified

using optical metallographic techniques and so is easily discovered if formed during processing.

2.4.3 Other Phase Transformations

Chromium nitrides, which are formed at temperatures between 700 and 900°C, are particularly prevalent in modern duplex stainless steels due to their high nitrogen content. They are usually of the hexagonal Cr_2N form, although cubic CrN precipitates have been observed in weld heat affected zones[52]. Rapid cooling of the material following solution treatment results in the supersaturation of ferrite with nitrogen, promoting intragranular nitride growth. Any subsequent annealing produces grain boundary precipitation. As the phase is enriched with chromium, it depletes the surrounding region, thus increasing the material's susceptibility to intergranular corrosion. It has also been suggested that nitride precipitation can decrease the fracture toughness of the alloy[53].

Chi phase (χ) is a molybdenum-rich cubic intermetallic formed during annealing at temperatures between 700 and 900°C, thus it usually coexists with sigma phase, nitrides and carbides. Due to its small volume fraction compared to these other phases it is difficult to isolate its effects on material properties, but it is thought to be deleterious to both fracture and corrosion resistance[11].

Carbides, such as cubic $M_{23}C_6$ and orthorhombic M_7C_3 are precipitated at temperatures below 1000°C, predominantly on interphase boundaries[54]. They are quickly formed due to the high mobility of carbon atoms, and can embrittle the matrix, as well as causing sensitisation during welding. However, as the carbon content in modern duplex stainless steels is limited to levels below 0.03wt.%, the presence of carbides within the microstructure is very limited.

Secondary austenite (γ_2) is formed from decomposition of ferrite, most commonly by the eutectoidal formation of sigma phase, or the growth of Widmanstätten laths during welding. However, at temperatures below 650°C, austenite has been observed to form from an isothermal shear transformation similar to that of martensite[55]. Secondary austenite is normally chromium-depleted compared to the primary form, leading to a localised reduction of pitting corrosion resistance.

R-Phase is a molybdenum-rich trigonal intermetallic compound which forms at temperatures between 550 and 750°C and is often found to nucleate on bands of dislocations, as well as grain boundaries. They are associated with a reduction in toughness and corrosion resistance[56].

Other precipitates such as **π phase**[56], **G phase**[57], **τ phase**[35] and **Cu particles**[30] have been identified in duplex stainless steels, but they occupy such a small volume fraction, that it difficult to isolate their individual effects upon material properties.

2.5 MECHANICAL PROPERTIES

Duplex stainless steels generally have superior mechanical properties to that of other stainless grades, including improved impact toughness and ductility and higher yield and tensile strengths (figure 2.5). This allows substantial weight (and cost) savings to be made for thick-walled constructions when substituting duplex for austenitic stainless steels (which have similar corrosion properties). They have a high thermal conductivity and low thermal expansion coefficient, which facilitate easy welding of a structure. Duplex stainless steels are more difficult to machine than austenitic alloys, due to their high yield strength, low carbon content and low volume fraction of non-metallic inclusions. However, much research has been performed in

this area, and the optimum conditions necessary for machining are now well established[58]. The strong ferromagnetic properties of the material also allow magnetic clamping during machining.

The high yield strength of duplex stainless steels is primarily due to their large ferrite content. However, it is also derived from solid solution strengthening of the matrix, both substitutional (Cr, Mo), and interstitial (N)[59], as well as Hall-Petch strengthening due to the fine grain size of the material. Cold deformation can also be used to increase the yield stress without a significant reduction in material toughness[60].

The toughness of duplex stainless steels has been well reviewed[61] and is superior to that of ferritic grades. This is because as well as the austenite colonies being intrinsically tough, they also act to retard cleavage fracture of the ferrite phase. However, the highly alloyed ferrite matrix is prone to embrittlement from α' formation[62,63], as well as interstitial element contamination (especially oxygen and hydrogen[64]). Grain boundary precipitates such as sigma, $M_{23}C_6$ and chi phases can also result in a drastic reduction in toughness[65,66,67]. The fracture behaviour of these materials is further discussed in the next chapter,

The fatigue strength of duplex stainless steels are generally superior to that of austenitic grades and found to be directly related to the yield stress[68]. Cold deformation further improves the properties as the crack growth threshold is reduced[69]. However, the crack growth rate can be accelerated if the ferrite matrix is embrittled by thermal ageing[70], or hydrogen embrittlement (corrosion fatigue)[71].

2.6 CORROSION PROPERTIES

The primary reason for the development of duplex stainless steels was their excellent corrosion properties, which are generally superior to that of austenitic or ferritic grades[14]. Stainless steels are corrosion resistant due to their passive layer of hydrated Cr_2O_3, which although only 20-30Å thick, is extremely adherent and resistant to attack (if abraded or scratched, it immediately reforms). The level of corrosion protection increases with chromium content, hence in a duplex steel the austenite phase is more susceptible to corrosion than ferrite, due to partitioning of chromium between phases (although the level of partitioning can be reduced by nitrogen additions). Highly alloyed duplex stainless steels have a superior corrosion resistance to even that of other grades, as various alloying additions are used to extend the passive potential range (figure 2.6). However, under certain conditions, stainless steels are susceptible to localised forms of chemical attack, namely intergranular or pitting corrosion, and stress corrosion cracking.

Intergranular corrosion can occur following segregation of reactive solute atoms, such as Mo or B to grain boundaries[22] which results in the region becoming prone to preferential attack in aggressive environments. Stainless steels can also be susceptible to intergranular corrosion if metal carbides are formed along grain boundaries during welding or heat treatment, depleting the surrounding area of chromium (sensitisation). However, due to their low carbon content (<0.03wt.%) this is rarely a problem in duplex steels.

Pitting Corrosion is a highly localised form of corrosion, resulting from shallow surface pits nucleated at microstructural features such as grain boundaries, inclusions and precipitates. Anodic dissolution occurs within these pits (the opposing cathodic reaction proceeds on the outer surface) resulting in the formation of metal ions which can react with migrating halide ions to produce hydrogen ions (acids). The local

pH can be reduced to such an extent that the passive potential of the oxide film is exceeded, resulting in general corrosion. Various alloys additions can be used to increase the passive potential of the surface film (figure 2.6). Thus a pitting resistance equivalent number (equation 2.2) has been elucidated to predict the susceptibility of a material to pitting corrosion. However, this only includes Cr, Mo and N additions, and hence fails to account of other alloying additions. Note that alloying additions which promote phase transformations can increase the risk of pitting corrosion, as multiple precipitation provides more nucleation sites for reaction to occur. The rate of corrosion is accelerated at higher temperatures, as the rate of dissolution and halide ion diffusion is increased. A less localised form of pitting corrosion is crevice corrosion, which can occur within crevices or at shielded surfaces where a stagnant solution is present.

Stress Corrosion Cracking, which can result in the structural failure of a material at a stress level well below the usual fracture stress, can occur if a material is subjected to a tensile stress (either residual or applied) within a corrosive (particularly chloride) environment. Failure is generally nucleated by a surface pit, from which crack propagation results perpendicular to the stress field. The mechanisms of growth are complex, but it is generally thought that whilst anodic dissolution occurs at the crack tip, repassivation of the metal ions is prevented by plastic deformation, thus allowing localised corrosion to occur at the crack tip. The passive film can be further disrupted by the migration of anodically dissolved hydrogen ions to the crack tip, resulting in hydrogen embrittlement[1]. High levels of nitrogen can influence the stress corrosion cracking resistance, as this increases the stacking fault energy of the ferrite phase, encouraging twin deformation, which facilitates mechanical depassivation of the surface film[72]. The rate of dissolution increases with temperature, as well as stress level. Stress corrosion cracking is generally nucleated by pitting corrosion, thus a material's PREN can be used to predict the susceptibility of a steel to such cracking. Generally super duplex stainless steels have an excellent resistance to stress corrosion cracking (figure 2.7).

2.7 WELDING BEHAVIOUR OF DUPLEX STAINLESS STEELS

No matter how well controlled the phase balance and microstructure of the base material, a poor weld can contain intermetallic phase precipitates, alloy segregation and a non-uniform phase balance, resulting in poor mechanical and corrosion properties[73]. Therefore the weld is often the critical component of a structure, thus much research is in progress to determine how its properties may be optimised[74,75].

The nature of the welding process has a critical effect upon the weld microstructure[76,77]. There is considerable economic advantage and ease of use associated with a flux-shielded process such as manual metal arc (MMA) welding. However, this can impart high levels of hydrogen and oxygen to the microstructure, resulting in hydrogen cracking and oxide inclusions around the weld. Gas-shielded processes such as tungsten inert gas (TIG) welding produce cleaner welds, but are slower to perform and more expensive. TIG welds are also usually associated with a higher heat input, thus facilitating sigma phase formation.

Duplex stainless steel weldments are very sensitive to the cooling rate following solidification. The situation is further complicated in multipass welds, where adjacent beads are continually re-heated and cooled during the welding process. If the weld is cooled too slowly, precipitation of sigma and other phases can occur[15], resulting in poor mechanical and corrosion properties. Contrary to this, the microstructure generally solidifies as a fully-ferritic structure, whereupon austenite grains nucleate and grow under a diffusion-controlled process. Thus if the weld is cooled too rapidly, there is insufficient time for austenite to form, resulting in a non-ideal phase balance. The ferrite phase can also become supersaturated with nitrogen, producing chromium nitride precipitation[78]. However, the kinetics of austenite formation may be accelerated if the filler material for the weld is overalloyed compared to the parent metal, especially with nickel and nitrogen.

Welding produces a heat affected zone (HAZ) within the parent microstructure. Heating from the weld can result in α' embrittlement, ferrite grain growth and carbide, nitride and intermetallic phase precipitation[79] all of which are deleterious to the mechanical and corrosion properties[80]. Secondary austenite formation can also occur[81], which is chromium-depleted and thus susceptible to corrosion. Although the heat input to the heat affected zone can affect the phase balance due to austenite dissolution, the cooling rate has been shown to be the critical parameter in determining the HAZ toughness and corrosion properties[82].

Other problems can arise as a result of the welding process. The weld often solidifies in a directional manner, resulting in anisotropic mechanical properties. Residual stresses can accumulate due to thermal-induced contraction of the weld during cooling, thus promoting stress corrosion cracking. Thus although duplex stainless steels are generally more weldable than austenitic and ferritic alloys[83], care must be taken during production to ensure good structural properties.

In conclusion it can be seen that super duplex stainless steel structures can be produced which have superior material properties to those of ferritic and austenitic stainless steels. However, this project is primarily concerned with the micromechanisms of fracture, and thus it is necessary to explore the development of fracture mechanical models, in order to relate these properties to the microstructure.

References:-

[1]LLEWELLYN D.T., Steels Metallurgy and Applications, pub.Butterworth-Heinemann, Oxford, 1992.

[2]HONEYCOMBE R.W.K. & BHADESHIA H.K.D.H., "Steels, microstructure and properties", pub.E.Arnold, London, 1995.

[3]LESLIE W.C., "The physical metallurgy of steels", pub.McGraw-Hill, London, 1981.

[4]PICKERING F.B., "The metallurgical evolution of stainless steels", pub.ASM, 1979.

[5]JOSHI A. & STEIN D.F., Corrosion, 28, p231, 1972.

[6]NELSON D.E., BAESLACK W.A. & LIPPOLD J.C., Welding J., 66, p241, 1987.

[7]MARSHALL P., "Austenitic stainless steels - microstructure and properties", pub.Elvisier, 1984.

[8]ROSCOE C.V. & GRADWELL K.J., 'The history and development of duplex stainless steels', proc.conf."Duplex Stainless Steels '86", The Hague, Holland, pub.Netherlands Institute of Welding, pp1-16, 1986.

[9]CHARLES J, 'Super duplex stainless steels - structure and properties', Proc.conf."Duplex Stainless Steels'91", Beaune, France, pub.Editions de Physique, pp3-47, 1991.

[10]SOLOMON H.D. & DEVINE T.M., 'Duplex stainless steels - a tale of two phases', proc.conf."Duplex Stainless Steels'91", Beaune, France, pub.Editions de Physique, pp693-756, 1991.

[11]NILSSON J.O., 'Overview: super duplex stainless steels', Mat.Sci.Tech., 8, pp685-700, 1992.

[12]BAIN E.C. & GRIFFITHS W.E., 'An introduction to the iron-chromium-nickel alloys', Trans.Amer.Inst.Min.Met.Eng., 75, pp166-213, 1927.

[13]SMITH L.M. & CELENT M., 'Life-cycle costing - are duplex stainless steels the cost-effective choice?', proc.conf."Duplex Stainless Steels '94", Glasgow, U.K., pub.TWI, paper KIX, 1994.

[14]BERNHARDSSON S., 'The corrosion resistance of duplex stainless steels', Proc.conf."Duplex Stainless Steels'91", Beaune, France, pub.Editions de Physique, pp185-210, 1991.

[15]BAESLACK W.A. & LIPPOLD J.C., 'Phase transformation behaviour in duplex stainless steel weldments', Metal Construction, 20, pp26-31, 1988.

[16]BROWN E.L., WHIPPLE T.A. & KRAUSS G., 'Metallography of duplex stainless steel castings', Proc.conf."Duplex Stainless Steels'83", St Louis, Missouri, USA, Ed.R.A.Lula, pub.ASM, pp665-691, 1983.

[17]SCHAEFFLER A.L., Met.Prog., 56, pp680-681, 1949.

[18]LONG C.J. & DELONG W.T., Weld J., 52, pp281-297, 1973.

[19]HAYES F.H., HETHERINGTON M.G. & LONGBOTTOM R.D., 'Thermodynamics of duplex stainless steels', Mat.Sci.Tech., 6, pp263-271, 1990.

[20]ISHIZAWA Y. & INAZUMI T., 'Effect of alloying element and ferrite-austenite ratio on SCC and pitting corrosion of duplex stainless steels', proc.conf."Duplex Stainless Steels '86", The Hague, Holland, pub.Netherlands Institute of Welding, pp392-398, 1986.

[21]NEWMAN R.C. & FRANZ E., J.Electrochem.Soc., p223, 1984.

[22]SEDRICKS A.J., 'Corrosion of stainless steels', Corrosion of Stainless Steels, John Wiley & Sons, New York, 1979.

[23]ATAMERT S. & KING J.E., 'Crack initiation mechanisms in duplex stainless steel HAZ microstructures', Acta Met.Mat., 39, p273-285, 1991.

[24]SAKAI J., MATSUSHIMA I., KAMEMURA Y., TANIMURA M. & OSUKA T., proc.conf."Duplex Stainless Steels", pub.ASM, p211, 1982.

[25]ONOYAMA M., HAYASHI N., SHITANI K & SUEHITO T., 'Evaluation of corrosion resistance of a duplex stainless steel in H_2S-CO_2-Chloride environments', Proc.conf."Duplex Stainless Steels'83", St Louis, Missouri, USA, Ed.R.A.Lula, pub.ASM, pp191-209, 1983.

[26]OKAMOTO H., 'The effect of tungsten and molybdenum on the performance of super duplex stainless steels', proc.conf "applications of stainless steel'92", 2, pp360-369, 1992.

[27]HERTZMAN S., NILSSON M. & JARGELIUS-PETTERSSON R., 'Influence of W and Cu on microstructure, mechanical properties and corrosion resistance in super duplex weld metals', proc.conf."Duplex Stainless Steels '94", Glasgow, U.K., pub.TWI, paper1, 1994.

[28]CHARLES J., 'Structure and mechanical properties of duplex stainless steels', proc.conf."Duplex Stainless Steels '94", Glasgow, U.K., pub.TWI, paper KI, 1994.

[29]SMITH C.J.E., RUCKMAN J.C., & LAWRENCE G.D., 'Identification of precipitates in a duplex steel', Met.&Mat., 7, pp234-240, 1973.

[30]SOYLU S. & HONEYCOMBE R.W.K., 'Microstructural refinement of duplex stainless steels', Mat.Sci.Tech., 7, pp137-145, 1991.

[31]GUHA P. & CLARK C.A., 'Properties and applications of high chromium duplex stainless steels', Proc.conf."Duplex Stainless Steels'83", St Louis, Missouri, USA, Ed.R.A.Lula, pub.ASM, pp355-369, 1983.

[32]ROSCOE C.V., GRADWELL K.J. & LORIMER G.W., 'Structure-property relationships in a series of duplex stainless steels', proc.conf."Duplex Stainless Steels'84", London, pub.IOM, pp563, 1984.

[33]WANG X.G., DUMORTIER D. & RIQUIER Y., 'Structural evolution of Zeron 100 duplex stainless steel between 550 and 1100°C', proc.conf."Duplex Stainless Steels'91", Beaune, France, pub.Editions de Physique, pp128-134, 1991.

[34]CHARLES J, 'Super duplex stainless steels - structure and properties, Proc.conf."Duplex Stainless Steels'91", Beaune, France, pub.Editions de Physique, pp151-168, 1991.

[35]REDJAÏMIA A., METAUER G. & GANTOIS M., 'Decomposition of delta ferrite in a Fe-22Cr-5Ni-3Mo-0.03C duplex stainless steel. A morphological and structural study', Proc.conf."Duplex Stainless Steels'91", Beaune, France, pub.Editions de Physique, pp119-126, 1991.

[36]BROWN J.E., CEREZO A., GODFREY T.J., HETHERINGTON M.G. & SMITH G.D.W., 'Quantitative atom probe analysis of spinodal reaction in ferrite phase of duplex stainless steel', Mat.Sci.Tech., 6, pp293-300, 1990.

[37]STRANGWOOD M. & DRUCE S.G., 'Ageing effects in welded cast CF3 stainless steel', Mat.Sci.Tech., 6, pp237-247, 1990.

[38]HU Z.W., HSU S.S. & JIANG X.L., 'HREM study on α' and γ_2 precipitation in an aged wrought duplex stainless steel at 500°C', Scripta.Met.Mat., 25, pp645-650, 1991.

[39]AUGER P, DANOIX F, MENAND A, BONNET S, BOURGOIN J & GUTTMANN M., 'Atom probe and transmission electron microscopy study of ageing of cast duplex stainless steels', Mat.Sci.Tech., 6, pp301-313, 1990.

[40]LASALLE J.C. & SCHWARTZ L.H., Acta Met., 34, p989, 1986.

[41]SOLOMON H.D. & LEVINSON L.M., 'Mössbauer effect study of 475°C embrittlement of duplex and ferritic stainless steels', Acta Met., 26, pp429-442, 1978.

[42]CHANDRA D. & SCHWARTZ L.H., 'Mössbauer effect study of the 475°C decomposition of Fe-Cr alloy', Met.Trans., 2, pp511-519, 1971.

[43]PUMPHREY P.H. & AKHURST K.N., 'Ageing kinetics of CF3 cast stainless steel in temperature range 300-400°C', Mat.Sci.Tech., 6, pp211-219, 1990.

[44]NICHOL T.J., DATTA A. & AGGEN G., Met.Trans., 11A, p573, 1980.

[45]CAHN J.W., 'On spinodal decomposition in cubic crystals', Acta Met., 10, pp179-183, 1962.

[46]MAEHARA Y., OHMORI Y., MURAYAMA J., FUJINO N. & KUNITAKE T., 'Effects of alloying elements on σ phase precipitation in δ–γ duplex phase stainless steels', Met.Sci., 17, pp541-547, 1983.

[47]KASPER J.S., DECKER B.F. & BELANGER J.R., 'The crystal structure of the sigma phase in the Co-Cr system', J.Appl.Phys., 22, pp361-362, 1951.

[48]BLENKINSOP P.A. & NUTTING J., 'Precipitation of the sigma phase in an austenitic steel', J.Iron Steel Inst., 205, pp953-958, 1967.

[49]PARAYIL T.R. & HOWELL P.R., 'Decomposition of deformed ferrite in a duplex stainless steel', Mat.Sci.Tech., 2, pp1131-1139, 1986.

[50]IRISARRI A.M. & ERAUZKIN E., 'Effects of the heat treatment on the fracture toughness and corrosion embrittlement of a duplex stainless steel 22.05', Proc.conf."Duplex Stainless Steels'91", Beaune, France, pub.Editions de Physique, pp779-785, 1991.

[51]JOSEFSSON B., NILSSON J.O. & WILSON A., proc.conf."Duplex Stainless Steels'91", Beaune, France, pub.Editions de Physique, p67, 1991.

[52]HERTZMAN S., ROBERTS W. & LINDENMO, from "Duplex Stainless Steels'86", The Hague, Holland, p257, 1986.

[53]NILSSON J.O., WILSON A., JOSEFSSON B. & THORVALDSSON T., conf.proc."Stainless Steels'92, Stockholm, pub.IOM, p280, 1992.

[54]SOUTHWICK P.D. & HONEYCOMBE R.W.K., 'Precipitation of $M_{23}C_6$ at austenite/ferrite interfaces in duplex stainless steel', Met.Sci., 16, pp475-481, 1982.

[55]SOUTHWICK P.D. & HONEYCOMBE R.W.K., 'Decomposition of ferrite to austenite in 26%Cr-5%Ni stainless steel', Met.Sci., 14, pp253, 1980.

[56]NILSSON J.O. & LIU P., Mat.Sci.Tech, 7, pp853-862, 1991.

[57]MILLER M.K. & BENTLEY J., 'APFIM and AEM investigation of CF8 and CF8M primary coolant pipe steels', Mat.Sci.Tech., 6, pp285-292, 1990.

[58]CARLBORG C.G., NILSSON Å. & FRANKLIND P-Å., 'Machinability of duplex stainless steel', proc.conf." Stainless Steels '91", Stockholm, Sweden, pp686-696, 1992.

[59]WAHLBERG G. & DUNLOP G.L., 'Nitrogen strengthening of duplex stainless steels', proc.conf."Stainless Steel '87", York, U.K., pub.IOM, pp291-299, 1988.

[60]NYSTRÖM M., KARLSSON B. & WASÉN J., 'The influence of prestraining and 475°C annealing on the mechanical properties of a duplex stainless steel (SAF2205)', Proc.conf."Stainless Steels'90", Chiba, Japan, pub.ISIJ, pp738-745, 1991.

[61]NICODEMI W., ROBERTI R., & LAVECCHIA G.M., 'Duplex stainless steel microstructure and toughness', proc.conf." Stainless Steels '91", Stockholm, Sweden, pp270-279, 1992.

[62]BONNET S, BOURGOIN J. CHAMPREDONDE J, GUTTMAN D. & GUTTMAN M., 'Relationship between evolution of mechanical properties of various cast duplex stainless steels and metallurgical and ageing parameters: outline of current EDF programmes', Mat.Sci.Tech., 6, pp221-229, 1990.

[63]CHUNG H.M. & LEAX T.R.,'Embrittlement of laboratory and reactor aged CF3, CF8 and CF8M duplex stainless steels', Mat.Sci.Tech., 6, pp249-262, 1990.

[64]ZHENG W. & HARDIE D., 'The effect of hydrogen on the fracture of a commercial duplex stainless steel', Corr.Sci., 32, pp23-36, 1991.

[65]NILSSON J.O. & WILSON A., ' Influence of isothermal phase transformations on toughness and pitting corrosion of super duplex stainless steel SAF2507', Mat.Sci.Tech., 9, pp545-554, 1993.

[66]ERAUZKIN E. & IRISARRI A.M., 'Influence of microstructure on the fracture toughness and fracture topography of a duplex stainless steel', Eng.Mat.Struct., 15, pp129-137, 1992.

[67]SCOPPIO L. & BARTERI M., 'Effect of microstructure and composition on the mechanical properties of some duplex stainless steels', proc.conf." Stainless Steels '91", Stockholm, Sweden, pp260-269, 1992.

[68]ITURGOYEN L. ALCALÁ J. & ANGLADA M., 'The influence of ageing at 475°C on the fatigue crack propagation of a duplex stainless steel', proc.conf."Stainless Steels'90", Chiba, Japan, pub.ISIJ, pp746-753, 1991.

[69]NYSTRÖM M., KARLSSON B. & WASÉN J., 'Fatigue crack growth of duplex stainless steels', proc.conf."Duplex Stainless Steels'91", Beaune, France, pub.Editions de Physique, pp795-802, 1991.

[70]MARROW T.J. & KING J.E., 'Temperature effects on fatigue crack propagation in a thermally aged super duplex stainless steel', proc.conf."Duplex Stainless Steels'91", Beaune, France, pub.Editions de Physique, pp169-176, 1991

[71]MATHIS R., 'Initiation and early growth mechanisms of corrosion fatigue cracks in stainless steels', J.Mat.Sci., 22, pp907-914, 1987.

[72]MAGNIN T., LeCOZE J. & DESESTRET A., 'Twinning and stress corrosion cracking of ferrite phases of duplex stainless steels', proc.conf. "Duplex stainless steels'83", St Louis, Missouri, USA, ed.R.A.Lula, pub.ASM, pp535-551, 1983.

[73]BOPPERT C & DRAUGELATES U., 'Mechanical properties and corrosion resistance of welded superduplex cast alloys', proc.conf."Duplex Stainless Steels '94", Glasgow, U.K., pub.TWI, paper 73, 1994.

[74]LILJAS M., 'The welding metallurgy of duplex stainless steels', proc.conf."Duplex Stainless Steels '94", Glasgow, U.K., pub.TWI, paper KV, 1994.

[75]NASSAU L. MEELKER H. & HILKES J., 'Welding duplex and super-duplex stainless steels', proc.conf."Duplex Stainless Steels'91", Beaune, France, pub.Editions de Physique, pp303-323, 1991

[76]KOTECKI D.J., 'Welding processes for duplex stainless steels', proc.conf."Duplex Stainless Steels '94", Glasgow, U.K., pub.TWI, paper KVI, 1994.

[77]GUNN R.N., 'Comparison of corrosion and mechanical properties of weldments in wrought 25%Cr superduplex stainless steels', proc.conf."Duplex Stainless Steels '94", Glasgow, U.K., pub.TWI, paper32, 1994.

[78]KOKAWA H., TSORY E. & NORTH T.H., 'Nitride precipitation in duplex stainless steel weld metal', ISIJ Int., 35, pp1277-1283, 1995.

[79]ATAMERT S. & KING J.E., 'Super duplex stainless steels, HAZ microstructures', Mat.Sci.Tech., 8, p896-911, 1992.

[80]LIPPOLD J.C., LIN W., BRANDI S., VAROL I. & BAESLACK W.A., 'Heat-affected zone microstructures and properties in commercial duplex stainless steels', proc.conf."Duplex Stainless Steels '94", Glasgow, U.K., pub.TWI, paper 116, 1994.

[81]NILSSON J.O., KARLSSON L. & ANDERSSON J.O., 'Secondary austenite formation and its relation to pitting corrosion in duplex stainless steel weld metal', Mat.Sci.Tech., 11, pp276-283, 1995.

[82]JANA S., 'Effect of heat input on the HAZ properties of two duplex stainless steels', J.Mat.Proc.Tech., 33, pp247-261, 1992.

[83]WALKER R.A., 'Duplex and high-alloy steels - corrosion resistance and weldability', Mat.Sci.Tech., 4, pp78-84, 1988.

Alloy	Type	C	Si	Mn	P	S	Cr	Mo	Ni	Others
Austenitic	**301S16**	0.15	1.00	2.00	0.045	0.030	16-18	-	6-8	-
Austenitic	**304S11**	0.03	1.00	2.00	0.045	0.030	17-19	-	9-12	-
Austenitic	**310S24**	0.15	1.00	2.00	0.045	0.030	23-26	-	19-22	-
Austenitic	**316S11**	0.03	1.00	2.00	0.045	0.030	16-18	2-2.5	11-14	-
Austenitic	**321S31**	0.08	1.00	2.00	0.045	0.030	17-19	-	9-12	0.8Ti
Ferritic	**403S17**	0.08	1.00	1.00	0.040	0.030	12-14	-	1.00	-
Ferritic	**405S17**	0.08	1.00	1.00	0.040	0.030	12-14	-	1.00	0.3Al
Ferritic	**409S19**	0.08	1.00	1.00	0.040	0.030	10-12	-	1.00	1.0Ti
Ferritic	**434S17**	0.08	1.00	1.00	0.040	0.030	16-18	1-1.3	1.00	-
Martensitic	**410S21**	0.10	1.00	1.00	0.04	0.03	11-13	-	1.0	-
Martensitic (cont.trans.)	**Armco 17-7PH**	0.07	0.30	0.50	-	-	17.0	-	7.0	1.1Al
Duplex	**SAF2304**	0.03	0.50	1.20	-	-	23.0	0.2	4.0	0.1N/0.2Cu
Duplex	**SAF2205**	0.03	0.50	1.50	-	-	22.0	3.0	5.5	0.15N
Duplex	**UR52N**	0.03	0.30	1.20	-	-	25.0	3.0	6.5	0.17N/.2Cu
Duplex	**Zeron25**	0.03	1.00	1.50	-	-	25.0	3.0	6.5	0.16N 0.5Cu/.3W
Super-Dup.	**DP3W**	0.03	?	?	-	-	25.0	3.0	7.0	0.25N/2W
Super-Dup.	**SAF2507**	0.03	<1.0	<2.0	-	-	25.0	4.0	7.0	0.3N
Super-Dup.	**UR52N+**	0.03	0.30	1.00	-	-	25.0	4.0	7.0	0.3N/2Cu
Super-Dup.	**Zeron100**	0.03	<1.0	<1.0	-	-	25.0	3.5	7.0	0.25N 0.7Cu/.7W

Table 2.1 - Composition of typical stainless steels[1,14]

(compositions in wt.%)

Type of precipitate	Nomimal chemical formula	Temperature range (°C)	Space group	Lattice parameter (nm)
δ	-	-	Im3m	a=0.286-0.288
γ	-	-	Fm3m	a=0.358-0.362
σ	Fe-Cr-Mo	600-1000	$P4_2/mnm$	a=0.879, c=0.454
Cr_2N	Cr_2N	700-900	P31m	a=0.879, c=0.447
CrN	CrN	700-900	Fm3m	a=0.413-0.447
χ	$Fe_{36}Cr_{12}Mo_{10}$	700-900	I43m	a=0.892
R	Fe-Cr-Mo	550-650	R3	a=1.090, c=1.939
π	$Fe_7Mo_{13}N_4$	550-650	$P4_132$	a=0.647
τ	?	550-650	Fmmm	a=0.405, b=0.484, c=0.286
M_7C_3	M_7C_3	950-1050	Pnma	a=0.452, b=0.699, c=1.211
$M_{23}C_6$	$M_{23}C_6$	600-950	Fm3m	a=1.056-1.065
G	$Ti_6Ni_{16}Si_7$	500-750	Fm3m	a=1.14
α'	Cr-rich	<550	Im3m	a=0.2866

Table 2.2 - Summary of phases present in duplex stainless steels[11,28,35]

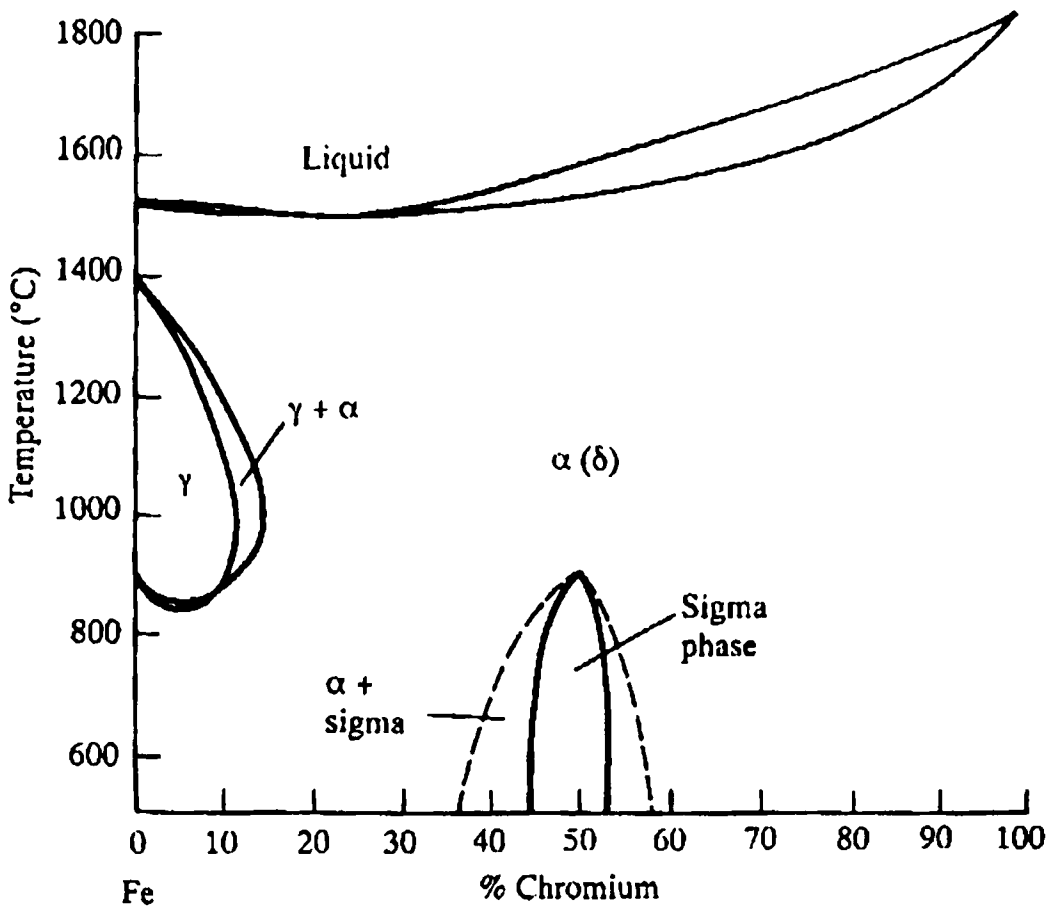

Figure 2.1 - Phase diagram for the Fe-Cr system[1]

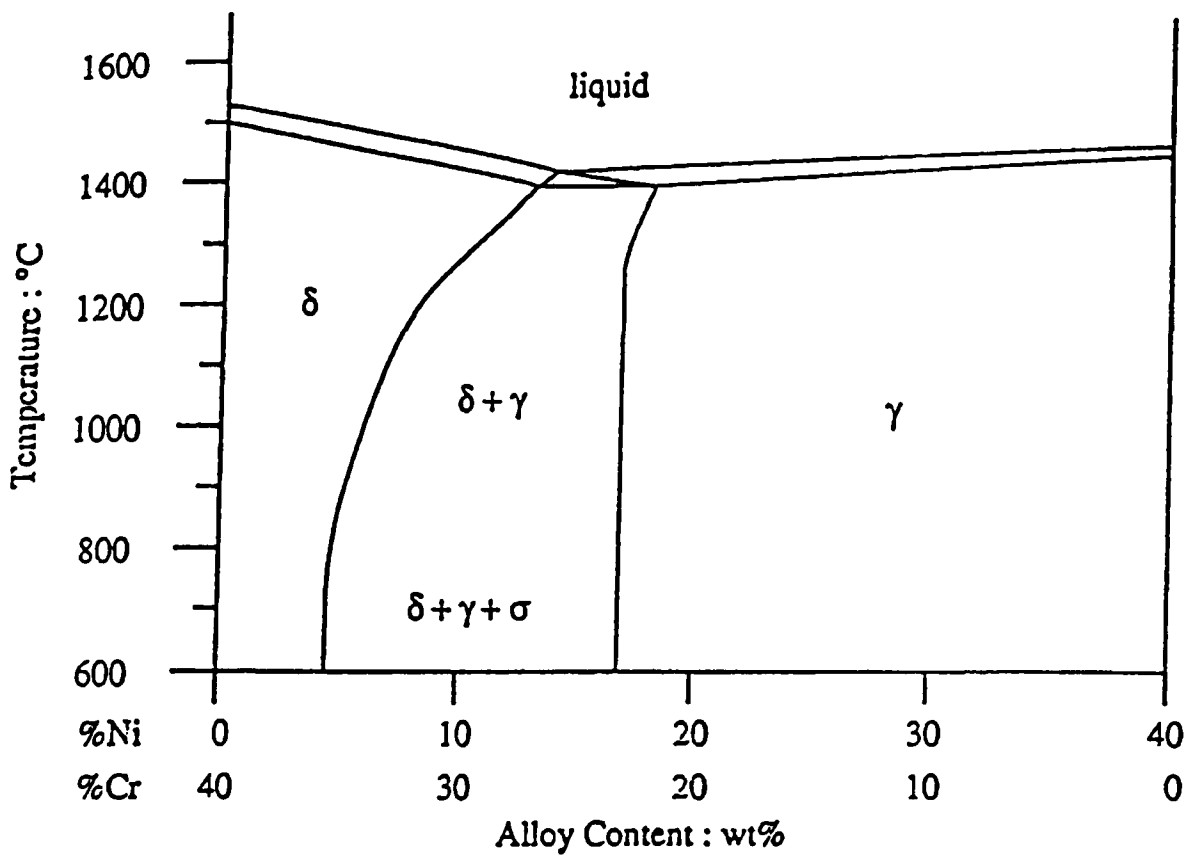

Figure 2.2 - Phase diagram for the Fe-Cr-Ni system[10] (60wt.%Fe)

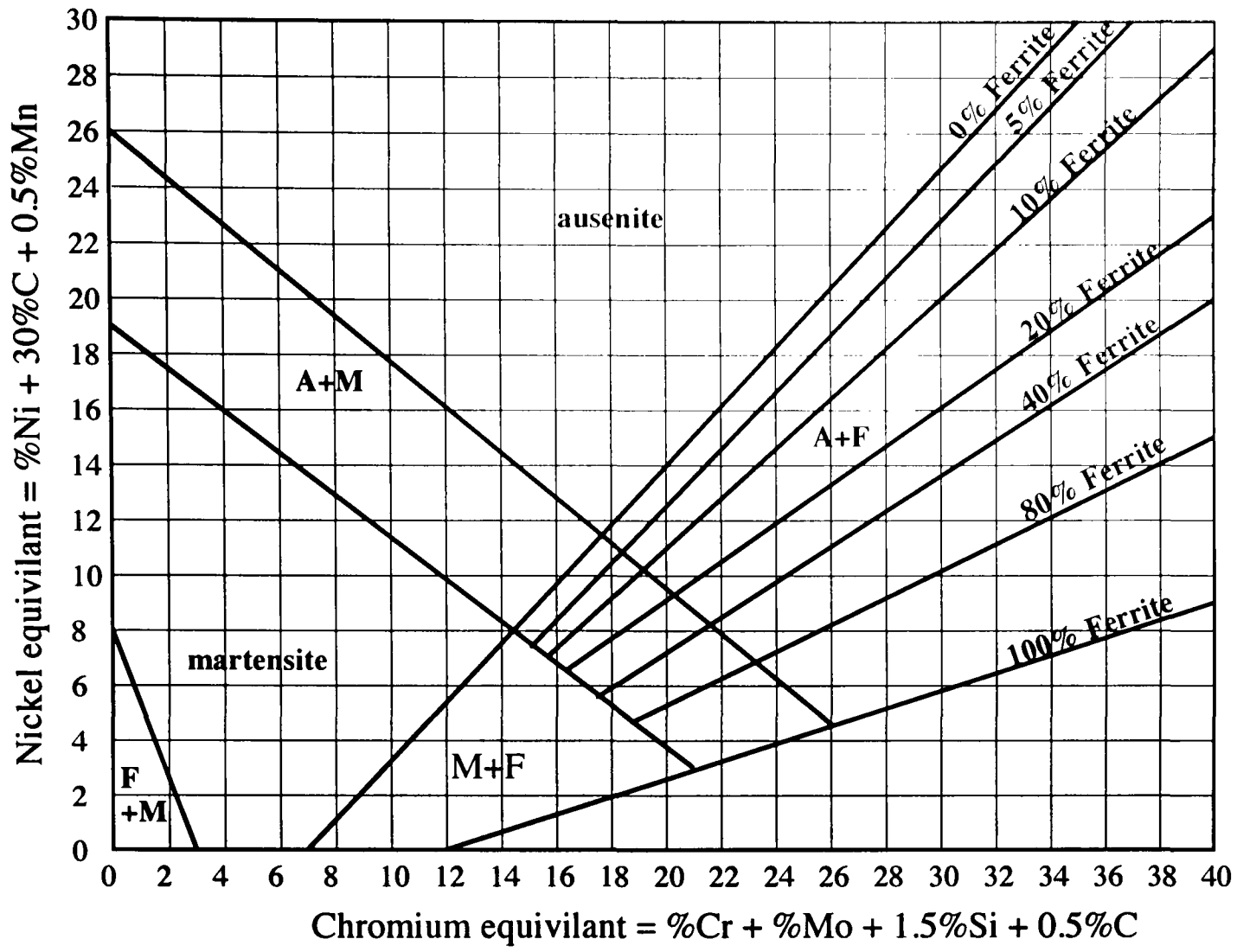

Figure 2.3 - Schlaeffer diagram, predicting the amount of α and γ present in weldments as a function of Cr and Ni equivilants[10]

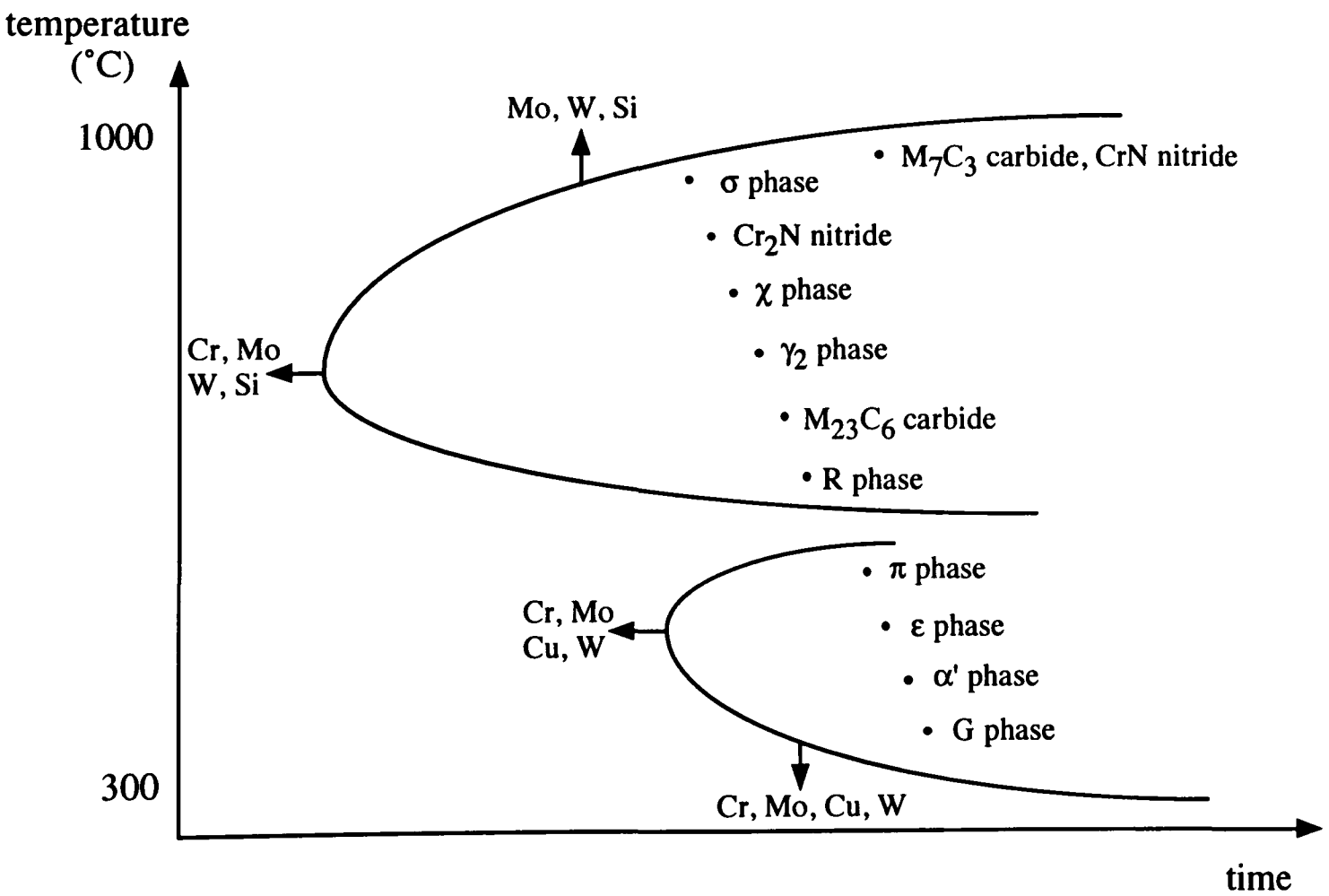

Figure 2.4 - Time-temperature-transformation curves for duplex stainless steels and effect of alloying elements[34]

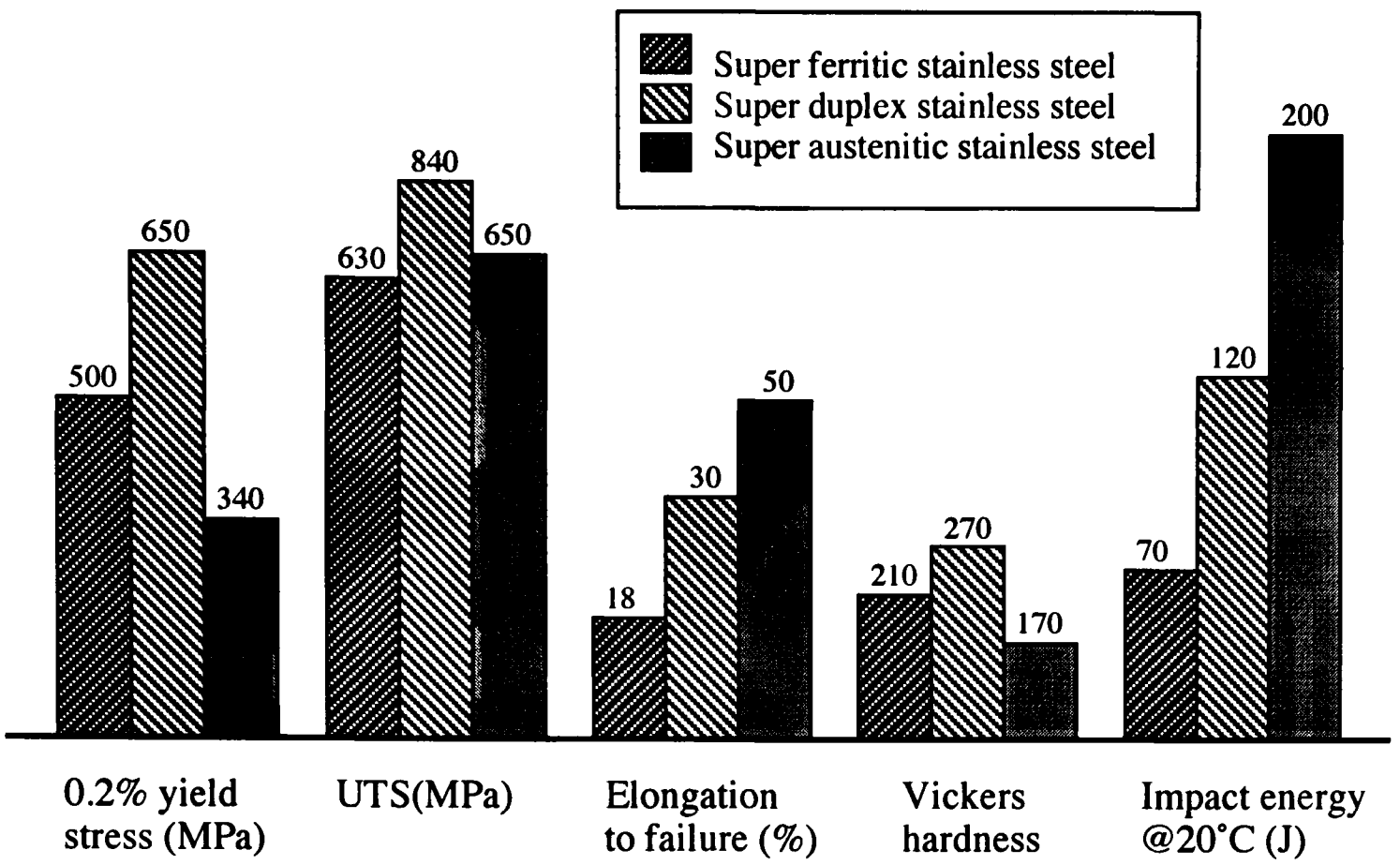

Figure 2.5 - Comparison of Mechanical Properties between types of Stainless Steels (CHA91b)

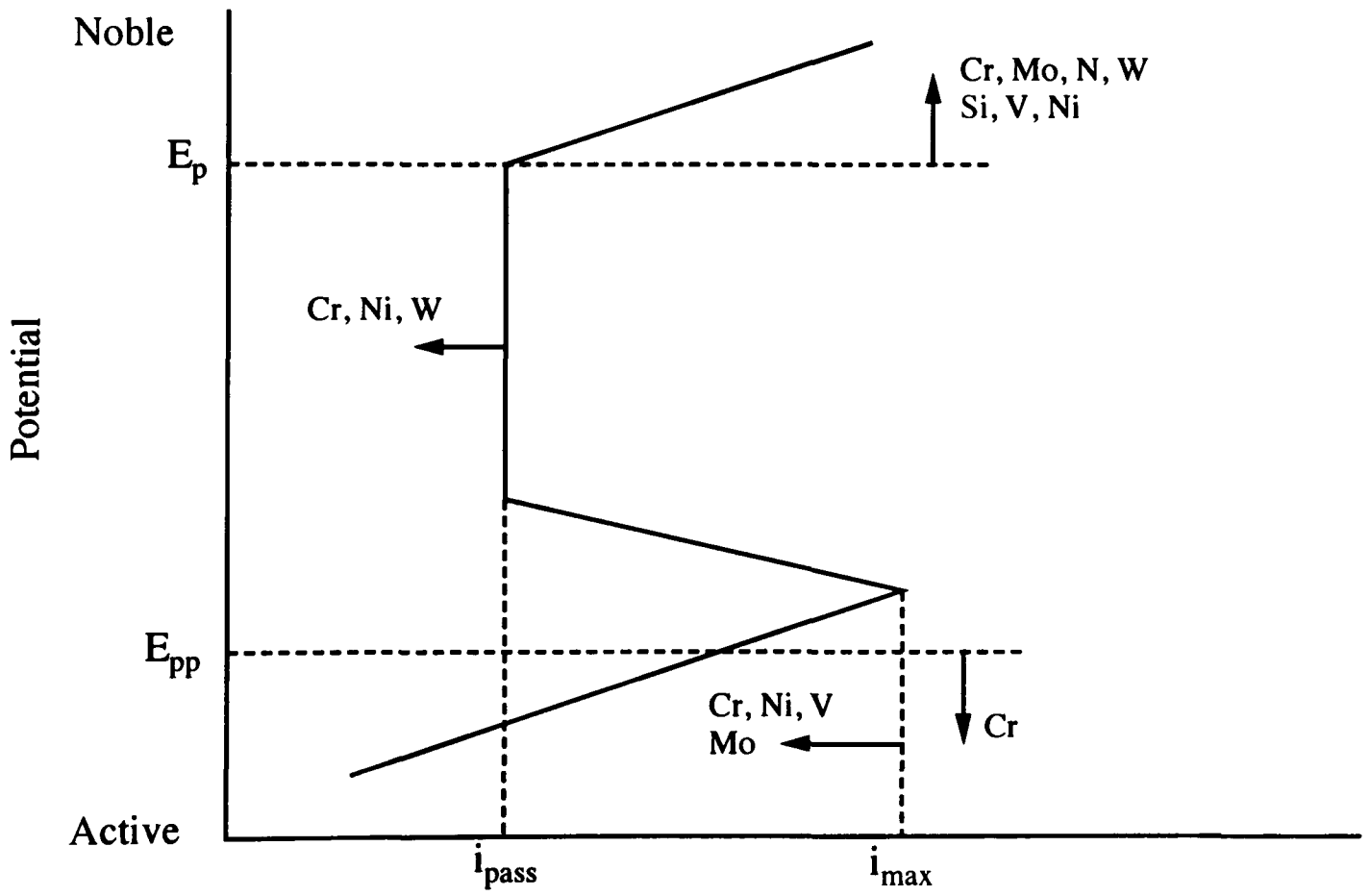

Figure 2.6 - Effect of alloying elements upon the anodic polarisation curve of a stainless steel (ROS86)

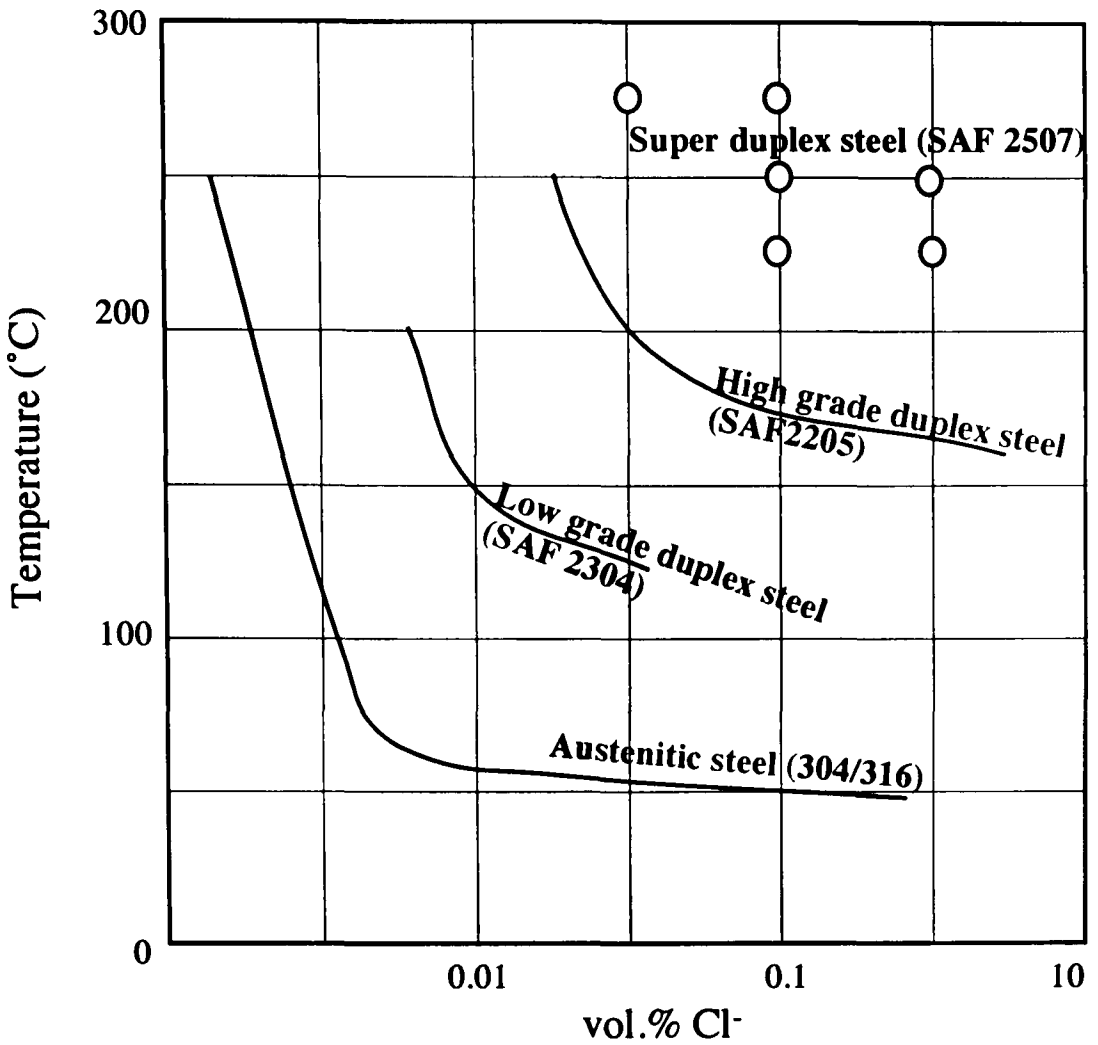

Figure 2.7 - Comparison of stress corrosion cracking resistance between different stainless steels[34] (tests at 1000hrs and $\sigma_{app}=\sigma_{ys}$ - note that open circles indicate tests where no stress corrosion cracking had occurred)

3 - FRACTURE

In order to explore the fracture behaviour of duplex stainless steels, it is necessary to understand the fundamentals of more general fracture mechanical models. Following the advent of all-welded structures in the early 20th Century, which was in turn accompanied by a large number of unexplained structural failures (most notably the Liberty ships of World War II), it became necessary to better understand the mechanisms of stress distribution and fracture. From this, early fracture mechanics concepts were evolved, specifically Linear Elastic Fracture Mechanics (LEFM), which attempted to model fracture in brittle systems. However, for more ductile materials such as steels, a newer approach called Elastic-Plastic Fracture Mechanics (EPFM) was introduced. More recently, models have been advanced which relate the fracture event to microstructural parameters. The development of these models has been well documented[1,2,3] and the following is an overview of the key elements.

3.1 LINEAR ELASTIC FRACTURE MECHANICS

3.1.1 The Griffith Model

In 1920 Griffith[4] became the first person to attempt to quantitatively analyse a fracture mechanics problem by modelling the propagation of scratches within glass. He considered a crack, length 2a, in an infinite plate of unit thickness, subjected to a uniaxial tensile stress, σ (figure 3.1). Using a thermodynamic approach, he argued that for a crack to grow, the total energy of the system, U, must be decreased, i.e. the elastic energy released from crack extension must exceed that of the surface energy created. Therefore in equilibrium:

$$\frac{dU}{da} = 0 = \frac{d\left(U_0 + U_a + U_\gamma - F\right)}{da} \qquad \text{.....(3.1)}$$

where U_0 is the elastic energy of the uncracked plate (constant), U_a is the change in elastic energy from crack growth, U_γ is the change in surface energy from crack growth and F is the work performed by external forces (zero for 'fixed grip' conditions).

Using a solution developed by Inglis[5] for the elastic stresses around an elliptical hole in an infinite plate, Griffith calculated the elastic energy release rate as:

$$U_a = \frac{\pi\sigma^2 a^2}{E} \qquad .....(3.2)$$

and thus showed that at the crack energy equilibrium:

$$\frac{d}{da}\left(\frac{\pi a^2\sigma^2}{E}\right) = \frac{d}{da}(4a\gamma_e) \qquad .....(3.3)$$

where γ_e is the elastic surface energy and E the Young's modulus of the bulk material. The left hand side of eqn.3.3 is known as the energy release rate, G (elastic energy released in infinitesimal crack extension), and the right the crack resistance, R (surface energy created in infinitesimal crack extension). When G is equal to R, a critical value of energy release rate, G_c, is achieved, which when exceeded results in unstable crack growth and hence fracture. The critical stress, σ_c for this to occur can be calculated as:

$$\sigma_c \geq \sqrt{\left(\frac{2E\gamma_e}{\pi a}\right)} \qquad .....(3.4)$$

However, this model assumes a uniaxial stress state, which is unrepresentative of real materials where stress constraints occur. When a bulk material is subjected to a tensile stress, the surface area is subjected to plane (biaxial) stress conditions (σ_1 & σ_2 variable, σ_3=0) whereas the centre of the material experiences a triaxial stress state (plane strain: $\sigma_3=\nu(\sigma_1+\sigma_2)$). Although the above equations are valid for plane stress conditions, they need to be modified to describe those of plane strain. From elasticity theory it can be shown that for a plane strain state the tensile strain, ε, for a tensile stress, σ is given by:

$$\varepsilon = \frac{\sigma}{E}(1-\nu^2) \qquad .....(3.5)$$

where ν is Poisson's ratio. Thus the plane strain critical tensile stress can be calculated as:

$$\sigma_c \geq \sqrt{\left(\frac{2E\gamma_e}{\pi a(1-\nu^2)}\right)} \qquad .....(3.6)$$

These equations are based on the assumption that the fracture event is purely elastic, i.e. of a completely brittle nature. Therefore, although this theory works well with materials such as glass, it is invalid for those that deform with even limited plasticity, such as metals. Irwin[6] modified the Griffith expression to include a term for the work of plastic deformation, γ_p:

$$\sigma_c \geq \sqrt{\left(\frac{2E(\gamma_e+\gamma_p)}{\pi a(1-\nu^2)}\right)} \qquad .....(3.7)$$

For ductile metals the elastic surface energy term is insignificant compared to the work done in plastic deformation, and thus may be approximated to:

$$\sigma_c \geq \sqrt{\left(\frac{E\gamma_p}{\pi a(1-\nu^2)}\right)} \qquad .....(3.8)$$

Orowan[7] independently accounted for plasticity by introducing a G_{crit} expression into the Griffith equation, which gave a similar result.

3.1.2 The Stress Intensity Factor

A major advance in the development of fracture mechanics for structural materials was made when Irwin[8] proposed a stress intensity analysis. He used linear elasticity theory to describe the stress state in the crack tip region, using the mathematical procedures of Westergaard[9]. A series of linear solutions were developed for each of the three types of crack loading (figure 3.2); opening (mode I), in-plane shear (mode II) and out-of-plane shear (mode III) . The magnitude of the stress is described in terms of a stress intensity factor K (which is conventionally given a subscript I, II or III to describe mode I, II or III loading respectively) as:

$$\sigma_{ij} = \frac{K}{\sqrt{2\pi r}} f_{ij}(\theta) \qquad .....(3.9)$$

where r and θ are the cylindrical polar co-ordinates with respect to the crack tip (figure 3.3). In order to calculate the stress intensity factor for real situations, it can be shown that the general form of K is represented by:

$$K = \sigma\sqrt{\pi a}.f\left(\frac{a}{W}\right) \qquad .....(3.10)$$

where f(a/W) is a dimensionless geometrical parameter dependent upon the crack length to component thickness ratio.

The stress intensity factor can be related to Griffith's calculation of fracture stress to provide a critical stress intensity for the onset of fracture, K_C. The critical stress intensity for mode I fracture K_{IC} is known as the fracture toughness of a material, and it is standard to only apply this for plane strain conditions (the plane stress fracture toughness is represented as K_C).

The stress intensity model can also be linked to Griffith's thermodynamic model. By calculating the energy release rate using an integral of the work done by surface forces in creating infinitesimal crack extension (the virtual work theorem[10]), G can be expressed as:

$$G = \frac{K^2}{E}\left(1-\nu^2\right) \qquad .....(3.11)$$

Note that care should be taken in relating the stress intensity to energy release rate. The critical failure stress can be calculated by combining eqns.3.10 and 3.11 to produce:

$$\sigma_c = \sqrt{\left(\frac{EG_{IC}}{\pi a\left(1-\nu^2\right)}\right)} \qquad .....(3.12)$$

which is consistent with the original Griffith equation if $G_{IC} = 2\gamma_e$. However, this is only true for a perfectly brittle material. If any ductility is present, this equation is invalidated as σ_c relates only to the local tensile stress at the instant of infinitesimal crack extension, whereas G_{IC} includes plastic deformation energy dissipated prior to catastrophic failure.

The importance of the critical stress intensity factor is that it is a constant material parameter (for an isotropic microstructure with constant stress state and temperature conditions). Hence once it has been measured for a given material, the stress distribution of any structure composed of this material may be calculated, and the failure stress for a given flaw size predicted. In addition, K values are simply additive, and so a complex, multiple stress system may be analysed. Note that in general $K_{IC} < K_{IIC} \leq K_{IIIC}$ and therefore K_{IC} is usually the most important structural parameter for design purposes.

3.1.3 Plastic Zone Size

The stress field solutions described above are not valid for real materials, as the stresses would tend to infinity approaching the crack tip. To prevent this, plastic deformation must occur, and hence there is a finite plastic zone around the crack tip. In it's simplest form, this can take the form of a cylinder, radius r_y (figure 3.4). The Inglis solutions for elastic stress distribution mentioned above, give the one-dimensional stress field as:

$$\sigma_{11} = \sigma\sqrt{\frac{\pi a}{2\pi r}} = \frac{K_I}{\sqrt{(2\pi r)}} \qquad .....(3.13)$$

Assuming the material behaves in a perfectly elastic/perfectly plastic manner with a sharp interface, the plastic zone size may be estimated by substituting the yield stress σ_{ys} for σ_{11} to give:

$$r_y = \left(\frac{1}{2\pi}\right)\left(\frac{K_I}{\sigma_{ys}}\right)^2 \qquad .....(3.14)$$

McClintock and Irwin[11] showed that in practice, the plastic zone size would have to be greater than that above, in order to provide an equilibrium of stress distribution. They showed that the plastic zone would actually have a diameter of $2r_y$. This in turn would increase the local stress intensity, thus effectively increasing the crack length. This effective increase in length was found to be equal to r_y (figure 3.5).

Dugdale[12] provided another analysis of plastic zone size by assuming that all plastic deformation is concentrated in a strip ahead of the crack. He argued that the crack was effectively extended by an amount Δa_n, over which it behaves as a perfectly plastic material, i.e. the stress field (which acts to close the crack) is equal to the yield stress (figure 3.6). By superimposing the stress fields of an infinite crack in tension with that of a crack with closure stresses at the tip, he showed that:

$$\left(\frac{a}{a+\Delta a_n}\right)=\cos\left(\frac{\pi\sigma}{2\sigma_{ys}}\right) \qquad .....(3.15)$$

It can be seen that as $\sigma \to \sigma_{ys}$, then $\left(\frac{a}{a+\Delta a_n}\right)\to 0$, and thus the plastic zone extends across the infinite plate as the yield stress is approached. This can be simplified ($a>>\Delta a_n$, thus $\frac{a}{a+\Delta a_n}\approx\frac{a-\Delta a_n}{a}$, and the cos term can be expanded by a Taylor approximation) to produce:

$$\Delta a_n=\frac{\pi}{8}\left(\frac{K_I}{\sigma_{ys}}\right)^2 \qquad .....(3.16)$$

Note that only the first 2 terms of the Taylor expansion are used, as the fracture stress can be assumed to be much smaller than the yield stress, i.e. $\sigma<<\sigma_{ys}$.

The above expressions were calculated assuming plane stress conditions. Under a plane strain state, the plastic zone size is reduced, as it is constrained by the triaxial stress field. McClintock and Irwin[11] have estimated the plastic zone size for this case as:

$$r_y\approx\left(\frac{1}{6\pi}\right)\left(\frac{K_I}{\sigma_{ys}}\right)^2 \qquad .....(3.17)$$

Therefore for a non-infinite plate, the size of the plastic zone, and hence the fracture toughness, will vary across the specimen as the stress state changes from plane stress (surface) to plane strain (centre). This an important consideration for specimen size in K_{IC} tests (as discussed in section 3.1.4).

Both the Irwin and Dugdale models give reasonable estimates of the plastic zone size, but only for their specific zone shapes. An impression of the plastic zone shape in real materials can be derived from classical yield criteria (such as those of Von Mises and Tresca) using first order size approximations[13] (figure 3.7). More advanced methods such as finite element (FEM) analysis can be used to give more accurate estimates of plastic zone size and shape [14,15,16].

3.1.4 LEFM Toughness Testing

The resistance of a material to crack extension may be measured using a standard K_{IC} test. From eqn.3.10, solutions of the geometrical function f(a/W) have been developed[17] to allow calculation of the fracture toughness for a number of standard notched test specimens. In order to conform to LEFM conditions, the tip radius and plastic zone of the notch must be as small as possible. Thus a precrack is fatigued into a specimen prior to testing, using a small R (K_{min}/K_{max}) ratio to ensure that K_{max} is small compared to that of fracture (K_{IC}).

As discussed in section 3.1.3, the plastic zone size varies across the specimen width as the stress state changes, and hence the fracture toughness varies according to testpiece width (figure 3.8). It can be seen that above a certain testpiece width, the toughness tends to a minimum value where the specimen is predominantly (around 90% crack plane area) in a state of plane strain. This is taken to be the plane strain fracture toughness, K_{IC} of the material.

Various international standards have been developed in order to ensure that a K_{IC} test specimen is large enough to be valid, and the British standard[18] states that in order for this to be so:

$$(B,\ W-a,\ a) \geq 2.5\left(\frac{K_{IC}}{\sigma_y}\right)^2 \qquad \text{and } 0.45 \leq \left(\frac{a}{W}\right) \leq 0.55 \qquad \text{.....(3.18)}$$

where B and W are specimen width and depth respectively (generally B=2W). From Irwin's estimations for the plane stress and plane strain plastic zone sizes (eqns.3.14 and 3.17) it can be calculated that $B \geq 16r_y$ (plane stress) and $B \geq 50r_y$ (plane strain). Hence the standard ensures that for a valid specimen, the material is in a predominantly plane strain state, and that the width of the plane strain plastic zone is small compared to the uncracked area. Also, the dimensional criteria ensure that testpiece width and uncracked ligament depth (W-a) are equal, hence efficient use is made of the material.

During testing, a load-displacement curve is obtained, the nature of which varies according to the material behaviour (figure 3.9). For type II (pop-in) and III (brittle fracture) curves, the fracture toughness is calculated from the critical load P_Q. However, for a type I curve, where fracture is preceded by a significant amount of stable crack growth, the critical load is taken at the intersection of a 5% secant line. From the variation of f(a/W) with crack length, it can be shown that this is roughly equivalent to a (plastic) crack extension of 2%. This corresponds to the maximum allowable plane strain plastic zone size under the specimen size constraints above. Specimens for which extensive crack growth occurs such that:

$$\frac{P_{max}}{P_Q} \geq 1.10 \qquad \text{.....(3.19)}$$

are deemed invalid, as the K_{IC} value calculated at 2% crack extension would be a large underestimate of the actual material toughness.

The K_{IC} test is however limited in its applications. For many structural metals such as steel, the material is so ductile that size constraints make it is impossible to produce manageable specimens that are valid. Also, for real engineering service situations, the material is often subjected to a transitional or plane stress state. A model for plane stress fracture toughness testing (K_C) has been produced by Fedderson[19]. He used thin, centre-cracked panels in tension to measure the stress intensity variation during crack growth, from initiation to failure. However, the results are of limited value, as they are not an absolute material constant, being only consistent for a given

specimen thickness and similar a/W values. Therefore, other testing methods are necessary.

Finally, it should be noted that although the above fracture tests are scientifically desirable for measuring a material's toughness, they are time consuming and expensive, and thus are not always practical from an industrial perspective. Several qualitative tests, most notably the Charpy test[20] have been developed. The Charpy test involves the measurement of the impact energy of a large pendulum hammer upon a standard sized notched specimen. The principal problem of the test is that the specimens have low constraint (they are usually subsize for plane strain conditions) and thus the impact toughness is not an absolute material parameter. Also, the loading conditions are dynamic, and as such do not create a uniform stress field within the test specimens. However, for ease of use this test remains an industry favourite and toughness criteria for structures are invariably based upon impact values. An improvement to the standard test is to instrument the Charpy machine to record the variation of load during impact, and to use fatigue pre-cracked specimens[21], but this is not yet widely practised.

Some investigators[22,23,24] have attempted to elucidate empirical relationships between Charpy and fracture toughness values. However, it is difficult to compare test results, as fracture toughness relates only to stable crack growth prior to unstable failure, whereas impact toughness values incorporate the total energy of fracture across the whole specimen. In addition the high strain rate imposed by a Charpy test during testing (which has been calculated[25] as up to $3000s^{-1}$) can have a significant effect upon the fracture mechanisms and hence toughness values[26]. Therefore, such comparisons are generally confined to a given material under specific conditions and as such are of limited general value.

3.2 ELASTIC PLASTIC FRACTURE MECHANICS

LEFM was developed to describe fracture under largely elastic conditions and is therefore only applicable to relatively brittle materials. Modifications to include crack tip plasticity are limited, as excessive deformation distorts the elastic stress field, and hence many materials are too ductile to be accommodated within this model. Therefore, elastic-plastic fracture mechanics (EPFM) has been developed to describe material deformation where fracture occurs after large scale plasticity relative to the crack.

The difficulty with EPFM material behaviour is that it involves slow, stable crack growth, and as such is impossible to describe as a single parameter. Also, the crack tip stress fields are much more complex than for LEFM and difficult to model. However, it is possible to predict crack initiation using an elastic-plastic parameter. There are two common approaches to this; the J-integral energy balance concept, widely used in the USA, and the crack opening displacement (COD) approach, developed in the U.K. and used throughout this thesis.

3.2.1 The J-Integral Approach

The J-integral was first introduced by Rice[27] who considered the behaviour of a sharp crack in a non-linear elastic material. J is essentially defined as the non-linear elastic equivalent of G, such that:

$$J = \frac{d(F - U_a)}{da} \qquad .....(3.20)$$

The energy balance for crack extension (eqn.3.1) can be valid for non-linear as well as linear elastic behaviour. From this, the potential energy of crack extension, U_p, which includes all the terms that could contribute to non-linear behaviour (U_γ is assumed irreversible) can be written as:

$$U_p = U_0 + U_a - F \qquad .....(3.21)$$

Since U_0 is a constant, this can be differentiated to give:

$$\frac{dU_p}{da} = \frac{d(U_a - F)}{da} \qquad .....(3.22)$$

Therefore from eqn.3.21:

$$J = -\frac{dU_p}{da} = \frac{K^2(1-\nu^2)}{E} \qquad .....(3.23)$$

as by definition, J and G are equivalent for elastic loading conditions.

The derivation of J is highly mathematical, but in essence it is describes the crack tip stress and displacement fields via an integral, incremental length ds, of the strain density (w) and traction vector T_i (directional shearing force) along a contour (Γ) around the crack tip:

$$J = \int_{\Gamma}\left(wdy - T_i(\delta u / \delta x)ds\right) \qquad .....(3.24)$$

and

$$w = \int_0^{\varepsilon_{ij}} \sigma_{ij} d\varepsilon_{ij} \qquad T_i = \sigma_{ij} n_j \qquad .....(3.25)$$

where x and y are respectively directions parallel and perpendicular to the crack length, and n_j the components of the unit vector normal to Γ. Rice showed that for a closed contour J=0 and as such is path independent. Therefore J may be calculated remote from the crack tip and therefore outside the plastic zone, such that an elastic calculation can be used to produce an elastic-plastic energy release rate.

It has been shown that J can be used to characterise the stress distribution ahead of the crack tip for a non-linear material (e.g. using the HRR singularity[28,29]) and hence can be used as a material parameter to describe fracture toughness. J is only valid for non-linear elastic, and therefore reversible behaviour, and so it is not strictly valid if actual plastic deformation has occurred. Also, it assumes that no unloading occurs in the material, hence it is only valid up to the onset of crack extension. However, a critical value J_{IC} may be defined at this point[30] which is a material property analogous to G_{IC} predicting the onset of crack growth. This is becoming increasingly used to assess structural integrity for non-linear materials with the introduction of design

curves[31]. Despite the limitations after the onset of fracture, J may still be used to describe material behaviour during stable crack growth by the use of J-resistance curves[32].

3.2.2 The Crack Opening Displacement Approach

The crack opening displacement (COD) approach was originally developed to allow toughness assessments of steels, specifically welded structures, to be made. It was Wells[33], who noted that during K_{IC} testing of steels, the crack faces were displaced prior to failure by an amount that increased with the material's toughness. He argued that fracture was controlled by plastic strain in the crack tip region and that the lateral displacement, the COD (δ), of the crack surface was a measure of this plastic strain. Therefore, δ would be expected to reach a critical value upon crack initiation. He used Irwin's plastic zone model of an effectively extended crack tip to calculate the crack opening at the physical crack tip and showed that:

$$\delta = \frac{4K_I^2}{E\pi\sigma_{ys}} = \frac{4G}{\pi\sigma_{ys}} \qquad .....(3.26)$$

Burdekin and Stone[34] provided an alternative method of calculating the COD. They expanded the Dugdale strip yielding model, to calculate the crack opening as:

$$\delta = \frac{8a\sigma_{ys}}{\pi E}\ln.\sec\left(\frac{\pi\sigma}{2\sigma_{ys}}\right) \qquad .....(3.27)$$

This can be expanded to:

$$\delta = \frac{8a\sigma_{ys}}{\pi E}\left(\frac{1}{2}\left(\frac{\pi\sigma}{2\sigma_{ys}}\right)^2 + \frac{1}{12}\left(\frac{\pi\sigma}{2\sigma_{ys}}\right)^4 + ...\right) \qquad .....(3.28)$$

which, assuming that fracture occurs well below the yield stress ($\sigma << \sigma_{ys}$) can be reduced to:

$$\delta = \frac{K_I^2}{E\sigma_{ys}} = \frac{G}{\sigma_{ys}} \qquad .....(3.29)$$

This varies slightly from eqn.3.26. In general, the crack opening displacement is found to be represented by:

$$\delta = \frac{G}{m\sigma_{ys}} \qquad .....(3.30)$$

where m is a constant between 1 and 2 depending upon specimen geometry and material type (which can be experimentally determined[35]). The above derivations are important, as they show that in the elastic region, the COD model is consistent with LEFM concepts. From eqn.3.25 it can be seen that J and δ may be related as:

$$J = m\sigma_{ys}\delta \qquad .....(3.31)$$

It has been shown that this relationship is also valid under non-LEFM conditions[36].

In practice, the actual crack tip opening displacement of a specimen is difficult to measure, and so it is ascertained by measuring the plastic displacement, V_p, at the crack mouth between 2 knife edges (figure 3.10). This model assumes that plastic rotation occurs around a central point at a specific distance below the crack base, defined by a rotational factor, r. Note that although the exact rotational point can differ between materials due to a variation in work-hardening behaviour, a value of $r \approx 0.4$ has been experimentally determined for ferritic steels[37], and it is standard to apply this to all metals. From similar triangles it can be seen that:

$$\frac{\delta}{r(W-a)} = \frac{V_p}{r(W-a)+a+z} \qquad .....(3.32)$$

where z is the knife edge thickness. Therefore the COD can be calculated as:

$$\delta = \frac{r(W-a)V_p}{r(W-a)+a+z} \qquad .....(3.33)$$

However, this hinge model is only accurate when the elastic deformation is small compared to the plastic component. Therefore, in practice the elastic COD is calculated from the applied load and the plastic displacement calculated from a load-displacement curve (by extrapolation of the elastic region). The British Standard[38] for COD calculation imposes m and r values of 2 and 0.4 respectively to define δ as:

$$\delta = \frac{K_I^2\left(1-\nu^2\right)}{mE\sigma_{ys}} + \frac{0.4(W-a)V_p}{0.4W+0.6a+z} \qquad .....(3.34)$$

Various load-displacement curves can be obtained from a COD test (figure 3.11) and as such produce a variety of critical COD terms. These include δ_c, which identifies the point at which unstable fracture occurs after zero or less than 0.2mm of ductile crack growth (lower shelf behaviour), δ_u where unstable fracture occurs after greater than 0.2mm of ductile crack growth (transition behaviour), δ_i at the onset of stable crack growth (analogous to J_{IC}) and δ_m where a maximum load plateau occurs (upper shelf behaviour).

The COD concept is essentially flawed, as eqn.27 can only strictly be applied to an infinite plate and assumes no work-hardening occurs. Unlike K_{IC} and J tests, solutions for specific specimen geometries cannot be calculated. However, COD tests provide a useful comparison of fracture resistance between ductile materials. In addition, the critical load and crack length for structural failure to occur may be made using a COD design curve.

3.2.3 The COD Design Curve

An analytical COD design curve was originally introduced by Burdekin and Stone[34] in order to relate the critical COD value to the maximum permissible strain in a cracked structure. They introduced a dimensionless COD, Φ, defined by:

$$\Phi = \frac{\delta E}{2\pi\sigma_{ys}a} = \frac{\delta}{2\pi\varepsilon_{ys}a} \qquad .....(3.35)$$

where ε_{ys} is the elastic strain at yield. A calculation based upon the Dugdale model, was used to obtain an expression for the normalised failure strain in the vicinity of a crack, $\varepsilon_f/\varepsilon_{ys}$. From this a plot of Φ vs. $\varepsilon_f/\varepsilon_{ys}$ could be obtained for various crack size to gauge length (a/Y) ratios. However, when compared to experimental values it was found[39] that the results lay on a broad scatter band and that there was no discernible effect of (a/Y) ratio (figure 3.12). It can also be seen that the results deviated from the theoretical curve when $\varepsilon_f/\varepsilon_{ys}>0.5$. This is because the model is based upon an infinite plate and hence only valid for local yield conditions. In practice, sufficient plastic deformation (i.e. $\varepsilon_f/\varepsilon_{ys}>0.5$) causes general yield across the net section, invalidating the calculation.

Therefore, the analytical approach is useless if $\varepsilon_f/\varepsilon_{ys}>0.5$ and so an empirical approach must be used.

This problem was alleviated by drawing an empirical design curve above the data points on the graph. It was found that this curve was of the form:

$$\Phi = \left(\frac{\varepsilon_f}{\varepsilon_{ys}}\right)^2 \qquad \text{for } \varepsilon_f/\varepsilon_{ys}<0.5$$

$$\Phi = \frac{\varepsilon_f}{\varepsilon_{ys}} - 0.25 \qquad \text{for } 0.5<\varepsilon_f/\varepsilon_{ys}<2 \qquad .....(3.36)$$

This was modified by Dawes[40]. He assumed that $\varepsilon_f/\varepsilon_{ys} \approx \sigma_{tot}/\sigma_{ys}$ (where σ_{tot} is the total stress present in the region, including residual stresses) and thus calculated the maximum permissible crack size, a_{max}, at a critical COD value δ_{crit} such that:

$$a_{\max} = \frac{\delta_{crit} E \sigma_{ys}}{2\pi\sigma_1^2} \qquad \text{for } \sigma_{tot}/\sigma_{ys}<0.5$$

$$a_{\max} = \frac{\delta_{crit} E}{2\pi\left(\sigma_1 - 0.25\sigma_{ys}\right)} \qquad \text{for } 0.5<\sigma_{tot}/\sigma_{ys}<2 \qquad .....(3.37)$$

Typical results are shown in figure 3.13, and it is apparent that the curve is a conservative estimate. This can be verified as, by arranging eqn.3.37 it can be seen that:

$$\delta_{crit} = \frac{2\pi\sigma_1^2 a_{\max}}{E\sigma_{ys}} = \frac{2K_I^2}{E\sigma_{ys}} \qquad .....(3.38)$$

This is twice the value of COD obtained from eqn.3.29.

Various standards e.g.PD6493[41], have been published to implement the COD design curve towards defect tolerance predictions for welded structures. Although this approach is only empirical, its use is now well established in industry[42,43], and has been shown[44] to provide an accurate fitness for purpose assessment.

3.3 MICROMECHANISMS OF FRACTURE FOR FERRITIC STEELS

Although the fracture mechanics models previously discussed in this chapter provide methods of predicting the failure stress of metals, they provide only a macroscopic description of fracture behaviour. Events occurring on the microstructural scale ahead of the crack tip can be expected to dictate the crack growth behaviour, and hence it is important to relate the fracture event to microstructural parameters. This section deals with the development of a so-called 'microscopic' model of fracture, specifically for cleavage fracture of ferritic steels.

3.3.1 Development of the Cleavage Cracking Model

From early observations of fracture, it was shown that cleavage fracture occurred in notched iron tensile specimens at higher test temperatures than for that of smooth specimens. Orowan[45] suggested that cleavage was controlled by a critical fracture stress which he postulated to be temperature independent. Therefore, the triaxial stress state in a notched specimen exceeds the fracture stress at a higher test temperature than for the lower uniaxial stress state of a smooth specimen (figure 3.14). This model introduced the important concept of a critical tensile stress criterion for cleavage fracture, but failed to account for the mechanisms by which cleavage fracture could occur.

An important experiment by Low[46] on iron tensile specimens tested at low temperature revealed that the yield stress in compression was always less than or equal to the fracture stress in tension. This indicated that dislocation motion was a necessary precursor to cleavage fracture. This was supported by Knott and Cottrell's[47] observation from slow bend tests of double-notched specimens that stable microcracks were nucleated within the material prior to cleavage failure, indicating that they were nucleated by a deformation process.

3.3.2 Microcrack Formation in Mild Steel

There are several mechanisms to account for microcrack formation in mild steel. Hull's model[48] of twin-nucleated microcracks suggested that the growth of the microcrack is the critical factor for cleavage. He suggested that upon intersection of twinning dislocations producing $(1\bar{2}1)$ and (121) twins, an interface on the (101) plane is produced:

$$\frac{a_0}{6}[111]_{(1\bar{2}1)} + \frac{a_0}{6}[1\,\bar{1}\,1]_{(121)} \rightarrow \frac{a_0}{3}[101]_{(010)} \quad .....(3.39)$$

Each such dislocation effectively forms a small hole along the interface, and thus if a large number of such 'holes' are present, together with a sufficient tensile stress, cleavage will occur along the (010) plane. This was a suitable explanation for the observed low temperature behaviour. It should be noted that twins are often also observed at higher test temperatures adjacent to cleavage cracks. This is due to the high propagation rate of cleavage fracture promoting twin deformation (which can occur at a much higher rate than that of slip) and hence their appearance is not necessarily related to the nucleation event[49].

Stroh[50] modified an earlier model by Zener[51] involving a crack nucleating from the stress concentration ahead of a dislocation pile-up against a sessile barrier (e.g. grain boundary, Lomer-Cottrell lock). He thus suggested that the critical stage of fracture was the strain-controlled nucleation of the microcrack and showed that:

$$\tau_{eff} \equiv \tau_y - \tau_i \geq \left(\frac{12\pi\mu\gamma_e}{(1-\nu)d}\right)^{\frac{1}{2}} \quad .....(3.40)$$

where τ_{eff} is the effective shear stress on the slip plane, τ_y the yield stress of shear, τ_i the friction stress, μ the shear modulus, and d the grain diameter. However, Cottrell[52], suggested that microcrack growth was the critical stage of fracture. He showed that a microcrack could be formed by the energetically favourable coalescence of two glissile dislocations to form a sessile dislocation

$$\frac{a_0}{2}[\bar{1}\,\bar{1}\,1]_{(101)} + \frac{a_0}{2}[111]_{(\bar{1}01)} \rightarrow a_0[001]_{(001)} \quad .....(3.41)$$

Other dislocations gliding on the orthogonal (101) and $(\bar{1}01)$ slip planes are then attracted together, resulting in a high density of dislocations piling up around the sessile dislocation. This effectively drives a wedge into the (001) cleavage plane, thus forming a microcrack. He showed that the critical fracture stress, σ_f, required to grow such a crack was given by:

$$\sigma_f \geq 2\left(\frac{\beta\mu\gamma}{d}\right)^{\frac{1}{2}} \qquad .....(3.42)$$

where β is a constant close to 1

Although both the Stroh and Cottrell models were consistent with the experimental observation that cleavage was more prevalent in a fine grain sized material[46], only Cottrell's growth controlled model could account for the observation of stable microcracks at the notch root[53] (indicating that microcrack formation did not necessarily lead to failure). Also Stroh's model only considered the shear strain necessary to produce cross-slip, and neglected the critical tensile stress that had been shown experimentally to effect the cleavage behaviour.

However, the above models can only properly describe fracture initiation in clean, single phase metals. In practice structural materials, such as mild steel, contain a large amount of second phase particles and inclusions. McMahon[54] found that cleavage fracture in mild steel was promoted by the presence of carbides, and that large inclusions had a greater effect than smaller ones. Smith[55] used these results to form a model for microcrack formation due to dislocation pile-up against a grain boundary carbide film, thickness C_0. Assuming the Hall-Petch relationship[56] to calculate the effective shear stress acting on the carbide, he showed that:

$$C_0\sigma_f^2 + k_y^2\left(\frac{1}{2} + \frac{2\tau_i\sqrt{C_0}}{\pi k_y}\right)^2 \geq \frac{4E\gamma_p}{\pi(1-\nu^2)} \qquad .....(3.43)$$

where k_y is the Hall-Petch constant. If the energy of dislocation pile-up is ignored, this can be reduced to:

$$\sigma_f \geq \left(\frac{4E\gamma_p}{\pi C_0 (1-\upsilon^2)} \right)^{\frac{1}{2}} \qquad .....(3.44)$$

which is a form of the Griffith theory, with the microcrack extending across the carbide film thickness. Curry and Knott[57] investigated the formation of cleavage in a steel containing spheroidized carbides, and showed that:

$$\sigma_f \geq \frac{\pi}{2} \left(\frac{2E\gamma_p}{\pi r_c (1-\upsilon^2)} \right)^{\frac{1}{2}} \qquad .....(3.45)$$

where r_c is the 95th percentile carbide radius. For very fine-grained steels, which have a large grain boundary area, the critical event has been found to be the propagation of the microcrack across this boundary[3] such that the Griffith criterion becomes:

$$\sigma_f \geq \left(\frac{\pi E\gamma_{gb}}{d(1-\upsilon^2)} \right)^{\frac{1}{2}} \qquad .....(3.46)$$

where γ_{gb} is the plastic energy per unit area required to propagate a crack across a grain boundary. This assumes an equiaxed grain structure. Dolby and Knott[58] modified this expression to derive the fracture stress in fine-grained martensitic and bainitic microstructures with packet shaped morphologies. More recently, cleavage fracture models have been extended to describe failure in weld metals[59,60,61].

3.3.3 Determination of the Critical Cleavage Stress for Fracture

It has been established above that the fracture stress of a steel is the critical controlling variable for cleavage failure. Early measurements calculated this stress from the load at fracture and cross-sectional area at failure. However, these results were not rigorous because of the uncertainty of the reduction of area due to plastic instability. Using slow notch bend tests, it is possible to calculate the fracture stress at the coincident temperature of fracture and general yield from slip line field theory. By varying the notch angle in specimens, Knott[62] was able to measure the cleavage fracture stress and thus verify its temperature independence (although it has since been shown that there is often a weak variation of σ_f with temperature[63]).

The introduction of elastic-plastic finite element modelling allowed the fracture stress to be more easily calculated. The most widely used analysis, developed by Griffiths and Owen[64] is based upon the von-Mises yield criteria and predicts the position of the maximum tensile stress ahead of a blunt notch as a function of the applied stress to yield stress ratio (figure 3.15). This maximum tensile stress at failure is taken to be the microscopic cleavage fracture stress. This approach assumes that critical failure is nucleated within this region and Knott's observation of stable microcracks at the notch root appears to verify this.

3.3.4 The Prediction of Fracture Toughness from Microstructural Parameters

Richie, Rice and Knott[65] were amongst the first researchers to suggest a relationship between macroscopic fracture toughness, K_{IC}, and microscopic fracture mechanisms (the RKR model). Using a finite element solution from Rice and Tracey[66] they showed that the peak stresses ahead of a sharp crack were much greater than for a blunt notch, and hence the cleavage fracture stress is exceeded at a much lower applied stress than is actually observed for fracture. They postulated that cleavage could only occur when the fracture stress was exceeded over a characteristic distance, r^* (figure 3.16). Thus the general form of the stress intensity factor (eqn.3.10) can be redefined (for the purely elastic case) as:

$$K_{IC} = \sigma_f \sqrt{(2\pi r^*)} \qquad .....(3.47)$$

If this distance, together with the fracture stress is assumed to be temperature independent, the temperature dependence of fracture toughness can thus be predicted from the variation of the yield stress with temperature.

Ritchie et al experimentally found this characteristic distance to be equal to 2 grain diameters for mild steel. They argued for fracture to occur, the local stresses must be sufficient to propagate a microcrack into a neighbouring grain, hence the observed critical distance of 2d. In general, it has been shown[57] that there is no unique

relationship between critical distance and microstructure, although the RKR model has been extended to other microstructures with limited success[67,68]. The strength of the RKR model is that it introduces the concept that the fracture criterion is governed by local stresses and strains existing over an area ahead of the crack tip.

Curry and Knott[69] provided a statistical explanation of the RKR model, by suggesting that the controlling parameter for cleavage was the distribution of microcrack nuclei ahead of the crack tip. They found that in mild steel, the probability of cleavage was controlled by the distribution of carbide particles and that a finite area must be sampled ahead of the crack tip in order to encompass a large enough carbide particle to nucleate fracture. Hence cleavage failure can be expressed statistically as the probability of a nucleation site residing within the critical distance ahead of the crack tip. More advanced statistical models including Weibull extreme value statistics and weakest link theory have since been advocated[70,71,72], but these are only numererical representations of data and hence fail to provide any further insight into the micromechanisms of fracture.

3.3.5 The Brittle to Ductile Transition and Fibrous Fracture

The RKR model provides a good explanation of cleavage failure at low test temperatures (lower shelf behaviour.) The yield stress is high, ensuring that the plastic zone required to reach the critical fracture stress is small. However, as the test temperature is increased, the yield stress decreases and hence the plastic zone required for failure is enlarged (which in turn increases K_{IC}). At a critical test temperature, T*, when the peak of the elastic stress distribution is equal to the critical distance, the RKR model breaks down[73] (figure 3.17). This critical temperature can be affected by local constraint (specimen thickness), prestrain and material inhomogenaity, and hence is difficult to model.

In theory, cleavage cannot occur at test temperatures above T*. In practice however, the local yield stress can be raised by a fast growing crack such that cleavage fracture can still occur[74] (transition region behaviour). Note that fibrous fracture has been observed to occur below T* in the form of ductile tongues between cleavage facets[75]. This is because an advancing crack can encounter impenetrable barriers (such as particles or highly misoriented grains) which divert the crack around the region, leaving behind an unbroken ligament which subsequently ruptures in a ductile manner.

At still higher test temperatures, when the cleavage fracture stress cannot be achieved by any means, exclusively ductile fracture ensues (upper shelf behaviour). The micromechanisms of ductile fracture, incorporating void nucleation, growth and coalescence have been well reviewed[76,77,78] and will not be considered further, as this thesis is primarily concerned with low temperature cleavage fracture behaviour.

3.4 FRACTURE OF DUPLEX STAINLESS STEELS

3.4.1 Introduction

The previous discussion related the fracture behaviour of a ferritic steel to its microstructure in a quantitative manner and thus it might be hoped to extend these models to ferritic/austenitic duplex stainless steels. At first sight, the fcc austenite phase is ductile, hence the fracture behaviour is dependent upon the brittle ferrite phase and so the standard ferrite cleavage models might apply.

However, the stress distribution within a duplex stainless steel is much more complex than that of a single phase material. Although a simple law of mixtures can be applied to model the stress distribution, based upon the relative phase volume fractions[79], the situation is complicated by the variation in grain size[80] (and thus Hall-

Petch strengthening) and work hardening between phases[81]. In addition, duplex steels are clean (i.e. contain very few inclusions compared to austenitic alloys), hence it is not possible to trace the fracture initiation event to a single microstructural feature (such as a carbide). Finally, it cannot always be assumed that austenite remains a ductile phase, regardless of test conditions. The high strain rate of Charpy testing has been observed to trigger the martensitic transformation of austenite, which subsequently cleaves[82]. It has also been suggested that in very high nitrogen containing alloys, the austenite phase is sufficiently strengthened to fracture in a brittle manner[83,84]. Thus fracture models for duplex stainless steels are by necessity limited to qualitative descriptions of the micromechanisms of fracture and their effects upon fracture toughness.

3.4.2 Effect Of Microstructural Parameters Upon Fracture Behaviour

The room temperature fracture behaviour of duplex stainless steels is well established[85,86]. The fracture toughness is very high and comparable to that of austenitic steels. Both phases are ductile and voids are preferentially nucleated within the ferrite phase or upon phase boundaries. Hence the toughness values are found to be anisotropic if the microstructure is elongated. Currently, interest is centred on the low temperature fracture behaviour, where embrittlement of the ferrite matrix can result in much reduced toughness values.

Lower temperature fracture (<0°C) is generally characterised by mixed-mode failure of the phases. Ferrite has been shown to significantly strain harden at these temperatures due to restricted slip and dislocation/twin interactions[87]. The resulting high strain from deformation promotes the nucleation of cleavage cracks within the ferrite matrix, which subsequently propagate throughout the structure whilst the austenite phase ruptures in a ductile manner. Crack growth is strongly influenced by the interaction between crack tip and phase boundary[88], and some authors have suggested that delamination of this boundary can occur[89].

Various microstructural features have been shown to affect the ductile to brittle transition temperature. By prestraining the microstructure the transition temperature may be raised[90]. The grain size and crystallographic texture of a duplex stainless steel can also influence the fracture behaviour. It has been demonstrated that a strong rolling texture exists in both sheet[91] and bulk[92,93] specimens, resulting in highly anisotropic strength properties. Such textures have been shown to affect the fracture behaviour in a similar bcc material to ferrite (molybdenum) where an increase in the texture strength is accompanied by a decrease in impact toughness[94]. It has also been shown that the crystallographic orientation of austenite can influence the fracture behaviour, as certain ferrite/austenite orientations can restrict plastic deformation, thus promoting cleavage cracking[95]. However, since it is difficult to alter the texture strength of a material without affecting other parameters, it is difficult to isolate the effect of texture upon fracture behaviour.

The ductile to brittle transition temperature of duplex stainless steels can also be increased by ageing at temperatures between 280 and 500°C (the so-called '475°C embrittlement effect). This results in decomposition of the ferrite matrix to form α' precipitates, which restrict slip and encourages twin deformation behaviour. Thus the fracture behaviour of aged specimens simulates that of low temperatures[96,97]. In contrast, heat treatments at higher temperatures which precipitate intermetallic phases such as sigma, alter the fracture mechanism as these phases are intrinsically brittle and hence nucleate cleavage cracks internally[98].

The fracture toughness of weld metals and their heat affected zones are generally much reduced compared to that of the base metal[99,100]. Welds metals have a very fine grain size due to their rapid cooling rate, and contain inclusions imparted from the welding process. Partial dissolution of austenite grains in the heat affected zone, as well as general ageing of the matrix can also occur. Thus, ductility is limited and the work hardening rate is much higher than that of the base metal, hence the ductile to

brittle transition temperature is increased. Residual stresses due to thermal contraction of the weld can further raise the transition temperature. Reheating of weld beads[101] during multipass welding or stress-relieving heat treatments[102] can also nucleate brittle intermetallic phases within the matrix, which further promote cleavage fracture. Therefore, the fracture behaviour of a weld is often the critical factor in the performance of a structure.

In conclusion, although the fracture behaviour of duplex stainless steels is generally well understood, the exact micromechanisms of fracture (especially at low temperatures) have yet to be explained. Only limited work has been performed upon highly alloyed super duplex stainless steels and thus it is not certain to what extent the alloy content affects the fracture behaviour.

References:-

[1]EWALDS H.L. & WANHILL R.J.H., 'Fracture Mechanics', pub.E.Arnolds, London, 1984.

[2]KNOTT J.F., 'Fundamentals of Fracture Mechanics', pub.Butterworths, London, 1973.

[3]ANDERSON T.L., 'Fracture Mechanics', pub.CRC Press, Florida, 1995.

[4]GRIFFITH A.A., 'The phenomena of rupture and flow in solids', Phil.Trans.Roy.Soc., A221, pp163-198, 1921.

[5]INGLIS C.E., 'Stresses in a plate due to the presence of cracks and sharp corners', Trans.Inst.Nav.Archit., 55, pp219-241, 1913.

[6]IRWIN G.R., 'Fracture dynamics', in "Fracturing of metals", ASM, Cleveland, pp147-166, 1948.

[7]OROWAN E., 'Fracture and Strength of Solids', Reports Prog.Phys., 12, p185, Phys.Soc.London, 1949.

[8]IRWIN G.R., 'Analysis of stresses and strains near the end of a crack traversing a plate', J.Appl.Mech., 24, pp361-364, 1957.

[9]WESTERGAARD H.M., 'Bearing pressures and cracks', J.Appl.Mech., 60, pp49-53, 1939.

[10]KNOTT J.F. & ELLIOT D., 'Worked examples in fracture mechanics', pub.IOM, London, pp10-11, 1979.

[11]McCLINTOCK F.A. & IRWIN G.R., 'Plasticity aspects of fracture mechanics, fracture toughness testing, and its applications', ASTM STP 381, Philadelphia, pp84-113, 1965.

[12]DUGDALE D.S., 'Yielding in steel sheets containing slits', J.Mech.Phys.Sol., 8, pp100-104, 1960.

[13]HAHN G.T. & ROSENFIELD A.R., Acta Met., 13, p293, 1965.

[14]RICE J.R. & SORENSON E.P., 'Continuing crack tip deformation and fracture for plane strain growth in elastic-plastic solids', J.Mech.Phys.Sol., 26, pp163-186, 1978.

[15]TRACEY D.M., 'Finite element solutions for crack tip behaviour in small scale yielding', Trans.ASME, J.Eng.Mat.Tech, 98, pp146-151, 1976.

[16]MISHRA S.C. & PARIDA B.K., 'A study of crack-tip plastic zone by elastoplastic finite element analysis', Eng.Frac.Mech., 22, pp951-956, 1985.

[17]SRAWLEY J.E., 'Wide range stress intensity factor expressions for ASTM E 399 standard fracture toughness specimens', Int.J.Fract., 12, pp475-476, 1976.

[18]BS5447, 'Methods of Test for Plane Strain Fracture Toughness (K_{IC}) of Metallic Materials', British Standards Institute, London, 1977.

[19]FEDDERSON C.E., 'Evaluation and prediction of the residual strength of centre-cracked tension panels', Damage tolerance in aircraft structures, ASTM STP 486, Philadelphia, pp50-78, 1971.

[20]BS131, 'Notched bar tests', British Standards Institute, London, 1989.

[21]TURNER C.E.,'Measurement of fracture toughness by instrumented impact test', ASTM STP466, ASM, Philadelphia, pp93-114, 1970.

[22]YAJIMA H., HUANG Y., YAMAMOTO M., TADA M. & KITADA H., 'A suggested method of ship hull plating fracture toughness assessment', proc.conf. "International Offshore and Polar Engineering Conference 1996", Los Angeles, USA, pub.ISOPE, Colarado USA, 4, pp256-262, 1996.

[23]MARANDET B. & SANZ G., 'Evaluation of the toughness of thick medium strength steel by LEFM and correlation between K_{IC} and CV_N', ASTM STP631, ASM, Philadelphia, pp72-95, 1977.

[24]BARSOM J.M. & ROLFE S.T., 'Correlation between K_{IC} and Charpy V notch test results in the transition temperature range', ASTM STP466, ASM, Philadelphia, pp281-301, 1970.

[25]NORRIS D.M., 'Computer simulation of the Charpy V-notch toughness test', Eng.Frac.Mech., 11, pp395-410, 1979.

[26]DRAR H., 'On predicting the temperature and strain rate dependencies of the fracture toughness of plain carbon steel', Mat.Char., 31, pp91-97, 1993.

[27]RICE J.R., 'A path independent integral and the approximate analysis of strain concentration by notches and cracks', J.Appl.Mech., 35, pp379-368, 1968.

[28]HUTCHINSON J.W., 'Singular behaviour at the end of a tensile crack tip in a hardening material', J.Mech.Phys.Sol., 16, pp13-31, 1968.

[29]RICE J.R. & ROSENGREN G.F., 'Plane strain deformation near a crack tip in a power-law hardening material', J.Mech.Phys.Sol., 16, pp1-12, 1968.

[30]ASTM Standard E 813-81, Standard test method for J_{IC}, a measure of fracture toughness, Philadelphia, USA, 1982.

[31]TURNER C.E., 'A J-based design curve', in 'Advances in Elasto-Plastic Fracture Mechanics', L.H.Larsson ed., Applied Science Publ., London, p301-317, 1980.

[32]RICE J.R., DRUGAN W.J. & SHAM.T.L., 'Elastic-plastic analysis of growing cracks', ASTM STP 700, ASM, Philadelphia, pp189-221, 1980.

[33]WELLS A.A., 'Unstable crack propagation in metals: damage and fast fracture', proc.conf."Crack Propagation", Cranfield, UK, pp120-230, 1962.

[34]BURDEKIN F.M. & STONE D.E.W., 'The crack opening displacement approach to fracture mechanics in yielding materials', J.Strain Analysis, 1, p145-153, 1966.

[35]McMEEKING, J.Mech.Phys.Sol., 25, p357, 1977.

[36]HUTCHINSON J.W., 'Non-linear fracture mechanics', Technical University of Denmark, Copenhagen, 1979.

[37]VEERMAN C.C. & MULLER T., 'The location of the apparent rotation axis in notched bend testing', Eng.Frac.Mech., 4, pp25-32, 1972.

[38]BS54762, 'Methods for crack opening displacement testing', British Standards Institute, London, 1979.

[39]DAWES M.G., 'Fracture control in high strength yield weldments', The welding journal, 53, pp369-379, 1974.

[40]DAWES M.G., 'The COD design curve', in 'Advances in Elasto-Plastic Fracture Mechanics', L.H.Larsson ed., Applied Science Publ., London, p279-300, 1980.

[41]BSI PD6493, 'Guidance on some methods for the derivation of acceptance levels for defects in fusion welded joints', BSI, London, 1980.

[42]PISARSKI H.G., 'The CTOD approach to the specification of fracture resistant welded steel structures for Arctic service', proc.conf."Fracture toughness evaluation of steels for Arctic marine life", Ottowa, Canada, 8, 1983.

[43]NEVASMAA P., KORTLAINEN O., WALLIN K. & PORTER D., 'Fracture toughness assessment and HAZ strain-ageing resistance of thermomechanically processed steel subjected to cold forming before welding', proc.conf. "International Offshore and Polar Engineering Conference 1996", Los Angeles, USA, pub.ISOPE, Colarado USA, 4, pp154-159, 1996.

[44]BARLETT R.A., FROST S.R. & BOWEN P., 'Fracture toughness and defect assessment of low temperature carbon steel flanges', Int.J.Pres.Ves.&Piping, 48, p263-291, 1991.

[45]OROWAN E., Trans.Inst.Engrs.Shipbuilders Scotland, 89, p154, 1945.

[46]LOW J.R., Relation of properties to microstructure, pub.ASM, p163, 1954.

[47]KNOTT J.F. & COTTRELL A.H., J.I.S.I., 201, pp249-260, 1963.

[48]HULL D., 'Twinning and fracture of single crystals of 3% Si iron', Acta Met. 8, pp11-18, 1960.

[49]CURRY D.A., 'Cleavage micromechanisms of crack extension in steels', Met.Sci., pp319-326, 1980.

[50]STROH A.N., 'A theory of the fracture of metals', J.Adv.Phys., 6, p418-465, 1957.

[51]ZENER C., Trans.ASM, 40A, p3, 1948.

[52]COTTRELL A.H., 'Theory of brittle fracture in steel and similar metals', Trans.Am.Inst.Min.Met.Pet.Eng., 212, p192-203, 1958.

[53]KNOTT J.F., J.I.S.I., 205, pp288-291, 1967.

[54]McMAHON C.J. & COHEN M., 'Initiation of cleavage in polycrystalline iron', Acta Met., 13, p591-604, 1965.

[55]SMITH E., 'The nucleation and growth of cleavage microcracks in mild steel', proc.conf."Physical basis of yield and fracture", Oxford, p36-46, 1966.

[56]PETCH N.J., J.I.S.I., 173, 1953, p25.

[57]CURRY D.A. & KNOTT J.F., 'Effect of microstructure on cleavage fracture stress in steel', Met.Sci., 13, pp511-514, 1978.

[58]DOLBY R.E. & KNOTT J.F., 'Toughness of martensitic and martensitic-bainitic microstructures, with particular reference to heat affected zones', J.I.S.I., 210, pp857-865, 1972.

[59]McROBIE D.E. & KNOTT J.F., Effects of strain and strain ageing on fracture toughness of C-Mn weld metal', Mat.Sci.Tech., 1, p357-365, 1985.

[60]BOSE W., 'Influence of weld-metal inclusions on fracture', PhD thesis, University of Birmingham, U.K., 1995.

[61]TWEED J.H. and KNOTT J.F., 'Effect of reheating on microstructure and toughness of C-Mn weld metal', Met.Sci., 17, pp45-54, 1983.

[62]KNOTT J.F., 'Some effects of hydrostatic tension on the fracture behaviour of mild steel', J.I.S.I., p104-111, 1966.

[63]GROOM J.D.G., 'Effects of prestrain on fracture', PhD thesis, University of Cambridge, 1971.

[64]GRIFFITHS J.R. & OWEN D.R.J., J.Mech.Phys.Sol., 19, pp419-431, 1971.

[65]RITCHIE R.O., KNOTT J.F. & RICE J.R., 'On the relationship between critical tensile strength and fracture toughness in mild steel', J.Mech.Phys.Solids, 21, p395-409, 1973.

[66]RICE J.R. & TRACEY D.M., 'Computational Fracture Mechanics', in "Numerical Computer Methods in Structural Materials", Academic Press, New York, pp585-623, 1973.

[67]BOWEN P., DRUCE S.G. & KNOTT J.F., 'Micromechanical modelling of fracture toughness', Acta Met., 35, p1735-1746, 1987.

[68]RITCHIE R.O., SERVER W.L. & WULLAERT R.A., Met.Trans., 10A, p1557, 1979.

[69]CURRY D.A. & KNOTT J.F., 'Effect of microstructure on cleavage fracture toughness in mild steel', Met.Sci., 13, pp341-345, 1979.

[70]PINEAU A., ICF5, France, pub.Permagon Press, 2, p553, 1981.

[71]EVANS A.G., 'Statistical aspects of cleavage fracture', Met.Trans., 14A, pp1349-1355, 1983.

[72]CHEN J.H., YAN C. & SUN J., 'Further study on the mechanism of cleavage fracture at low temperature', Acta Met., 42, pp251-261, 1994.

[73]KNOTT J.F., 'The transition from fibrous fracture to cleavage fracture', Int.J.Pres.Ves.&Piping, 64, pp225-234, 1995.

[74]ZHANG J.Q., PhD thesis, University of Birmingham, 1996.

[75]HOAGLAN R.G., ROSENFIELD A.R. & HAHN G.T., 'Mechanisms of fast fracture and arrest in steels', Met Trans., 3, pp123-136, 1972.

[76]WILSDORF H.G.F., 'The ductile fracture of metals: a microstructural viewpoint', Mat.Sci.Eng., 59, pp1-19, 1983.

[77]GARRISON W.M. & MOODY N.R., 'Ductile Fracture', J.Phys.Chem.Sol., 48, pp1035-1074, 1987.

[78]KNOTT J.F., 'Micromechanisms of fibrous crack extension in engineering alloys', 14, pp327-336, 1980.

[79]CHO K & GURLAND J., 'The law of mixtures applied to the plastic deformation of two phase alloys of coarse microstructures', Met.Trans, 19A, pp2027-2040, 1988.

[80]REISNER G. & WERNER E., 'Plasticity and fracture of an austenitic-ferritic duplex steel', Z.Metallkn., 85, pp265-272, 1994.

[81]WELMAN W.H.M., GADGIL V.J. & KOLSTER B.H., 'Mechanical behaviour of duplex stainless steel', proc.conf."Duplex Stainless Steels'91", Beaune, France, pub.Editions de Physique, pp184, 1991.

[82]STRANGWOOD M. & DRUCE S.G., 'Ageing effects in welded cast CF3 stainless steel', Mat.Sci.Tech., 6, pp237-247, 1990.

[83]FOCT J. & AKDUT.N., 'Cleavage-like fracture of austenite in duplex stainless steel ', Scipta.Met.Mat., 29, pp153-158, 1993.

[84]MÜLLNER P, SOLENTHALER C, UGGOWITZER P.J. & SPEIDAL M.O., 'Brittle fracture in austenitic steel', Acta Met.Mat., 42, pp2211-2217, 1994.

[85]JOHANSSON R.E. & NILSSON J.O., 'Fracture toughness of austenitic and duplex stainless steels', proc.conf."Duplex Stainless Steels'84", London, pub.IOM, pp446-451, 1984.

[86]ROBERTI R., VECCHIA G.M., BERTANZI R. & NICODEMI W., 'Room temperature crack initiation and growth under sustained load in a superduplex stainless steel', proc.conf."Duplex Stainless Steels '94", Glasgow, U.K., pub.TWI, paper 106, 1994.

[87]ATAMERT S. & KING J.E., 'Crack initiation mechanisms in duplex stainless steel HAZ microstructures', Acta Met.Mat., 39, p273-285, 1991.

[88]YONG-TANG N.M., YAO K.F. & CHEN N-P., 'In-situ fracture experiment on duplex stainless steel', Mat.Sci.Eng, A117, pp157-165, 1989.

[89]ERAUZKIN E. & IRISARRI A.M., 'Effect of the testing temperature on the fracture toughness of a duplex stainless steel', Scripta.Met.Mat., 25, pp1731-1736, 1991.

[90]NYSTRÖM M., KARLSSON B. & WASÉN J., 'The influence of prestraining and 475°C annealing on the mechanical properties of a duplex stainless steel (SAF2205)', Proc.conf."Stainless Steels'90", Chiba, Japan, pub.ISIJ, p738-745, 1991.

[91]HUTCHINSON W.B., USHIODA K. & RUNNSJÖ G., 'Anisotropy of tensile behaviour in a duplex stainless steel sheet', Mat.Sci.Tech., 1, pp728-730, 1985.

[92]HUTCHINSON W.B., SCHLIPPENBACH U.V. & JONSSON J., 'Textures and anisotropy in duplex stainless sheet', from "Duplex Stainless Steels86", The Hague, Holland, pp326-330, 1986.

[93]ULHAW A., WEILAND H. & BUNGE H.J., 'Textures and microstructures in duplex stainless steel', Mat.Sci.Tech., 10, pp289-298, 1994.

[94]WELCH P.I. & DAVIES G.J., 'Texture and cleavage in molybdenum', Textures & Microstructures, 6, pp21-38, 1983.

[95]JOLY P., COZAR R. & PINEAU A., 'Effect of crystallographic orientation of austenite on the formation of cleavage cracks in ferrite in an aged duplex stainless steel', Scripta Met., 24, pp2235-2240, 1990.

[96]HALE G.E. & GARWOOD S.J., 'Effect of ageing on fracture behaviour of cast stainless steel and weldments', Mat.Sci.Tech., 6, pp230-235, 1990.

[97]ITURGOYEN L. ALCALÁ J. & ANGLADA M., 'The influence of ageing at 475°C on the fracture resistance of a duplex stainless steel', Proc.conf."Duplex Stainless Steels'91", Beaune, France, pub.Editions de Physique, pp757-764, 1991.

[98]LI J., WU T. & RIQUIER Y., 'Sigma phase precipitation and its effects on the mechanical properties of a super duplex stainless steel', Mat.Sci.Eng., A147, pp149-153, 1994.

[99]DHOOGE A. & DELEU E, 'Weldability and fracture behaviour of duplex and superduplex stainless steels', proc.conf."Duplex Stainless Steels '94", Glasgow, U.K., pub.TWI, paper 77, 1994.

[100]SCHÄFER K., 'The optimisation of corrosion, low temperature toughness and strength properties of welded duplex and super duplex pipelines', proc.conf."Duplex Stainless Steels '94", Glasgow, U.K., pub.TWI, paper 59, 1994.

[101]NEUBERT V. & DÖLLING R., 'CTOD and impact investigations on duplex stainless steel base and weld materials', proc.conf."Duplex Stainless Steels '94", Glasgow, U.K., pub.TWI, paper 114, 1994.

[102]NILSSON J.O. & LIU P., 'Ageing at 400-600°C of submerged arc welds of 22Cr-3Mo-8Ni duplex stainless steel and its effect on toughness and microstructure', Mat.Sci.Tech., 7, pp853-862, 1991.

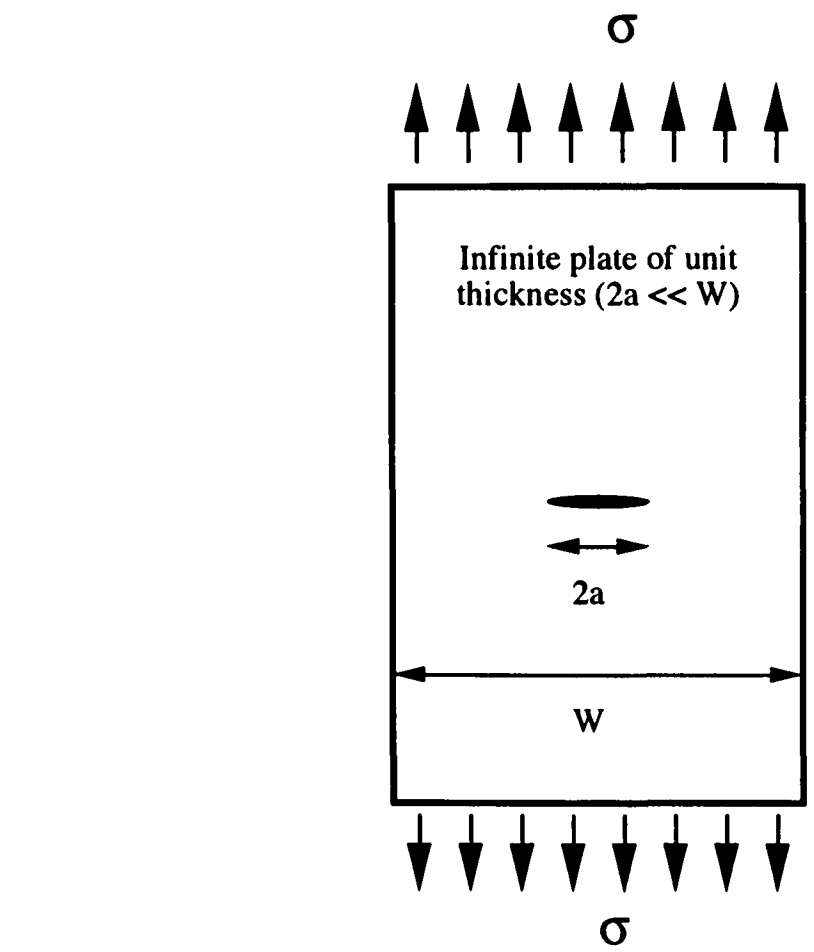

Figure 3.1 - A through-cracked plate

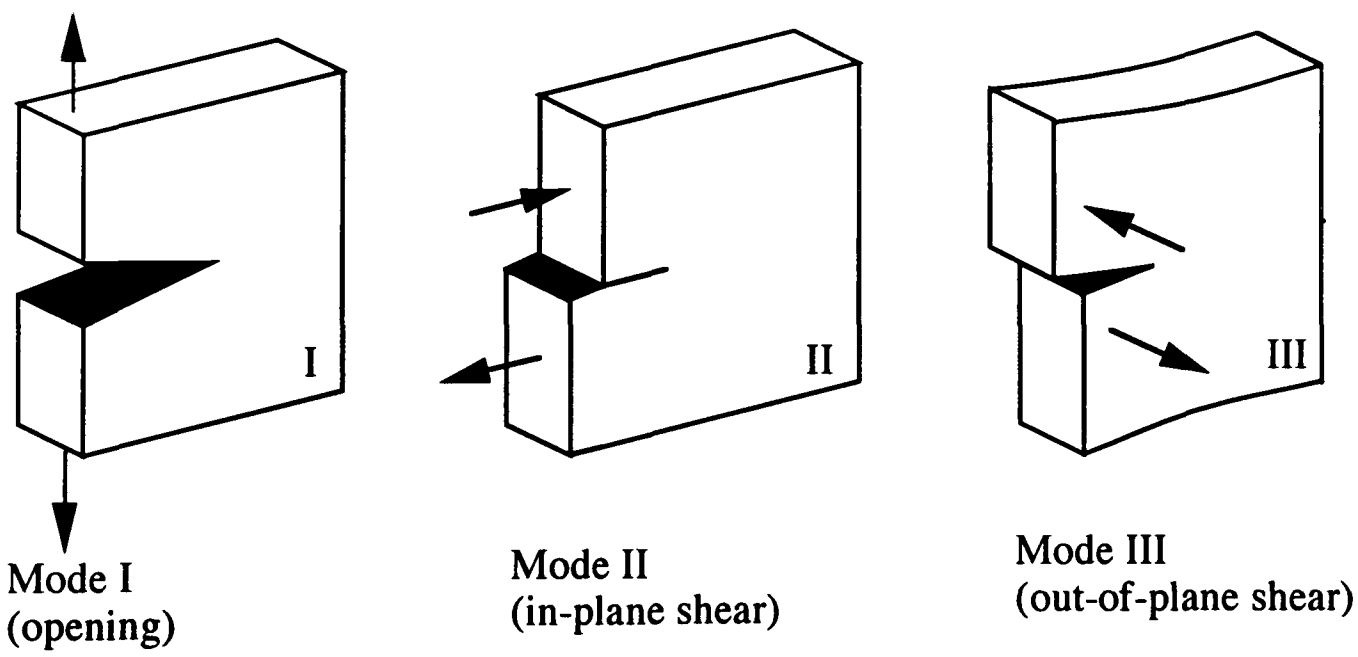

Figure 3.2 - The three modes of loading that can be independently applied to a crack

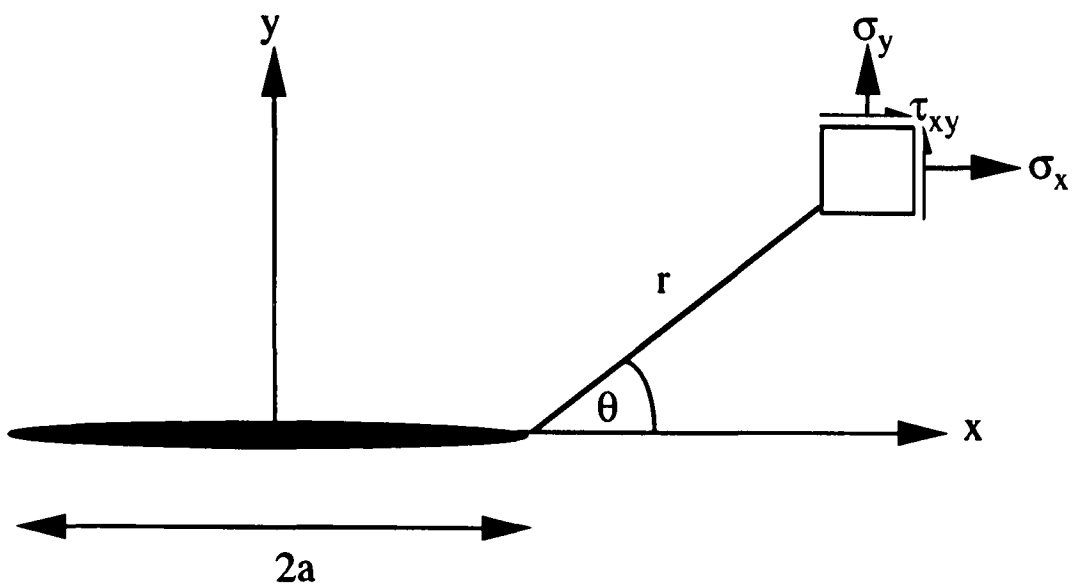

Figure 3.3 - Stresses ahead of the crack tip

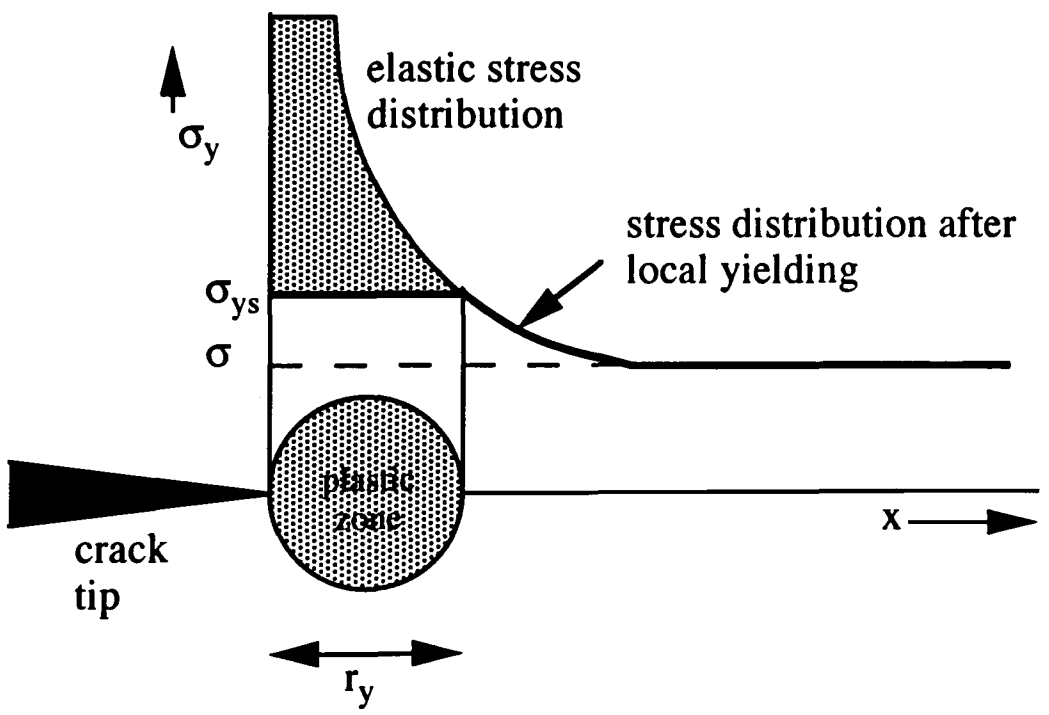

Figure 3.4 - A first approximation to the crack tip plastic zone

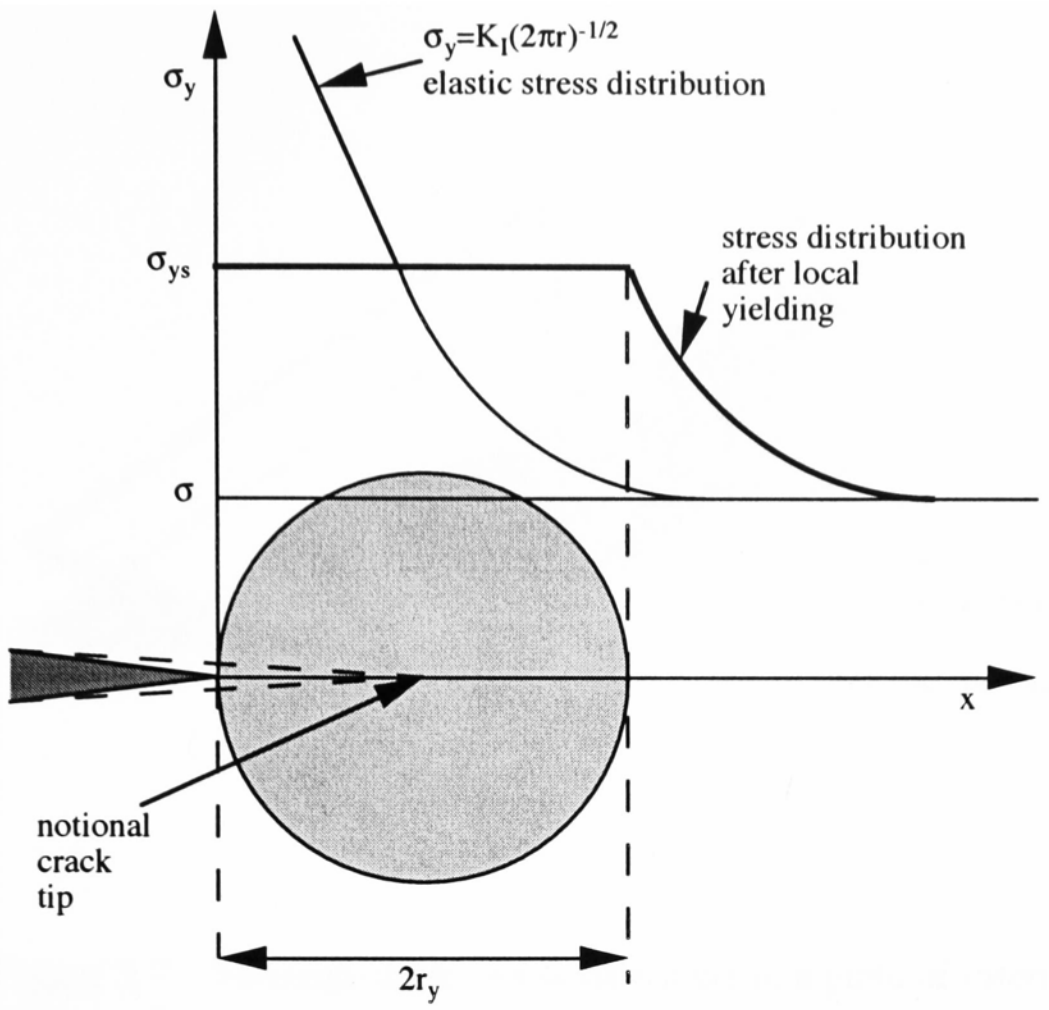

Figure 3.5 - The Irwin plastic zone size[1]

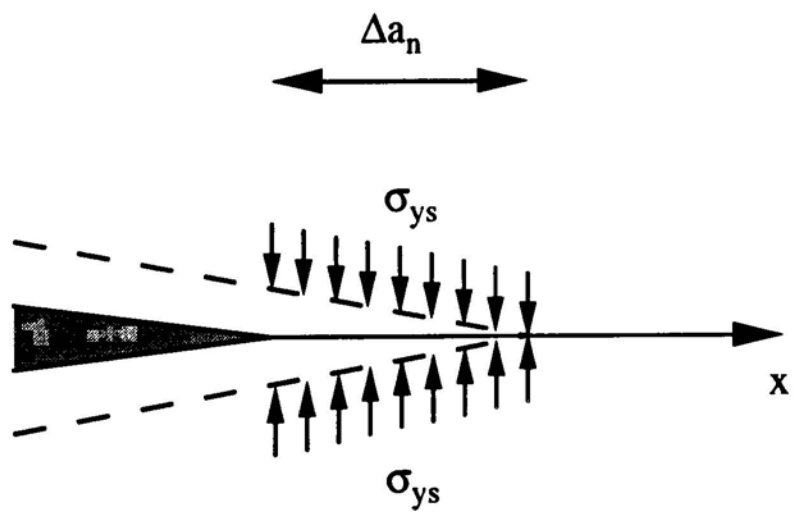

Figure 3.6 - Schematic of Dugdale's plastic zone analysis[1]

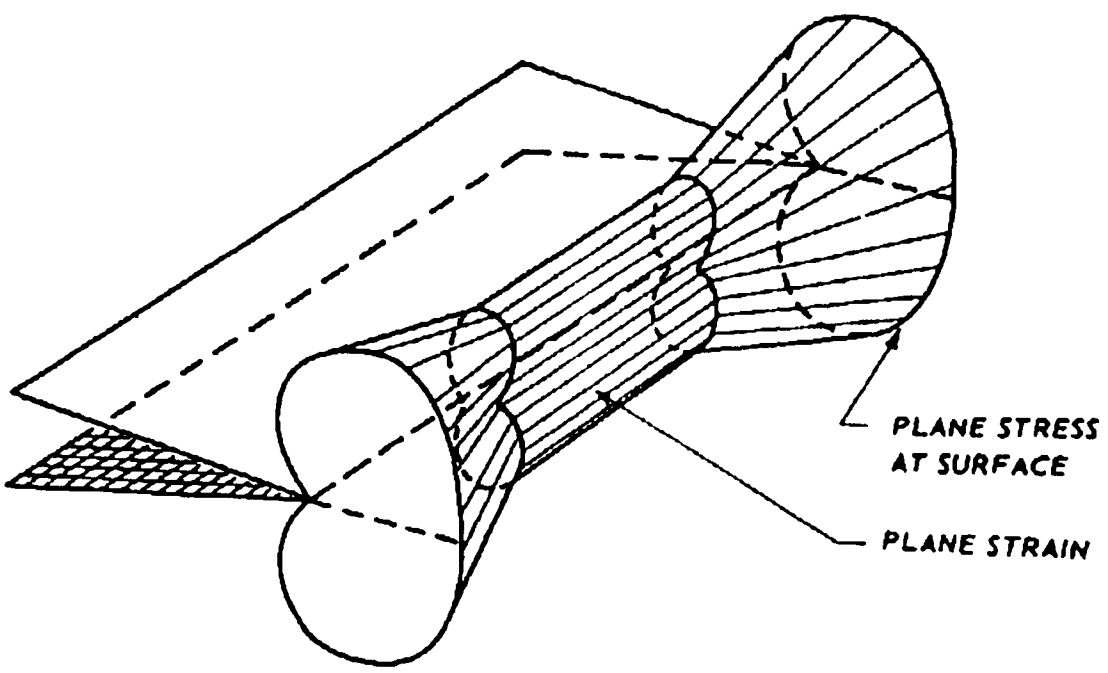

Figure 3.7 - Through-thickness plastic zone in a plate of intermediate thickness[1]

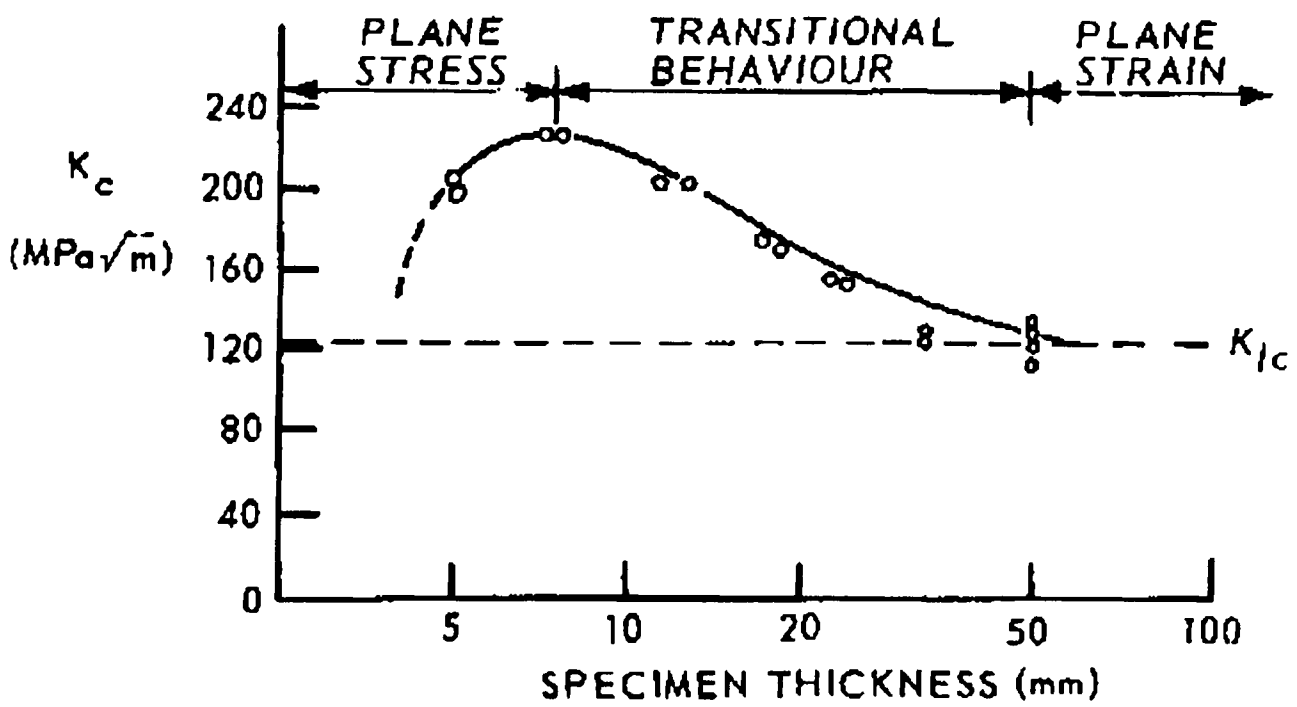

Figure 3.8 - Effect of thickness on K_C behaviour for a high strength maraging steel[1]

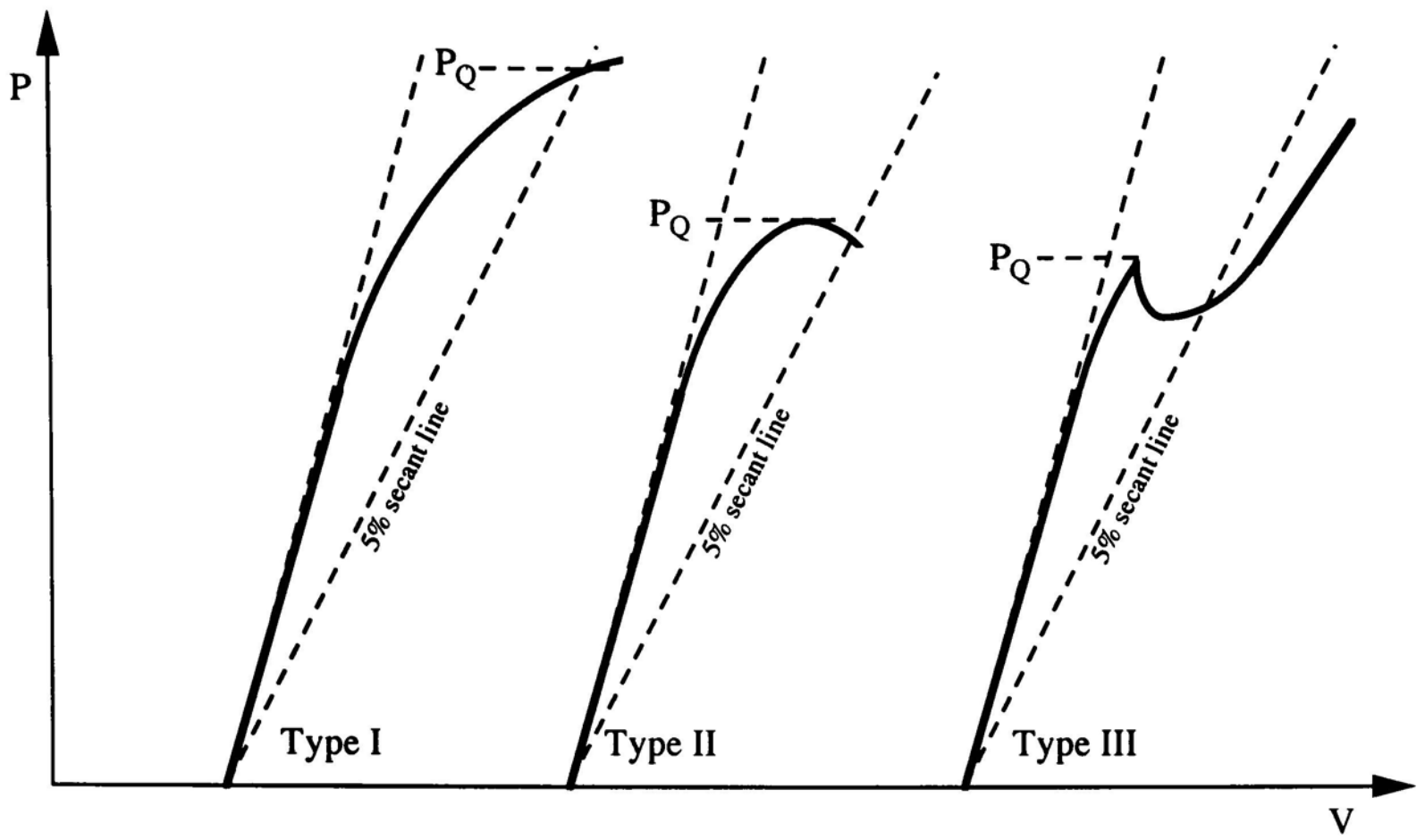

Fig.3.9 - Principal types of load-displacement curves during K_{IC} testing

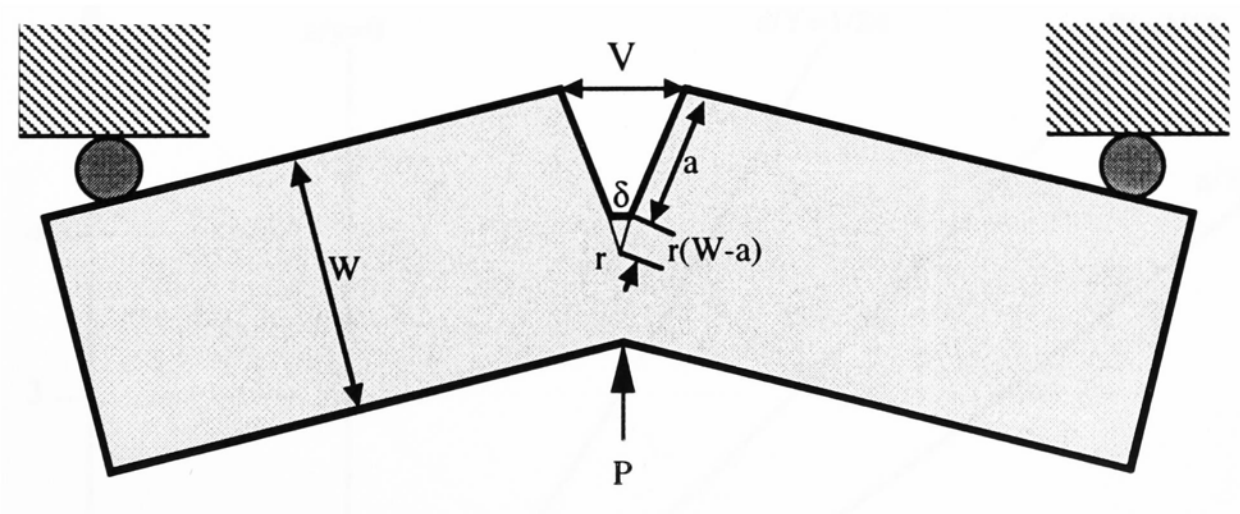

Figure 3.10 - The hinge model for estimating COD from 3-point bend specimens

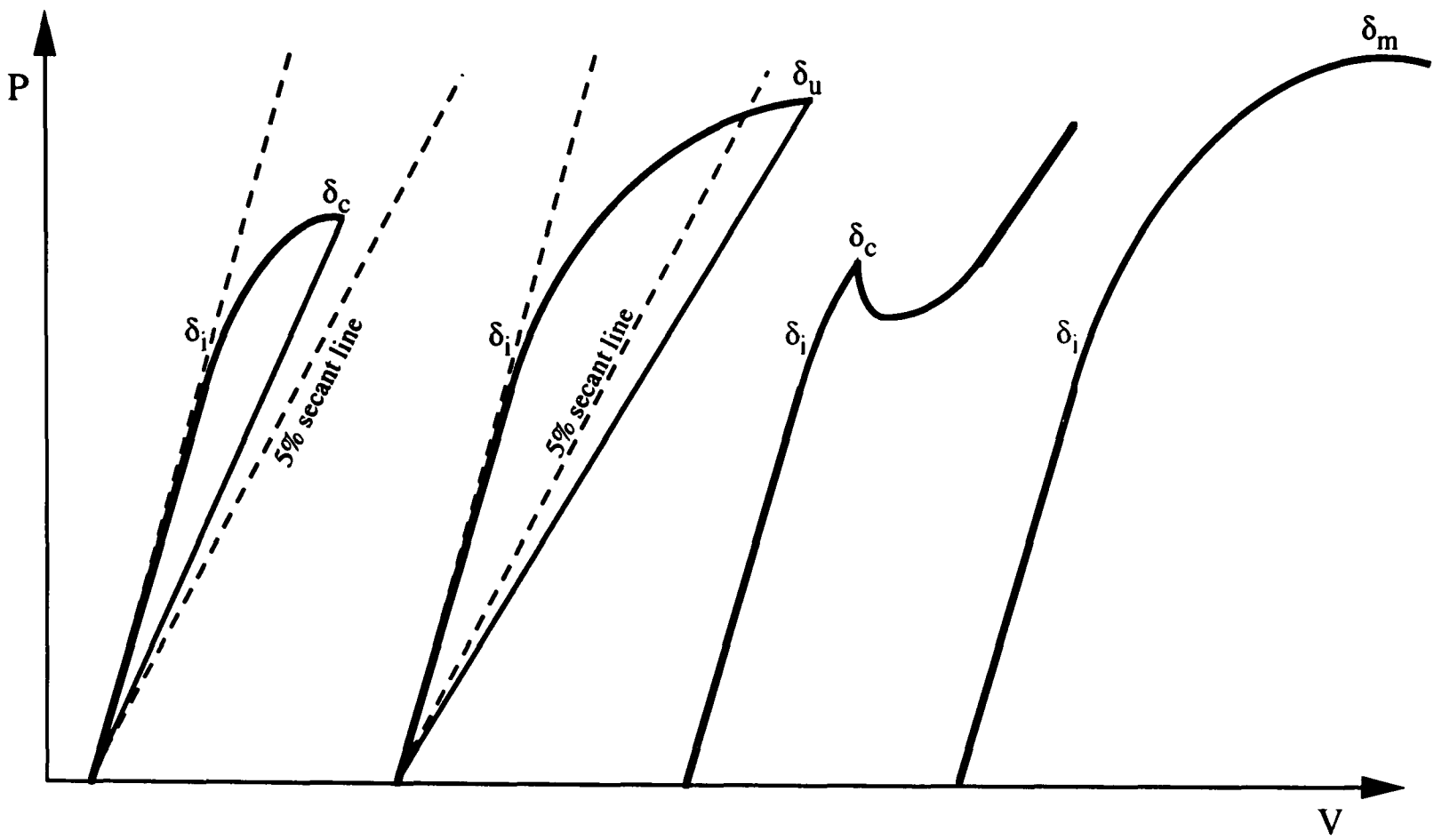

Fig.3.11 - Principal types of load-displacement curves during COD testing

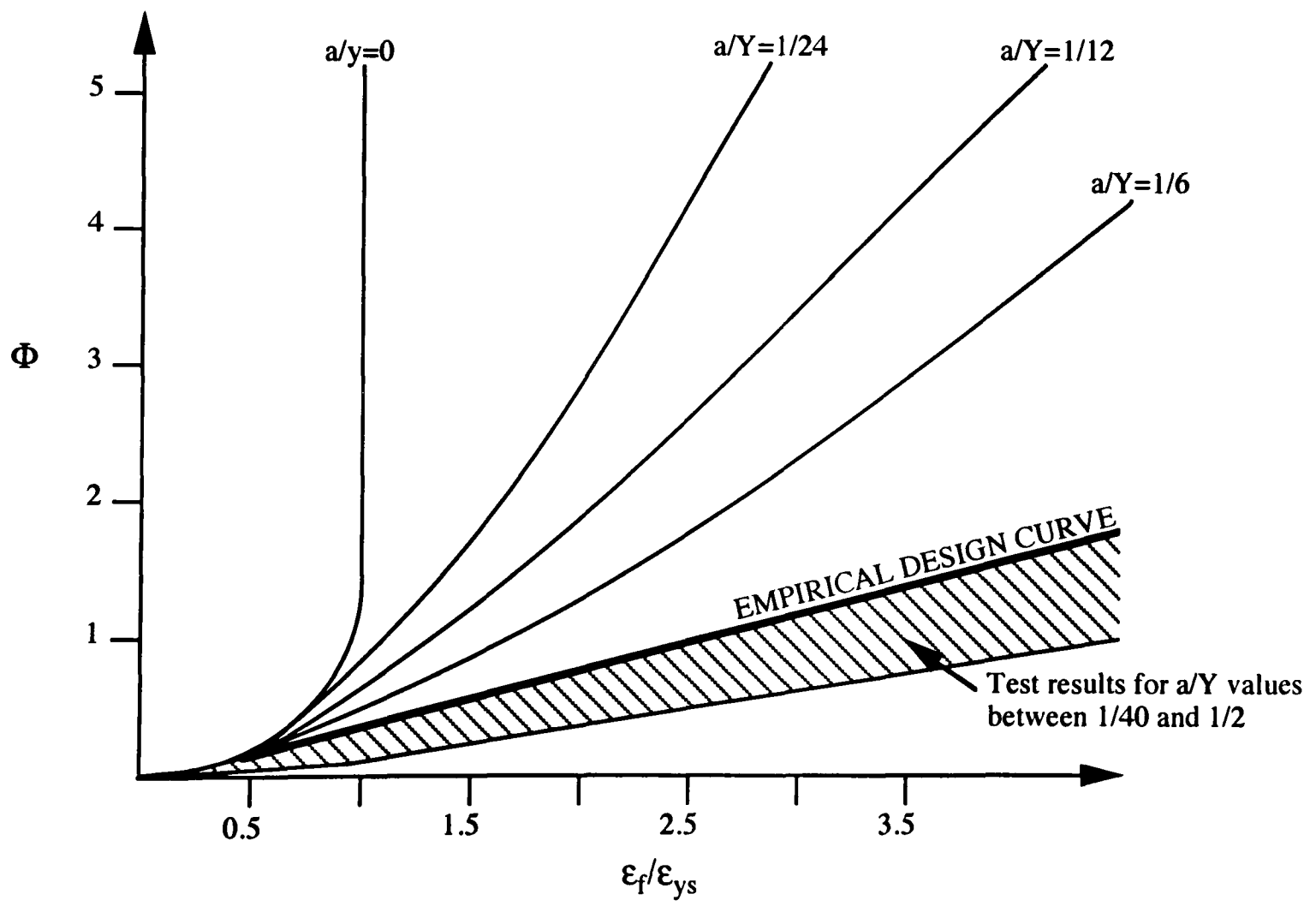

Figure 3.12 - Comparison of the analytical COD design curve (for an infinite plate) with experimental results, to produce an empirical curve[1]

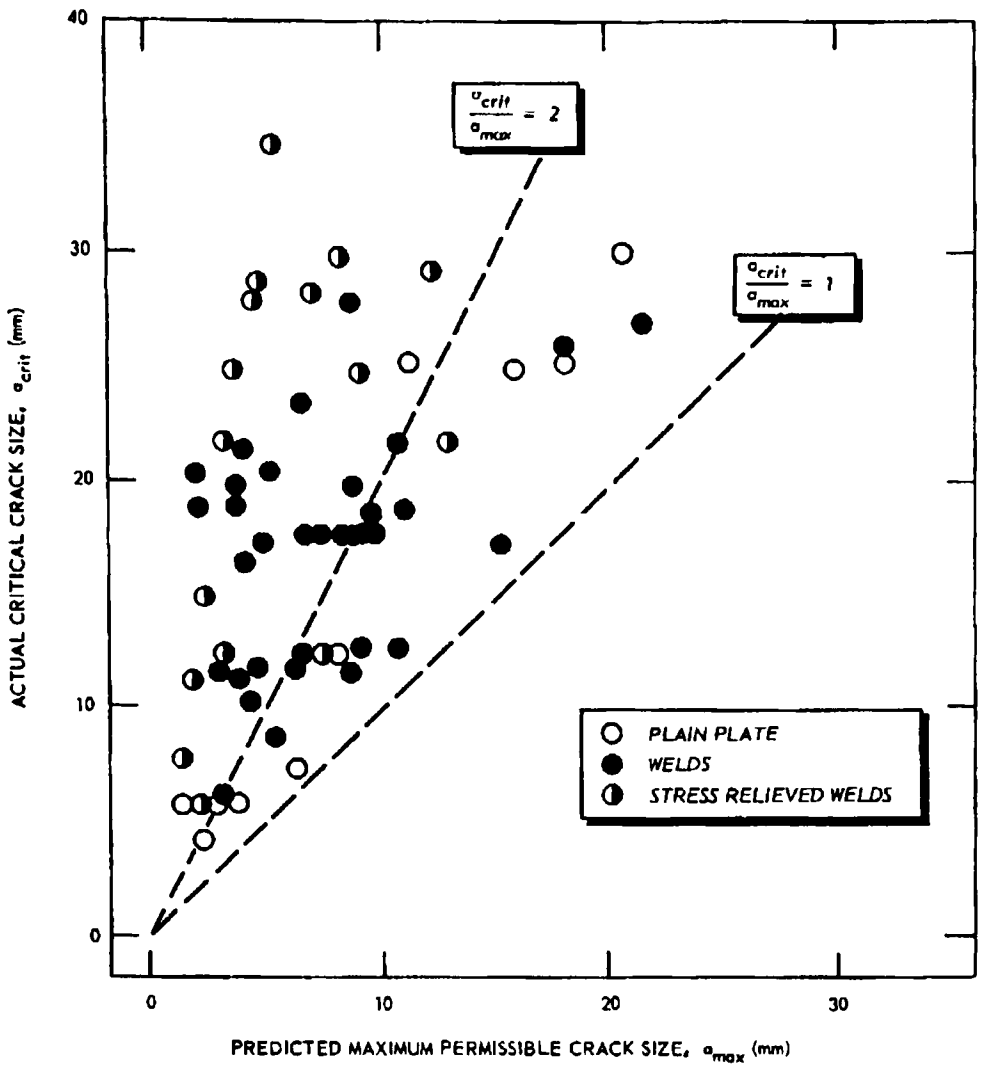

Figure 3.13 - Correlation of COD design curve predictions with actual crack sizes showing that the curve is a conservative estimate[34]

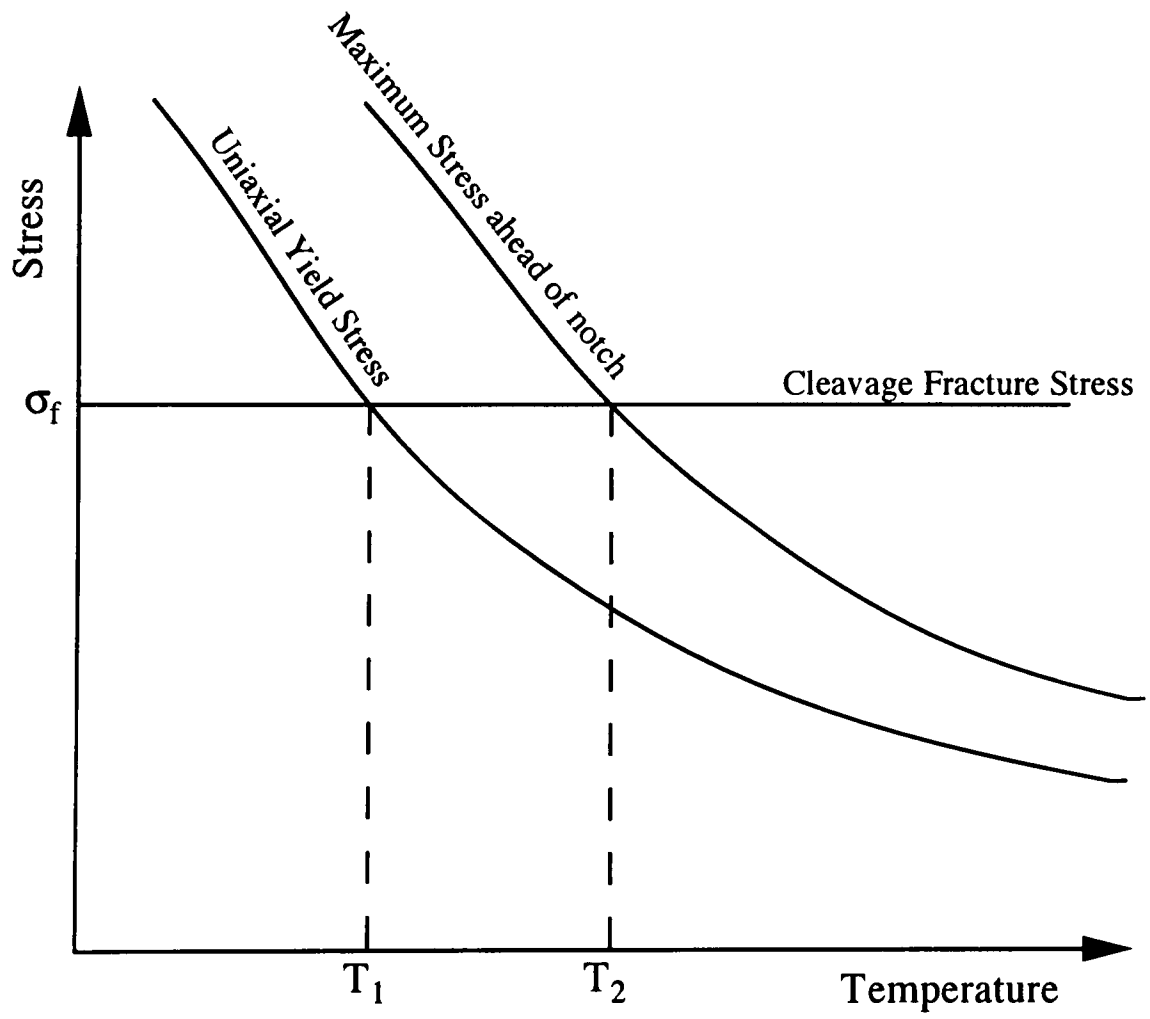

Figure 3.14 - The Orowan model of cleavage fracture showing that cleavage occurs at a higher temperature in notched tensile specimens (T_2), as opposed to smooth specimens (T_1), due to stress concentration ahead of the notch.

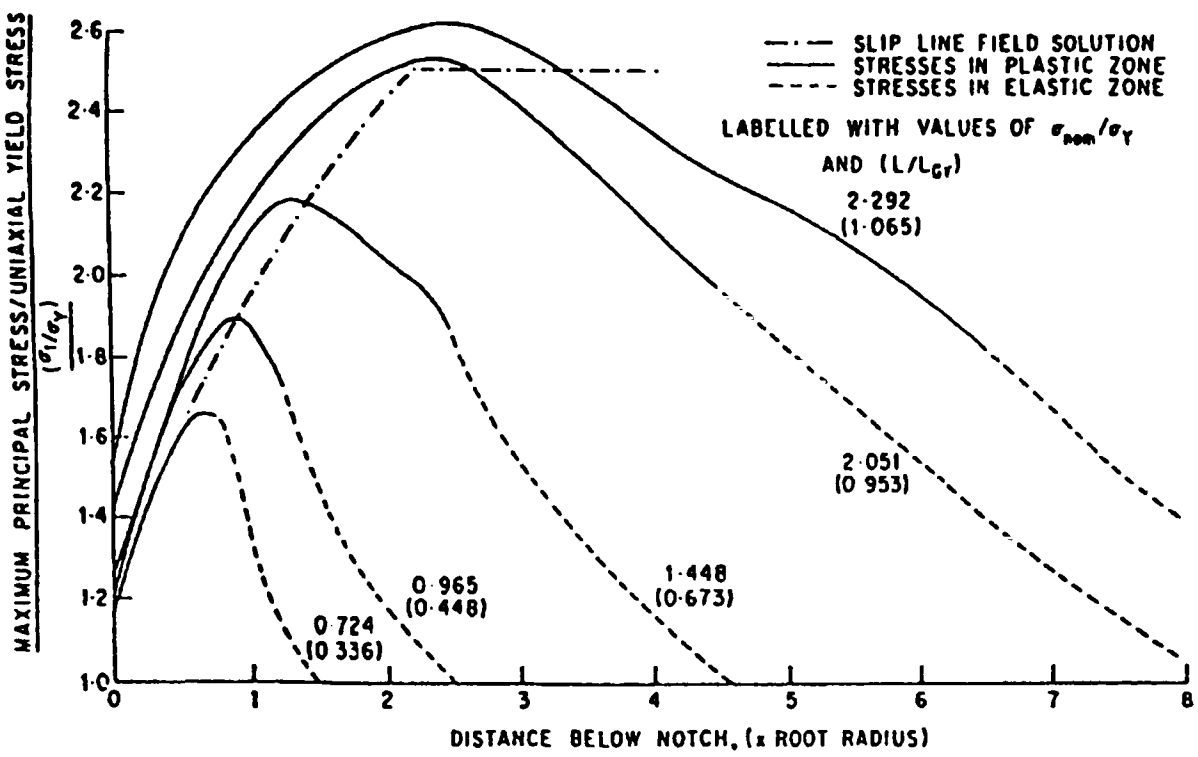

Figure 3.15 - The Griffiths-Owen solutions for the stress distibution ahead of the notch[64]

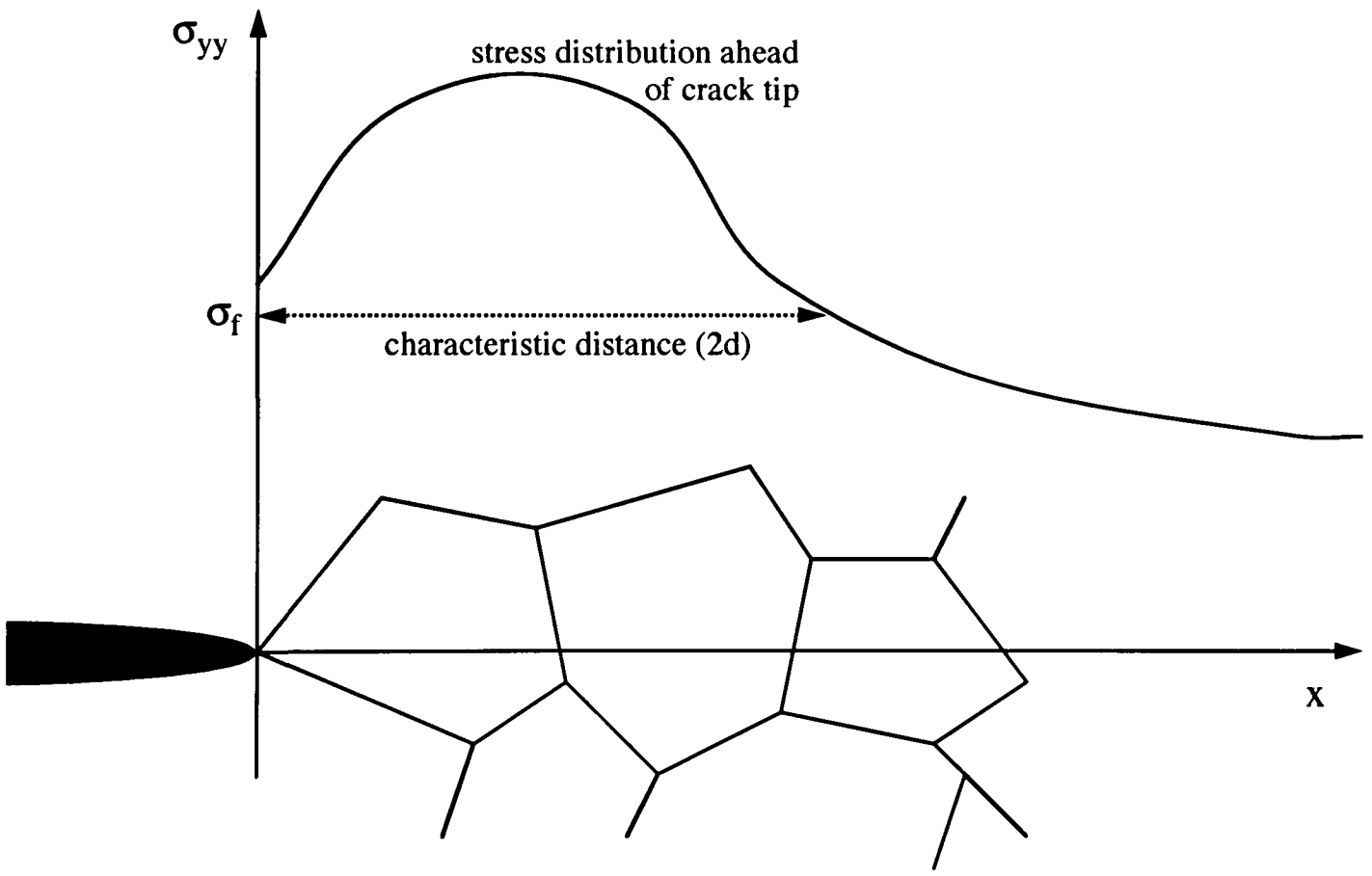

Figure 3.16 - The RKR model

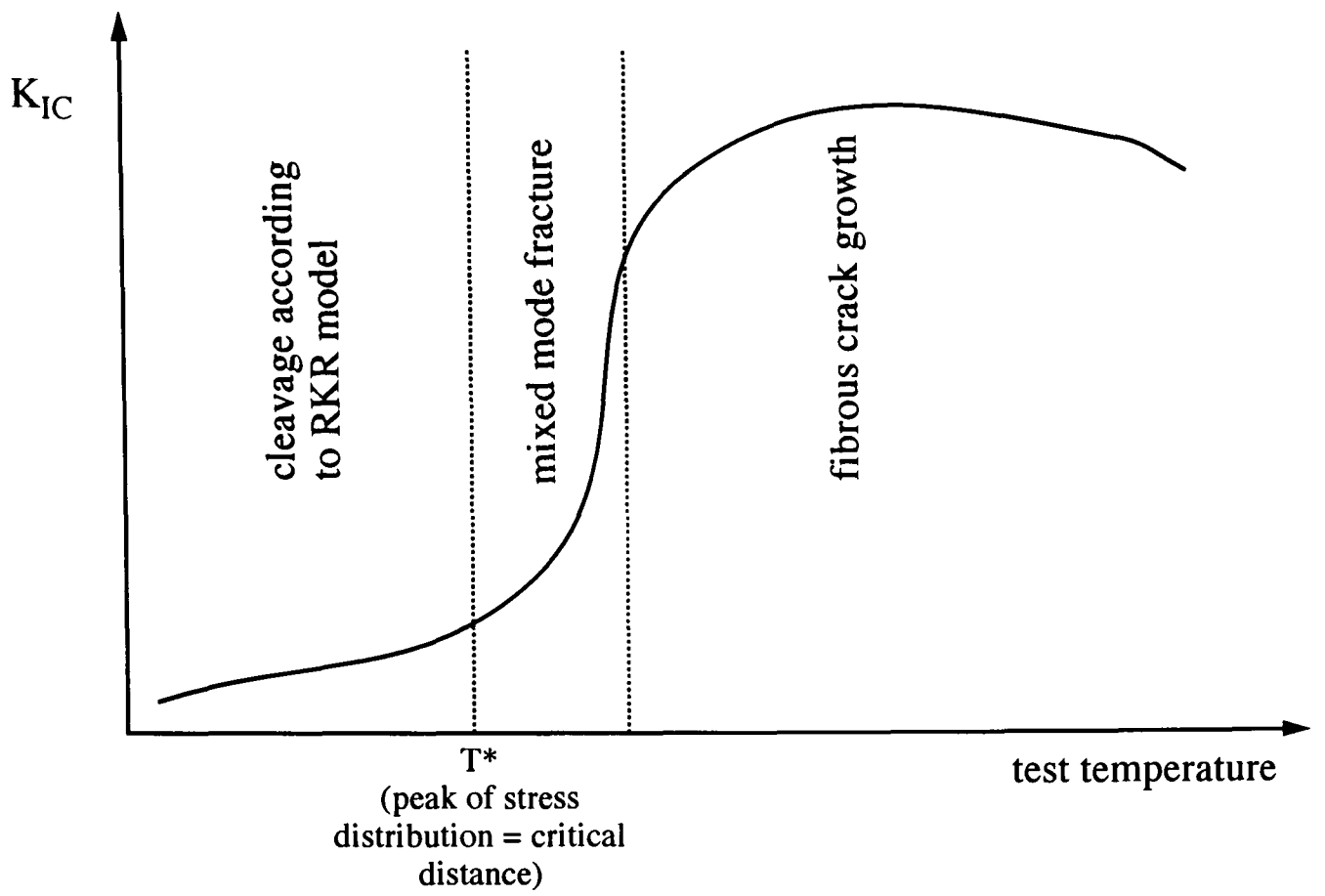

Figure 3.17 - The brittle to fibrous transition

4 - EXPERIMENTAL METHODS

4.1 MATERIAL

The alloy investigated was Zeron 100, a super duplex stainless steel manufactured by Weir Materials Services Ltd. The material was supplied in a number of different product forms resulting from various production routes. These were: cross-rolled plates of varying thickness (15, 20, 35mm); pipes extruded from ingot (external diameter 80mm, wall thickness 15mm); pipes produced from a powder metallurgy extrusion route (external diameter 200mm, wall thickness 13mm); hot-isostatically pressed (HIP'd) pipes (external diameter 325mm, wall thickness 25mm). All product forms were subsequently solution treated. The production procedures for each form are summarised in table 4.1, and the measured chemical compositions (from spark erosion analysis) shown in table 4.2.

Welded sections were produced from 20mm plate material, using multipass welds across a double 'V' notch (figure 4.1). A 330mm manual metal arc (MMA) weld was manufactured, together with two 300mm (TIG) weld, using welding consumables of an identical composition to that of the parent material. The welding conditions for each process are shown in table 4.3, and the measured chemical compositions (from spark erosion analysis) in table 4.4.

Testpieces were machined using tungsten carbide tools. Charpy specimens were cut in a number of different orientations from each product form. Testpieces from the welded sections were machined perpendicular to the weld line, centred in the weld. COD specimens were cut in a similar manner, although specimens cut from the full plate-thickness were used for the welded sections. Tensile and compression specimens were machined in only one orientation, i.e. parallel to the rolling/extrusion direction for

the wrought forms, and along the weld line centre for welds. Testpiece orientations are summarised in figure 4.2.

Limited investigations at an early stage of this study were made of the effects of heat treatment upon the fracture behaviour of Zeron 100. Specimens were heated for 2, 5, 10 and 45 minutes at a temperature of 850°C in a conventional muffle furnace in order to precipitate sigma phase. To produce alpha-prime hardening, material was aged at a temperature of 425°C for 100hrs. Following heat treatment, specimens were water quenched. Note that the times given are for the total time of the testpiece within the furnace, rather than the actual time of the testpiece at furnace temperature. The variation of specimen temperature with time was recorded via a thermocouple strapped to the specimens.

4.2 MICROSTRUCTURAL ANALYSIS

From the literature review, it can be seen that the microstructure has a critical effect upon the fracture behaviour of a material. Therefore, thorough analysis of the microstructure was required for all product forms, including measurements of grain size and shape, phase composition and chemical segregation, residual stress, microhardness and crystallographic texture.

4.2.1 Optical Microscopy

The microstructures of all the as-received and heat-treated microstructures were examined. In order to account for any anisotropy present, samples were cut perpendicular to the three principal axes for each product form. Specimens were sectioned using a diamond slitting wheel, hot-mounted in conducting bakelite and ground flat on SiC paper to a 1200 grit finish. They were then subsequently polished

with diamond paste to 1μm a metallographic finish. A grain/twin boundary etch of 10% oxalic acid was used to reveal the microstructure. The samples were electro-etched (with the specimen anodic) using a current density of 10mA/mm^2 applied to the specimen surface area for approximately 10 seconds, or until the specimen had acquired a faint yellow tinge. If necessary, a subsequent electroetch of 40% KOH solution was briefly used (under identical conditions to the oxalic acid etch) to improve contrast between the phases.

The etched microstructures were examined and photographed at various magnifications using a high resolution Leica optical microscope. In some cases a Quantimet 500 image analysis system was used to measure the phase balance and grain size. However, due to weak contrast between phases, a standard linear intercept/mesh technique was generally found to be preferable.

4.2.2 Scanning Electron Microscopy

The microstructures of all product forms were also analysed at higher magnifications in a JEOL-6300 scanning electron microscope (SEM). Samples were prepared as for optical examination, but polished to a 0.25μm finish and not etched. They were examined in the electron back scattered imaging mode at 20kV using a small working distance (8mm) and large probe size (>500nm) to improve the electron yield at the detector. Contrast between phases was achieved due to their difference in atomic number and hence backscattering coefficient[1].

An energy dispersive X-ray (EDX) analyser in the microscope was used to make quantitative measurements of the elemental compositions of each phase, to allow comparisons between the different product forms and to identify any segregation occurring through the plate/pipe thickness. To minimise the effects of beam current fluctuation, a lifetime of 100s was used for each analysis at 2000-3000 counts per second. An average of five measurements was taken for each area investigated.

4.2.3 Transmission Electron Microscopy

For certain specimens, it was found desirable to view the bulk microstructure at a higher resolution, and hence these were examined using transmission electron microscopy (TEM) analysis. Slices 0.5mm thick were machined perpendicular to the rolling/extrusion direction with a slow speed diamond saw. These were mechanically ground to a thickness of 150μm, punched into discs, and further ground to a thickness of 100μm. The foils were twin-jet electropolished using a solution of 2% perchloric acid in 2-butoxyethanol at a temperature of -10°C and 60V to produce a central hole, and subsequently examined in a Phillips CM20 TEM, operating at 200kV. Precipitates were identified using selected area diffraction pattern (SADP) analysis[2].

4.2.4 Residual Stress Analysis

The ferrite and austenite phases have a significant mismatch in thermal expansion coefficient[3], and therefore the rapid cooling of the bulk material during solution treatment was thought likely to introduce significant residual stresses. It has been shown that these stresses can influence the fracture behaviour of a material[4], and thus it is important to quantify any variation between product forms. Due to its ease of use and large depth of analysis compared to X-ray techniques, a "blind hole" drilling technique[5] was used. This involves the measurement of stress relief from incremental drilling via a strain gauge array (figure 4.3) from which any internal stresses present could be calculated.

Sections of the rolled plate along all three principal directions were examined to gauge any directionality present in the residual stresses, but only the transverse face was examined for the other product forms. The sample surface was ground flat to 1200 grit SiC, cleaned with acetone, and a strain gauge triangle[6] bonded to the surface. Holes were drilled at approximately 11μm depth intervals from the specimen surface to a total depth of 1.15mm. The hole diameter D_0 was found to be approximately 1.85mm. It is important to note that at depths where $Z/D_o>0.5$ (Z=hole depth),

incremental depth increases have a negligible effect on the surface strain relief, and hence the technique can only measure residual stresses to a depth of less than 0.9mm. From the strains measured, the principal stresses σ_1 and σ_2 (σ_3=0) were calculated, together with the mean residual stress, σ_m where $\sigma_m = \frac{(\sigma_1 + \sigma_2 + \sigma_3)}{3}$.

4.2.5 Microhardness and Hardness Testing

In order to investigate the effects of any surface work-hardening of the product forms, as well as to quantify the effects of heat treatment, the microhardness of the ferrite and austenite phases was measured at intervals across the product form thicknesses. Sections perpendicular to the rolling/extrusion direction were cut, polished to a 1μm finish, and examined in the etched condition. Measurements were carried out using a Shimadzu type 'M' Vickers microhardness tester, with a load of 25g and a dwell time of 15s. An average of 5 measurements for both phases was used in each area examined.

Due to their fine microstructure, the welded sections could only be examined using a standard Vickers macro-hardness technique. The variation of hardness across the weld thickness and the heat-affected zone was measured using a Vickers machine at 30kg load and 10s dwell time. Specimens were ground to a 1200 SiC grit finish, and an average of 3 measurements per area taken.

4.2.6 X-Ray Texture Analysis

The mechanical behaviour of a metal has been shown to affected by the crystallographic texture[7], and so this was quantified for all product forms. A 20x20mm square sample (approximately 2mm thick) of each form was cut in the plane of the rolling/extrusion direction. These were ground to 1200 SiC grit and then polished with diamond paste to a 0.25μm finish to remove the surface layer of deformation, followed by a light etch with oxalic acid.

The textures of both phases were measured using a modified Siemens texture goniometer according to standard crystallographic methods[8,9]. Cu K_α radiation was used, selected by a graphite monochrometer in the diffracted beam. A scan of all specimen orientations at up to 60° from the vertical axis was made, for each of 3 reflections - {200}, {220} and {311} for the austenite and {200}, {211} and {321} for the ferrite, and background scans of the intensity taken at a wavelength close to each peak.

Although the textures are measured as pole figures, this is not an ideal description, as these are only projections, and hence can only describe two of the three degrees of freedom of a crystal orientation. Therefore, the measured textures were represented using an orientation distribution function (ODF) plot, which describe the grain orientations in full using the Euler angles φ_1, φ_2 and ϕ. These three angles define the extent of three sequential rotations which transform an orthogonal set of axes in the specimen reference system into an orthogonal set of axes in the crystal reference system (figure 4.4). The texture of a particular orientation is defined as the probability function (in Euler space) of a volume of material having that particular orientation. The ODF was calculated from three pole figures per specimen using Bunge's method[10]. The textures were graphically represented using parallel sections through Euler space, upon which were plotted contours of ODF intensity, from which the texture could be readily interpreted using a standard chart (figure 4.5).

4.3 MECHANICAL TESTING

4.3.1 Charpy Tests

Charpy tests were conducted on the material to study the effect of variations in test temperature, product form, notch orientation and heat treatment upon impact

toughness. These were performed on an Instron machine, using standard specimens (figure 4.6) according to procedures of BS131[11]. Specimens were cooled to temperature using a cryogenic unit with an isopentane bath, and held at temperature for 10 minutes before testing. Lower temperatures (<-110°C) were achieved using additions of liquid nitrogen. Tests were performed on two or three identical specimens for each condition. The lateral expansion of the shear lips during testing was measured for all specimens.

A series of tests was conducted at regular temperature intervals between room temperature and -196°C for the X-Z orientation of each product form (figure 4.2), to obtain complete ductile to brittle transition curves. Transition curves for additional orientations were also obtained, subject to restrictions defined by the product form dimensions. To obtain test specimens for the through-thickness (Z-X and Z-Y) orientations, 10x10x(section thickness) blocks were machined from 35mm plate, and electron beam welded together to produce a complete specimen (figure 4.7). Metallographic analysis was performed upon sections of these specimens to ensure that the weld HAZ did not encroach upon the critical area of fracture close to the notch.

Limited testing of heat treated material was performed in order to investigate the effects of ageing time and test temperature upon transition temperature and upper shelf toughness. Complete transition curves were also obtained for the welded plates. Each weld was tested, to check the reproducibility of the welding process, as well as the variation between TIG and MMA types.

4.3.2 COD Tests

As discussed in the fracture mechanics section, COD testing can provide an accurate assessment of a material's resistance to fracture due to the presence of a sharp crack. Therefore, COD tests were made in parallel to the Charpy tests so that results from the two types of test could be compared and correlated.

Tests were performed on a 250kN E.S.H. servo-hydraulic machine using standard specimens (figure 4.8) and the procedures of BS7448[12]. Due to specimen size constraints, smaller specimens were sometimes necessary, but in most cases the preferred geometry of W=2B was possible. Z-X and Z-Y specimens were produced using a similar method to that of the Charpy specimens. Due to limits upon the amount of welded material available, the weld specimens were notched from the top rather than the end of the weld. However, several specimens were notched 'end on' to check whether this had any significant effect upon fracture toughness values.

Specimens were fatigue pre-cracked in three-point bending at room temperature using an Amsler resonant fatigue vibrophore within the limits of the standard, and load-shedding techniques were used during crack growth to achieve this criterion. It was found that if the specimen surfaces were ground to a 1200 SiC grit finish, the crack extension could be readily monitored with the naked eye. Crack growth was stopped when the surface crack had grown to just under half the specimen depth, as it was found subsequent to fracture that the fatigue crack front had an extended bowed profile, and so had grown slightly further internally.

During testing, specimens were surrounded with an insulating jacket above a bath of liquid nitrogen. The temperature was monitored via a thermocouple strapped to the specimen with PTFE tape which allowed satisfactory thermal contact. It was found that by adjusting the level of nitrogen in the bath, the desired temperature could be achieved, which was stable for at least 15 minutes. A low-temperature clip gauge was used to measure the crack opening, which was displacement calibrated with the chart recorder prior to each test. After remaining at test temperature for 10 minutes, the specimens were loaded in three-point bending at a displacement rate of 1mm/min and a graph of clip gauge displacement versus applied load obtained. Subsequent to fracture, specimens were measured and calculated according to BS7448 (see section 3.2.2).

Tests were performed to complement the Charpy results, i.e. complete fracture toughness transition curves were obtained for all product forms in a number of orientations, all welded sections were tested, and the effects of heat treatment quantified. In addition, the effects of specimen size under otherwise identical test conditions was investigated.

4.3.3 Tensile Tests

In order to provide yield stress data to allow accurate calculation of COD values, tensile tests were conducted on rolled plate material in the as-received and heat-treated conditions, at temperatures between -196°C and room temperature. Standard Hounsfield no.13 specimens (figure 4.9) were cut perpendicular to the rolling direction. A 50kN screw driven Instron machine, using an extension rate of 1mm/min was used for the tests, according to BSEN 10002[13]. The temperature was recorded using a thermocouple strapped to the gauge surface. Specimens were suspended above a cryogenic vessel containing liquid nitrogen, and the height adjusted to achieve the required temperature. Using this technique the temperature could be stabilised to within ± 5°C of the desired test temperature. A load-time trace was obtained, and the stress-strain curves calculated assuming plasticity occurred only along the gauge length. The final gauge length and diameter after failure was recorded for all tests.

4.3.4 Low Temperature Hardness Tests

Due to only a limited amount of pipe material being available, it was found necessary to deduce the yield stress for these materials by other means. It has been shown for ferritic steels at room temperature[14] that the Vickers hardness number can be approximately related to the yield stress as:

$$\sigma_0 = \frac{V_{HN}}{3}(0.1)^n \qquad \text{.....(4.1)}$$

where σ_o is the yield stress, V_{HN} the Vicker's hardness number, and n the work hardening coefficient. Thus using a value of n calculated from the rolled plate stress-strain curves, an approximation of the room temperature yield stress can be made.

Assuming the work hardening of the material is unaffected by test temperature it may be possible to extend this model to low temperature testing. To obtain low temperature hardness and hence yield stress values, specimens were mounted in bakelite and cooled in a temperature-controlled isopentane bath. It was found impractical to perform in-situ hardness measurements. However, by briefly removing the specimen from the bath to make a single indent, and then replacing it until it returned to the test temperature, acceptable low temperature measurements could be made. An average of five points per test temperature were taken, using a load of 30kg and a dwell time of 10s. All product forms, including the rolled plate (to allow comparison between the different test methods) were tested.

4.3.5 Compression Tests

To provide further confirmation of the variation of yield stress with test temperature, a limited number of low-temperature compression tests were performed. Cylindrical specimens of 6mm diameter and 12mm gauge length were tested according to BSEN 24506[15]. Specimens were cooled in an identical fashion to that of the COD tests, and loaded on a 250kN E.S.H. servo-hydraulic machine at 1mm/min.

4.4 FRACTOGRAPHIC ANALYSIS

4.4.1 Scanning Electron Microscopy

Fractographic analysis was conducted using an Hitachi S4000 field emission gun (F.E.G.) scanning electron microscope at an accelerating voltage of 20kV, and magnifications of up to x6000. Fracture surfaces from both Charpy and COD tests were examined and compared. The area close to the notch/fatigue crack root was examined to identify the failure mechanisms involved, and check whether specimen failure could be traced to a particular initiation event. In areas of subsequent crack

growth, features such as facet or void sizes were measured so as to gauge the ease of crack advance in a qualitative manner.

In some cases, to identify phases or inclusions at sites of particular scientific interest, the fracture surfaces were examined in a JEOL6300 SEM to allow EDX analysis. Due to the roughness of the surface in not providing a uniform and efficient yield of X-rays for analysis, only very approximate qualitative measurements were possible, and in some cases even these could not be achieved satisfactorily.

4.4.2 Metallographic Sections

For some features of interest on the fracture face, it was desirable to identify the microstructure just below the surface. In these cases, sections perpendicular to the surface at the point of interest were cut using an Isomet diamond saw at slow speed to minimise surface damage. These were then metallographically prepared and examined optically as in section 4.2.1.

4.4.3 Electron Back Scattered Pattern (EBSP) Analysis

In some sections perpendicular to the fracture face, it was found that banded defects occurred in the microstructure just below the fracture surface. These could either have been twin defects or slip bands. By analysing the orientation of the grain (microtexture) on each side of the defect and at its centre, and by calculating the mis-orientation across the defect, its nature could be identified. This was achieved using electron backscattered pattern (EBSP) analysis.

EBSP analysis has been reviewed by a number of authors[16,17]. It relies on the fact that if the angle of incidence between an electron beam and the specimen surface is relatively small (<20°), a large proportion of the incidence electrons are backscattered from below the surface, and interact in the same way as Kikuchi diffraction to produce a pattern. Therefore, by measuring and analysing diffraction patterns, the local grain

orientation can be measured to a surface spatial resolution of 0.5μm. A schematic of the technique is shown in Figure 4.10.

For the analysis, an Hitachi S4000 FEG SEM was used, operating at 20kV with an incidence angle of 18°. It was found that specimens etched for optical microscopy were sufficiently flat to provide a sufficient electron yield. The backscattered pattern for points across each defect were photographed, and the misorientation measured across the defect boundary was used to identify its type.

References:-

[1]HUMPHREYS F.J. & GOODHEW P.J., "Electron microscopy and analysis", pub.Taylor & Francis, London, 1988.

[2]LORETTO M.H., "Electron beam analysis of materials", pub.Chapman & Hall, London, 1994.

[3]VERHAEGHE B., BRECHET Y., LOUCHET F., MASSOUD J.P. & TOUZEAU D., 'Internal stresses in an austenoferritic duplex stainless steel', Phys.Stat.Sol., 153, p47-56, 1996.

[4]GROOM J.D.G., "Effects of prestrain on fracture", PhD thesis, University of Cambridge, 1971.

[5]TECHNICAL NOTE TN-503-3, Measurements Group inc., N.Carolina, USA.

[6]TEA-XX-062RK-120 (supplied by Measurement Group Inc).

[7]HUTCHINSON W.B., SCHLIPPENBACH U.V. & JONSSON J., 'Textures and anisotropy in duplex stainless steel SS 2377', from "Duplex Stainless Steels'86", Holland, pp326-330, 1986.

[8]BATE P. & PRICE, 'A modified Siemens texture goniometer', J.Phys.E:Scientific Instruments, 20, pp51-54, 1987.

[9]HATHERLEY M. & HUTCHINSON W.B., 'An introduction to textures in metals', IOM monograph, no.5, pub.IOM, London.

[10]BUNGE H.J., "Mathematische methoden der texturanalyse", Akademieverlag, Berlin, 1969.

[11]BS131, "Notched bar tests", British Standards Institute, London, 1989.

[12]BS7448, "Static K_{IC}, CTOD and J testing of metallic materials", British Standards Institute, London, 1995.

[13]BSEN 10002, 'Tensile testing of metallic materials, British Standards Institute, London, 1990.

[14]CAHOON J.B., BROUGHTON W.H. & KUTZAK A.R., Met.Trans., 2, pp1979-1983, 1971.

[15]BSEN 24506, 'Specification for hardmetals: compression test', British Standards Institute, London, 1993.

[16]JUUL-JENSEN D. & RANDLE V., 'Combined advanced techniques in the study of annealing processes', proc.conf."Materials Architecture", N.Hansen et al eds., Risø, Roskilde DK4000, Denmark, pp103-126, 1989.

[17]DINGLEY D.J. & RANDLE V., 'Microtexture determination by electron back-scatter diffraction', J.Mat.Sci., 27, pp4545-4566, 1992.

<table>
<tr><th>Cross-Rolled Plate</th><th>Ingot-extruded Pipe</th><th>Powder-extruded Pipe</th><th>HIP'd Pipe</th></tr>
<tr><td colspan="4">Melted via an Electric Arc process</td></tr>
<tr><td colspan="2">Refined by argon-oxygen degassing</td><td colspan="2">Gas-atomised to powder</td></tr>
<tr><td colspan="2">Cast as a continuous ingot</td><td colspan="2" rowspan="2">Packed into pre-formed cans</td></tr>
<tr><td>Hot-rolled to plate</td><td>Hot-rolled to bar</td></tr>
<tr><td>Cross-rolled</td><td colspan="2">Hot-extruded into pipe</td><td rowspan="2">HIP'd @ 1100°C</td></tr>
<tr><td>Solution treated @1120°C, 30min</td><td>Solution treated @1100°C, 1hr</td><td>Solution treated @1100°C, 5min</td></tr>
<tr><td colspan="4">Water quenched</td></tr>
</table>

Table 4.1 - Processing routes for the various as-received product forms of Zeron 100

	Cr	Ni	Mo	N	Si	P	S	Cu	W	C	Mn	Fe
Cross-rolled plate	25.3	7.2	3.7	0.24	0.3	0.021	0.001	0.59	0.57	0.017	0.46	bal.
Extruded ingot	25.5	7.2	3.55	0.22	0.21	0.018	0.001	0.65	0.63	0.023	0.55	bal.
Extruded powder	25.8	7.0	3.46	0.28	0.43	0.015	0.002	0.71	0.70	0.030	0.69	bal.
HIP'd powder	25.8	7.0	3.46	0.28	0.43	0.015	0.002	0.71	0.70	0.030	0.69	bal.

Table 4.2 - Chemical compositions (wt.%) of Zeron 100 product forms

	Plate thickness (mm)	Electrode diameter (mm)	Voltage (V)	Current (A)	Heat input (kJ/mm)	Travel speed (mm/min)
MMA weld	20	2.4	21-25	80-100	0.5-1.0	50-150
TIG weld	20	2.4	11-14	135-145	0.7-1.5	250-255

Table 4.3 - Welding conditions for Zeron 100 MMA and TIG welds

	C	S	Si	W	Mn	Cr	Ni	P	Mo	Cu
TIG weld 1	0.025	<0.01	0.41	0.91	0.75	24.62	9.04	0.05	3.36	0.71
TIG weld 2	0.017	<0.01	0.33	0.50	0.66	23.32	8.93	0.04	3.04	0.65
MMA weld	0.036	<0.01	0.46	0.87	0.75	24.54	9.51	0.06	3.44	0.71

Table 4.4 - Chemical compositions for MMA and TIG welds

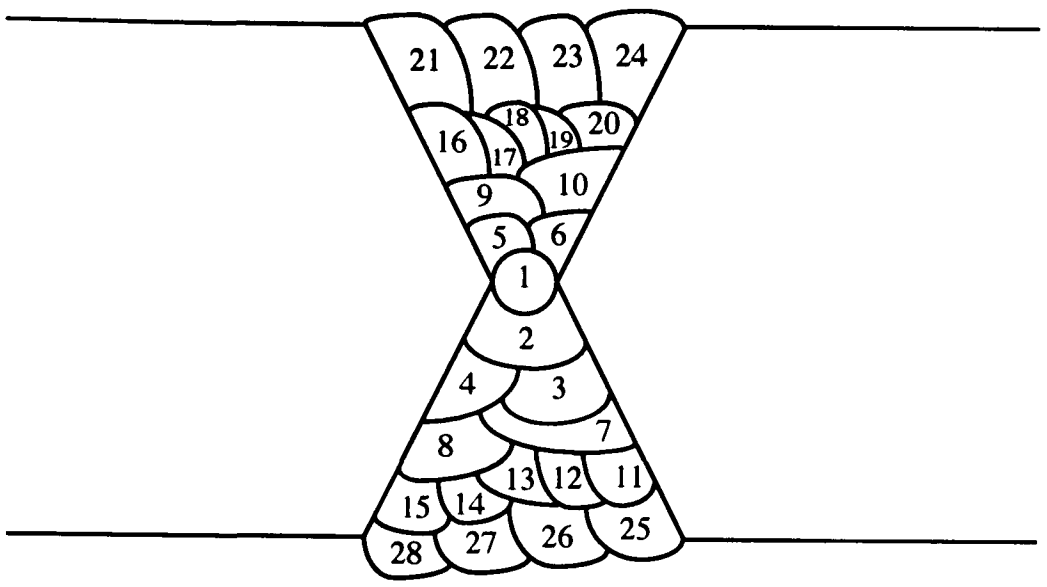

Figure 4.1 - Schematic of weld beads (TIG1 weld)

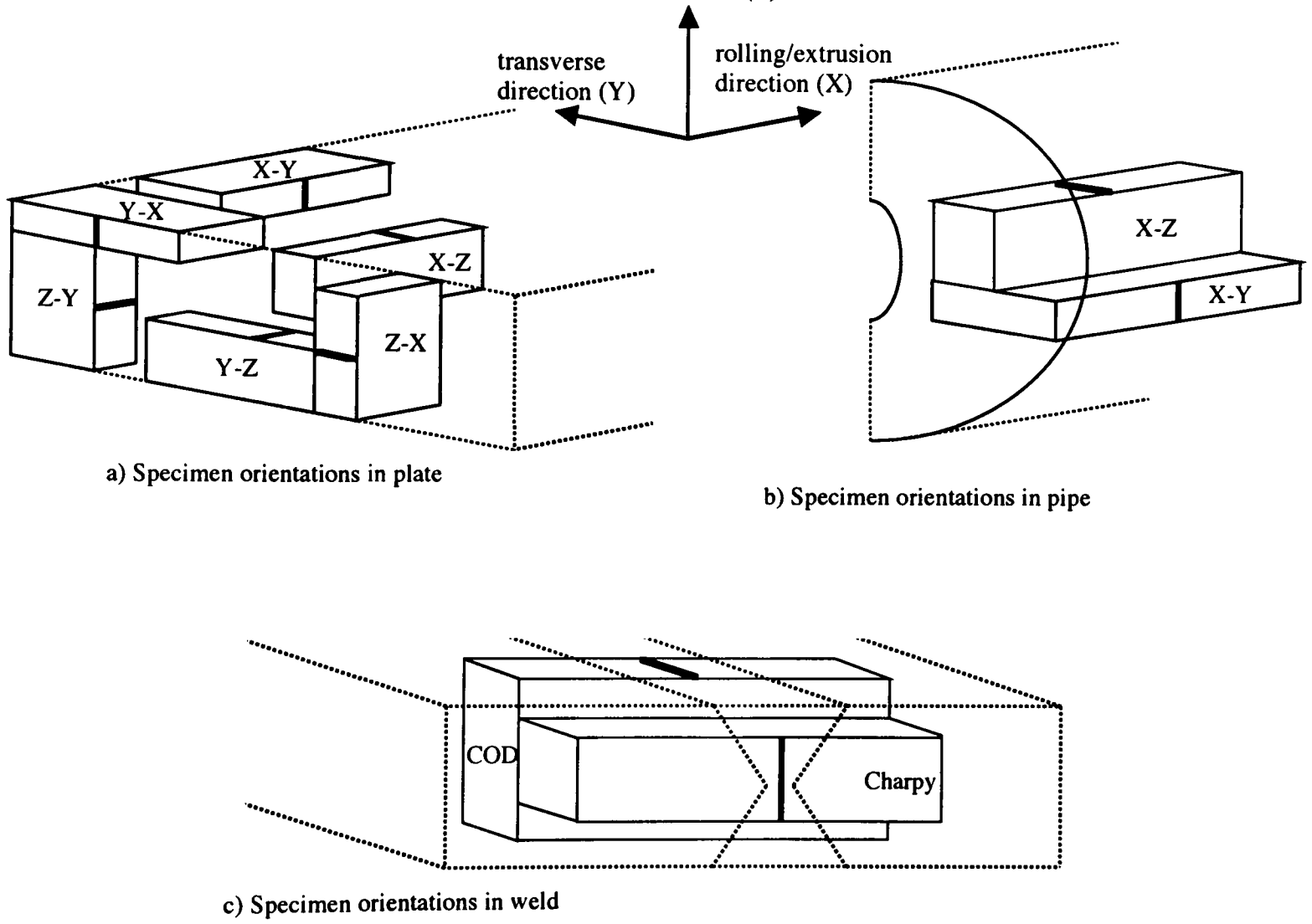

Figure 4.2 - Orientations of specimens cut from product forms

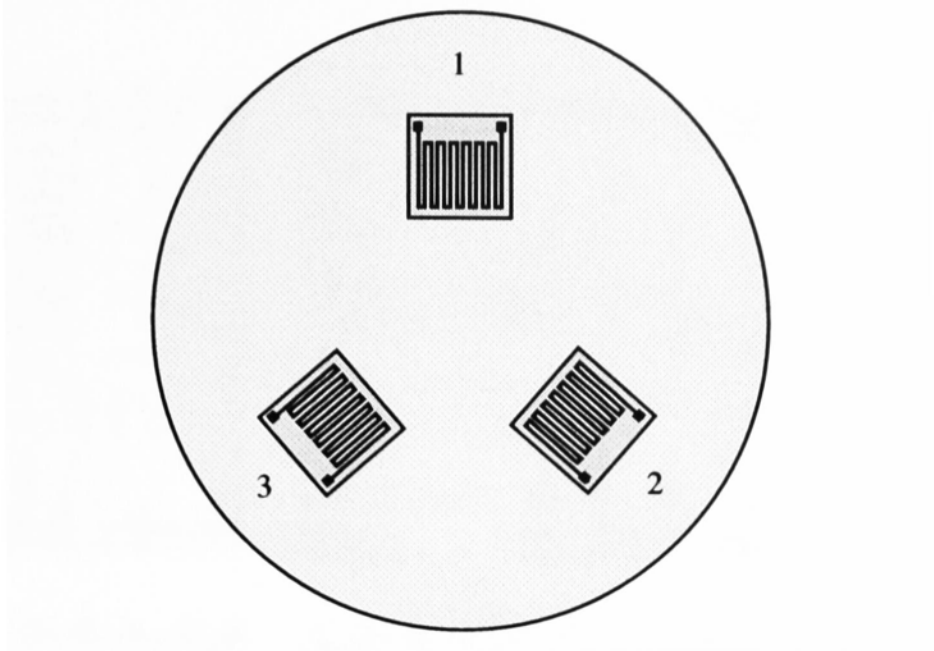

a) TEA-XX-062RR-120 strain gauge configuration

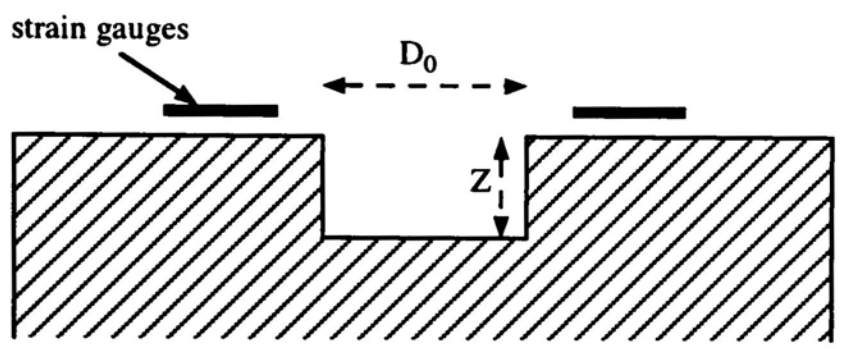

b) Sectional view of the drilled hole

Figure 4.3 - Blind hole drilling technique

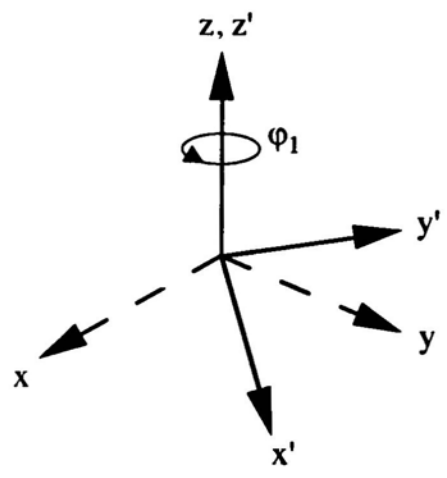

φ_1 – Rotation about specimen z

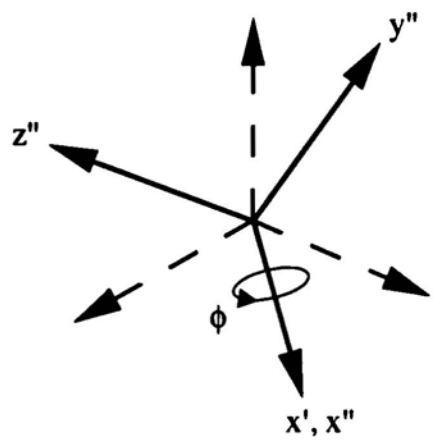

ϕ – Rotation about transformed x

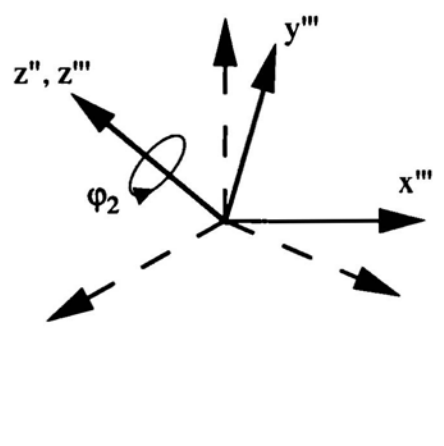

φ_2 – Rotation about transformed z

Figure 4.4 - Orientation transformations defined by the Euler angles

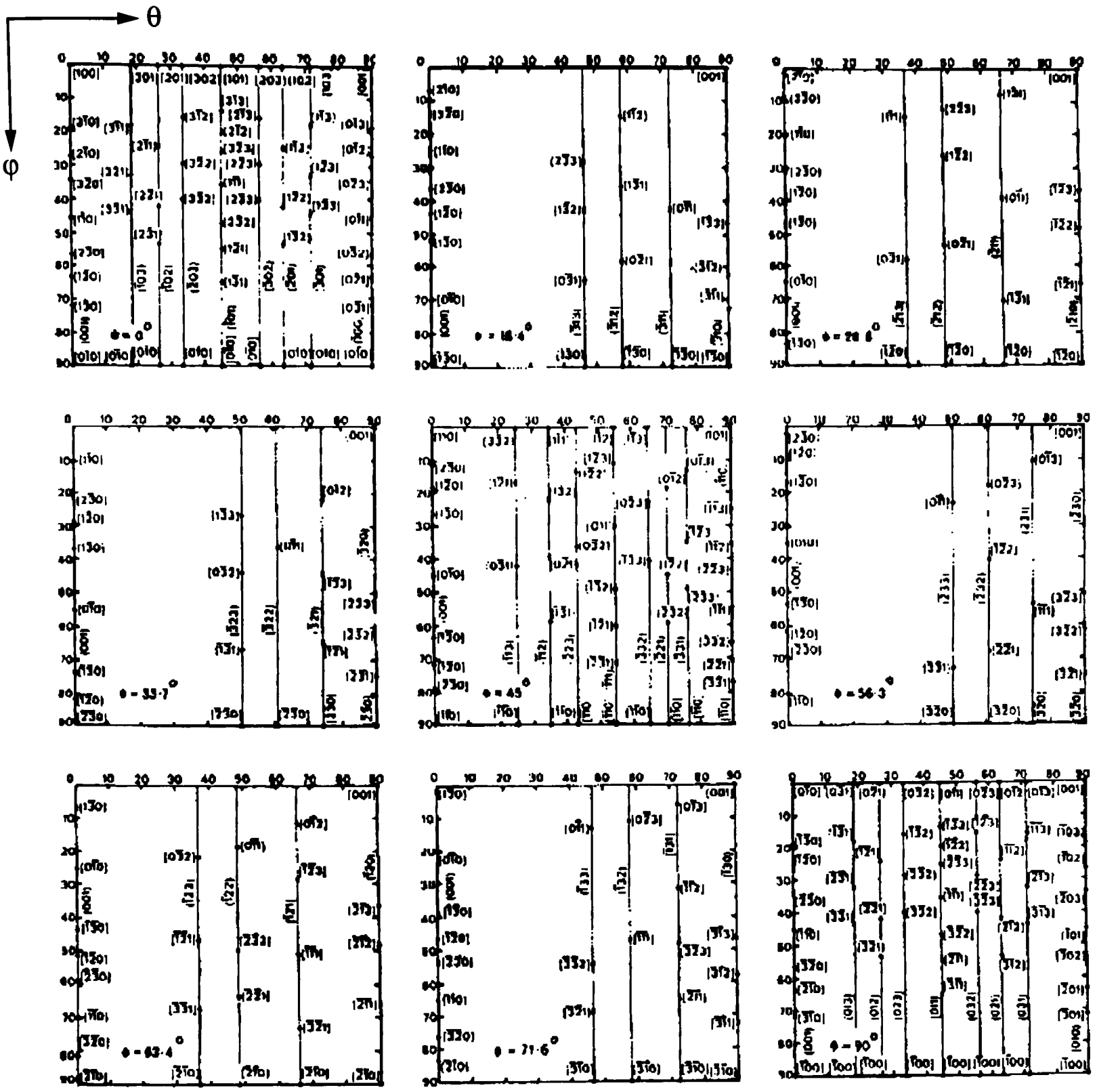

Figure 4.5 - Positions of the orientations (hkl)[uvw] in φ_2 section through ODF space[9]

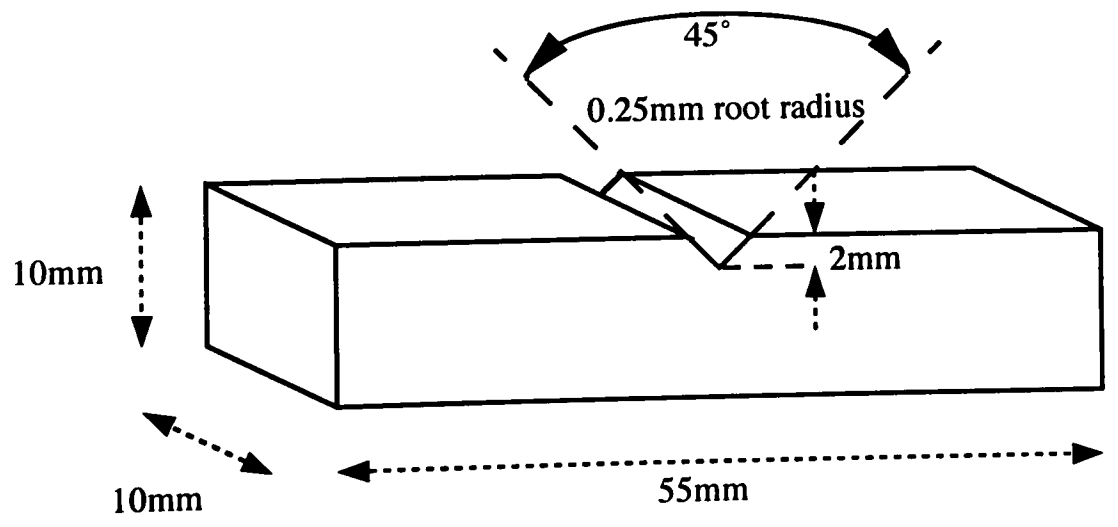

Figure 4.6 - Charpy testpiece configuration

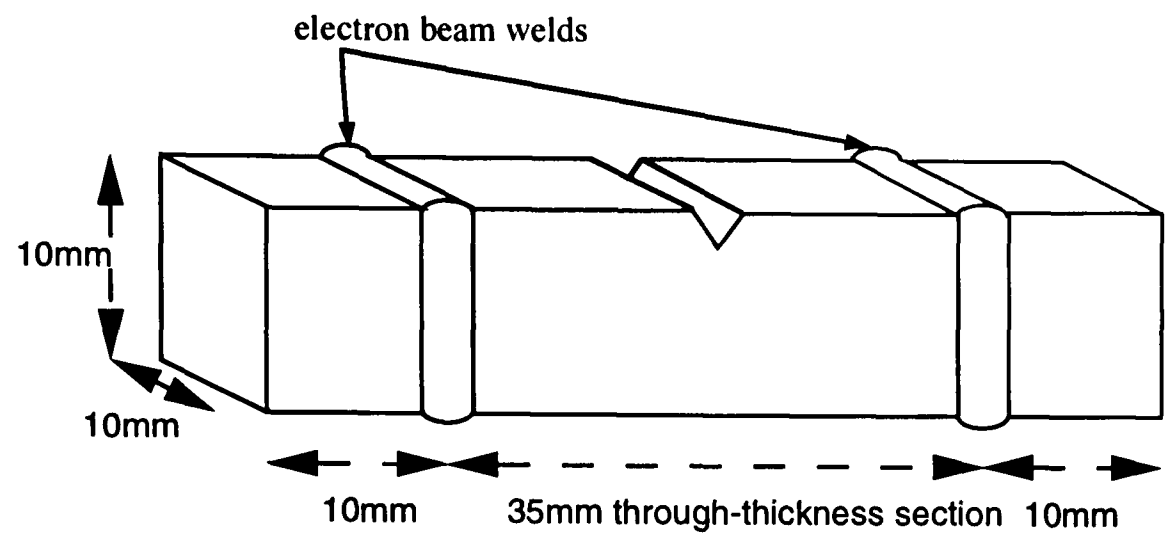

Figure 4.7 - Specimen configuration for Z-X and Z-Y orientated Charpy testpieces

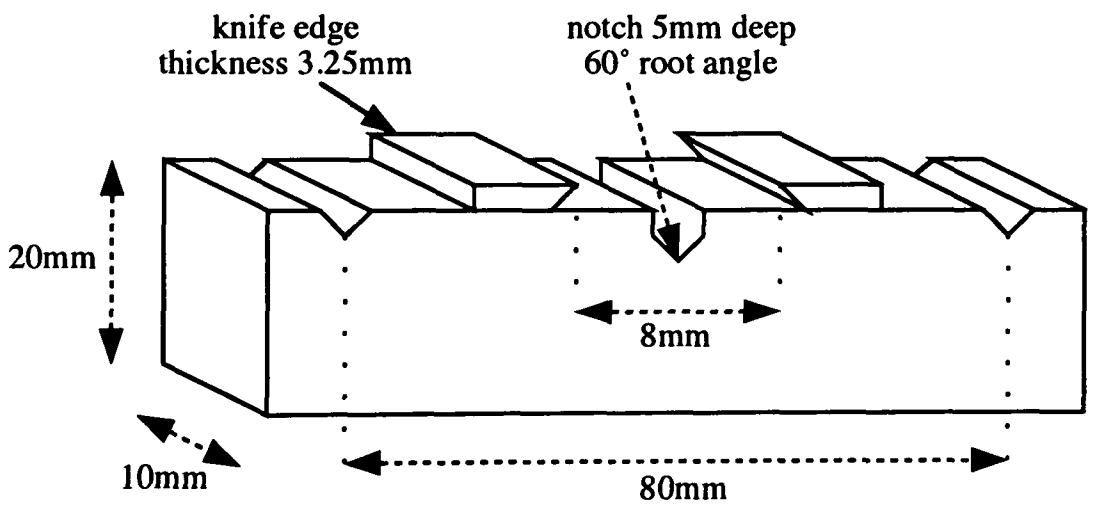

Figure 4.8 - COD Testpiece Configuration

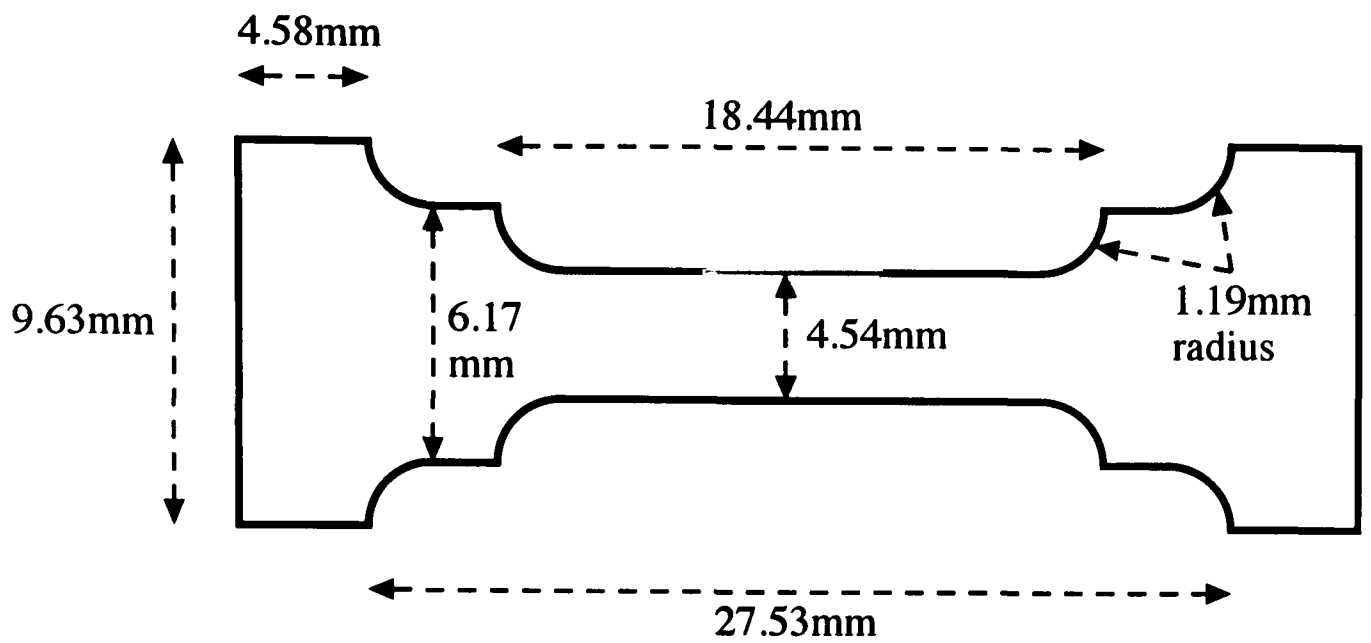

Figure 4.9 - Schematic of Hounsfield no.13 tensile testpiece

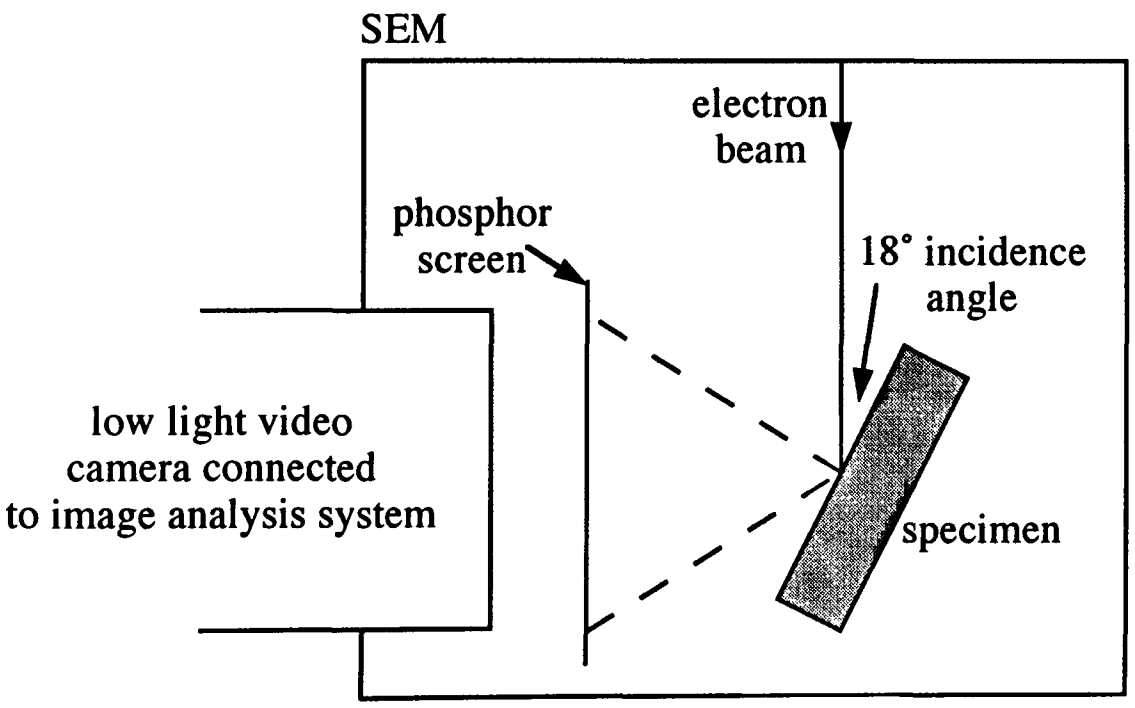

Figure 4.10 - Schematic of EBSP analysis system

5 - RESULTS

5.1 MICROSTRUCTURE

5.1.1 As-Received Product Forms

The various as-received Zeron 100 product forms were examined from three orthogonal directions to take account of any microstructural anisotropy. Optical micrographs of each material are shown in figure 5.1. Note that the etch reveals ferrite as the darker phase compared to austenite. Each form consisted of a ferrite matrix containing austenite grains, with an approximately 50:50 phase balance. There were however significant morphological differences between the microstructures. The rolled plate microstructure (of 15mm thickness) consisted of 'pancake' shaped grains, heavily banded along the rolling direction (figure 5.1a). The ingot-extruded pipe also contained highly elongated grains, but these were more tubular in shape than those of the plate (figure 5.1b). The powder-extruded pipe, which had a much smaller grain size than that of the other forms, again had tubular-shaped grains, but these were only slightly elongated (figure 5.1c). In contrast, the HIP'd microstructure was equiaxed, with a sharp angular grain shape (figure 5.1d). The phase fractions, grain sizes and aspect ratios of the different products forms are listed in table 5.1.

In some specimens, it was found that the grain size of the wrought product forms was slightly smaller at the surface than within their bulk (figure 5.2). This refinement was thought to be caused by higher strains in the near-surface region during processing, and was not expected to have a significant effect upon mechanical testing, as testpieces were generally machined from the centre of the material.

Although most mechanical testing employed 15mm thick rolled plate, some tests utilised plates of 20 and 35mm thickness due to specimen size constraints. The Vickers

hardness of each form was found to be similar (figure 5.3), and no discernible morphological difference in microstructure was detected between the 15 and 20mm thick plate. However, the 35mm thick plate was found to contain a slightly coarser grain size (figure 5.3).

The microhardness of the austenite and ferrite phases for the various product forms is shown in table 5.2. As expected, the ferrite was the harder phase, and this hardness increased with decreasing grain size. Only a slight hardness variation was detected across the width of each product form (figure 5.2).

SEM analysis was used to examine the materials at a higher magnification. No evidence of inclusions or grain boundary precipitation within the microstructure could be found. EDX analysis of the austenite and ferrite phases revealed no significant compositional variations between the different product forms (table 5.3). The ferrite phase was found to enriched with the elements molybdenum and chromium, whereas the austenite phase contained higher levels of nickel and copper. Traces of silicon in ferrite, and manganese in austenite were also detected, but these amounts were too small to be readily quantified. No chemical segregation was recorded across the bulk of the material.

Limited TEM investigations were made of the rolled plate microstructure. The interphase boundaries were found to be devoid of any precipitates (figure 5.4). Both phases generally had a low dislocation content, but the austenite grains contained many annealing twins.

Residual stress analysis using the hole drilling technique was performed on the rolled plate from three orthogonal directions and for the pipe product forms from one orientation only (perpendicular to the transverse direction). This revealed that there were strong tensile residual stresses present in the material, but only a slight variation was

recorded between the different product forms and various surface orientations (table 5.4). A typical analysis is shown in figure 5.5 and it can be seen that the mean stress reaches a plateau at a depth of around 0.6mm. The existence of tensile residual stresses was perhaps further suggested by the presence of bowed fatigue crack fronts within fracture toughness specimens (figure 5.6), implying the centre of the crack was accelerated by such stresses. However, it should be noted that this bowed crack front could also be due to the change in ductile constraint across the width of the specimen.

The crystallographic texture of each product form was measured using X-ray analysis. The texture strength was found to vary between materials, with the extruded powder form containing the sharpest texture and the HIP'd material being random (table 5.5). The austenite texture for the wrought materials was of a very weak {111} fibre type, with a maximum intensity only 2-3 times that of a purely random distribution. This was deemed to be insignificant due to the inaccuracies involved in the test. However, the ferrite phase was orientated with a much stronger {001}<110> texture, typical of a rolled bcc material. An ODF plot of this texture is shown in figure 5.7 and the texture was elucidated using a standard ODF map (figure 4.5). The variation in rolling texture between the wrought product forms was thought to be caused by partial recovery of the structure during hot-rolling/extruding. Such recovery was thought to have occurred within the rolled plate and extruded ingot forms, but to have been hindered in the extruded powder form. A parallel project[1] revealed from TEM analysis that the interphase boundaries in this material were covered with tiny particles from the gas atomisation process, and these would be expected to pin the boundaries thus preventing such recovery from occurring.

5.1.2 TIG and MMA Welds

The microstructures of the various weld metals (shown in figure 5.8) were found to contain a much finer grain size than that of the parent material (20mm rolled plate) and to have a much greater inclusion content. Typical microstructures consisted

of randomly orientated, highly elongated austenite laths within a ferrite matrix. A parallel project[1] confirmed by TEM analysis that the nature of these laths was of grain boundary austenite with Widmanstätten-type sideplates. Some smaller, more equiaxed austenite grains of an acicular nature were also present. Note that the proportion of acicular austenite was much greater in the root beads (figure 5.8c,d) than the surface beads (figure 5.8a,b), although there was no variation in phase balance between these two regions.

Both TIG welds were found to contain a similar microstructure and there were also no discernible morphological differences between the MMA and TIG welds (table 5.6). However, the inclusion content within the MMA weld (approximately $8x10^{16}m^{-3}$) was much greater than that of the TIG weld ($5x10^{15}m^{-3}$) (figure 5.9). Note that the MMA weld inclusions were much larger (average diameter 0.85μm) than those of the TIG weld (0.52μm). The various grain sizes are displayed in table 5.6.

Examination of the microstructure at higher magnifications within the SEM failed to find any precipitates of other phases present within the microstructure. The resolution of the EDX technique was insufficient to allow the precise elemental composition of the individual phases to be measured.

Typical heat affected zone (HAZ) microstructures are shown in figure 5.10. It can be seen that some austenite dissolution had occurred at the weld interface accompanied by ferrite grain growth, resulting in a 40μm thick band of coarse-grained ferrite along the interface. Some acicular austenite was also formed within the parent plate material. The extent of this HAZ was greater in the TIG than the MMA weld, presumably due to its higher heat input. However, the mechanical tests were designed to sample the centre of the weld metal, so the HAZ was not studied in any detail for this project.

The weld microstructures were too fine to allow microhardness measurements of the individual phases to be made. However, Vickers hardness profiles were obtained along the weld centre line throughout its thickness (figure 5.11). As can be seen, the TIG weld was generally harder than the MMA weld. No variation in hardness was recorded between the two TIG welds. A significant hardness increase was recorded with progressively deeper weld beads, indicating that reheating of the beads significantly affected their properties. Thus it was critical to ensure a constant notch depth for all weld metal fracture specimens to allow a rigorous comparison of results. A hardness profile across the width of the weld was also made (figure 5.12), indicating that the HAZ extended over 10mm into the parent material.

Residual stress measurements were taken at the centre of each weld, perpendicular to the weld line. The measured stresses (which were of a tensile nature) were found to be only slightly higher than that of the parent material (table 5.6).

5.1.3 Heat Treated Material

Significant changes within the microstructure were observed following heat treatment of the material at a temperature of 850°C. After only two minutes annealing, precipitates were found to have formed within specimens at the ferrite grain boundary triple points. The thermocouple attached to the specimens showed that the specimen temperature was only within 50°C of the furnace temperature after 90 seconds in the furnace, thus the nucleation process was virtually instantaneous. After five minutes annealing, these precipitates had grown along the ferrite/ferrite boundaries and formed a significant volume fraction of the microstructure (figure 5.13). No change in microhardness with heat treatment was detected for the austenite and untransformed ferrite phases. Samples aged for a longer period of time (45 minutes) were found to contain completely transformed ferrite grains, which had evolved into a coarse lamella structure (figure 5.14).

In general, the nucleation and growth rate of this phase was consistent between the different product forms. However, the extruded powder material contained a higher volume fraction of the phase than the other forms, presumably due to its fine grain size and hence greater grain boundary surface area for nucleation to occur. Thus after 10 minutes annealing, the extruded powder form had a phase volume fraction of 12%, compared to a 5% volume fraction for the other products.

EDX analysis of the microstructure revealed the phase to be rich in chromium and molybdenum, and deficient in nickel and copper compared to the untransformed ferrite. However, accurate quantitative measurements of the phase composition were not possible, as the phase size was equal to the limit of the EDX probe resolution. The second phase in the lamella structure was found to be slightly deficient in chromium. Thus this evidence suggested that the phase transformation occurring was the eutectoidal decomposition of ferrite to sigma and secondary austenite. Careful analysis at high resolution within the SEM failed to find any other precipitates present. Hence impact and fracture toughness specimens of the different product forms were heat treated to precipitate sigma phase, in order that the effect of sigma phase volume fraction upon fracture toughness could be assessed.

In contrast, annealing at a temperature of 425°C for 100 hours, failed to produce any visible evidence of a microstructural change. However, microhardness tests revealed significant hardening of the ferrite matrix during heat treatment, although the hardness of the austenite grains remained unchanged. Thus the phase transformation occurring was presumed to be that of α' formation. A parallel project[1] confirmed by TEM analysis that an α' phase dispersion had formed (via a spinodal decomposition mechanism) within the ferrite phase following this heat treatment.

A further specific heat treatment was used to reveal the dislocation structure and hence residual stress distribution within the microstructure. TEM analysis of the as-

received microstructure cannot reveal the original dislocation distribution, as this is disrupted during preparation of the foil. It is well known that prolonged annealing at a temperature of 550°C results in the precipitation of nitrides and R-phase, which preferentially nucleate upon dislocations arrays[2]. Hence this heat treatment can be used to decorate the original dislocation structure, which can be subsequently examined using TEM analysis.

The microstructure of the rolled plate material annealed at a temperature of 550°C for 5 hours is shown in figure 5.15. The phase interfaces were found to be covered with a thin (50nm) layer of hexagonal Cr_2N precipitates (which were identified using selected area diffraction pattern analysis). A precipitate free zone (PFZ) extended from the interphase boundary for roughly 0.5μm into the ferrite grain, before an intense band of α'/Cr_2N precipitates (which were too fine for unambiguous identification). The remainder of the ferrite grain bulk contained fine precipitates that were much smaller than those within the near-interfacial band (figure 5.16). No chemical segregation was detected within this band. A parallel project[1] revealed that upon further ageing (20 hours), coarse R-phase precipitates were formed in a band at a similar distance from the phase boundary (figure 5.17).

5.2 YIELD STRESS EVALUATION

In order to calculate results from the COD (fracture toughness) tests, it was necessary to elucidate the yield stresses of the different product forms. It is well known that the yield strength of wrought duplex stainless steels is anisotropic[3]. However, it was impractical to measure this stress for all fracture testpiece orientations, hence it was only measured with specimens that were elongated along the rolling/extrusion direction. This was anticipated as the orientation of maximum yield stress, thus any variation in

material strength with testpiece orientation would result in the fracture toughness data being conservative in terms of COD values.

Tensile tests were conducted using the as-received rolled plate material between temperatures of -196 and +20°C. Typical stress-strain curves are shown in figure 5.18. It can be seen that even at a test temperature of -196°C, high strains are achieved prior to fracture, with a large reduction of area (figure 5.19). The deformation process was observed to be highly anisotropic, resulting in the specimen necking into an oval shape (figure 5.20). Since no sharp yield point was observed in the stress-strain curves, the critical stress for failure was taken as that of 0.2% strain. Limited tensile tests of the weld metals and heat treated material were also performed and the results are shown in table 5.7.

Due to the limited amount of pipe product form material available, it was not possible to produce tensile test specimens for these, hence the yield stress of these specimens was calculated using low temperature hardness data (as discussed in section 4.3.4). The variation of Vickers hardness with test temperature for the various product forms is listed in table 5.8. In order to use this data to calculate the yield stress (equation 4.1), the work hardening coefficient of the material was required. This was obtained from the as-received rolled plate tensile data, by measuring the gradient of a ln.true stress versus ln.true strain plot (figure 5.21). It can be seen that this coefficient had a value of approximately 0.1 and this was constant for all test temperatures. The calculated yield stress versus test temperature curves are shown in figure 5.22. It can seen that there was good agreement between the experimental (tensile test) and calculated (hardness test) data apart from at a test temperature of -196°C, hence the hardness technique provided a useful estimation of low temperature yield stress. Note that in general for the COD calculation (equation 3.34), the elastic component of the calculation (which utilises the yield stress) is much smaller than the plastic component

(which does not include the yield stress), hence its value has only a minor effect upon the calculated COD.

It was observed that the yield stresses of the rolled plate, extruded ingot and HIP'd powder forms were virtually identical, whilst the extruded powder data values were slightly higher, presumably due to its smaller grain size compared to the other product forms. Hence it was decided to perform the COD calculations for the extruded ingot and HIP'd powder using the tensile test results of the rolled plate. For the powder extruded form, low temperature compression tests were made to check the accuracy of the hardness calculations. The results, as displayed in figure 5.23, showed good agreement between data, hence the compression values were used for extruded powder material COD calculations.

5.3 IMPACT AND FRACTURE TOUGHNESS TESTING

5.3.1 As-Received Rolled Plate

Specimens were tested using both COD and Charpy techniques in a number of notch orientations to gauge the degree of material anisotropy, and between test temperatures of -196 and +20°C. The results of the Charpy tests for all six orthogonal orientations of the as-received rolled plate material are shown in figure 5.24. The material did not exhibit a sharp ductile to brittle transition temperature; instead the change from upper to lower shelf behaviour gradually occurred between test temperatures of approximately -50 and -120°C. The temperature of this transition region appeared to be unaffected by notch orientation.

The Charpy impact toughness was found to be highly anisotropic. Specimens with the notch plane orientated (as defined in figure 4.2) orthogonal to the rolling

direction (X-Z and X-Y) were generally tougher than those with the notch plane normal to the transverse direction (Y-X and Y-Z). The through-thickness specimens, where the notch plane was orthogonal to the normal direction (i.e. was equivalent to the rolling plane, Z-X and Z-Y) had the lowest impact energies.

The orientation of the crack front had an additional affect upon the Charpy impact values. Specimens with the crack front orthogonal to the normal direction (X-Z and Y-Z) had large toughness values compared to those with the crack front normal to the transverse direction (X-Y and Z-Y). Specimens with the crack front orthogonal to the rolling direction had the lowest toughness values.

Figure 5.25 shows the results for COD tests using equivalent notch orientations to those of the Charpy specimens. It should be noted that the COD test is primarily concerned with relatively small crack tip opening displacements. Hence values over 0.5mm, which denote extremely ductile behaviour, are of interest only in terms of plastic collapse and load limit analysis. The transition from upper to lower shelf behaviour appeared to take place over a similar range of temperatures to that of the Charpy tests. Although the effect of notch and crack front orientation was less discernible than for the Charpy tests, similar trends appeared to exist.

The type of load-displacement curve for each COD test (as defined by BS7448[4]) appeared to be affected by the orientation of the crack front as well as the absolute COD value. Specimens with the crack front orientated perpendicular to the normal direction (X-Z and Y-Z) failed subsequent to maximum load attainment (δ_m) for COD values over 0.35mm (figure 5.26a), whilst the remainder failed in a pop-in (figure 5.26b) or critical (figure 5.26c) manner after limited crack growth (δ_u). However, specimens with other notch orientations showed a greater propensity for maximum load attainment (figure 5.26d), and only specimens with a COD of less than 0.078mm (for which there was no stable crack growth) exhibited critical (δ_c) failure.

5.3.2 As-Received Pipe Product Forms

The material dimensions of the pipe product form only allowed two testpiece orientations to be used; those with the crack plane perpendicular to the extrusion direction (X-Y and X-Z). The Charpy transition curves for these orientations are shown in figure 5.27. From the limited amount of testing performed (due to lack of material availability) it was difficult to distinguish the transition temperature range for each material. However, a number of trends are evident. First, the impact values showed similar anisotropic behaviour to the rolled plate material, where specimens with the crack front orthogonal to the normal direction (X-Z) were consistently tougher than those with the crack front normal to the transverse direction (X-Y). There was also a constant variation in impact toughness between product forms, with the extruded ingot material having the highest impact energy, and the HIP'd powder the lowest. By comparing results of the pipe and plate materials for similar (X-Z) orientations (figure 5.28), it can be seen that the product form order of decreasing toughness is; extruded ingot, rolled plate, extruded powder and HIP'd powder.

The COD transition curves for the pipe product forms showed similar trends of product form and crack front orientation to those of the Charpy tests (figures 5.29 and 5.30). More extensive testing was possible, hence there were sufficient data points to show that the temperature range of the transition region was similar for all product forms. Compared to the rolled plate material, more pipe product form specimens attained maximum load (δ_m) prior to failure. Only specimens with a very low (0.04mm) COD failed in a critical (δ_c) manner.

5.3.3 MMA and TIG Welds

The Charpy impact toughness transition curves for the weld metals are shown in figure 5.31. The toughness of all welds was much reduced compared to that of the parent material (20mm rolled plate). In general, the TIG1 weld was slightly tougher than the TIG2 weld whilst the MMA weld had very low impact values. The ductile to

brittle transition temperature range appeared to be slightly higher for the weld metals than that of the as-received product forms, with lower shelf values achieved at a test temperature of -80°C.

The results from COD tests of the weld metals showed similar trends to the Charpy results (figure 5.32). However, the failure mode was found to vary between the different weld techniques. TIG-welded specimens tested at test temperatures greater than -100°C consistently underwent pop-in failure(s) prior to stable crack growth and maximum load attainment (figure 5.33a). As these pop-in failures exceeded the 5% secant line according to BS7448, the COD measurements were taken at the crack extension of these events, resulting in very low COD values. At test temperatures below -100°C, TIG-welded specimens failed in a critical manner (figure 5.33b). However, MMA-welded specimens failed in a maximum load manner with very limited crack growth at all test temperatures (figure 5.33c).

5.3.4 Heat Treated Materials

The effect of sigma phase upon fracture behaviour was investigated by annealing rolled plate material at a temperature of 850°C for between 5 and 45 minutes. Specimen were tested at temperatures of -60 and -110°C (the temperature range of the ductile to brittle transition for the as-received material). The results of Charpy tests are shown in figure 5.34. No change was evident after 5 minutes annealing, whilst further annealing resulted in a sharp decrease in toughness. However the COD values decreased after a heat treatment of only 5 minutes (figure 5.35). The heat treated specimens all failed in a critical manner.

To investigate the effects of α' formation upon fracture behaviour, specimens were aged at a temperature of 425°C for 100 hours. Charpy testing revealed that the aged material was embrittled compared to the as-received product forms (figure 5.36). The ductile to brittle to transition temperature was increased and the upper shelf

toughness values decreased. COD tests also showed that the material toughness was much reduced by this heat treatment (figure 5.37), and the specimens exhibited critical failure.

5.4 FRACTOGRAPHIC ANALYSIS

5.4.1 As-Received Rolled Plate

Fracture surfaces from both COD and Charpy tests were examined in the SEM to elucidate the micromechanisms of the fracture process. Qualitative EDX analysis of the fracture surface was used to distinguish between austenite and ferrite grains, via the higher chromium/nickel ratio of the latter phase. There was found to be little variation between the fracture surfaces of Charpy and COD specimens. However, COD specimens contained a stretch width zone (SWZ) of stable ductile crack growth at the fatigue precrack base (figure 5.38), the width of which decreased with decreasing test temperature.

Examination of fracture surfaces from X-Z orientated rolled plate specimens revealed that at test temperatures above -80°C, the whole microstructure failed in a ductile manner by microvoid coalescence (MVC) with little or no ferrite cleavage (figure 5.39). The ferrite microvoids were much larger than those of the austenite phase (table 5.9), although both were similarly shaped. Very few inclusions were observed within these microvoids. At test temperatures between -80 and -100°C, occasional ferrite cleavage facets were observed, surrounded by ductile failure (figure 5.40). It was noticed that these cleaved grains were generally larger than the average grain size of the microstructure, suggesting that the preference for ferrite cleavage was dependent upon grain size. Below a test temperature of -120°C, ferrite failure was exclusively brittle, resulting in large cleavage facets interspersed with fully ductile austenite colonies

(figure 5.41). Although strong river lines were present on the cleavage facets, no evidence was observed of any definitive initiating sites within the grains. It was noted that at these lower test temperatures, the fracture surface was dominated by cleavage facets, and in some cases only approximately 10% of its area was composed of austenite, thus indicating that crack growth occurred preferentially within the ferrite phase.

At higher test temperatures, specimens did not fracture, but failed by plastic collapse at the crack base. This plastic failure appeared to deviate from the normal crack path and was directed along the transverse direction (figure 5.42a) At lower test temperatures where ferrite cleavage occurred (<-100°C), specimen fracture was accompanied by a large amount of crack deviation, with the crack extending in a stepped manner along the transverse direction (figure 5.42b). This stepped growth could be easily observed upon the fracture surfaces (figure 5.43a). The surface of the steps was composed of cleavage facets with ductile tearing between the steps (figure 5.43b). Non-planar crack growth was often accompanied by crack bifurcation, resulting in secondary crack formation at the notch root (figure 5.44a). Close inspection of these cracks revealed their surfaces to be composed almost exclusively of cleavage facets (figure 5.44b). Additional secondary cracks from bifurcation were also observed during subsequent crack growth (figure 5.45).

Although there was no difference observed between the micromechanisms of failure (at a given test temperature) for specimens with different notch orientations, the notch orientation was found to affect the overall appearance of the fracture surface.

Specimens with notches orientated along the normal direction (X-Z and Y-Z) both displayed non-planar crack growth, with the former having the greatest crack deviation. However, specimens with identical crack planes but orthogonal crack fronts (X-Y and Y-X) exhibited planar crack growth with no transverse crack bifurcation

(figure 5.42c). Instead, splits were formed along the direction of crack growth, the size of which increased with decreasing test temperature (figure 5.46). Close inspection revealed these cracks to be similar to those formed from crack bifurcation, as their surfaces were found to contain many cleavage facets (figure 5.47). In addition, shear lips were formed around these cracks (figure 5.48) which substantially increased the amount of ductile failure on the fracture surface.

Specimens tested with the notch and rolling plane equivalent (Z-X and Z-Y) failed in a planar manner with no major secondary cracking. Fracture surfaces from Z-X orientated specimens were very flat and similar to the step surfaces of transverse deviated cracks (figure 5.49). However, the surfaces of Z-Y specimens were slightly rougher and appeared to contain a greater proportion of austenite phase (figure 5.50).

5.4.2 As-Received Pipe Product Forms

There were no observed differences between the micromechanisms of failure (at a given test temperature) for the different as-received product forms, and the variations of microvoid and cleavage facet size (table 5.9) were consistent with that of the grain size. However, the crack path appeared to be dependent upon the microstructure. The extruded ingot material showed similar fracture behaviour to the rolled plate form (figure 5.51), including crack bifurcation and transverse deviation (X-Z orientation) and secondary cracking parallel to the crack path (X-Y orientation).

The extruded powder specimen fracture surfaces displayed similar crack path trends to the wrought product forms, but the extent of transverse crack growth and secondary cracking was much reduced. The ferrite cleavage facets were small, and the distribution of phases upon the surface more even than that of the other wrought product forms (figure 5.52).

The fracture surfaces for the HIP'd material specimens were planar with no transverse growth or major secondary cracking (figure 5.53). However, the surfaces were of an undulating nature and composed of more ferrite than austenite phase, indicating that local crack deviation still occurred around austenite grains. There were also many small, randomly orientated secondary cracks at interphase boundaries which were of a brittle nature.

5.4.3 MMA and TIG Welds

The fracture surfaces of weld specimens were planar with no transverse or secondary crack growth. There were no observed variations in fracture surface between the two TIG welds. At a test temperature of -40°C both welds failed in an exclusively ductile manner by microvoid coalescence (figure 5.54). The ferrite microvoids of the TIG weld were much larger than those of austenite, although smaller than those of the as-received product forms (table 5.9). However, the MMA weld microvoids were much smaller and similarly sized for both phases. The population of inclusions residing in microvoids was much larger in the MMA than TIG weld (figure 5.55). Qualitative EDX analysis of these inclusions revealed these to contain high levels of titanium and manganese.

The ductile to brittle transition temperature of the weld metal was found to be significantly higher than that of the as-received product forms. Ferrite cleavage facets could be observed at test temperatures of -50°C for the TIG and -70°C for the MMA welds (figure 5.56). At lower test temperatures (<-80°C), ferrite grains failed exclusively by cleavage whilst the austenite phase remained fully ductile (figure 5.57). Both phases were present in equal proportions on the fracture surface, but due to the fine grain size of the weld metals, the precise definition of cleavage facets was often unclear. However for larger grains where river lines were present, cleavage initiated from inclusions could often be observed, particularly upon MMA weld fracture surfaces (figure 5.56b).

Although the test procedure did not appear to affect the micromechanisms of failure at various test temperatures, the appearance of Charpy and COD fracture surfaces was different. Note that the notch orientations were different for Charpy and COD test specimens, with the notch being 'end-on' to the weld for the Charpy testpieces whilst COD testpieces were notched from the top. For COD specimens, particularly TIG-welded types, it was evident that within the temperature region of the ductile to brittle transition (between test temperatures of -50 and -100°C), the propensity for cleavage failure was increased close to the fatigue precrack root. This often resulted in large (1mm long) pop-in cleavage cracks that subsequently arrested to grow in a stable ductile manner (figure 5.58).

For Charpy test specimens there was no evidence of a change in failure mechanism during crack growth. However at lower test temperatures (<-50°C) one or more secondary cracks were formed central to the specimen along the direction of crack growth (figure 5.59). Examination of these crack surfaces revealed that they were of a brittle nature, similar to the secondary cracks of the as-received product forms. Note that this pop-in/secondary cracking behaviour was only evident in TIG-welded specimens.

5.4.4 Heat Treated Material

Limited investigations of the effect of heat treatment upon fracture behaviour was made for the rolled plate material. Specimens heat treated at a temperature of 850°C had markedly different fracture surfaces to those of the as-received product form. Testpieces were orientated in the X-Z direction, which produced transverse crack deviation for the as-received form. However, the amount of this deviation was found to be decreased with an increase in annealing time. Fracture surfaces of specimens annealed at temperature for 2 or 5 minutes contained small areas of cleavage interspersed with ductile failure (figure 5.60a). Qualitative EDX analysis was unable to distinguish between ferrite and sigma phase, but these cleaved areas were presumed to

be the latter as they did not have the appearance of previously observed cleavage facets. Further annealing (10 and 45 minutes) resulted in extensive cleavage of the fracture surface, interspersed with fine ductile austenite ligaments (figure 5.60b).

Specimens aged at a temperature of 425°C showed similar fracture surfaces to those of the as-received product form. However, the ductile to brittle transition temperature appeared to have increased with ageing, as limited evidence of cleavage could now be observed in specimens tested at room temperature (figure 5.61)

5.5 SUB-SURFACE ANALYSIS

5.5.1 Crack Path

The transverse deviation of the crack path through the rolled plate microstructure was investigated in more detail by arresting COD test specimens prior to unstable failure and examining metallographic sections perpendicular to the fracture surface. The crack path for test specimens that failed in a ductile manner by plastic collapse was difficult to follow due to the large opening at the crack tip, but in general the crack appeared to grow in the direction of the elongated austenite grains (figure 5.62a). The crack tip also appeared to have a path preference for the ferrite phase (figure 5.62b).

The crack path was more easily followed in brittle fracture specimens. A specimen tested at a temperature of -110°C was arrested following a pop-in event subsequent to limited stable crack growth (figure 5.63). It can be seen that although the crack tip had widened, no visible primary crack growth was evident. A large crack had formed approximately 250μm ahead of the main crack and grown in a transverse direction. At higher magnifications it can be seen this crack was exclusively resident within ferrite grains (figure 5.64).

A subsequent specimen tested at a temperature of -110°C was arrested after some stable crack growth had occurred following a pop-in event (figure 5.65). It can be seen that following bifurcation, the crack had advanced in a stepped manner along the normal/transverse directions. Note that between steps the crack did not grow in a linear manner, indicating that ductile tearing was occurring between steps. At higher magnifications it can be seen that this crack resided within the ferrite phase and appeared to deviate around austenite grains (figure 5.66). It was also noted that the crack showed a path preference within a region close to the interphase boundary. In many cases austenite grains were observed to bridge these ferrite cracks (figure 5.67).

The growth of secondary cracks within test specimens orientated in X-Y and Y-X directions was also investigated by analysis of fracture surface sections. Compared to transverse cracks from bifurcation, these had a large crack tip opening, even at low test temperatures (figure 5.68), suggesting that the crack grew in a ductile manner. However, examination at high magnifications revealed that the crack tip was only ductile at higher test temperatures (>-80°C), and that at lower temperatures, the crack advanced by the linking of microcracks within the ferrite phase (figure 5.69).

Although no arrested COD tests were made on other product forms, the crack path could be followed by examining sections of fracture surfaces. The ingot and powder extruded forms appeared to fail with stepped transverse crack deviations similar to the rolled plate. However, the HIP'd fracture surface showed that although the crack path was predominantly along the normal crack direction, the crack resided within the ferrite grains and deviated around the equiaxed austenite grains in a zig-zag manner (figure 5.70).

Examination of TIG-welded Charpy specimens revealed that the secondary cracks formed followed the fusion line between adjacent weld beads (figure 5.71a). During subsequent crack growth they were observed to deviate along the coarse-grained

HAZ interface. Examination of the crack tip revealed that growth occurred in a brittle manner (figure 5.71b)

5.5.2 Microcrack Initiation

In sections of broken testpieces from rolled plate specimens, planar defects were observed in the ferrite phase close to the fracture surface (figures 5.72, 5.73). These were presumed to be either slip bands or mechanical twin defects. They were concentrated in small clusters along the fracture surface, and their distribution was roughly equal throughout the crack length. Although some defects were observed at higher test temperatures (>-50°C), their density appeared to increase sharply with decreasing test temperature, especially once temperatures relating to lower shelf toughness values were approached. More defects were present within Charpy than COD test specimens. Examination of other product forms revealed that the defect population was roughly equal for all product forms (figure 5.74).

EBSP analysis was used to differentiate between these two types of defects. Figure 5.75a shows backscattered diffraction patterns measured from the centre of a defect (as shown in figure 5.72b), and from the parent ferrite grain. It can be seen that there is only a small orientation difference between the two, thus this defect was presumed to be a slip band. However, figure 5.75b shows diffraction patterns measured across the boundary of a different defect (as shown in figure 5.73b) and it can be seen that there was a large orientation variation. When these two different orientations were plotted, and the misorientation between them calculated (figure 5.76) it was found that the lattice was rotated by 60° about the [110] pole across the defect boundary. This is consistent with that of a twin boundary for a bcc structure. Note that there is little apparent visible differences between twin and slip band defects, supporting the use of an EBSP approach in their identification.

This procedure was used to differentiate between mechanical twins and slip bands throughout the microstructure for different test specimens. It was found that for test temperatures above -50°C, the few defects that existed were almost exclusively slip bands while at lower test temperatures, mechanical twins tended to more prevalent. However, it should be noted that this system of identification was limited by the resolution of the EBSP analysis technique, which was not much smaller than that of the defect width. Thus for a more rigorous examination of twin defects, it would be preferable to use TEM methods. Note that due to time constraints upon the EBSP analysis system, only rolled plate specimens were analysed using this technique.

Further analysis of test specimen sections revealed that occasionally small microcracks had nucleated in the ferrite phase and failed to grow past the austenite grains. In some cases, these cracks were observed to be bisected by twin defects (figure 5.77). Further evidence of the role of these mechanical twins in cleavage initiation could be found by examining the fracture surfaces of cleavage facets. Twin boundaries could often be observed where the river lines of a single cleavage facet were interrupted in a linear manner (figure 5.78).

References:-

[1]LI X., 'Prediction and assessment of duplex stainless steel microstructures susceptible to low temperature cleavage failure', PhD thesis, University of Birmingham, 1997.

[2]REDJAÏMA A., METAUER G. & GANTOIS M., 'Decomposition of delta ferrite in a Fe-22Cr-5Ni-3Mo-0.03C duplex stainless steel. A morphological and structural study', proc.conf."Duplex stainless steels'91", Beaune, France, pub.Editions de Physique, pp119-126, 1991.

[3]HUTCHINSON W.B., SCHLIPPENBACH U.V. & JONSSON J., 'Textures and anisotropy in duplex stainless steel', Mat.Sci.Tech., 10, pp289-298, 1994.

[4]BS7448, "Static K_{IC}, CTOD and J testing of metallic materials", British Standards Institute, London , 1995.

	Rolled Plate	Extruded Ingot	Extr. Powder	HIP'd Powder
Ferrite				
Phase Fraction	50	51	51	51
RD Grain Size	63	89	16	21
ND Grain Size	14	15	7.2	22
TD Grain Size	31	17	7.9	22
Aspect Ratio	4.5	5.9	2.2	1
Austenite				
Phase Fraction	50	49	49	49
RD Grain Size	65	84	18	22
ND Grain Size	22	16	9.2	23
TD Grain Size	17	18	11	22
Aspect Ratio	3.2	5.3	1.9	1

Table 5.1 - Phase fractions, grain sizes and aspect ratios of the as-received product forms (sizes are mean values in μm)

	Rolled Plate	Extruded Ingot	Extr. Powder	HIP'd Powder
Austenite	308	305	328	301
Ferrite	340	342	365	334

Table 5.2 - Microhardness of the phases within the as-received product forms (microhardness at 25g)

	Fe	Cr	Ni	Mo	Cu
Austenite					
Rolled Plate	63	25	8.7	2.8	0.6
Ingot-Extruded Pipe	63	25	9.4	2.3	1.0
Powder-Extruded Pipe	62	26	8.3	2.5	1.1
HIP'd Powder	63	26	8.2	2.5	0.8
Ferrite					
Rolled Plate	62	28	5.8	4.1	0.2
Ingot-Extruded Pipe	61	28	6.2	3.8	0.8
Powder-Extruded Pipe	61	29	5.4	3.9	0.7
HIP'd Powder	61	29	5.3	3.9	0.7
γ/α Partition Coefficient					
Rolled Plate	1.02	0.89	1.50	0.68	3.0
Ingot-Extruded Pipe	1.03	0.89	1.52	0.61	1.25
Powder-Extruded Pipe	1.02	0.90	1.54	0.64	1.60
HIP'd Powder	1.03	0.90	1.55	0.64	1.14

Table 5.3 - Elemental compositions and partition coefficients for the as-received product forms (compositions in (wt.%)

Product Form	Mean Stress at a Depth of 1mm (MPa)
Rolled Plate (Y surface)	-126
Rolled Plate (X)	-130
Rolled Plate (Z)	-120
Ingot Extruded Pipe (Y)	-135
Powder Extruded Pipe (Y)	-140
HIP'd Pipe (Y)	-120

Table 5.4 - Residual stresses measured within the as-received product forms

	Rolled Plate	Extruded Ingot	Extr. Powder	HIP'd Powder
Austenite	3	2	3	1
Ferrite	8	4	15	1

Table 5.5 - Variation of textural strength between as-received product forms

(texture strengths are scaled relative to that of random)

	MMA weld	TIG1 weld	TIG2 weld
Widmanstätten austenite			
length	32.2	28.2	34.3
width	2.5	2.1	2.4
aspect ratio	12.9	13.4	14.3
Acicular austenite			
length	4.2	3.8	4.1
width	2.9	3.1	3.0
aspect ratio	1.4	1.2	1.4
Mean residual stress (MPa)	144	135	143

Table 5.6 - Variation of grain size and residual stress between welds

Test temp. (°C)	As-received plate	Plate HT'd @425°C	Plate HT'd @465°C	Plate HT'd @850°C	TIG weld	MMA weld
20	598	1280	1131	780	903	894
-60	740	1326	-	-	1021	1028
-100	802	1384	1181	896	1136	1159
-130	833	1403	-	-	1253	1235
-196	1234	1430	1296	1277	1339	1326

Table 5.7 - Variation of 0.2% proof stress with test temperature (stress in MPa)

Test temp. (°C)	Rolled plate	Extruded ingot	Extr. powder	HIP'd powder
20	272	263	285	264
0	274	269	294	279
-30	272	264	287	273
-60	295	302	319	307
-90	327	326	334	315
-110	318	308	336	315
-196	382	392	416	392

Table 5.8 - Variation of hardness with test temperature (Vickers hardness @ 30kg)

	microvoid size @ -50°C	cleavage facet size @ -150°C
Ferrite		
rolled plate	12	32
extruded ingot	14	36
extruded powder	9.2	14
HIP'd powder	9.6	28
TIG weld	8.0	4.2
MMA weld	2.2	4.8
Austenite		
rolled plate	3.2	-
extruded ingot	3.8	-
extruded powder	3.5	-
HIP'd powder	2.5	-
TIG weld	1.9	-
MMA weld	1.7	-

Table 5.9 - Variation of microvoid and cleavage facet sizes (of ferrite phase) between as-received product forms (sizes are mean values in μm)

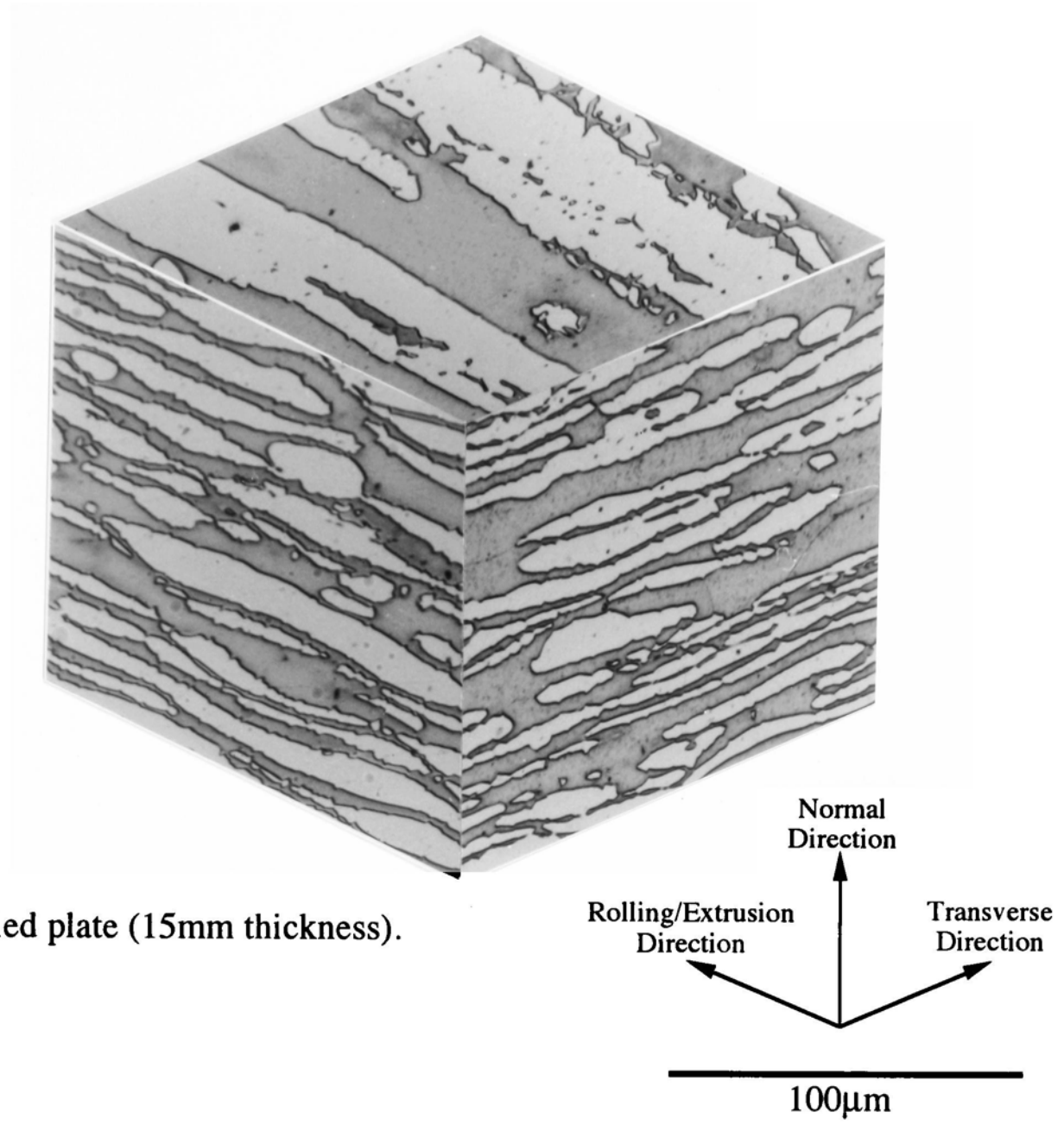

a) Rolled plate (15mm thickness).

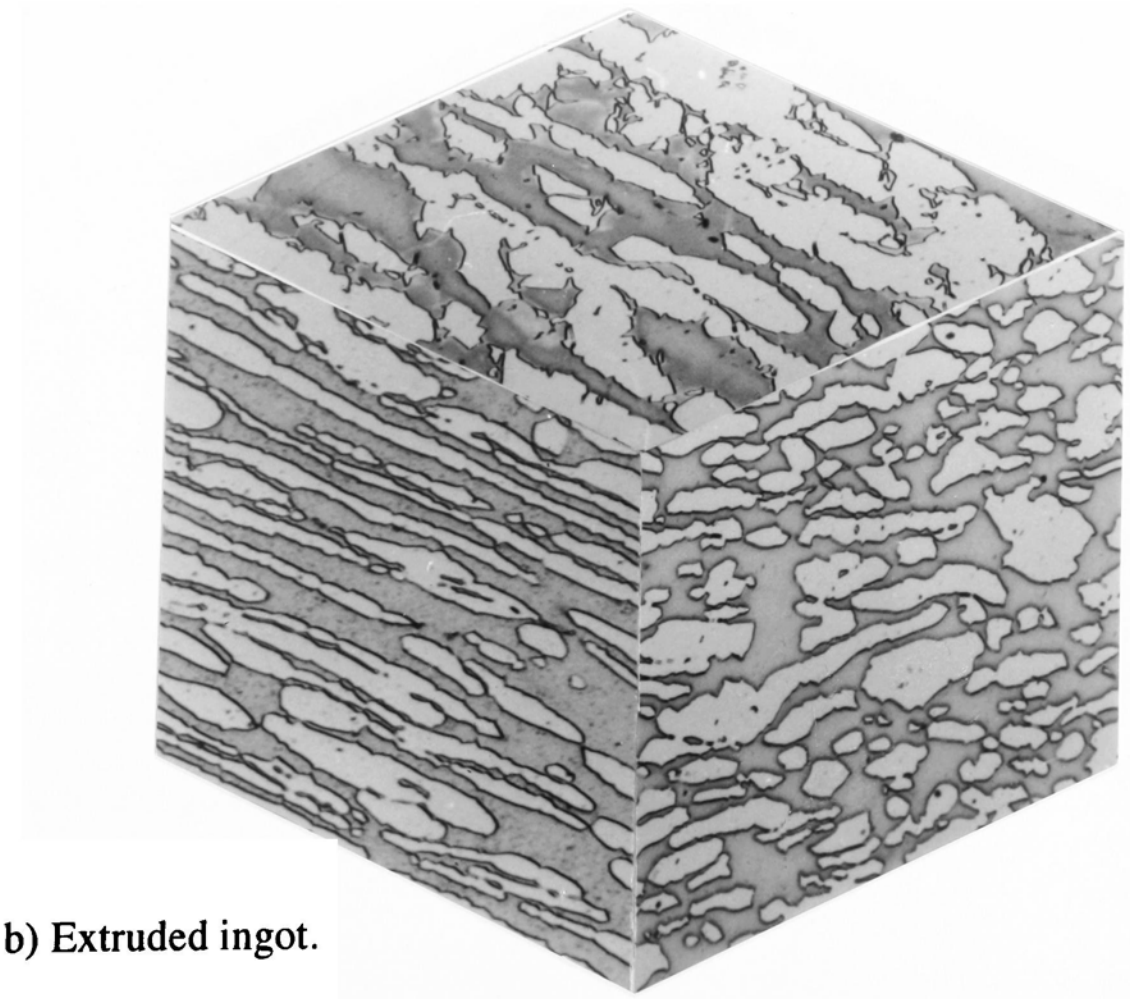

b) Extruded ingot.

Figure 5.1 - Microstructures of the as-received product forms

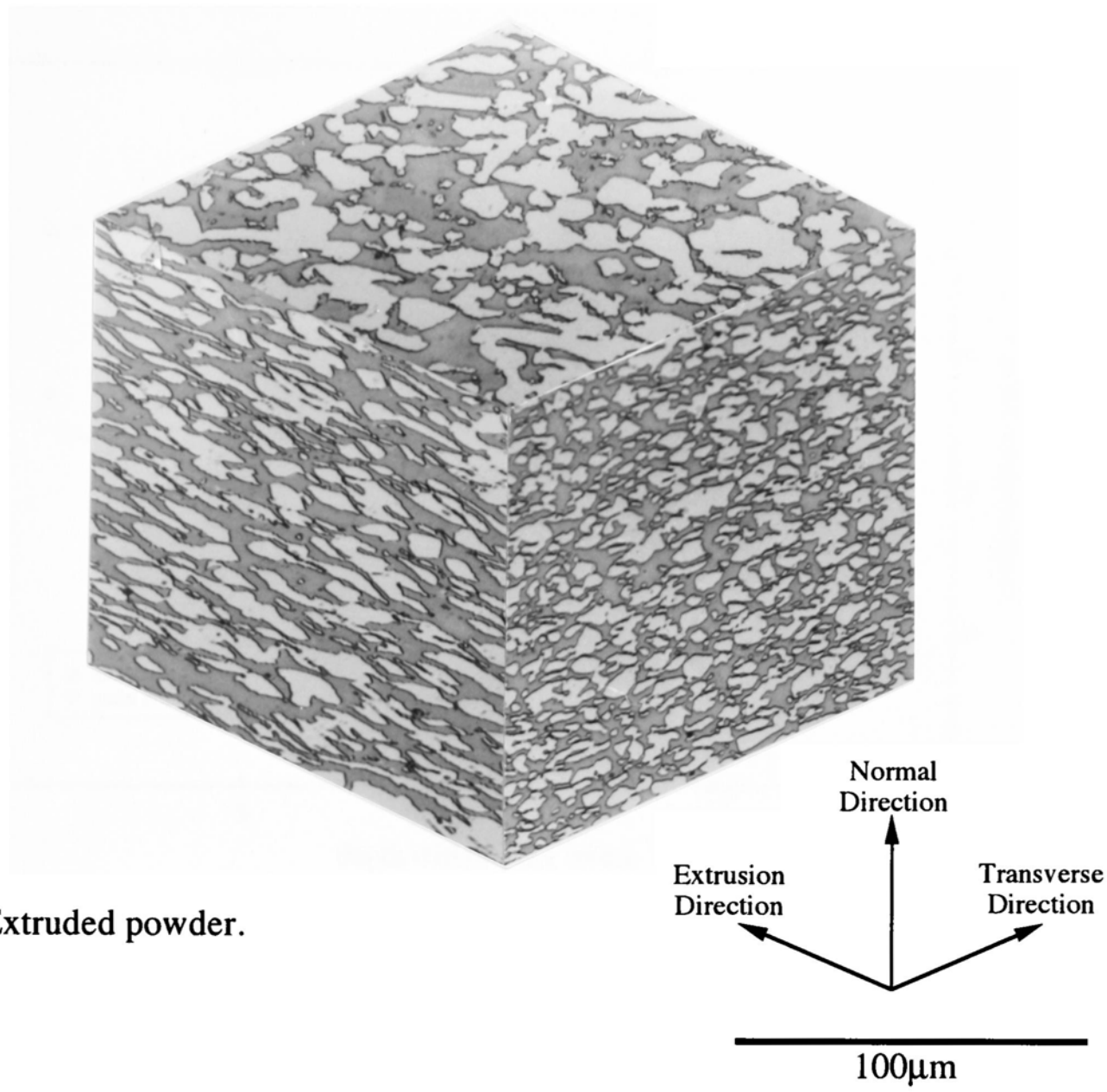

c) Extruded powder.

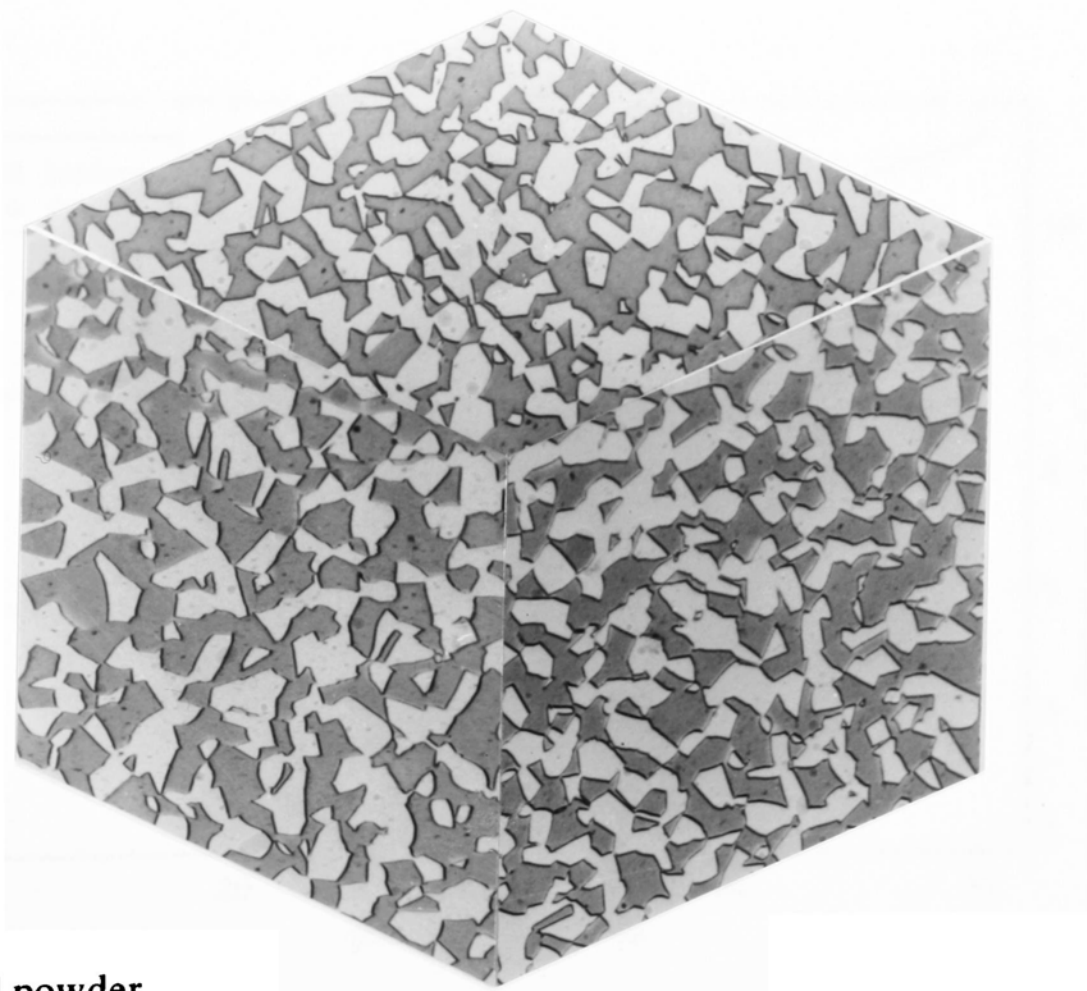

d) HIP'd powder.

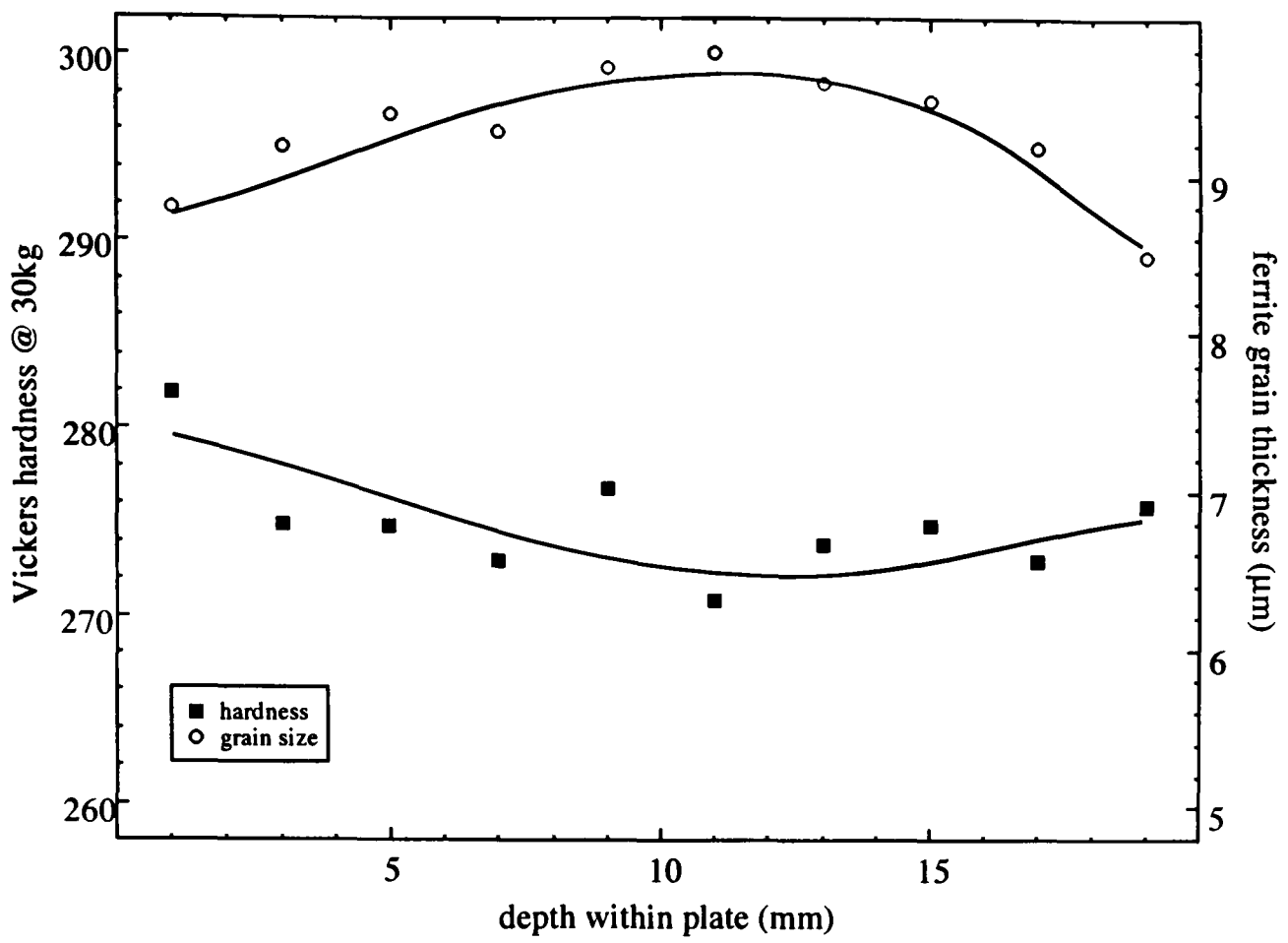

Figure 5.2 - Variation of grain size and hardness through normal thickness of rolled plate

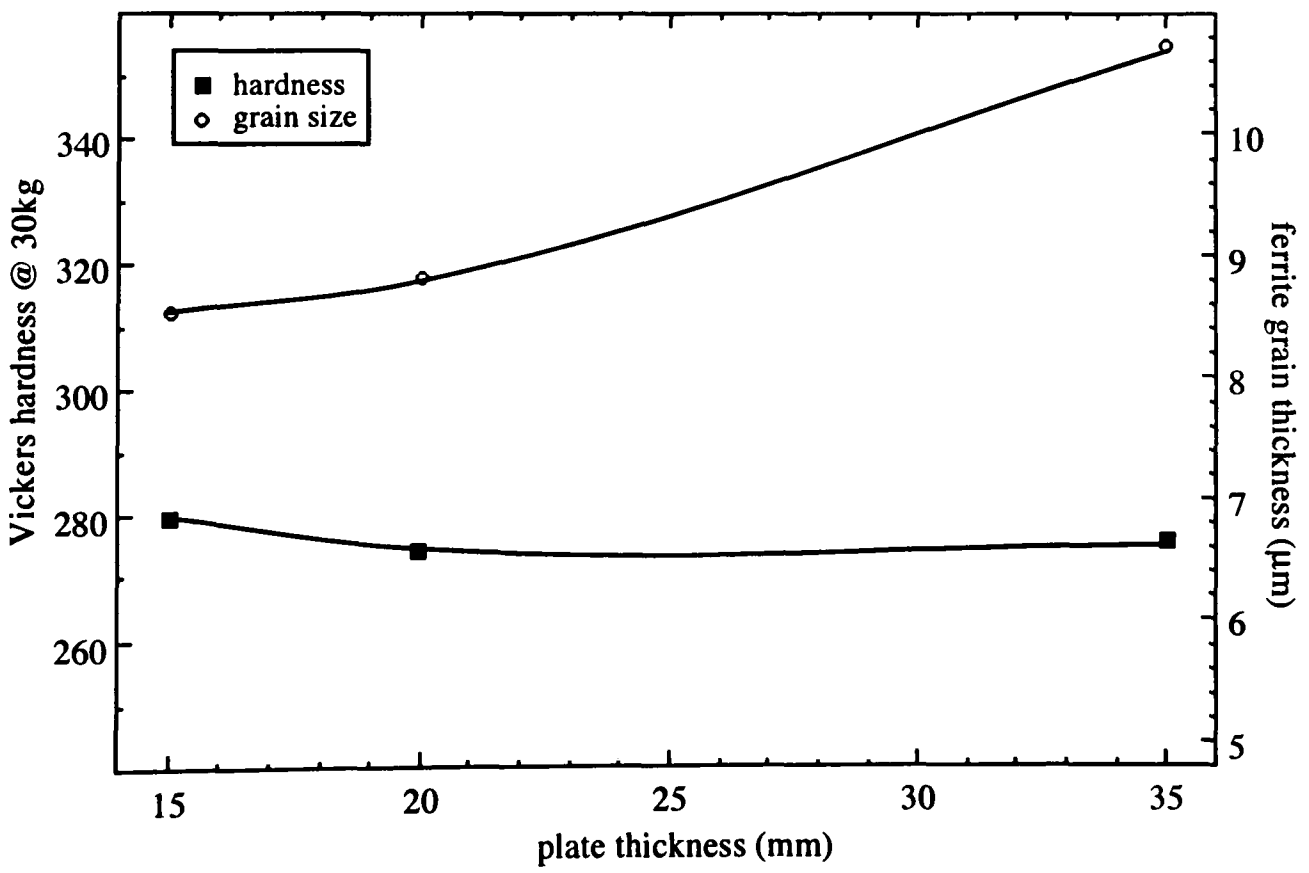

Figure 5.3 - Variation of grain size and hardness with rolled plate size

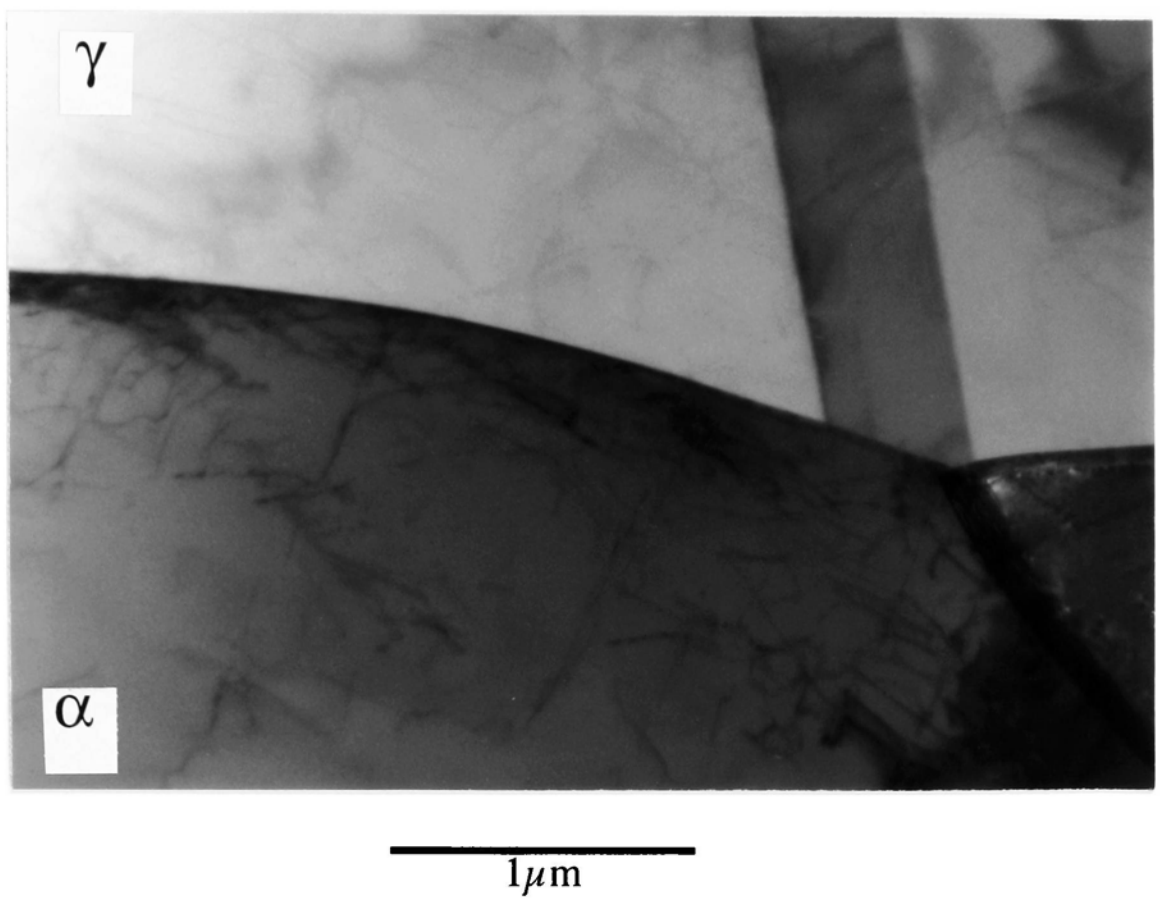

Figure 5.4 - TEM micrograph of interphase boundary in as-received rolled plate material showing precipitate-free surface

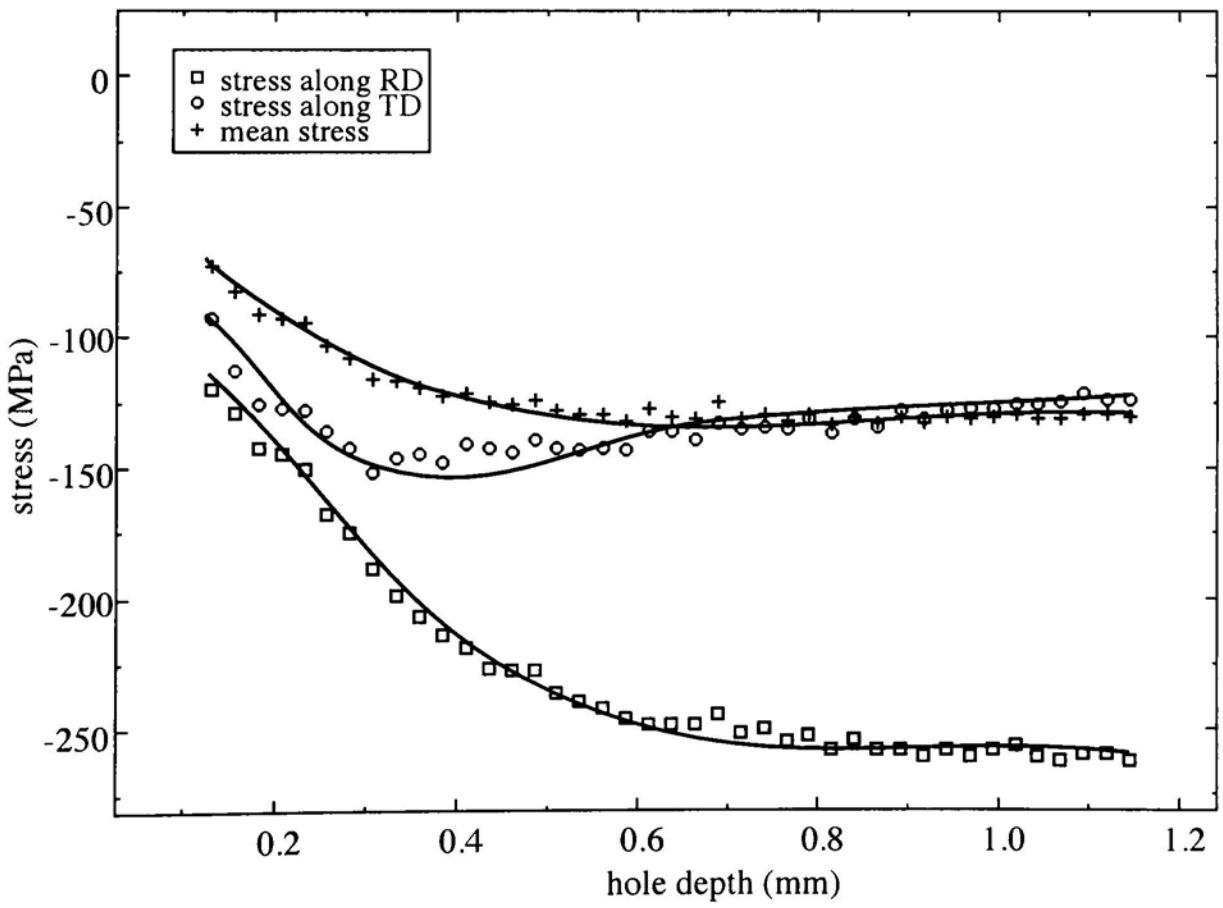

Figure 5.5 - Residual stress analysis of as-received rolled plate material (X-Z orientation)

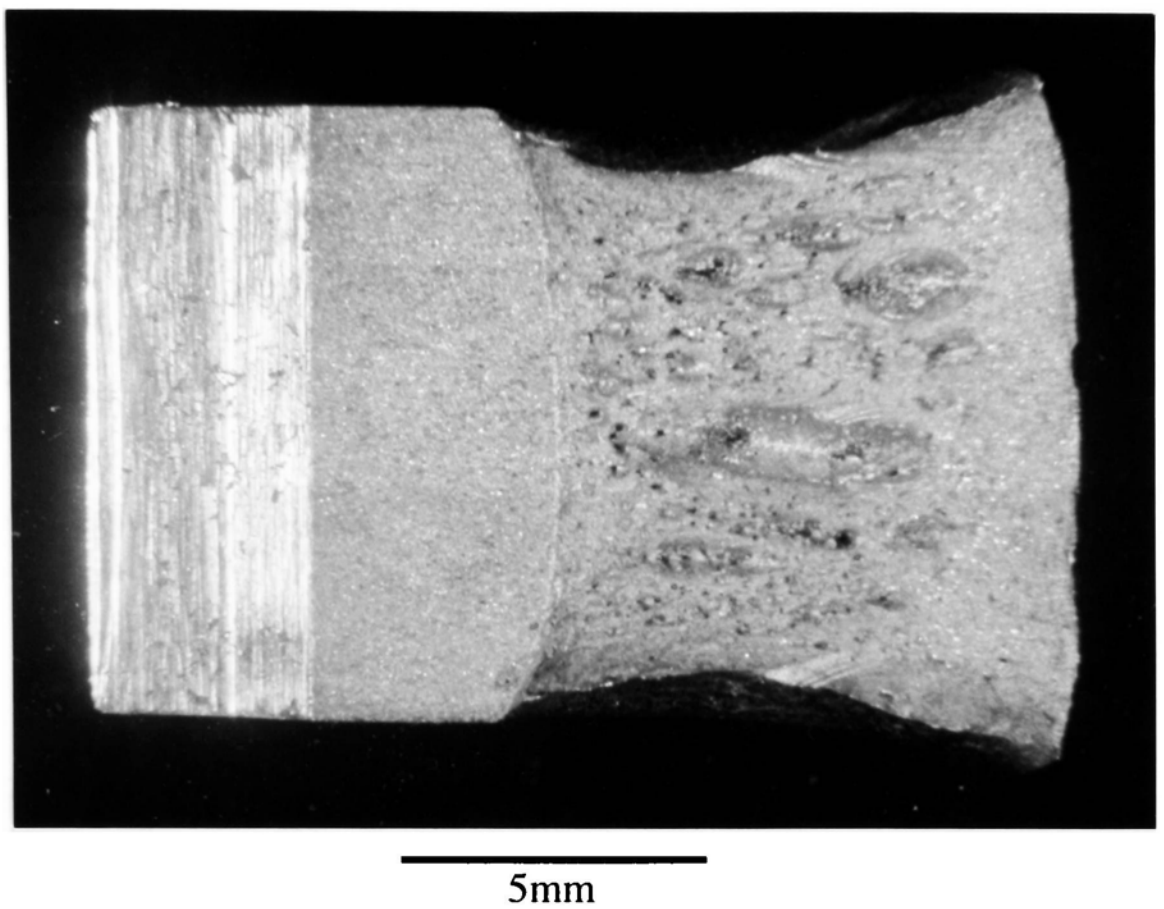

Figure 5.6 - Bowed fatigue precrack front for as-received rolled plate material (fatigued at room temperature)

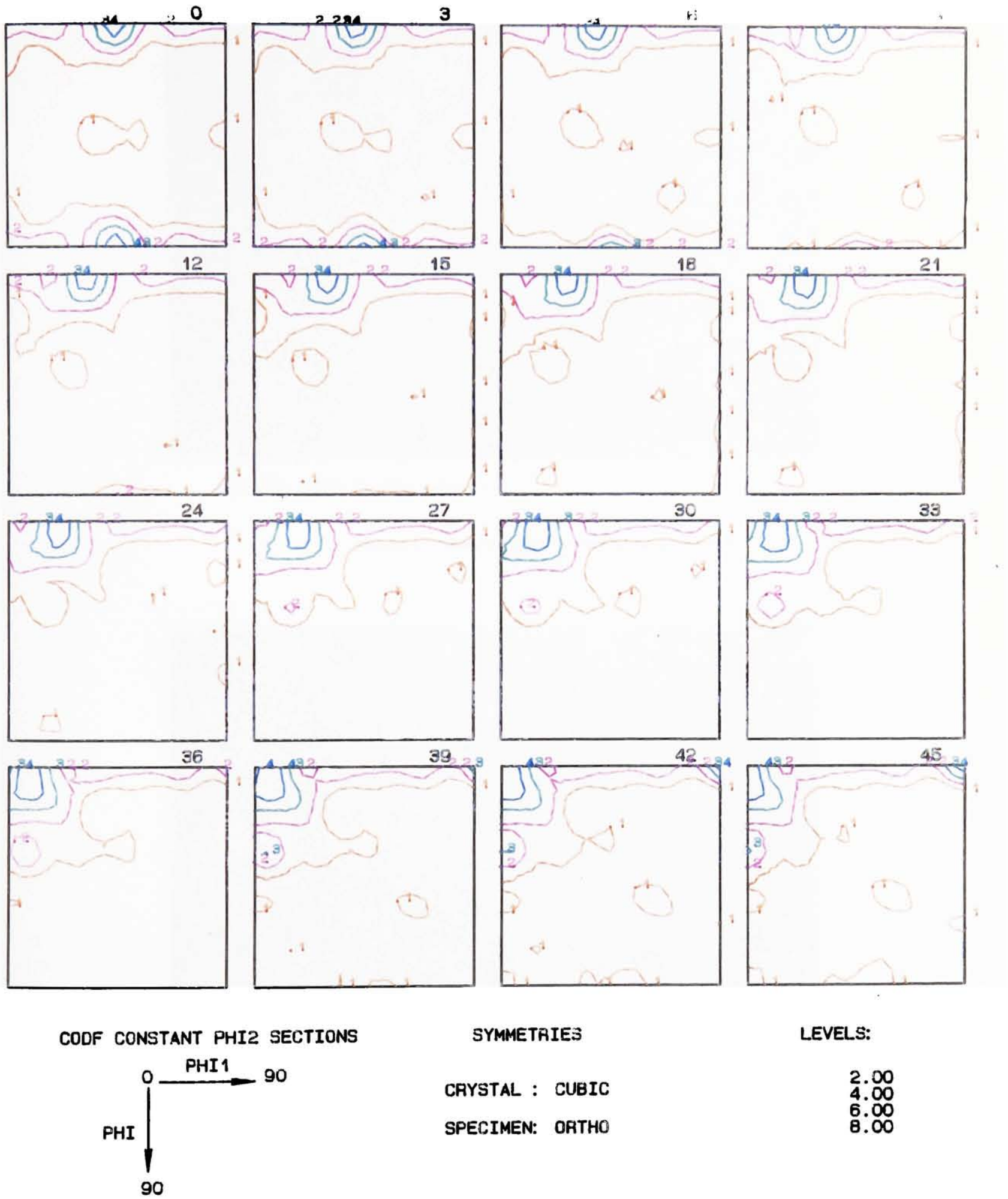

Figure 5.7 - ODF plot for ferrite phase of as-received rolled plate material showing strong {001}<110> bcc rolling texture

a) TIG weld (surface bead)

50μm

b) MMA weld (surface bead)

Figure 5.8 - Weld metal microstructures

c) TIG weld (root bead)

50μm

d) MMA weld (root bead)

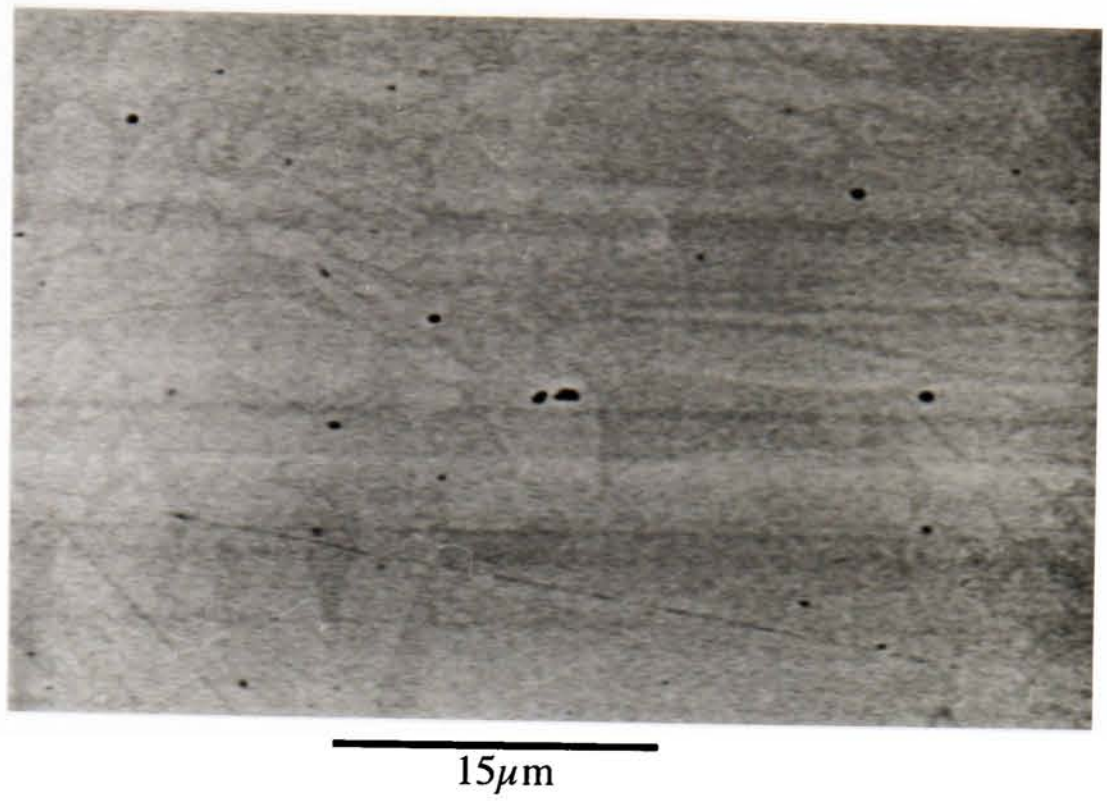

a) TIG weld

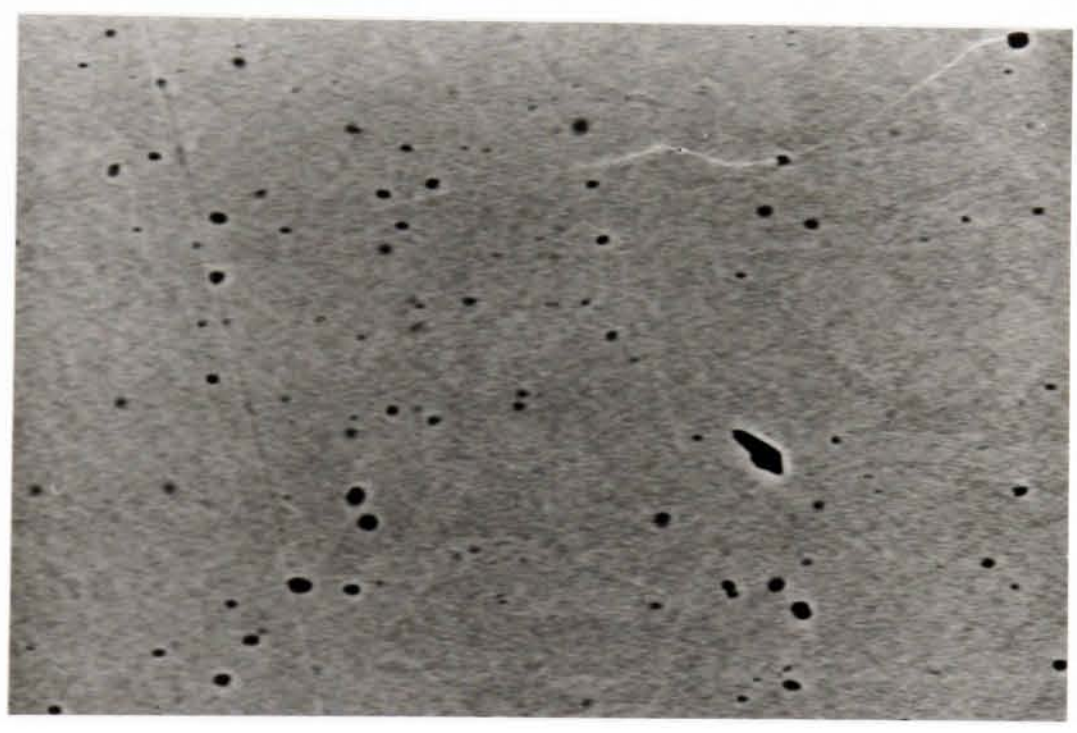

b) MMA weld

Figure 5.9 - Inclusion content of weld metals (SEM backscattered images)

100μm

a) TIG interface

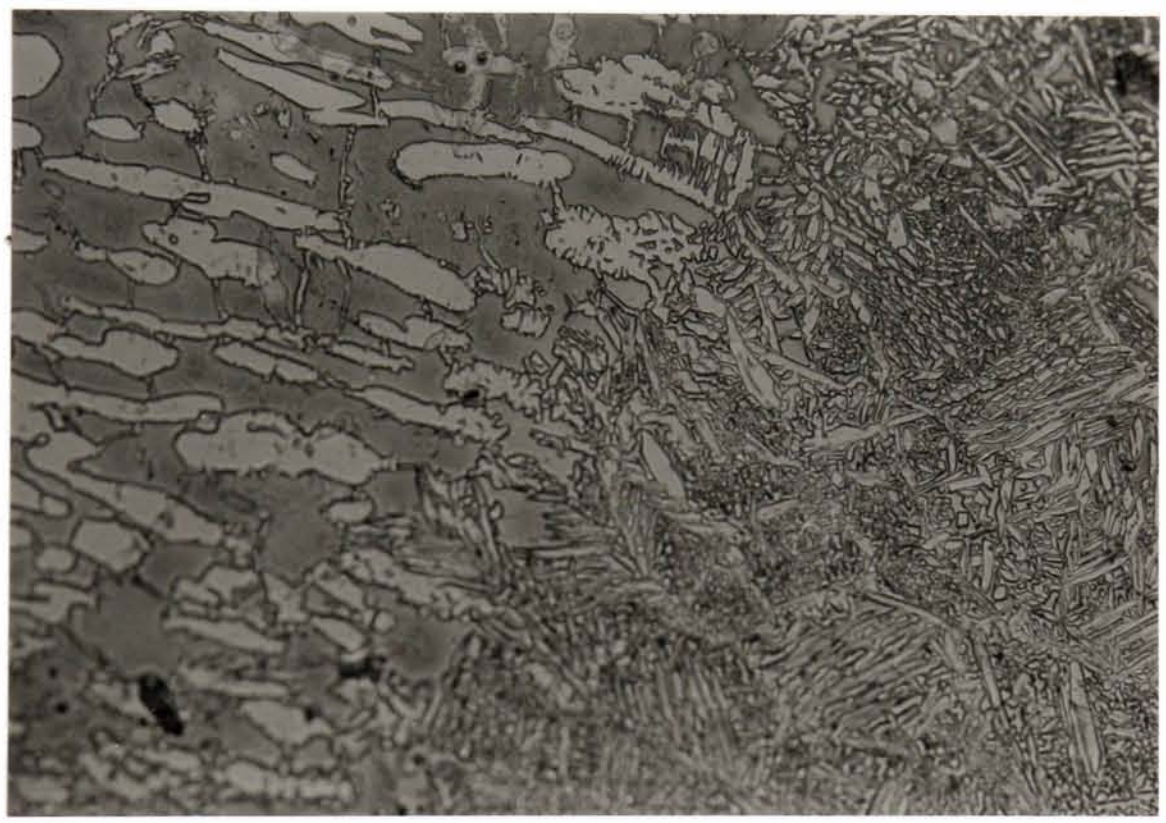

100μm

b) MMA interface

Figure 5.10 - Heat affected zones of weld metals (parent plate on left)

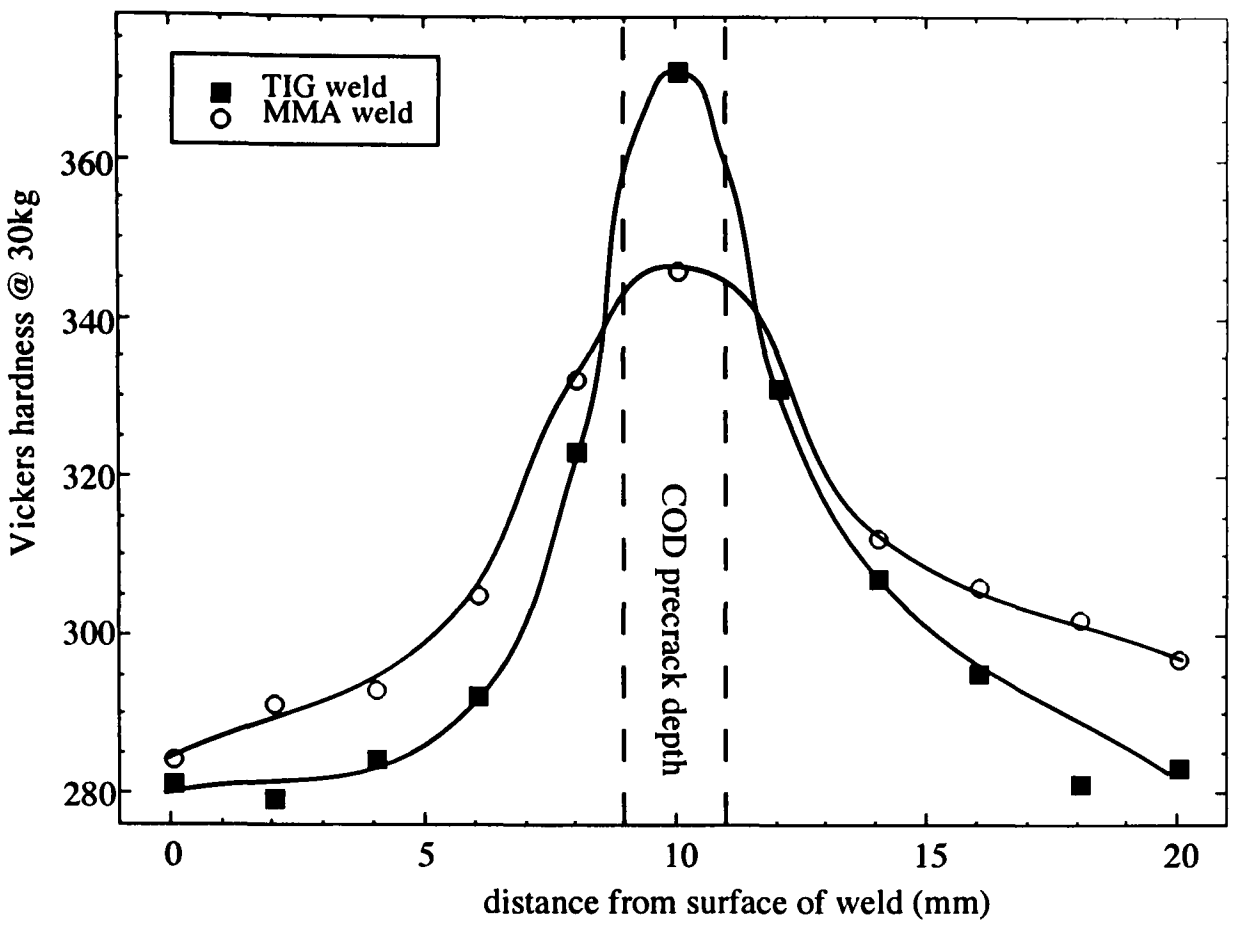

Figure 5.11 - Vickers hardness profile through weld depth

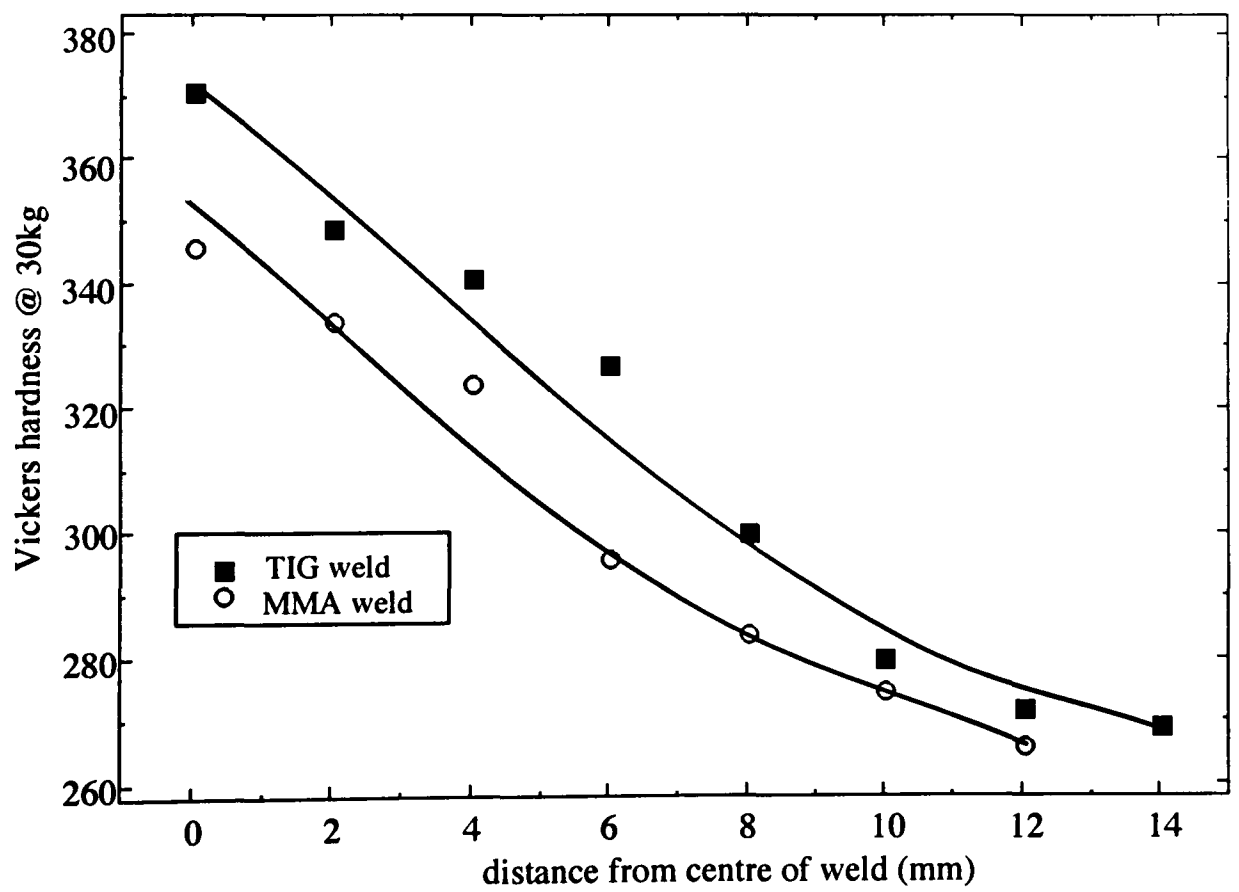

Figure 5.12 - Vickers hardness profile across heat-affected zone

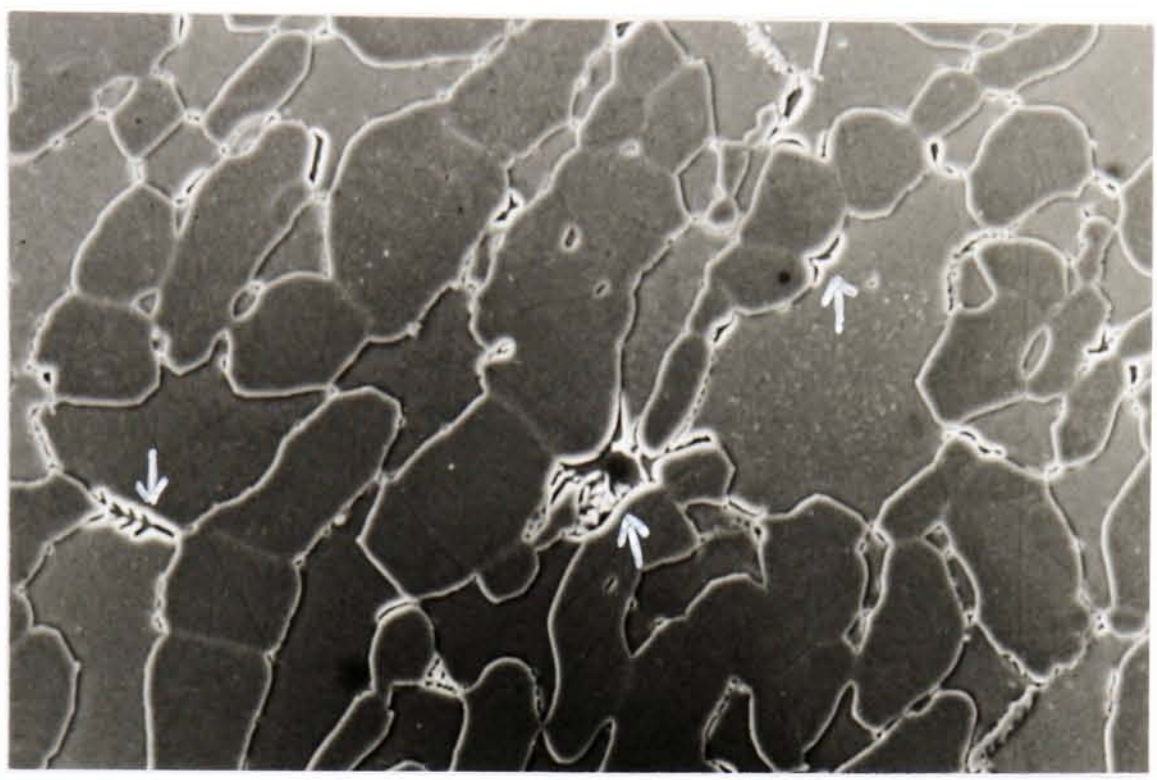

Figure 5.13 - Phase precipitation (arrowed) after 5 minutes annealing at a temperature of 850°C within rolled plate material

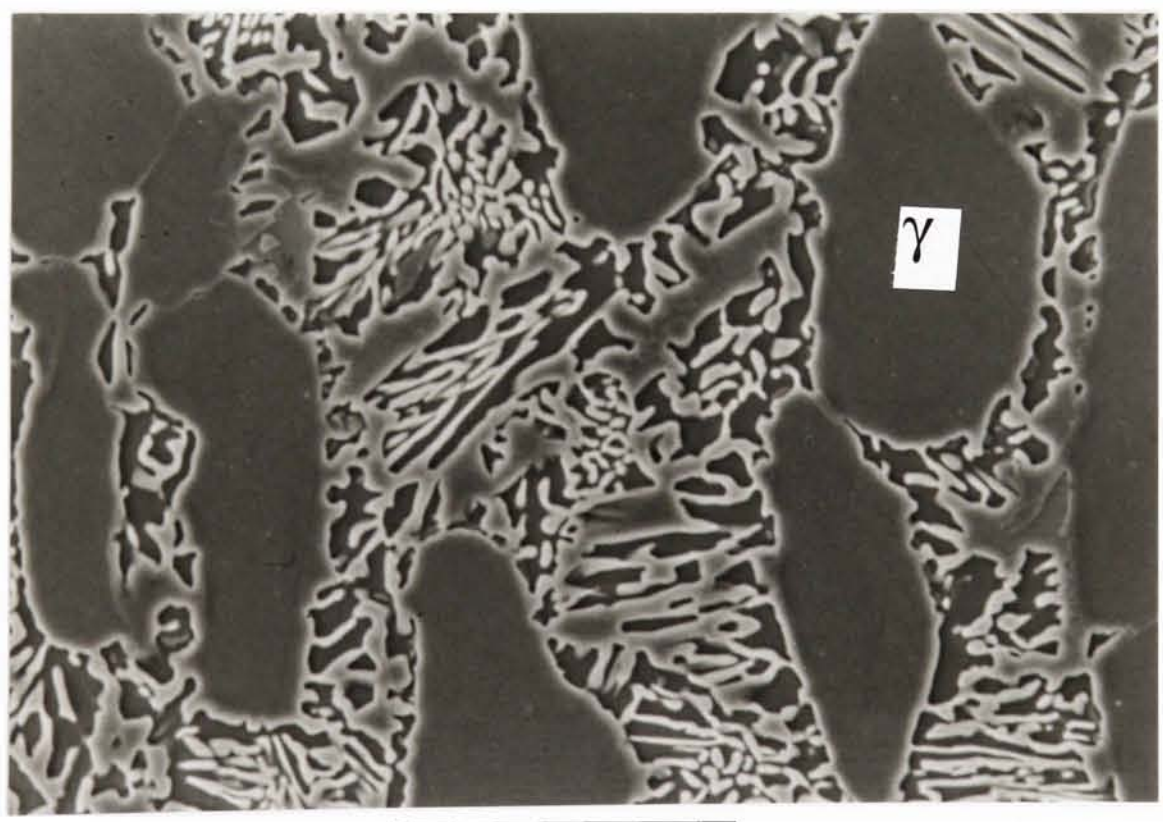

Figure 5.14 - Lamella structure from eutectoidal decomposition of ferrite after annealing for 45 minutes at a temperature of 850°C

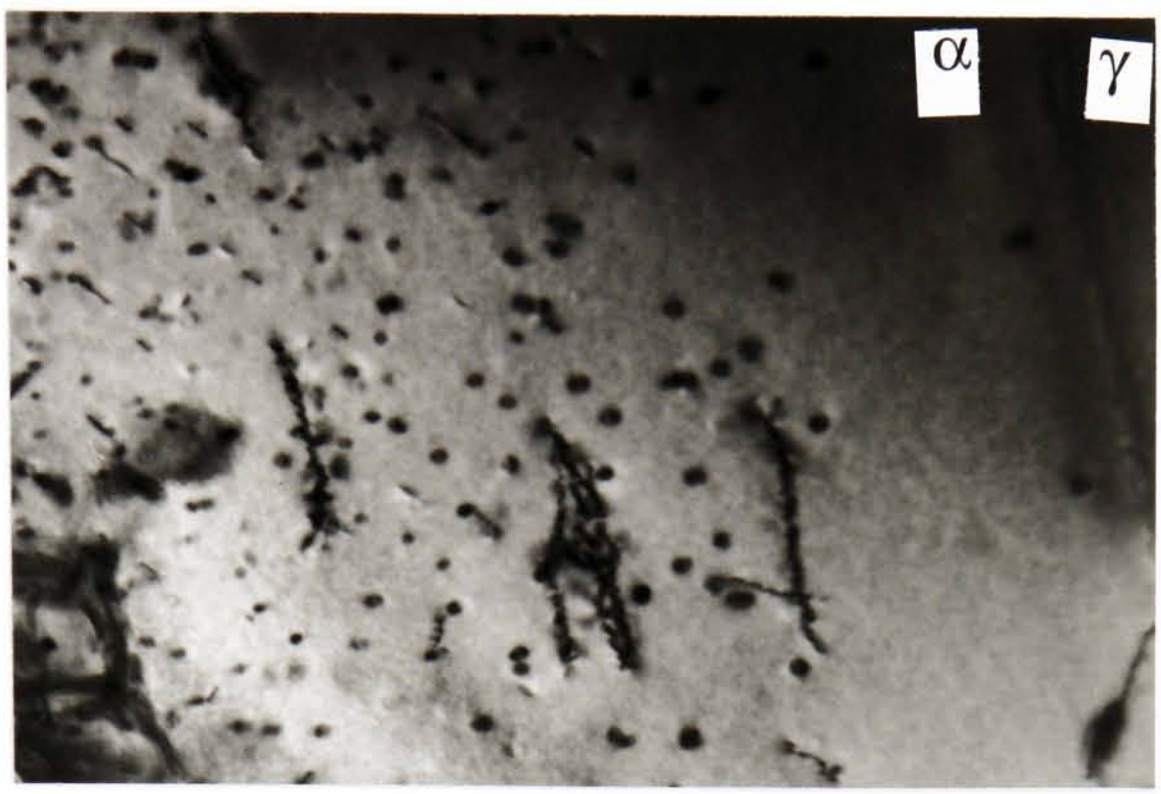

Figure 5.15 - TEM micrograph of near-interfacial region of rolled plate aged at a temperature of 550°C for 5 hours

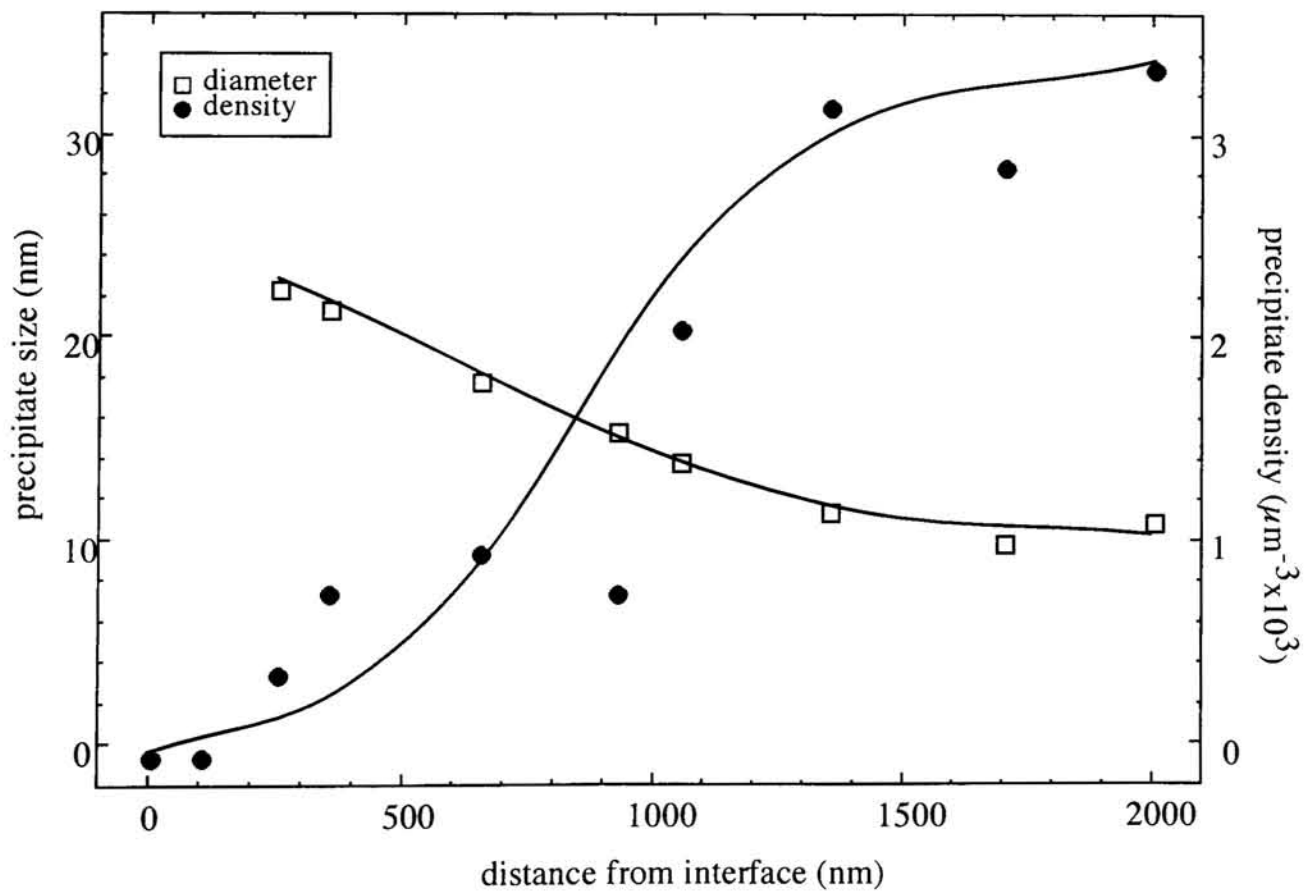

Figure 5.16 - Variation of precipitate size and density with distance from interface (rolled plate annealed at a temperature of 550°C for 5 hours)

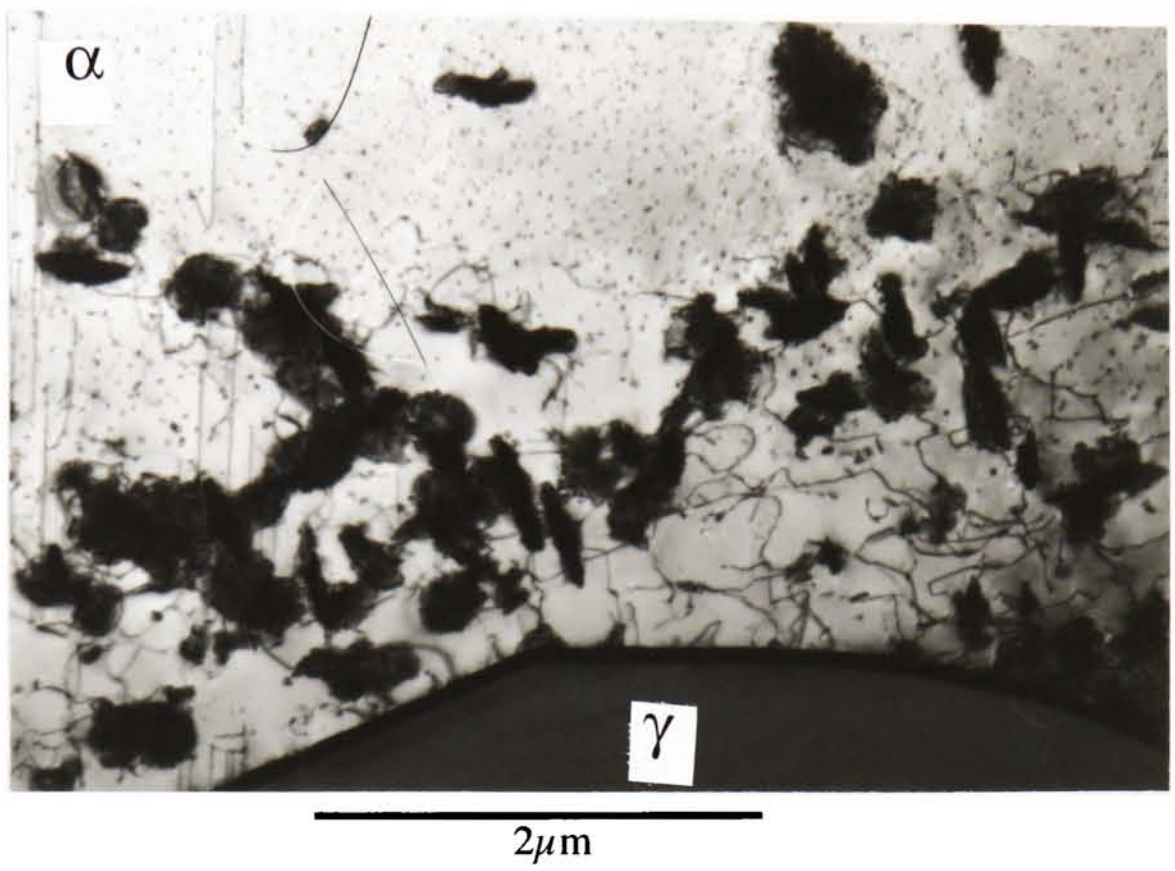

Figure 5.17 - Band of R-phase precipitates close to interphase boundary (rolled plate annealed at a temperature of 550°C for 20 hours) (Picture courtesy of X.Li[1])

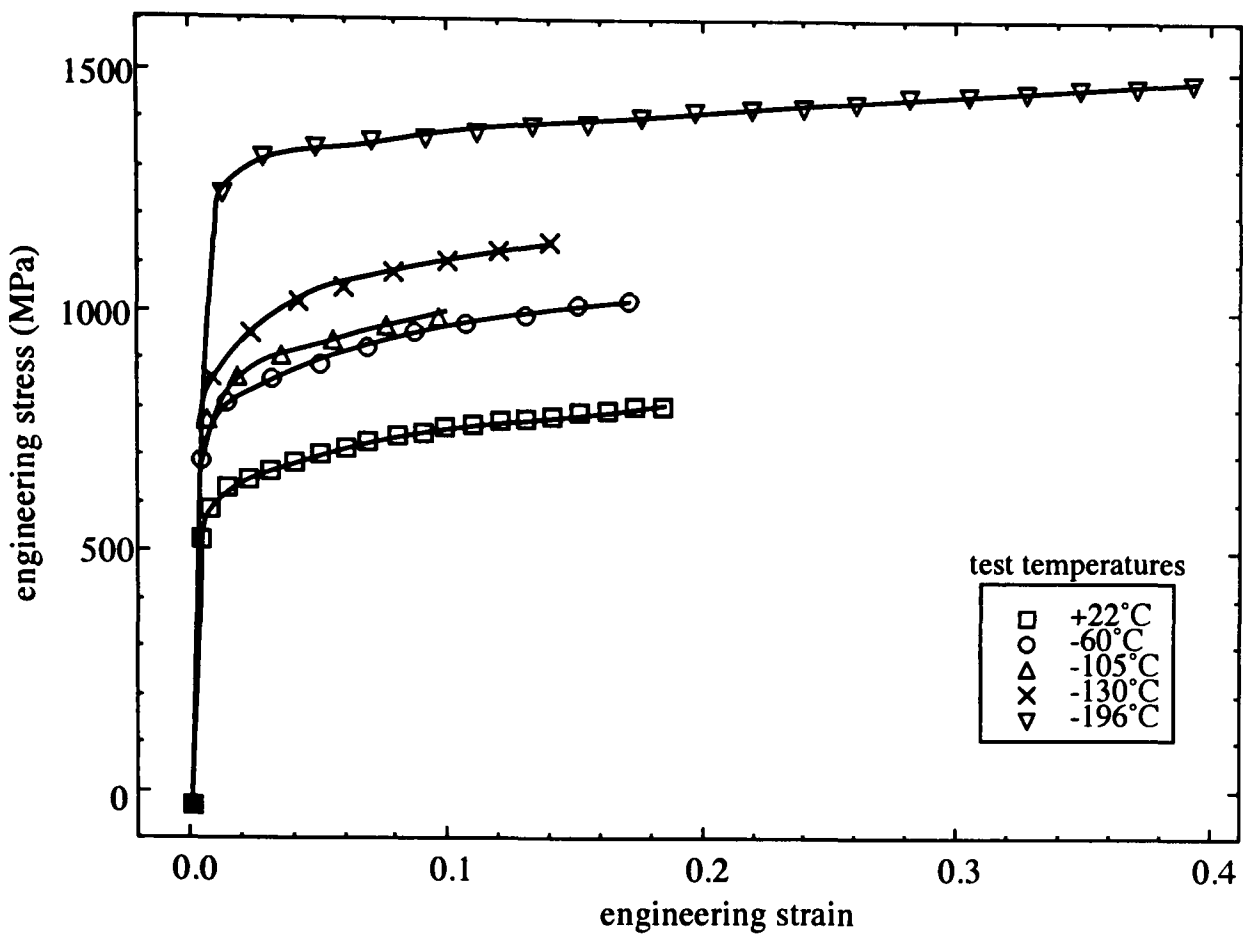

Figure 5.18 - Stress-strain curves for as-received rolled plate material

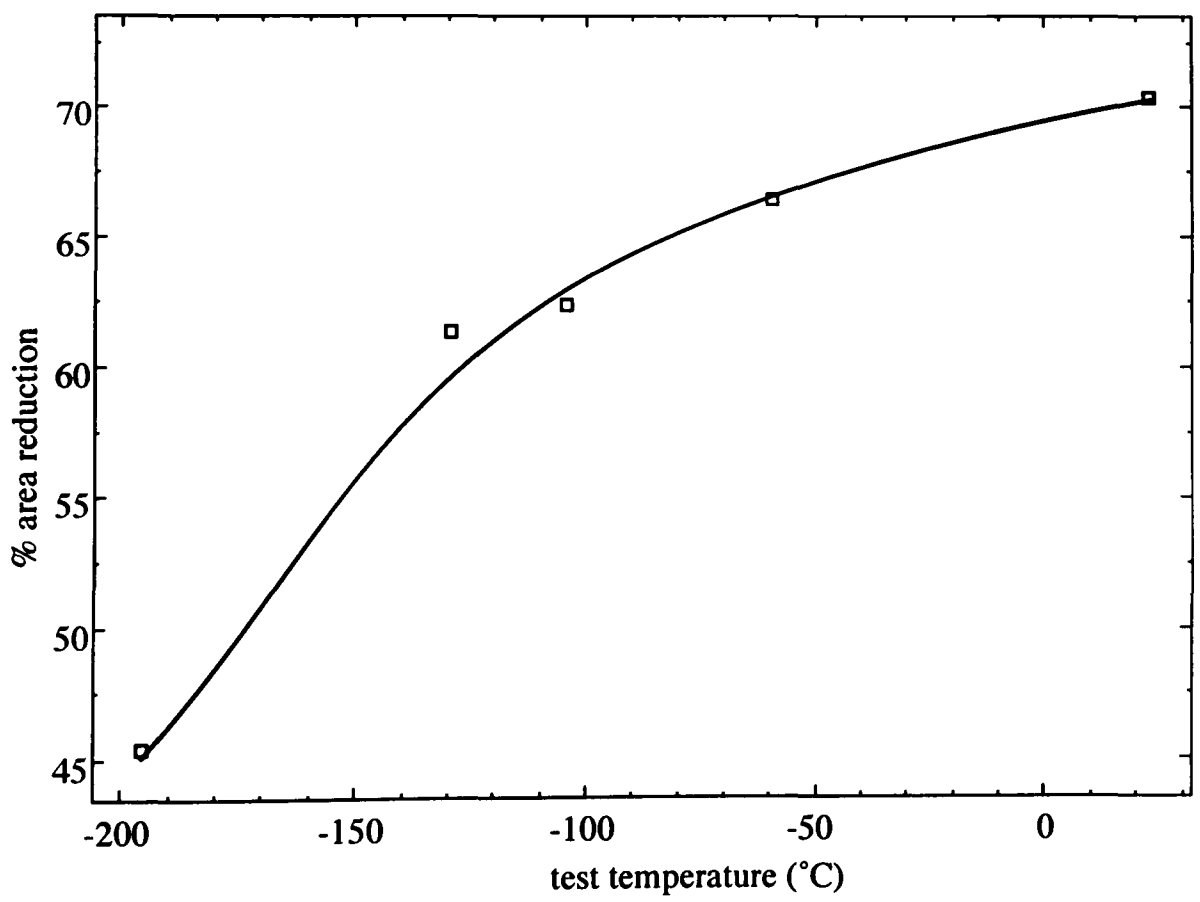

Figure 5.19 - Variation of gauge area reduction with test temperature (as-received rolled plate)

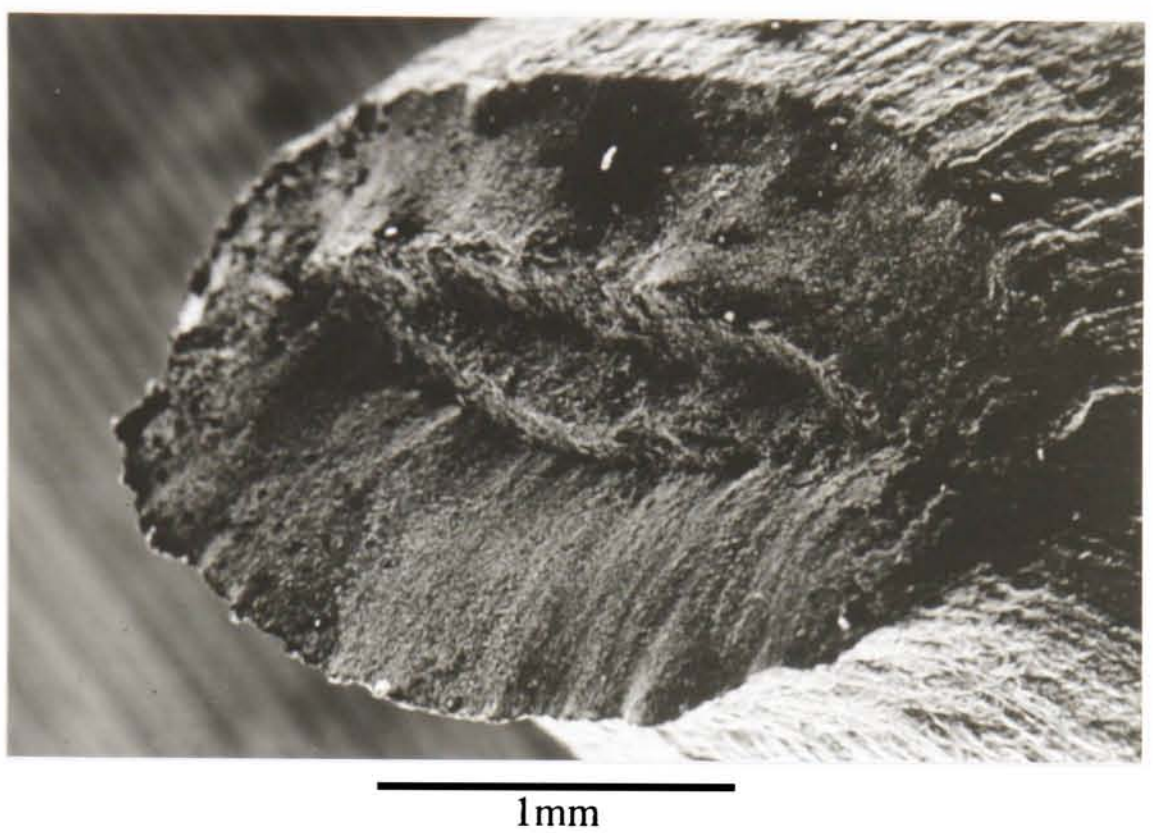

Figure 5.20 - SEM micrograph of tensile fracture surface, showing inhomogeneous deformation (as-received rolled plate tested at room temperature)

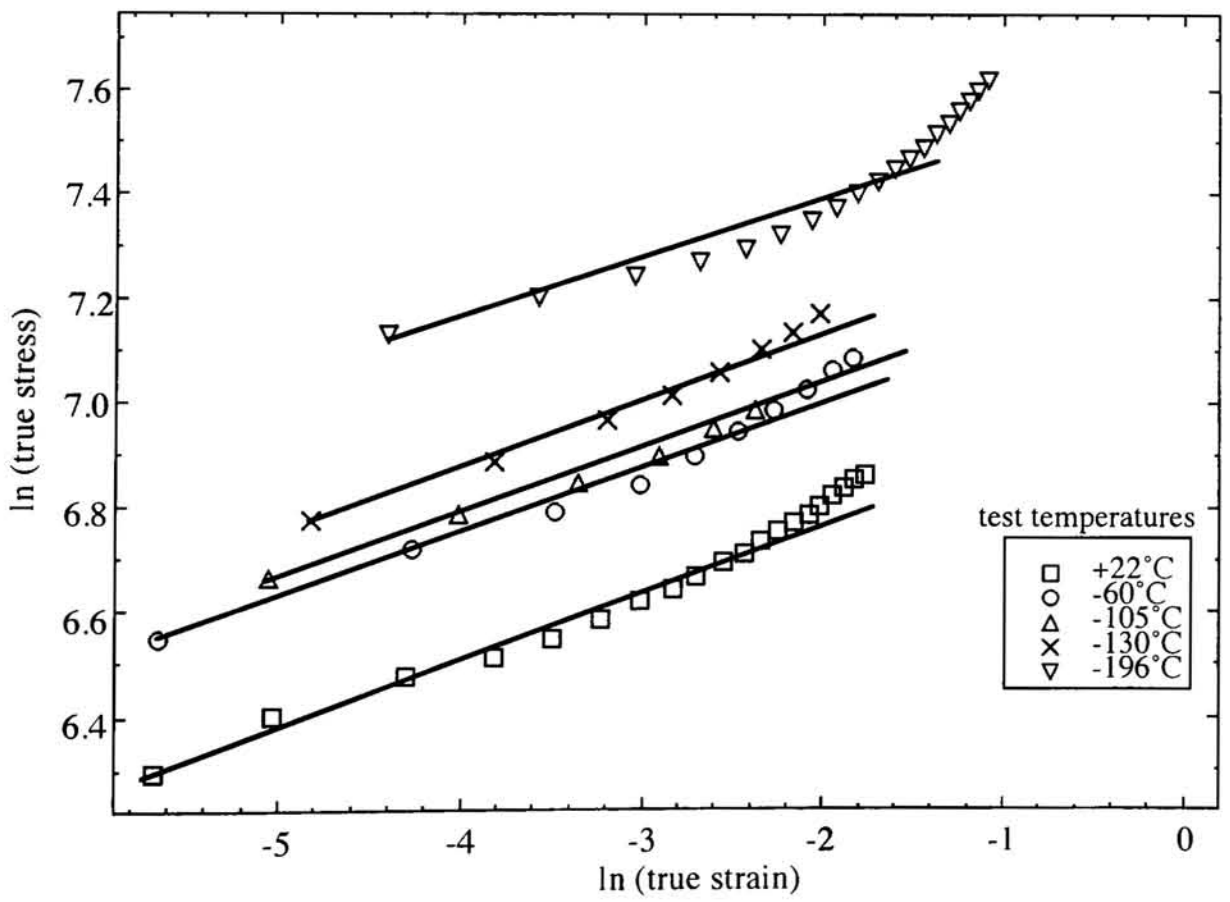

Figure 5.21 - Plot of ln.true stress vs. ln.true strain for as-received rolled plate material

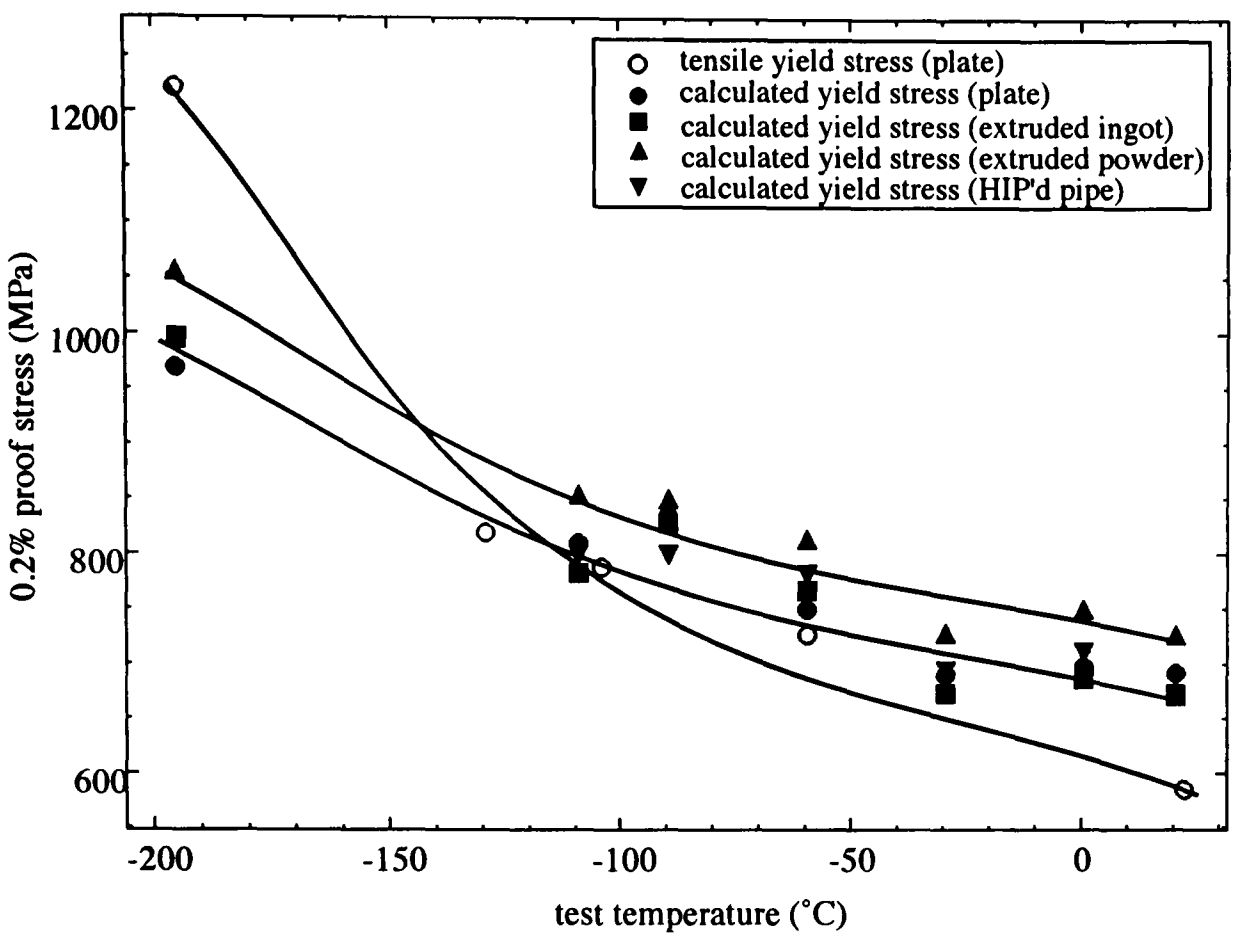

Figure 5.22 - Comparison of experimental (tensile test) and calculated yield stress data for as-received materials

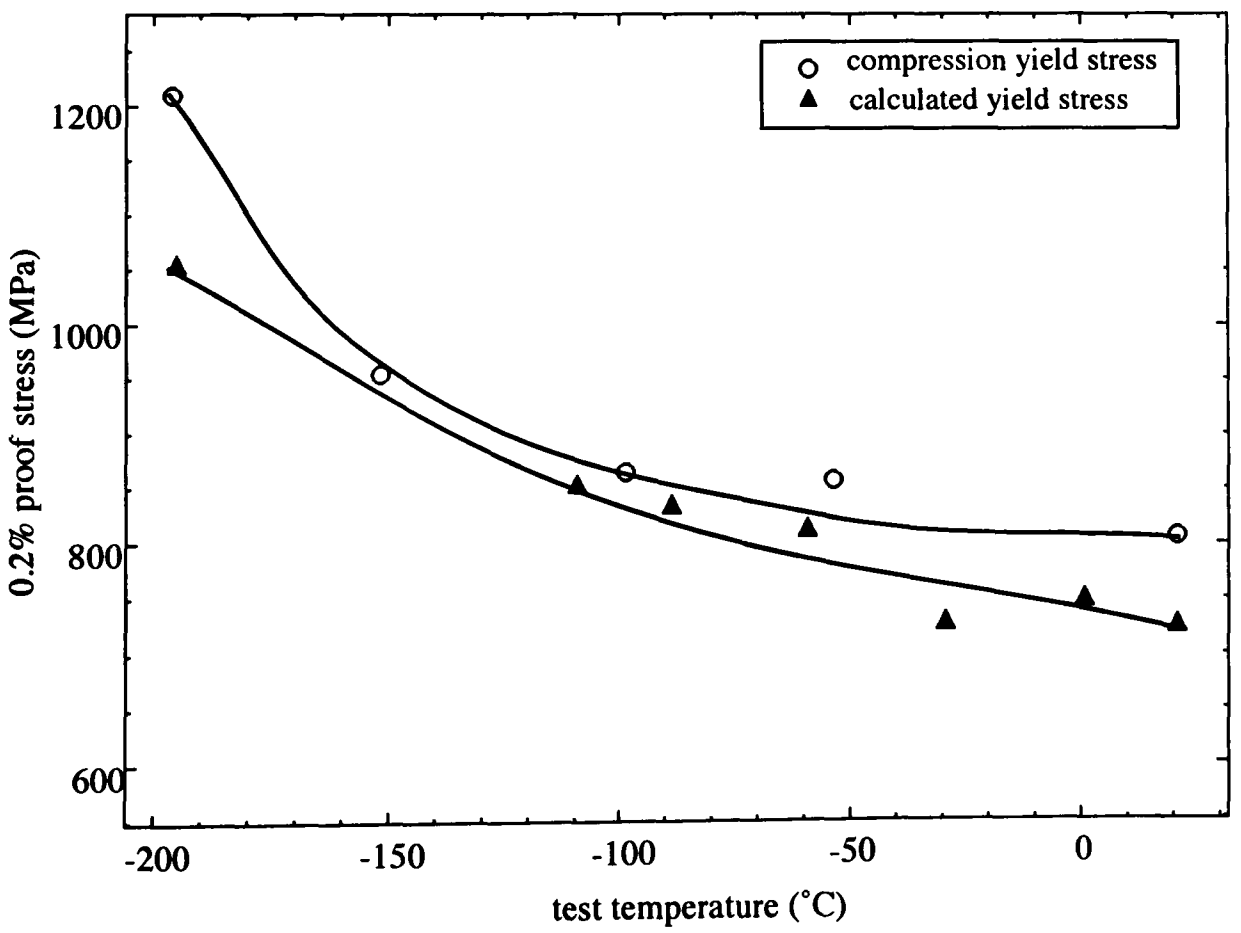

Figure 5.23 - Comparison of experimental (compression test) and calculated yield stress data for as-received extruded powder material

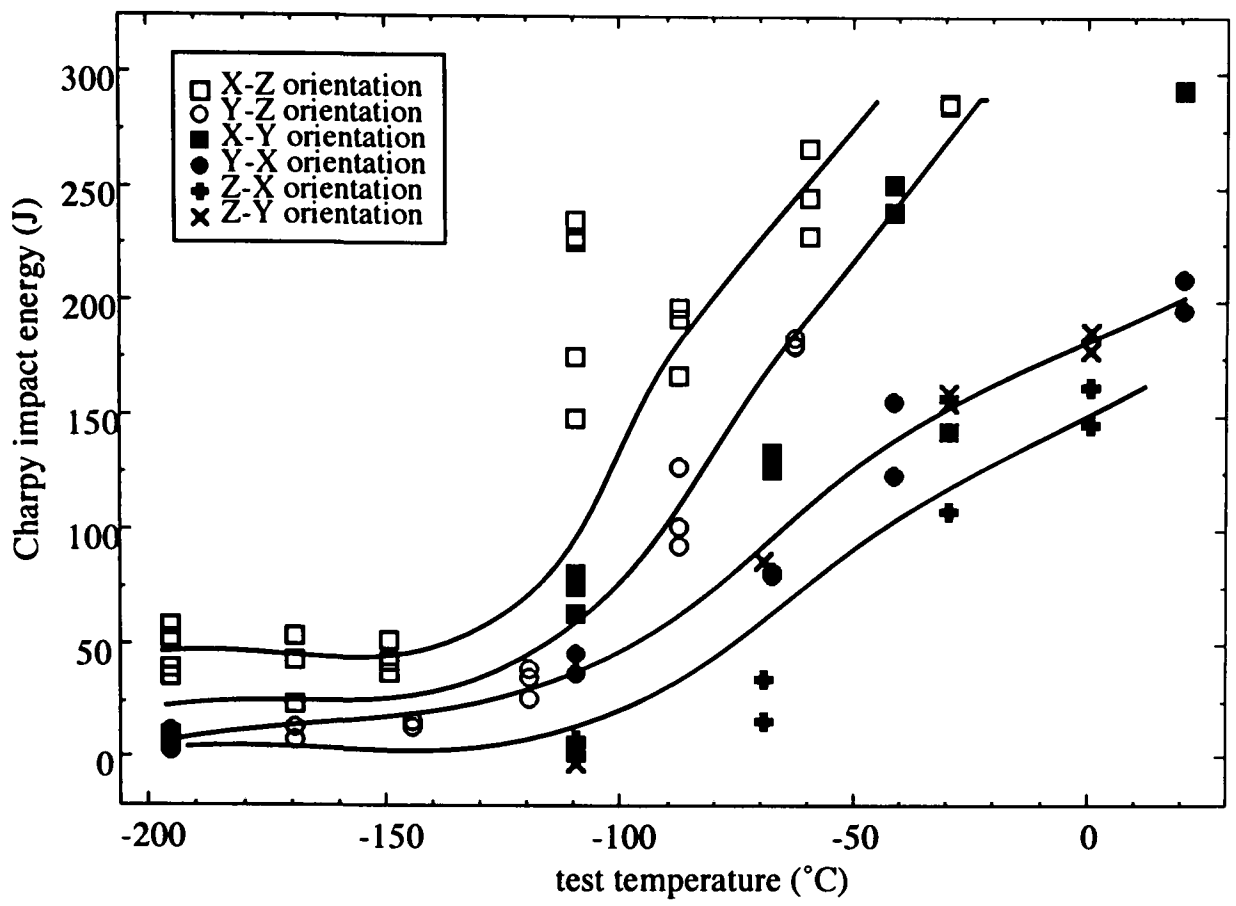

Figure 5.24 - Impact toughness transition curves for all six possible notch orientations of the as-received rolled plate material

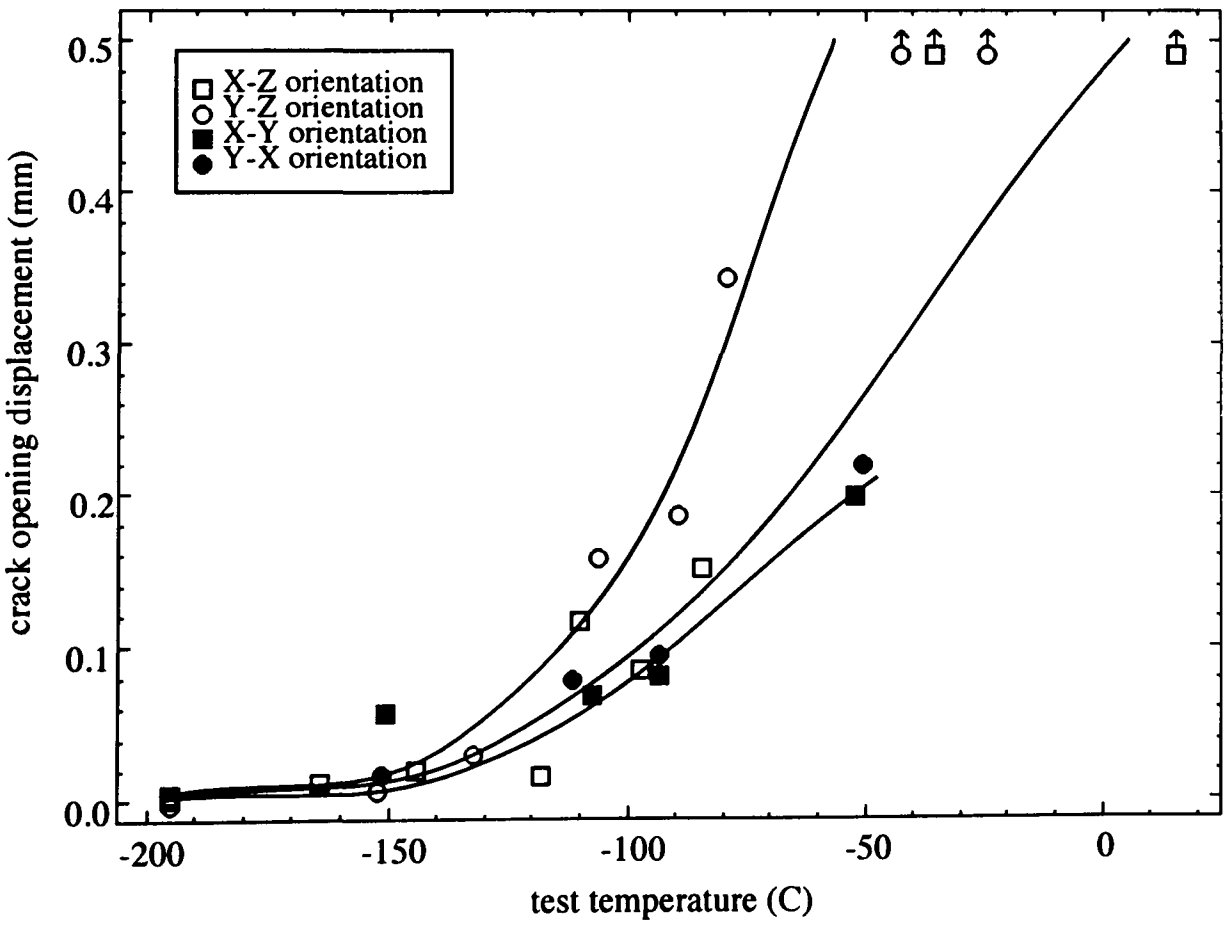

Figure 5.25 - Fracture toughness transition curves for as-received rolled plate material

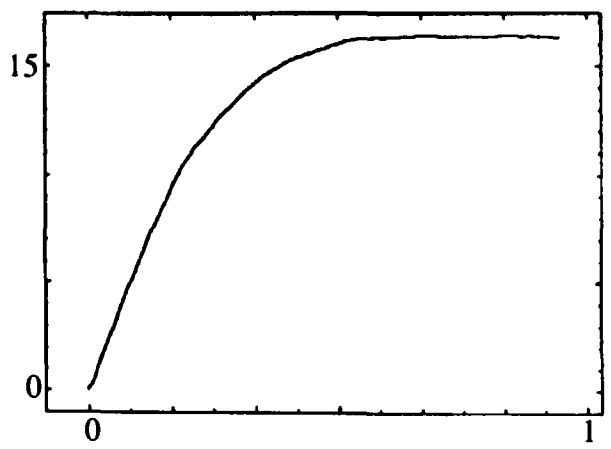

a) Maximum load attainment (X-Z, -40°C)

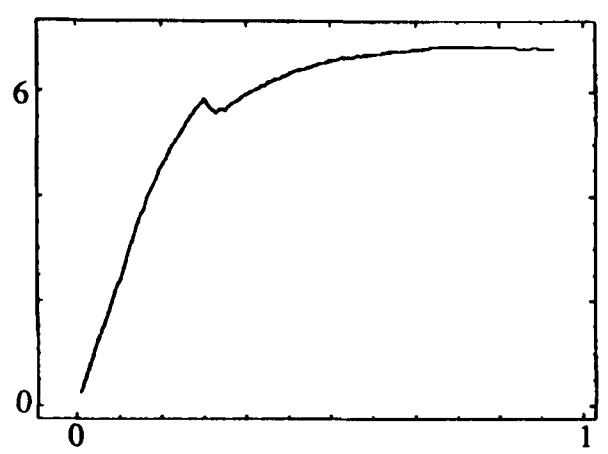

b) Pop-in failure (X-Z, -110°C)

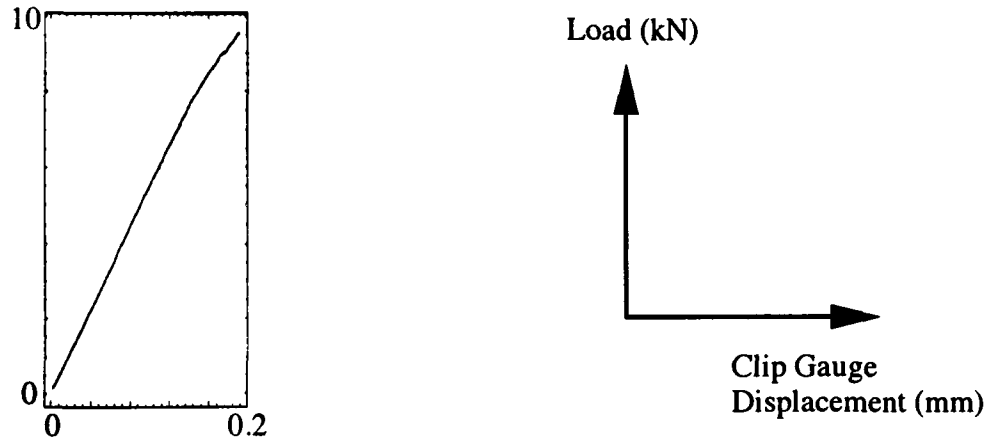

c) Critical failure (X-Z, -150°C)

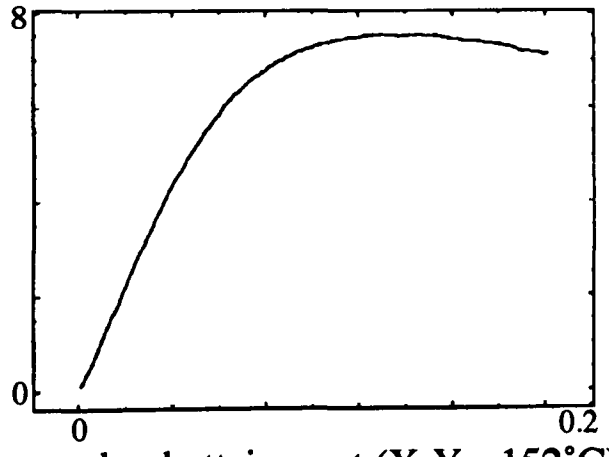

d) Maximum load attainment (X-Y, -152°C)

Figure 5.26 - Load-displacement curves for as-received rolled plate material

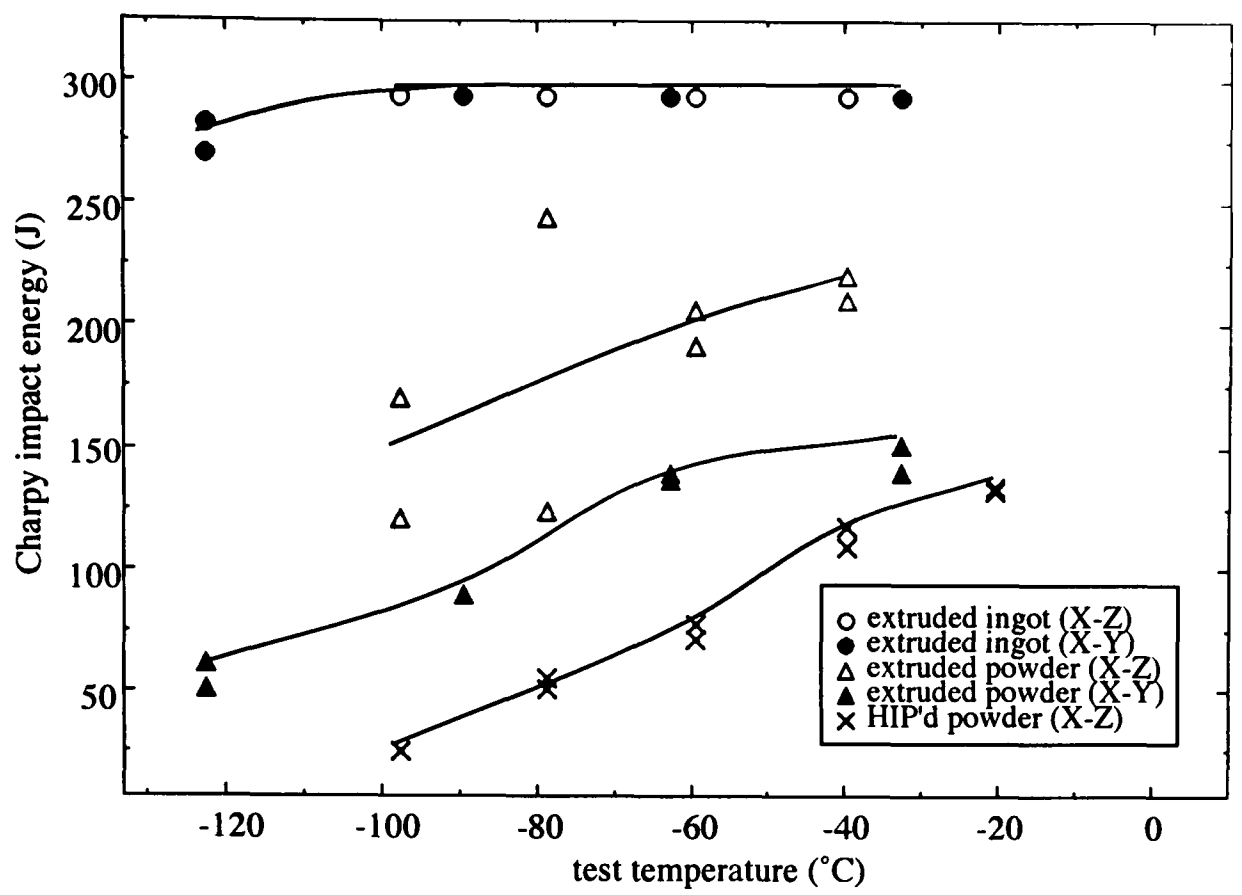

Figure 5.27 - Impact toughness transition curves for as-received pipe product forms

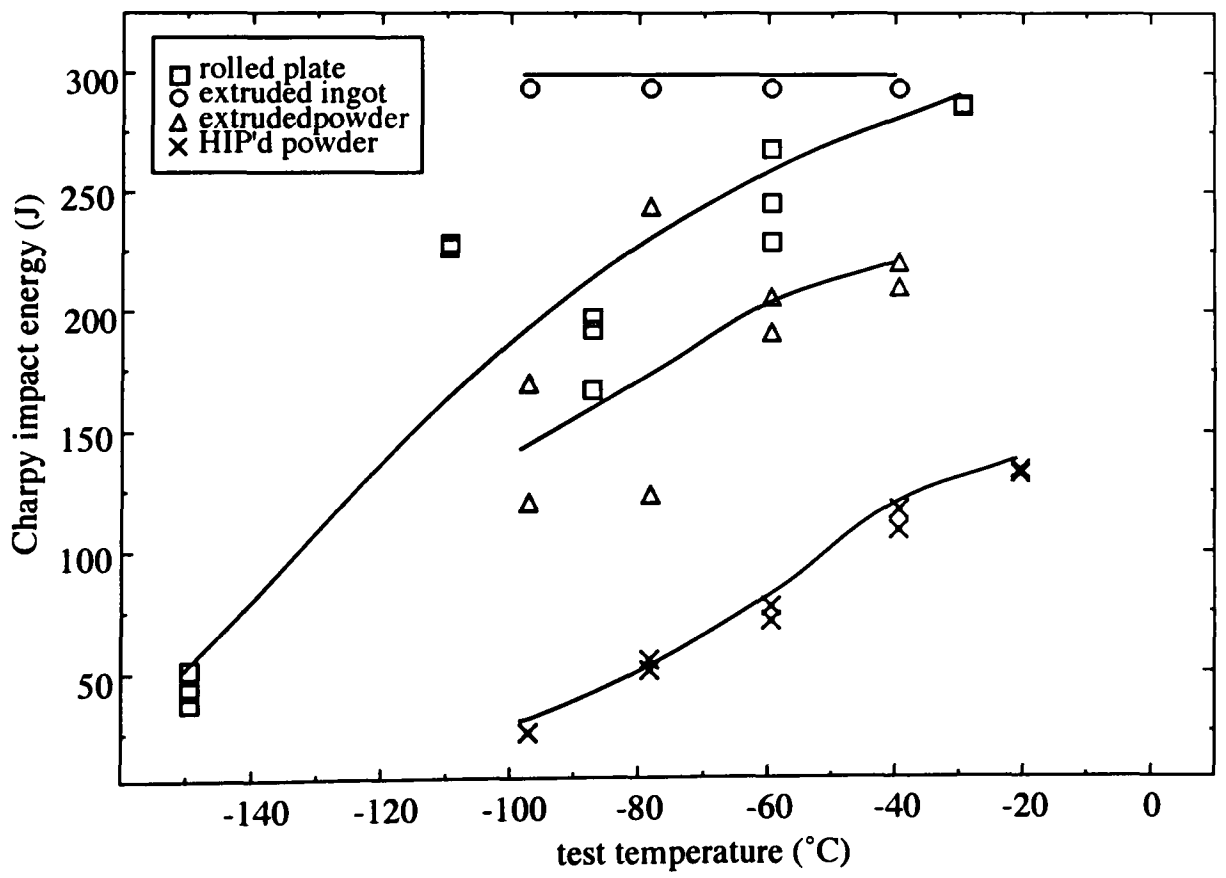

Figure 5.28 - Impact toughness transition curves for X-Z orientated as-received product forms

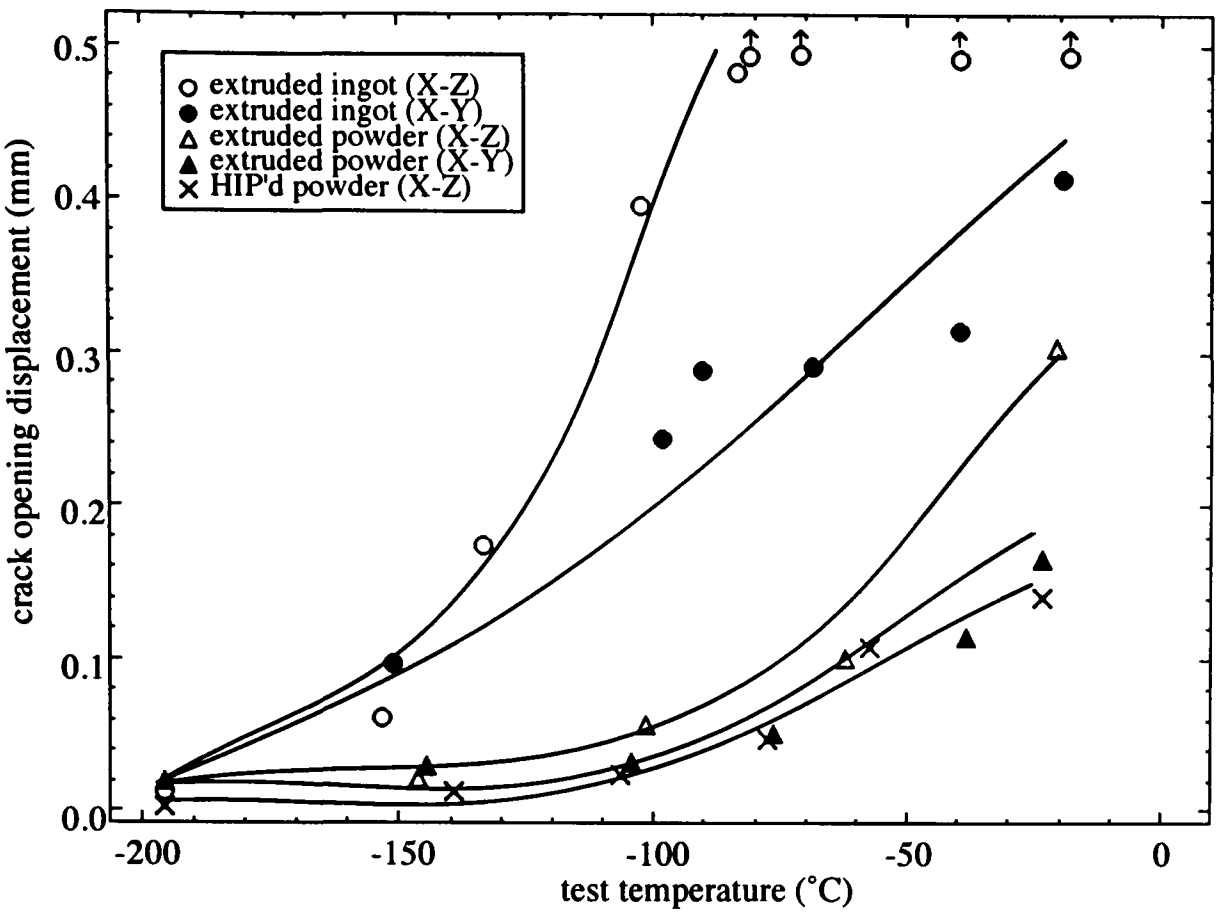

Figure 5.29 - Fracture toughness transition curves for as-received pipe product forms

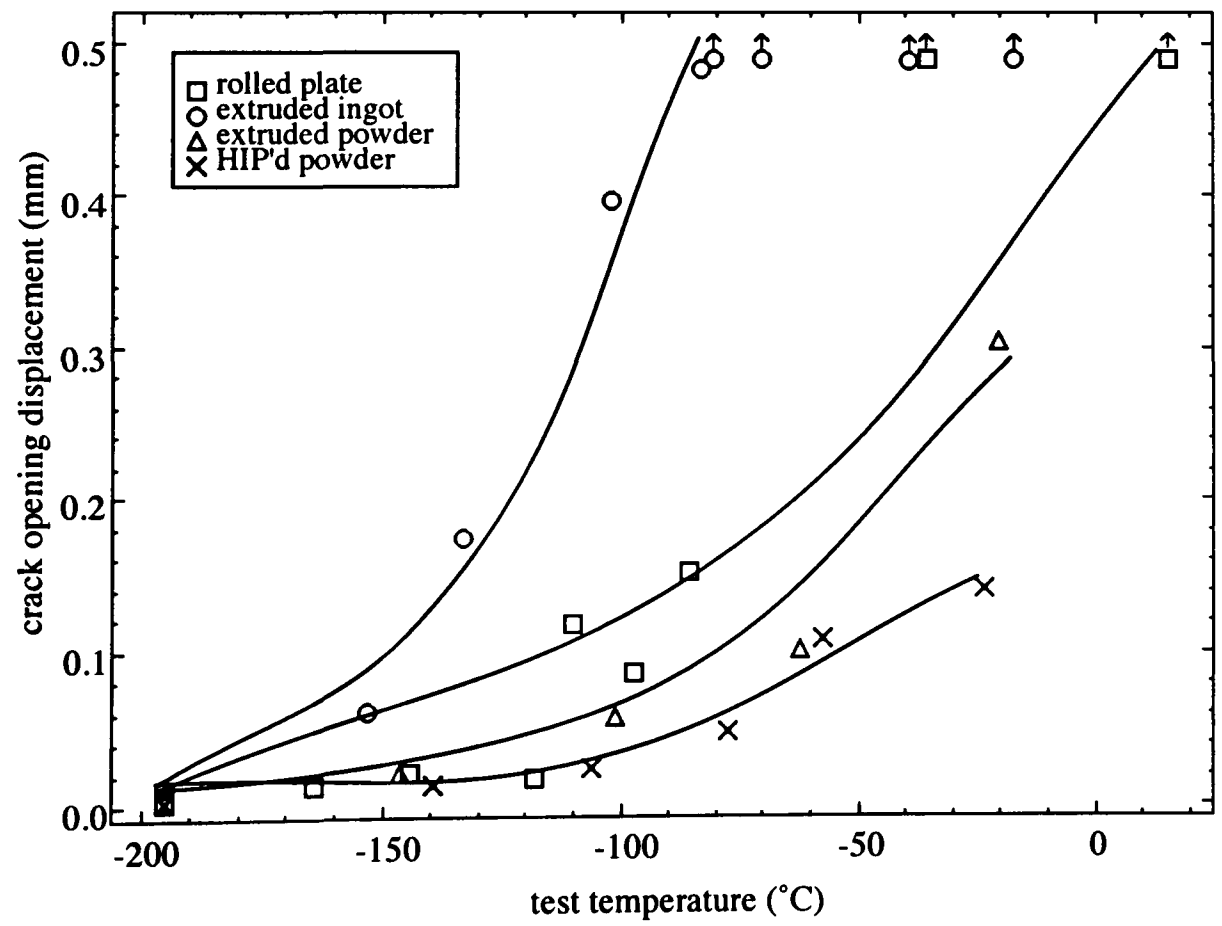

Figure 5.30 - Fracture toughness transition curves for X-Z orientated as-received product forms

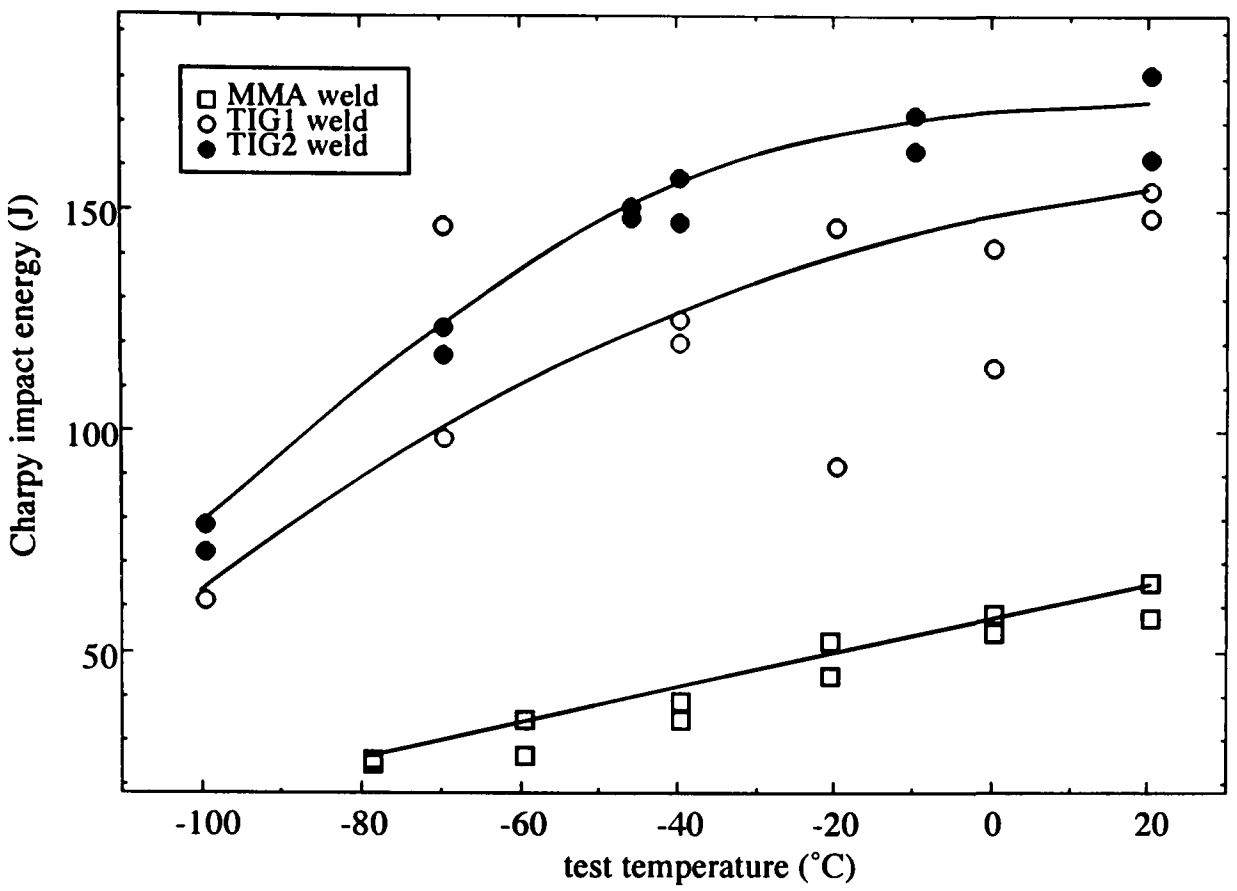

Figure 5.31 - Impact toughness transition curves for weld metals

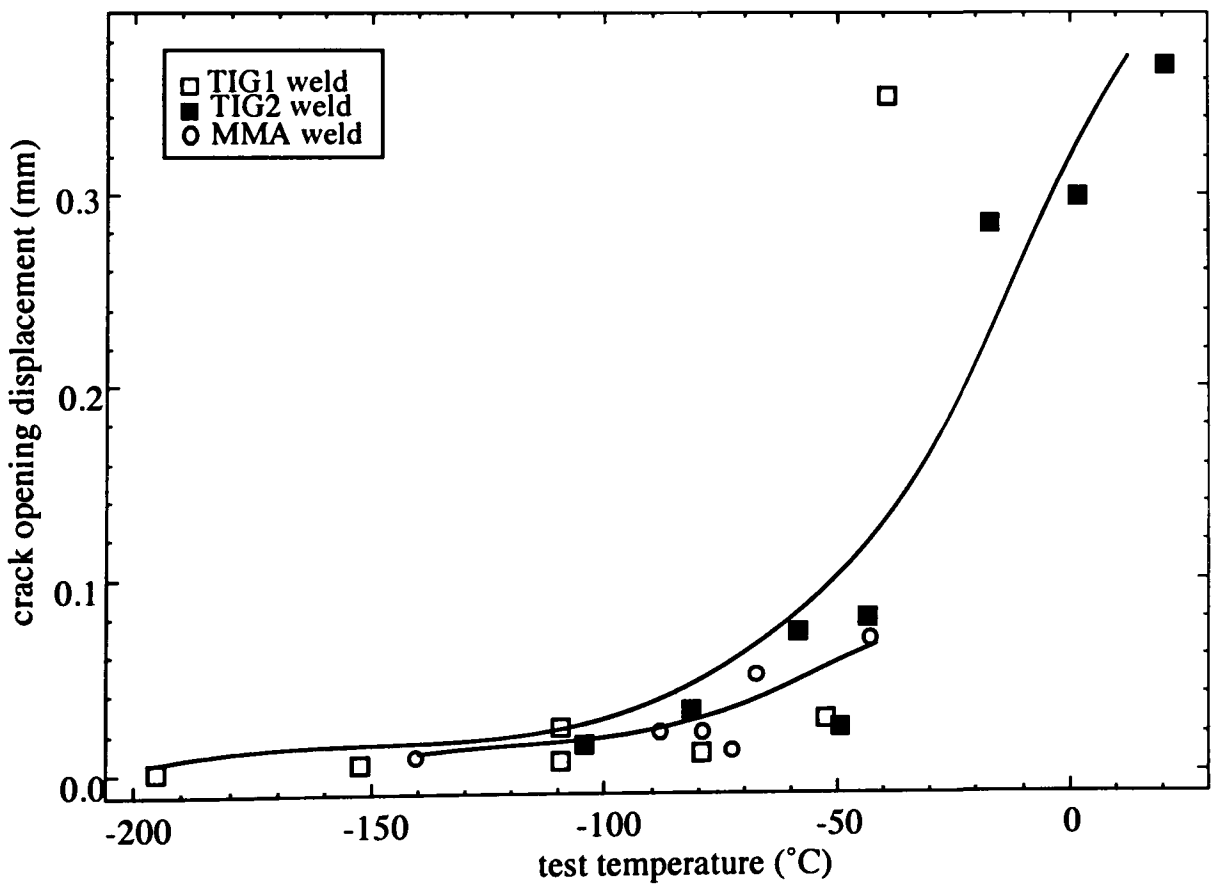

Figure 5.32 - Fracture toughness transition curves for weld metals

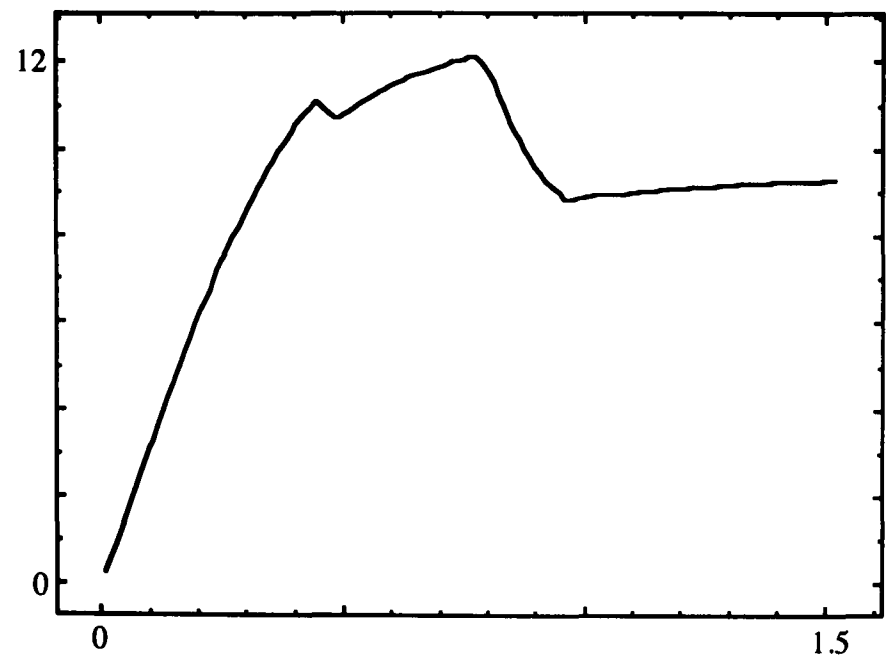

a) Pop-in (TIG, -50°C)

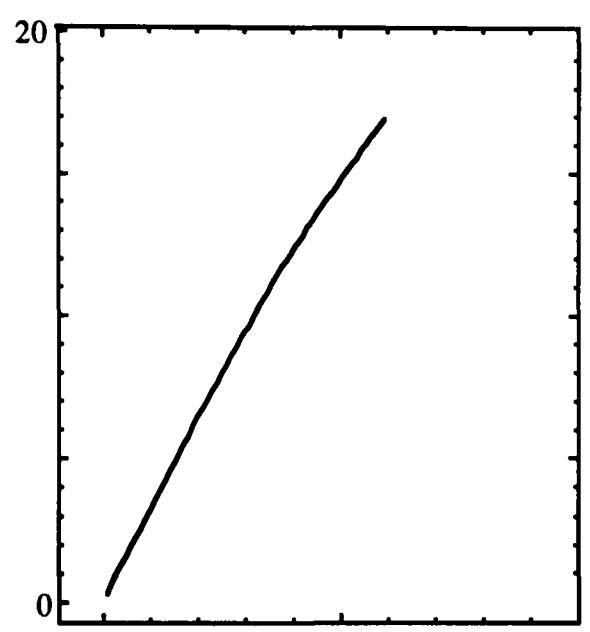

b) Critical load failure (TIG, -150°C)

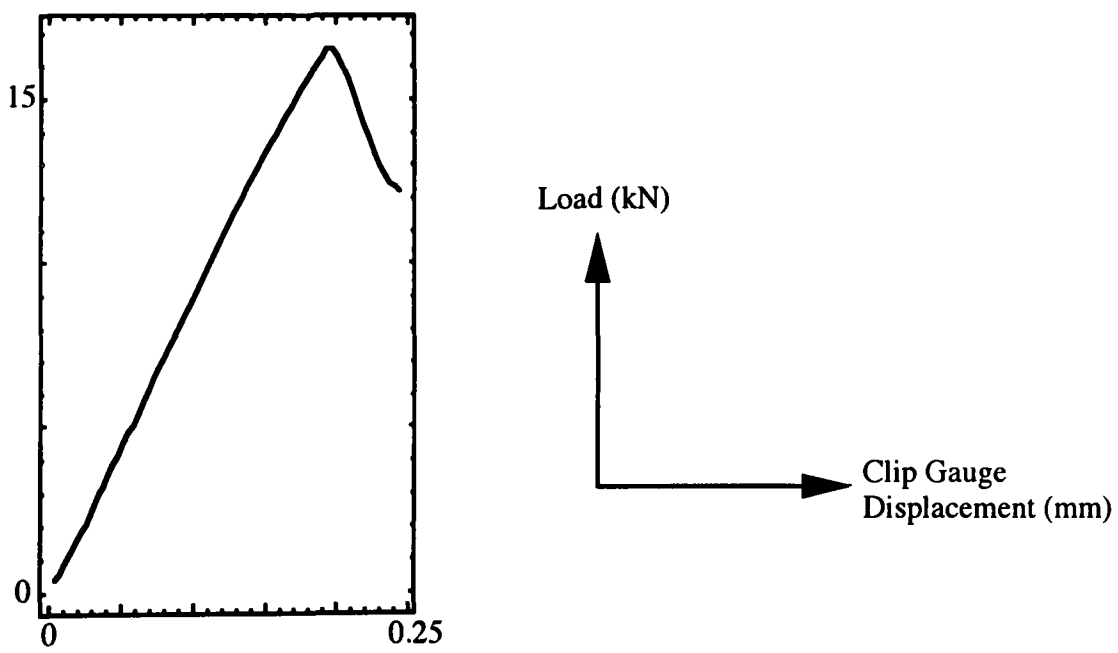

c) Maximum load failure (MMA, -40°C)

Figure 5.33 - Load-displacement curves for weld metals

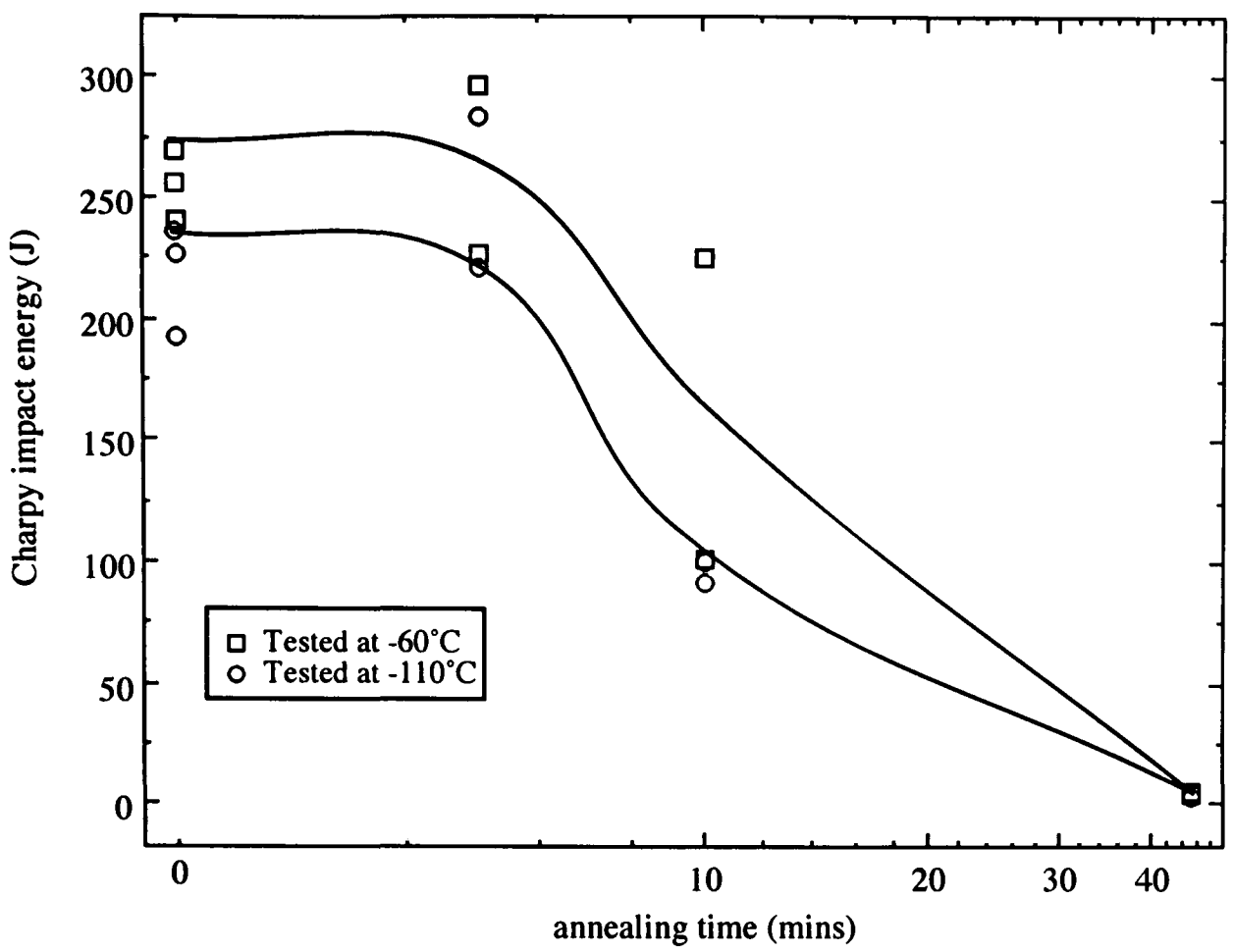

Figure 5.34 - Variation of impact toughness of rolled plate with annealing time at a temperature of 850°C (X-Z orientation)

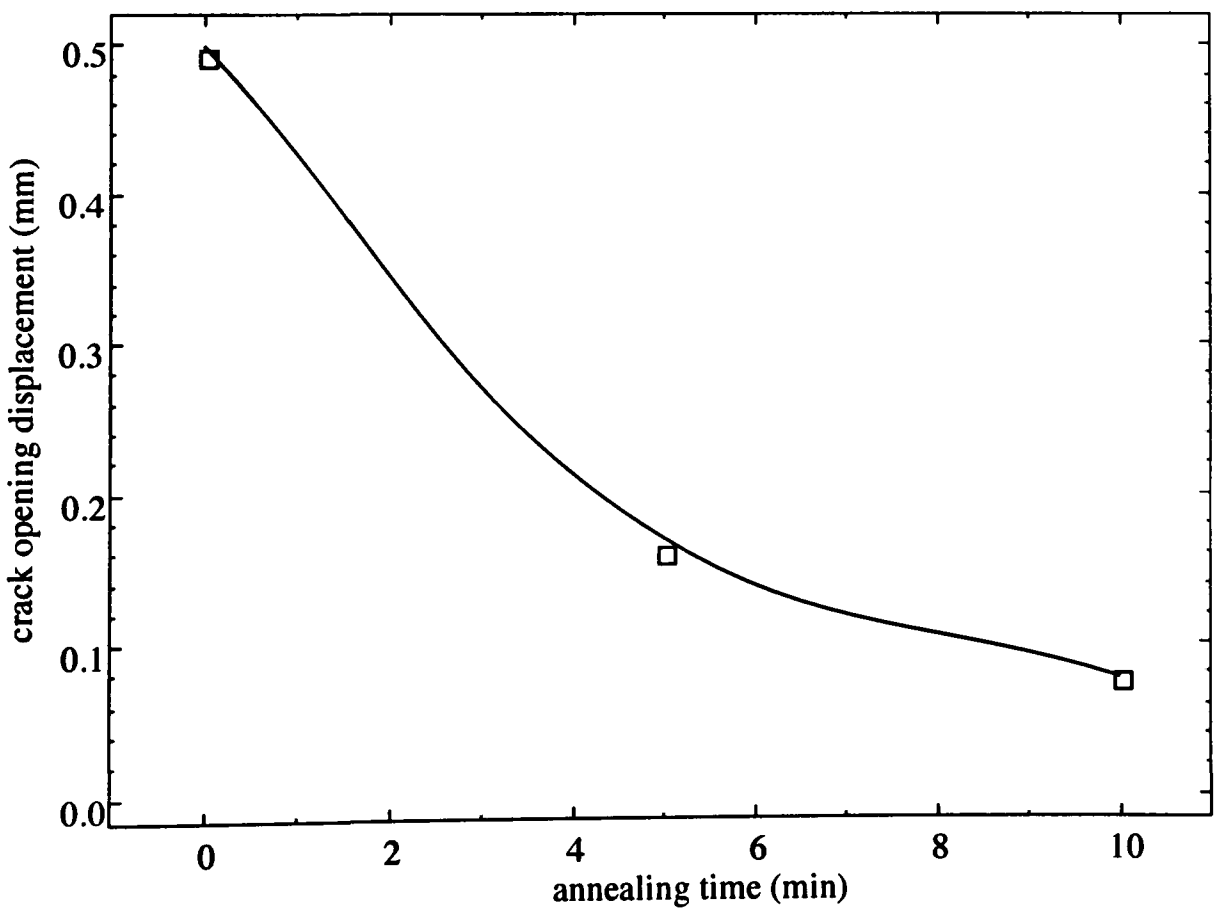

Figure 5.35 - Variation of fracture toughness of rolled plate with annealing time at a temperature of 850°C (X-Z orientation, -110°C)

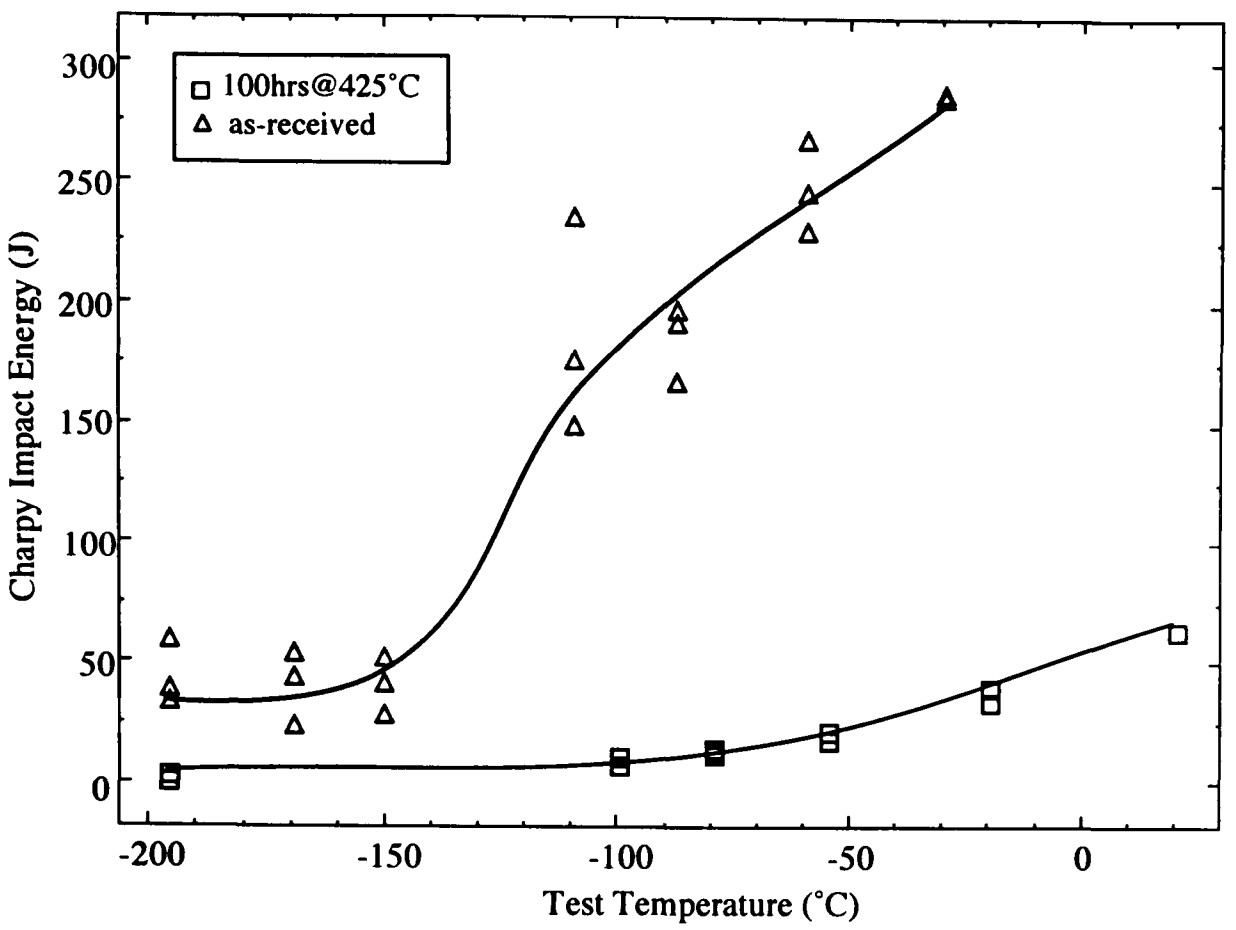

Figure 5.36 - Impact toughness transition curves for rolled plate aged at a temperature of 425°C for 100 hours (X-Z orientation)

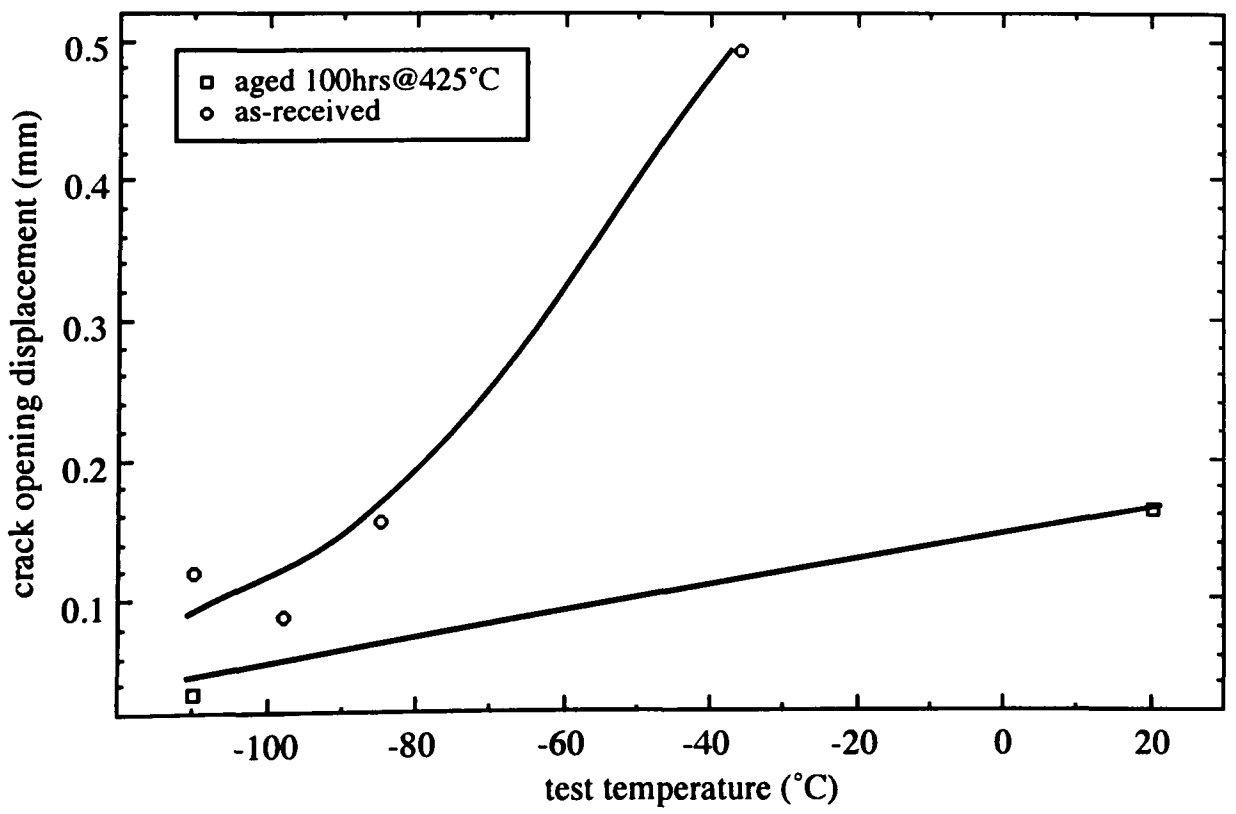

Figure 5.37 - Fracture toughness transition curves for rolled plate aged at a temperature of 425°C for 100 hours (X-Z orientation)

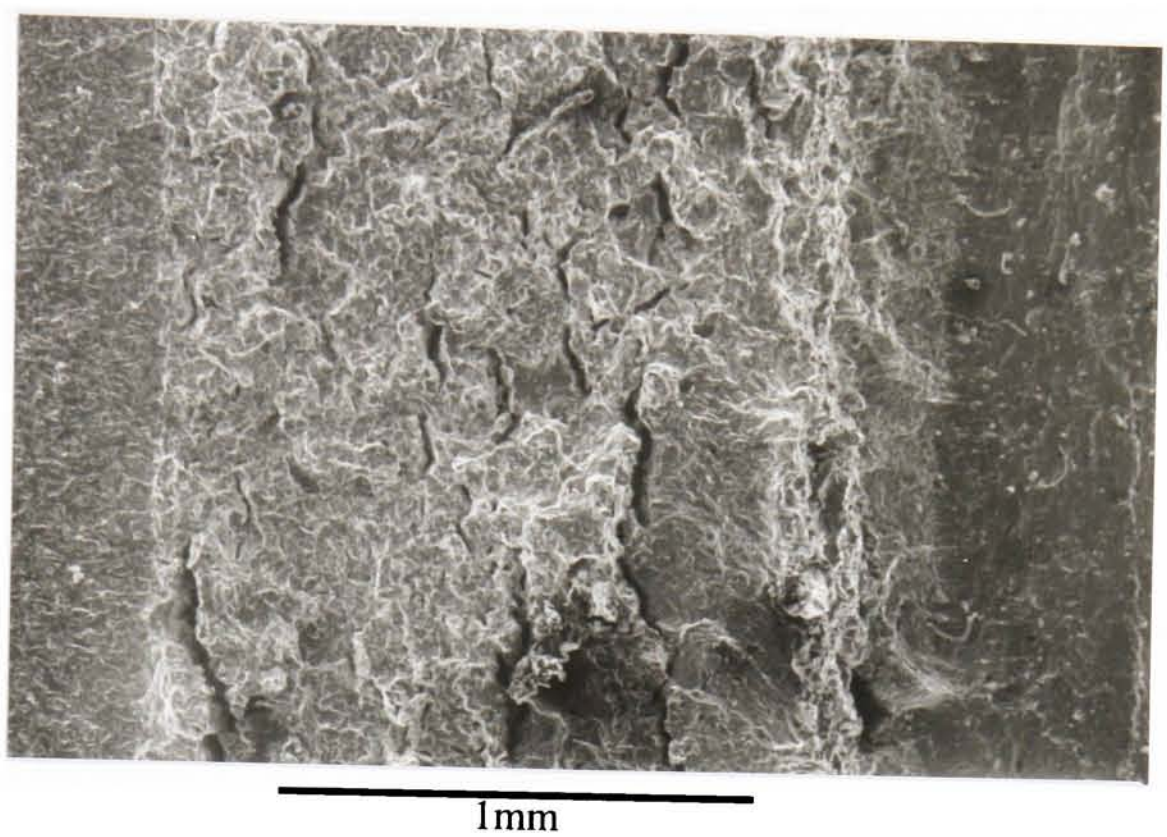

Figure 5.38 - Stretch width zone of COD specimen
(as-received extruded ingot, X-Y, -70°C, fatigue precrack on left)

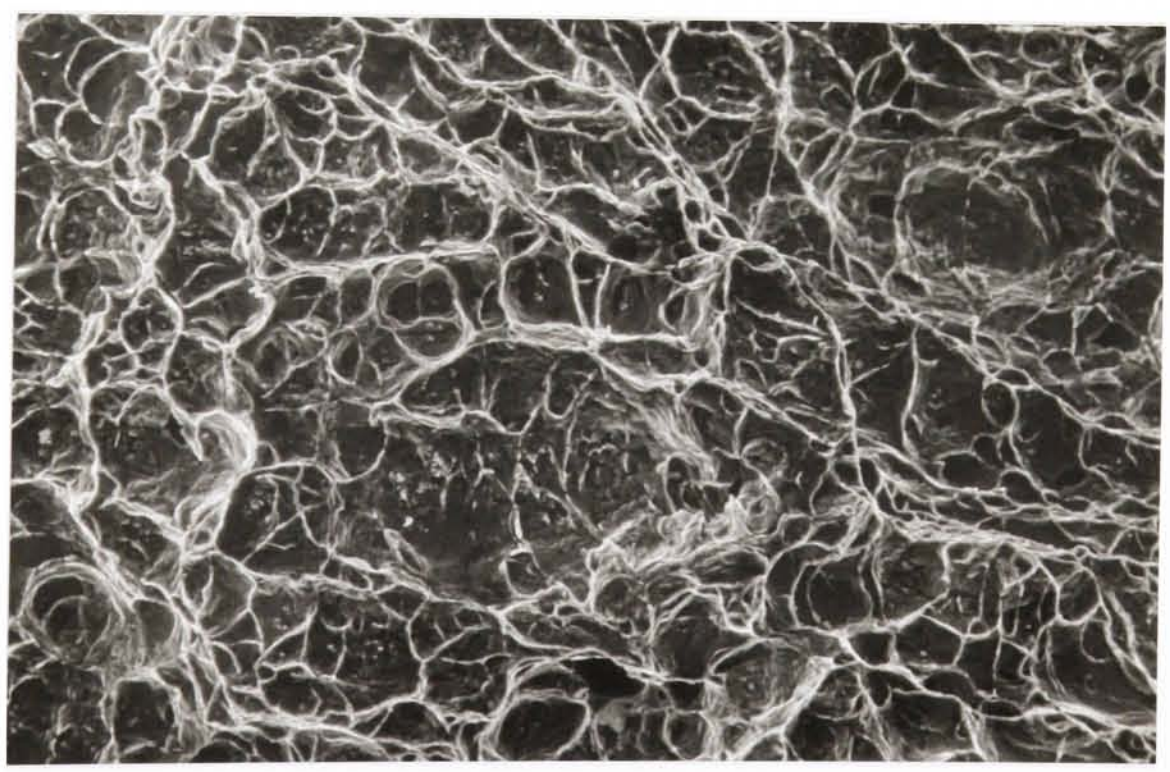

Figure 5.39 Microvoid coalescence of austenite and ferrite
(as-received plate, X-Z, -40°C)

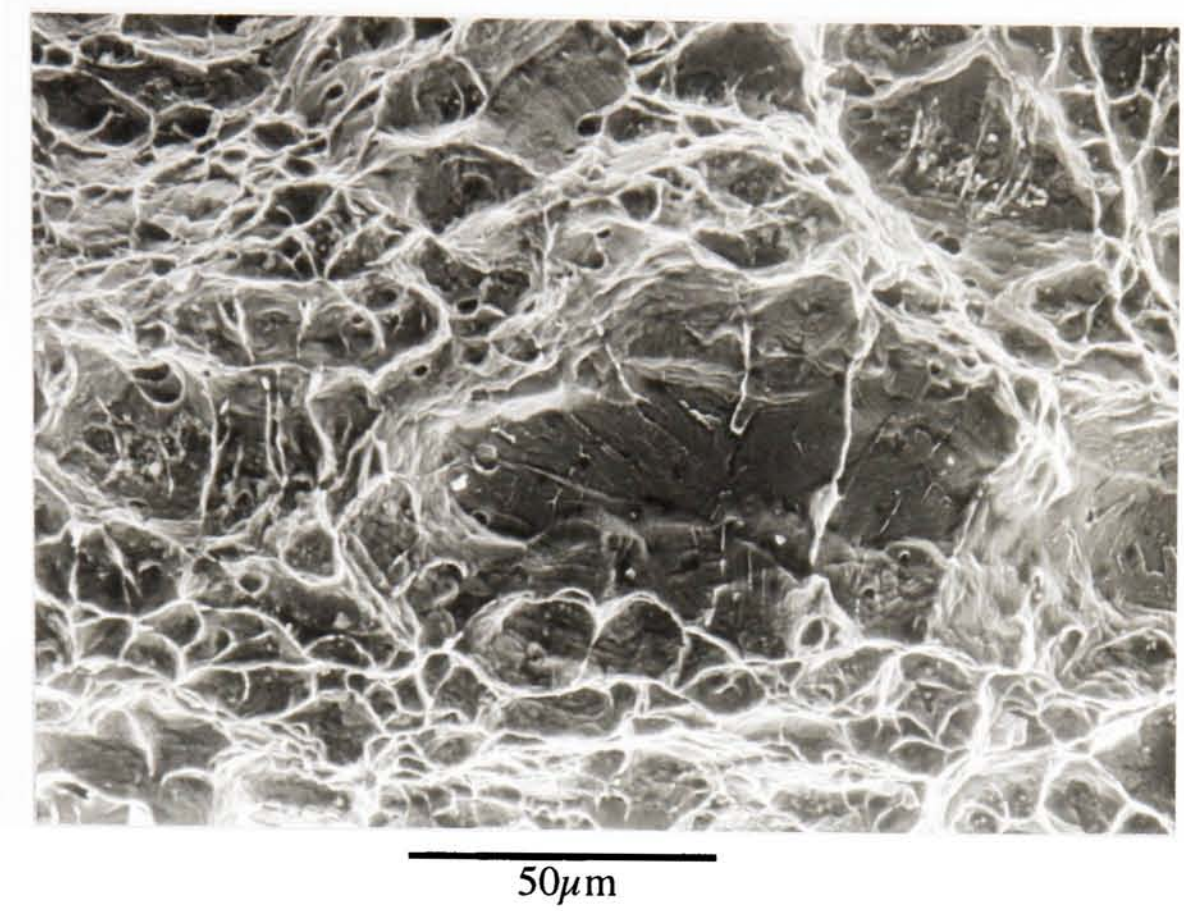

Figure 5.40 - Mixed-mode failure of ferrite, ductile failure of austenite (as-received plate, X-Z, -80°C)

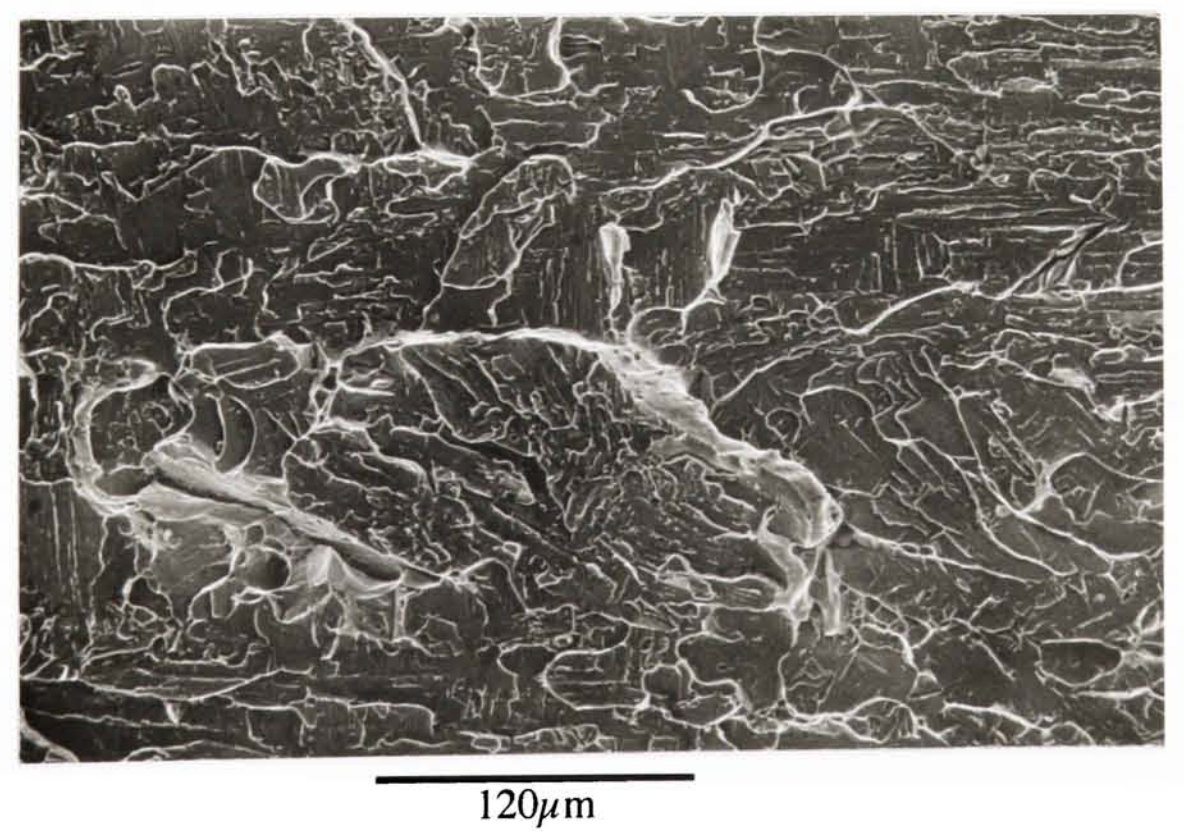

Figure 5.41 - Cleavage failure of ferrite, ductile failure of austenite (as-received plate, X-Z, -110°C)

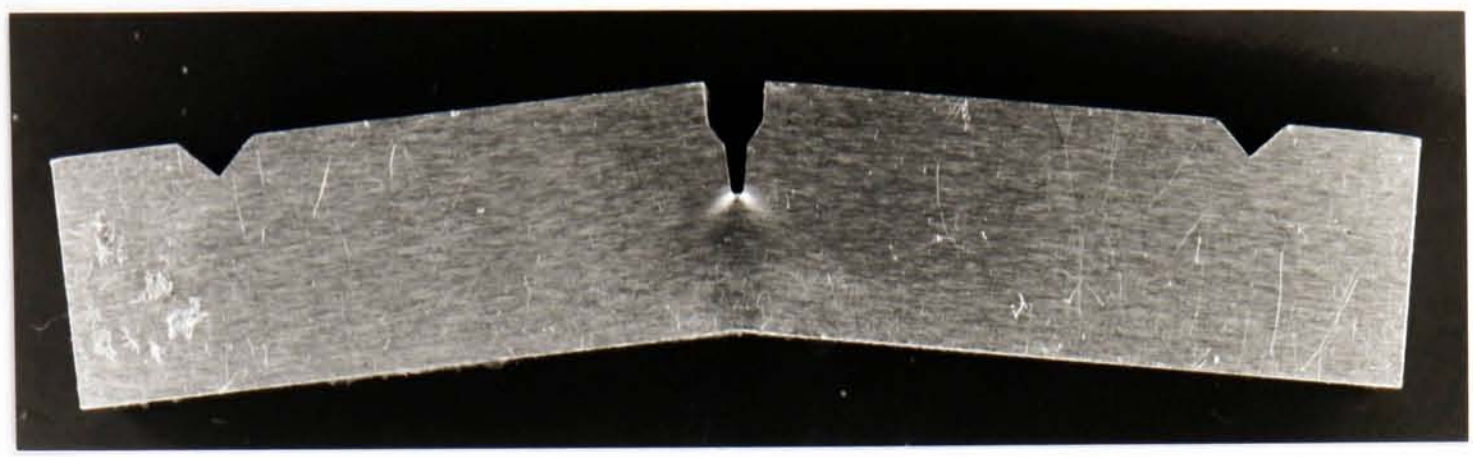

15mm

a) plastic collapse (X-Z, +20°C)

15mm

b) transverse crack growth (X-Z, -110°C)

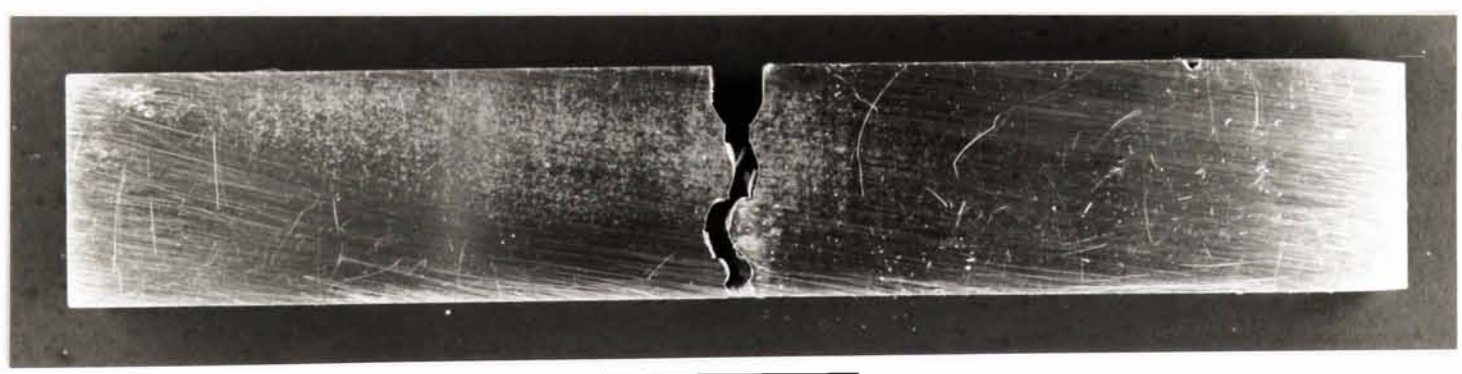

15mm

c) normal crack growth (X-Y, -85°C)

Figure 5.42 - Broken specimens from COD tests (as-received plate)

1mm

a) Cleaved steps on fracture surface (notch on left)

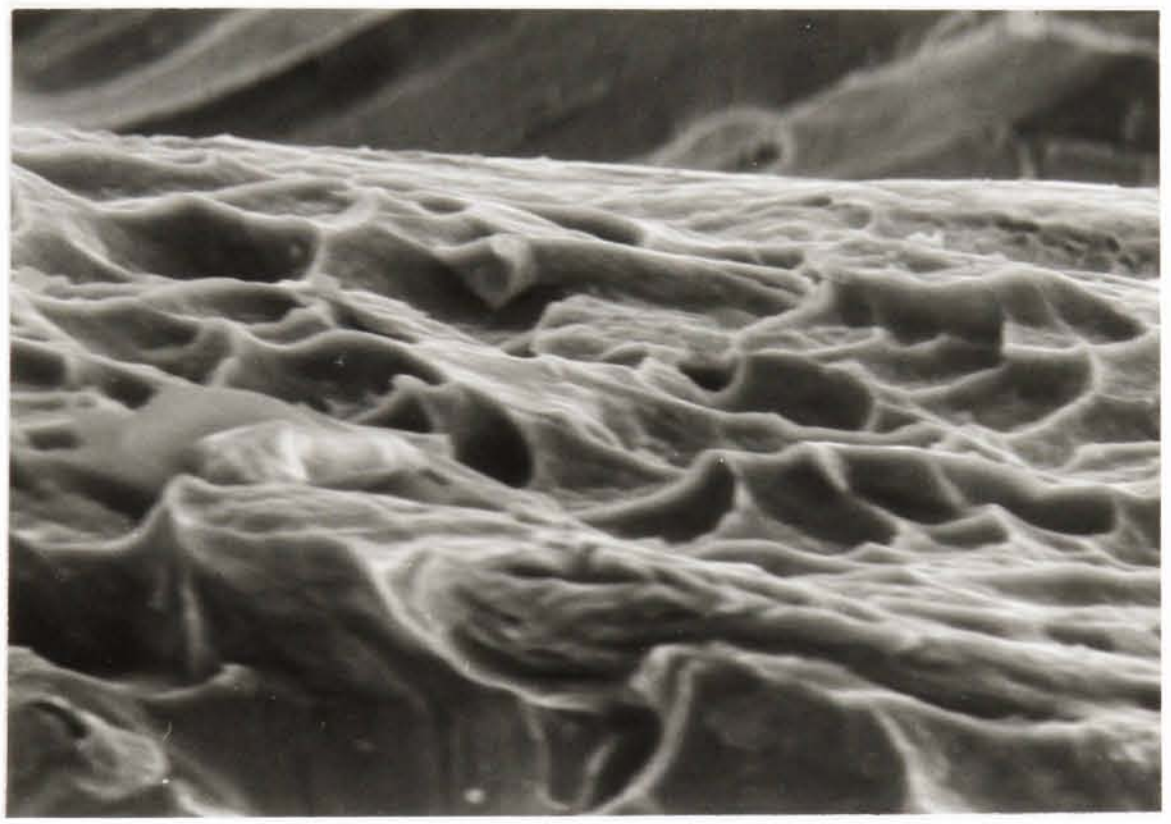

15μm

b) Ductile tearing between steps

Figure 5.43 - Stepped transverse crack growth (as-received plate, X-Z, -110°C)

1mm

a) Bifurcated crack (fatigue precrack at top)

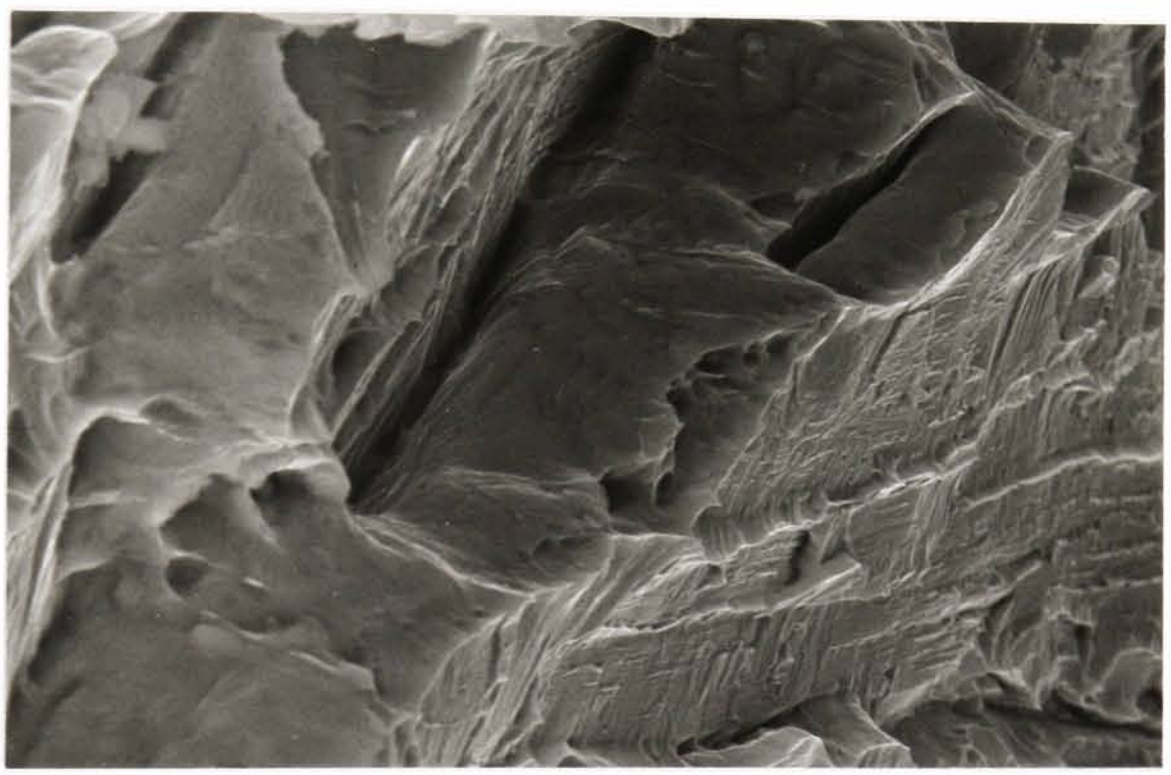

10μm

b) Surface of crack

Figure 5.44 - Secondary crack from bifurcation at fatigue precrack root (as-received plate, X-Z, -130°C)

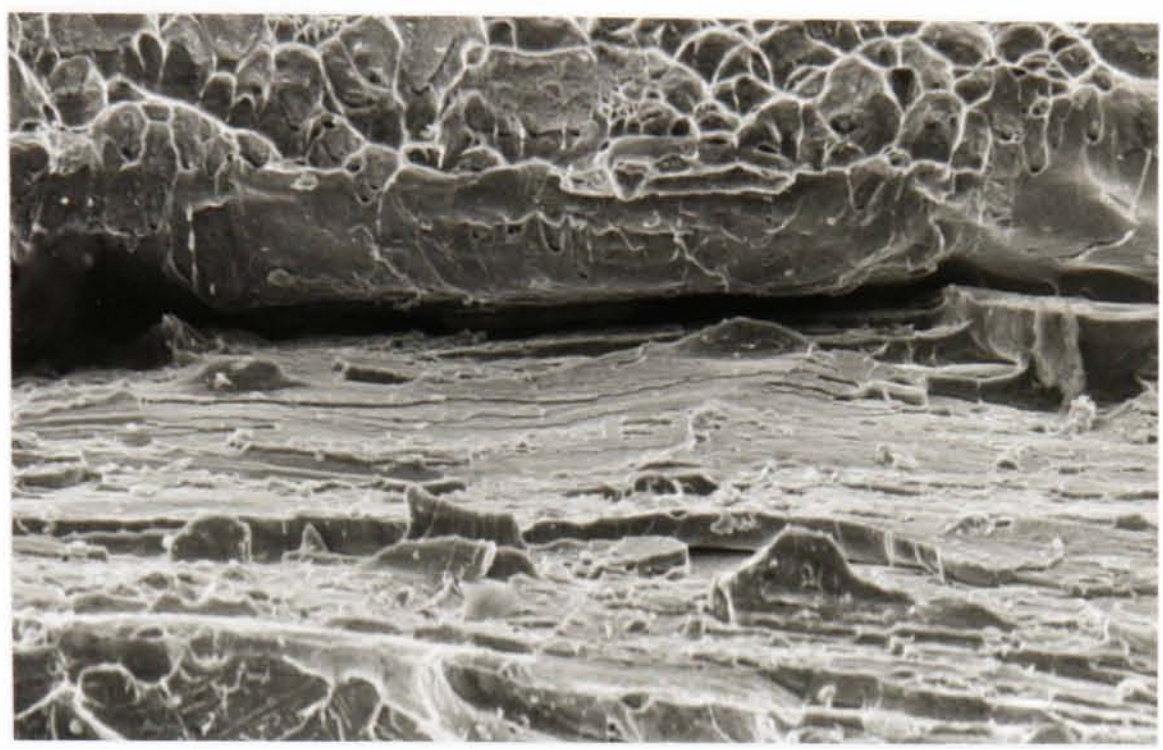

Figure 5.45 - Secondary crack formation during crack growth
(as-received plate, X-Z, -130°C)

1mm

a) Test temperature -50°C (fatigue precrack on left)

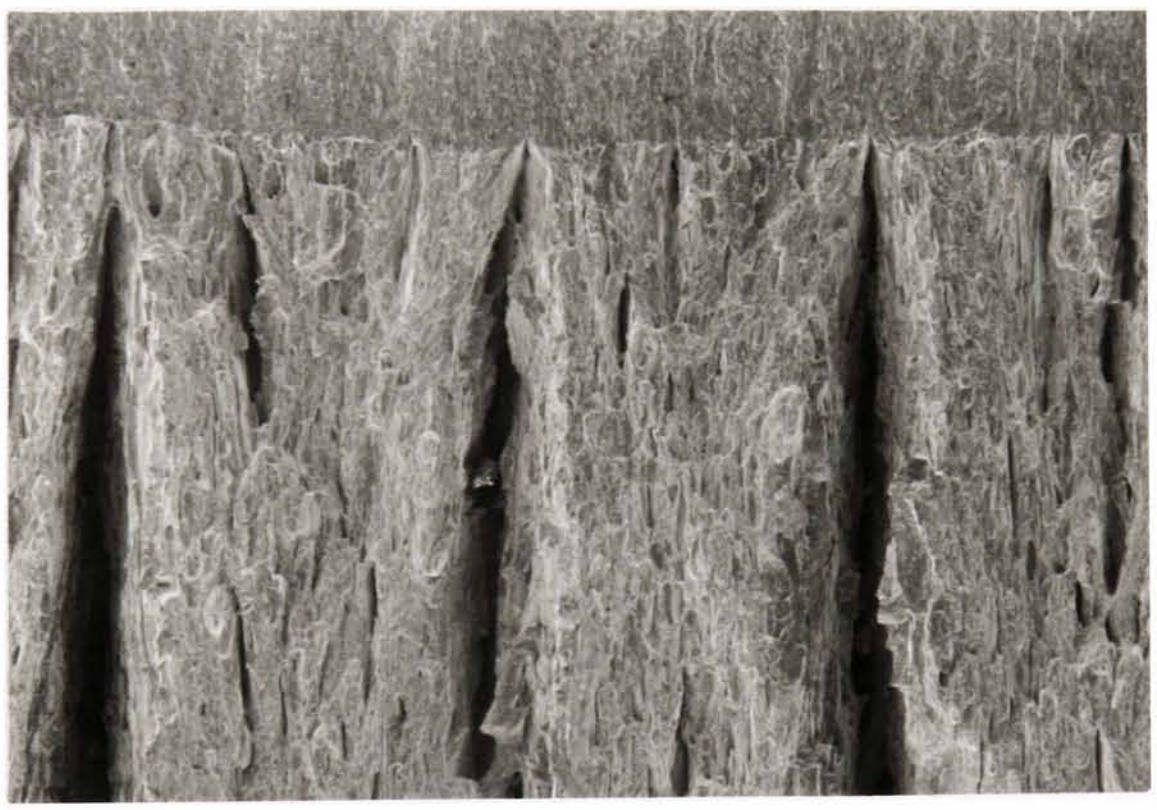

1mm

b) Test temperature -150°C (fatigue precrack at top)

Figure 5.46 - Secondary cracks aligned with crack path direction for X-Y orientated specimens (as-received plate)

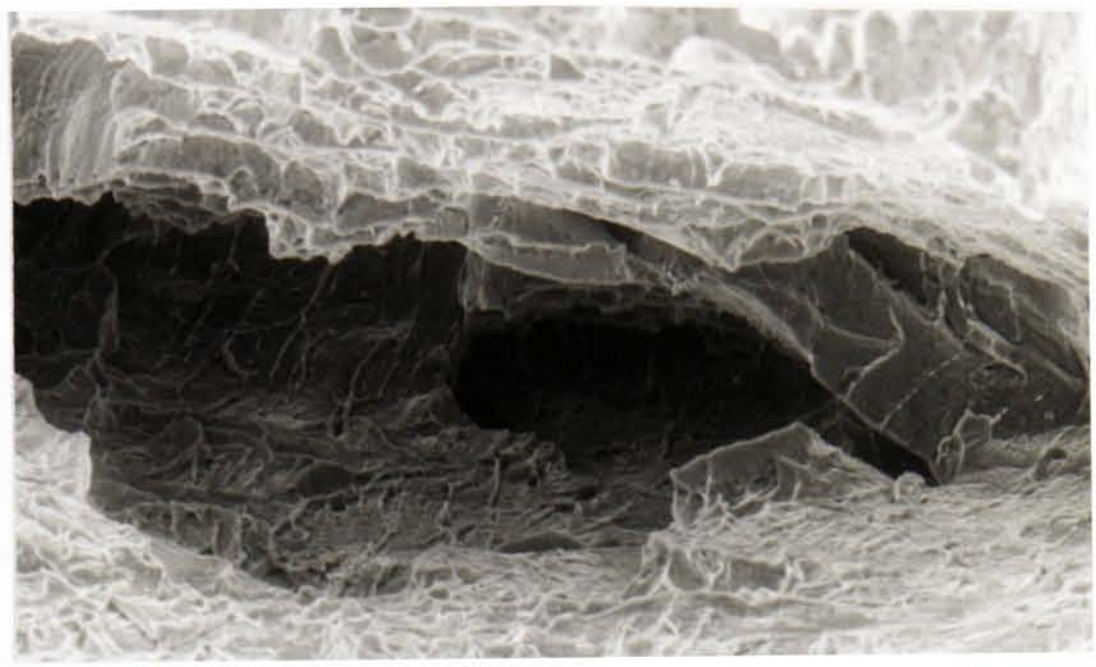

a) Test temperature -50°C

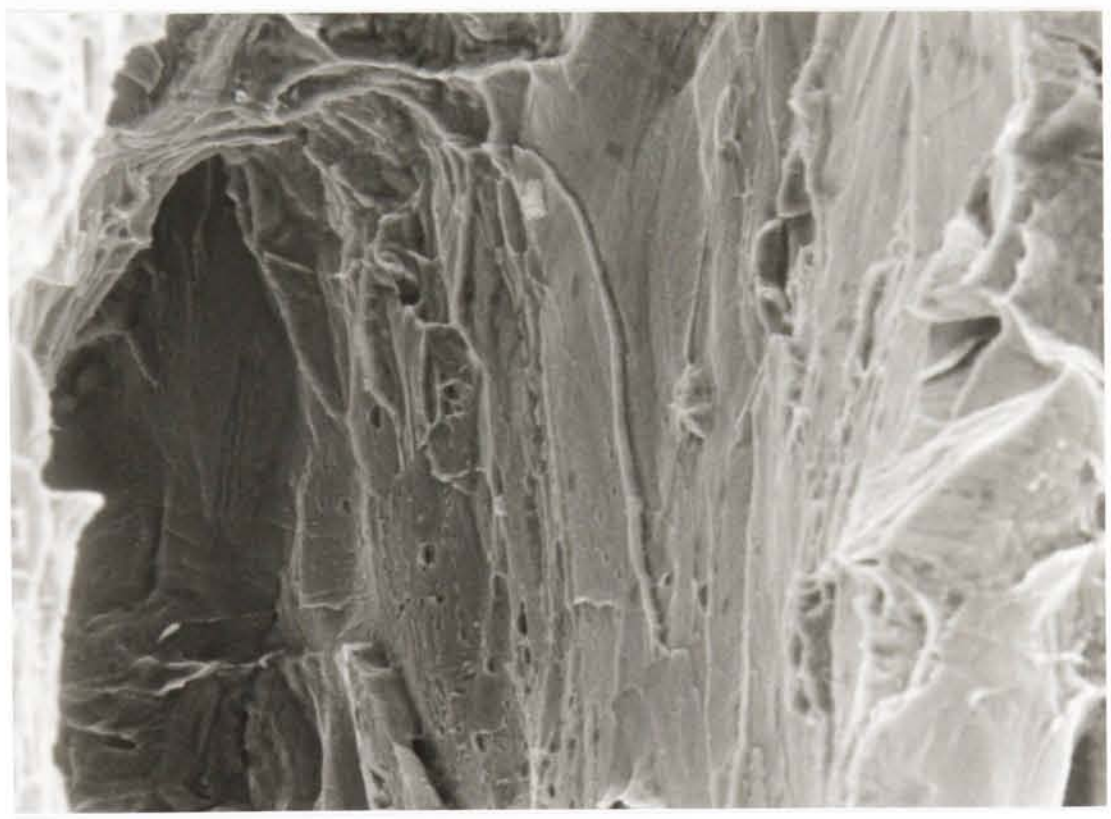

b) Test temperature -150°C

Figure 5.47 - Surface of secondary cracks from X-Y orientated specimens (as-received plate)

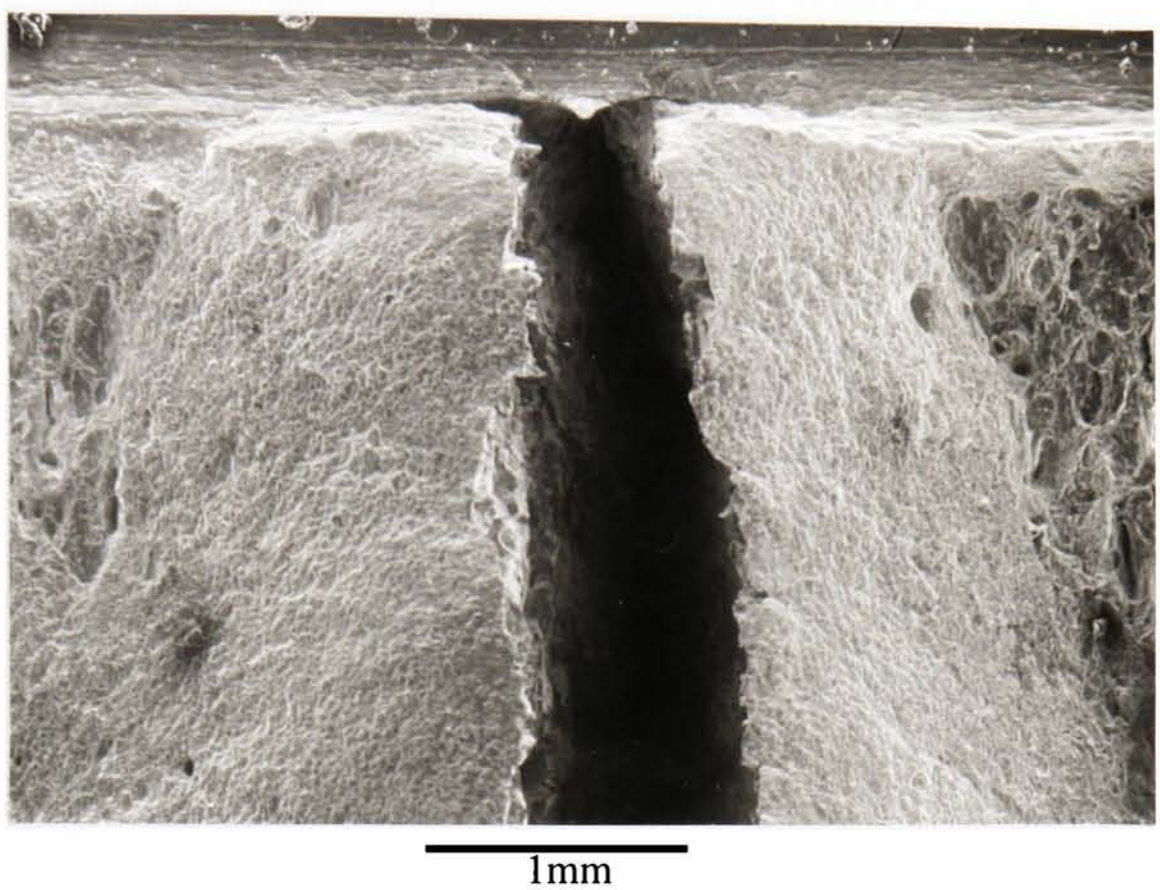

Figure 5.48 - Shear lips accompanying secondary cracks from X-Y orientated specimen (as-received plate, X-Y, -110°C, notch at top)

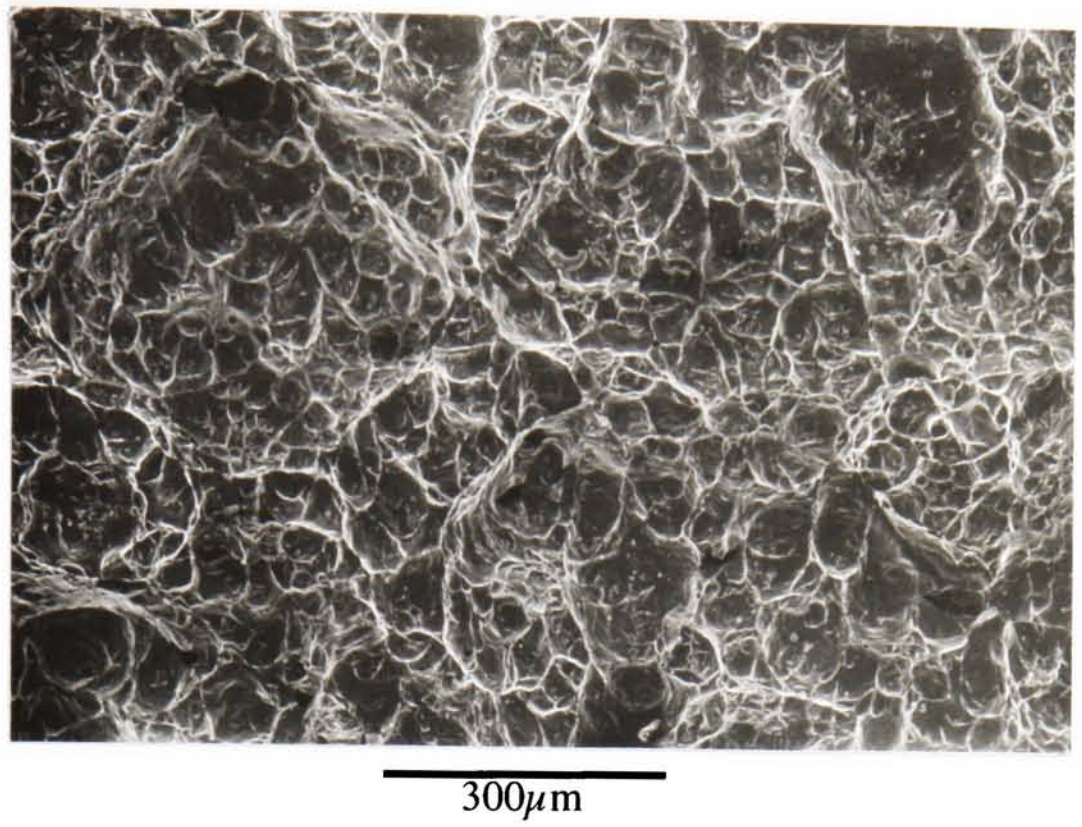

a) Microvoid coalescence of austenite and ferrite (-20°C)

b) Cleavage failure of ferrite, ductile failure of austenite (-140°C)

Figure 5.49 - Fracture surfaces of Z-X orientated specimens (as-received plate)

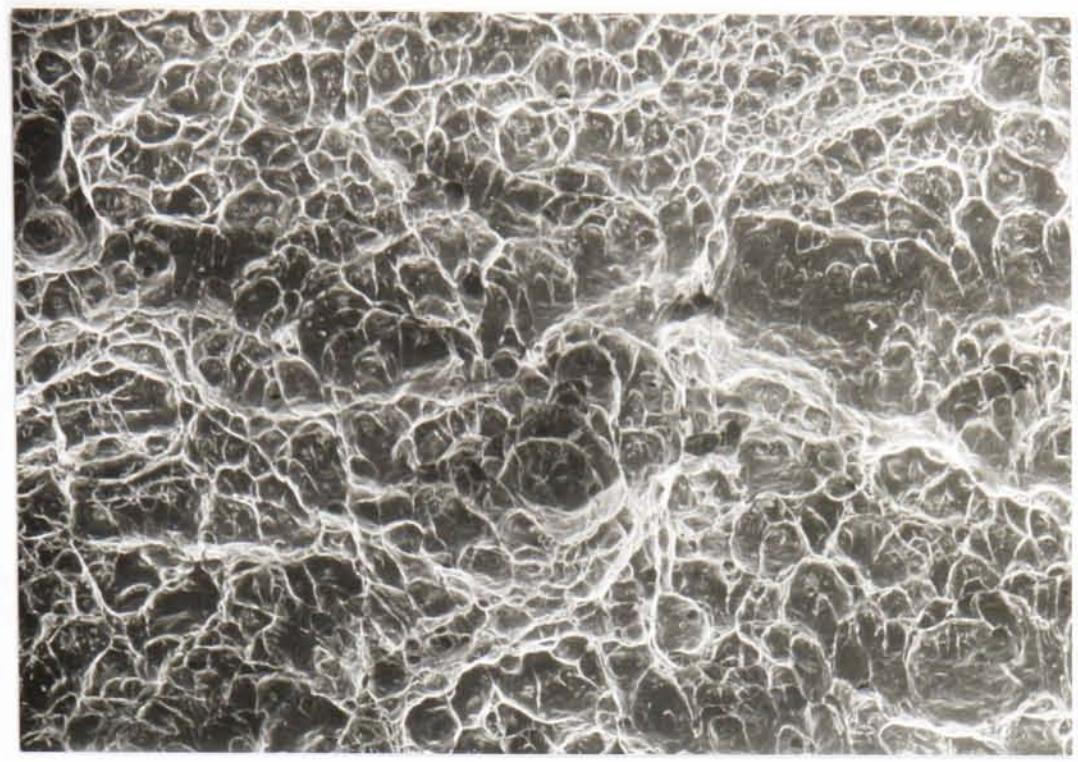

a) Microvoid coalescence of austenite and ferrite (-20°C)

b) Cleavage failure of ferrite, ductile failure of austenite (-140°C)

Figure 5.50 - Fracture surfaces of Z-Y orientated specimens (as-received plate)

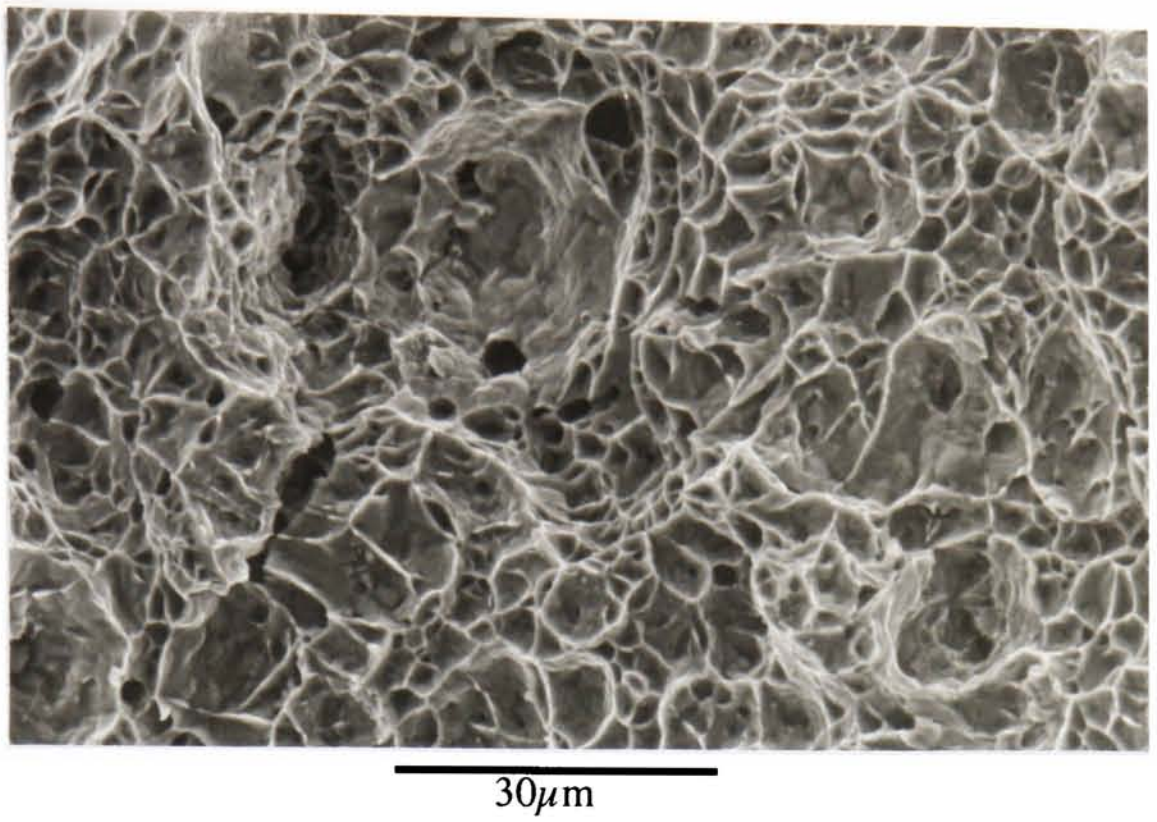

a) Microvoid coalescence of austenite and ferrite (X-Z, -30°C)

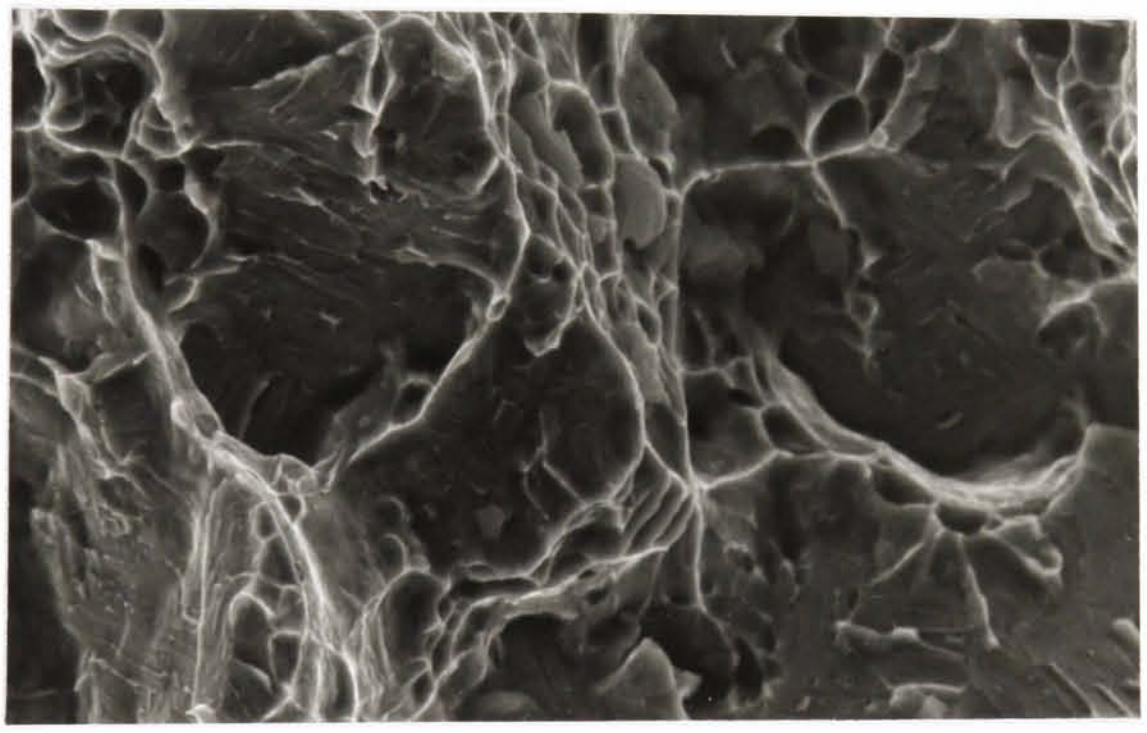

b) Cleavage failure of ferrite, ductile failure of austenite (X-Z, -150°C)

Figure 5.51 - Fracture surfaces of extruded ingot material

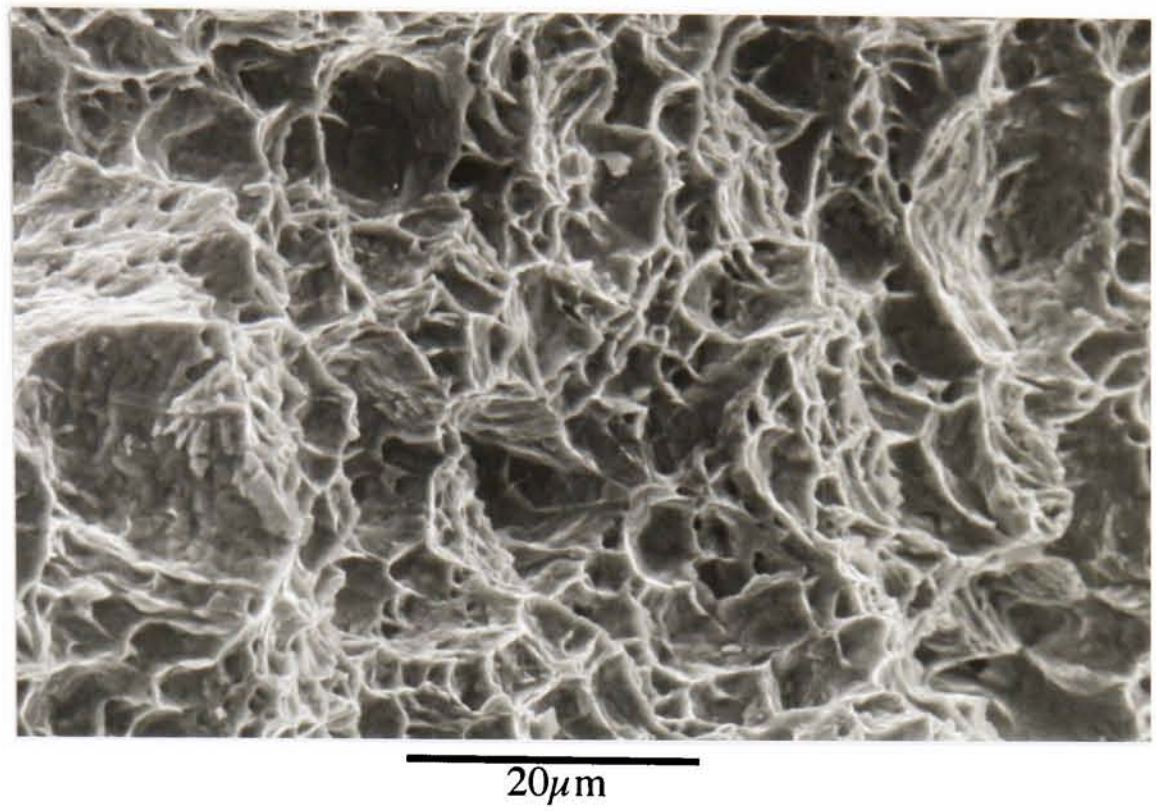

a) Microvoid coalescence of austenite and ferrite (X-Z, -60°C)

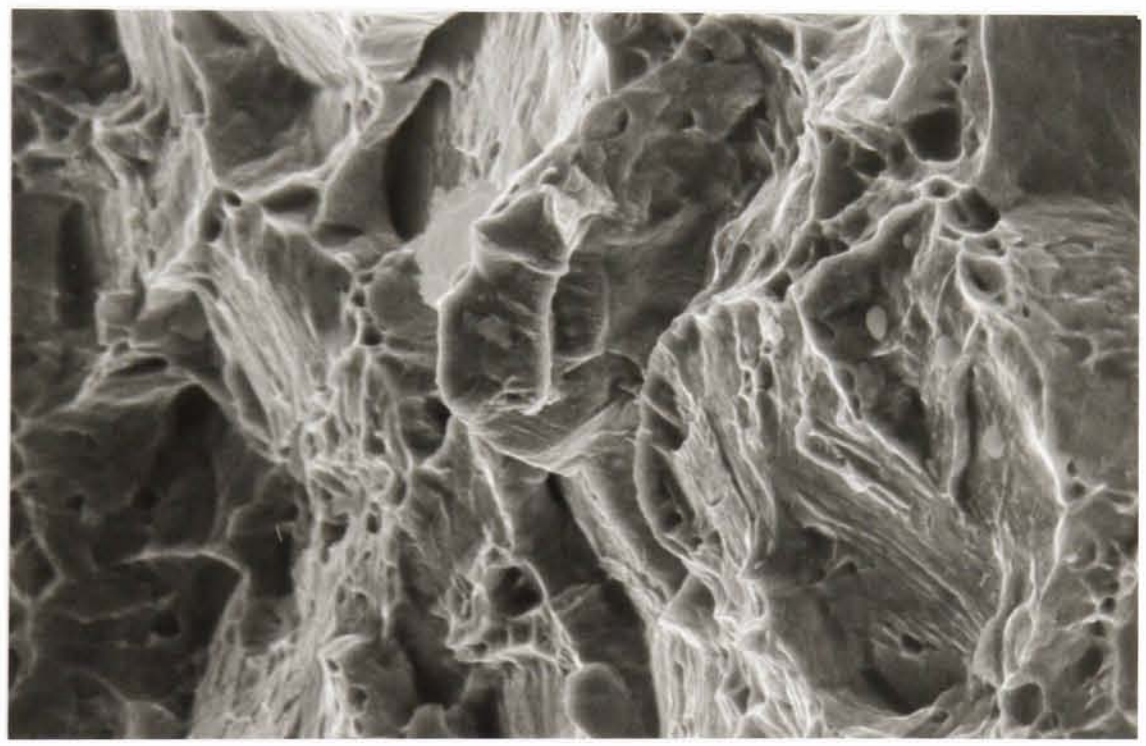

b) Cleavage failure of ferrite, ductile failure of austenite (X-Z, -150°C)

Figure 5.52 - Fracture surfaces of extruded powder material

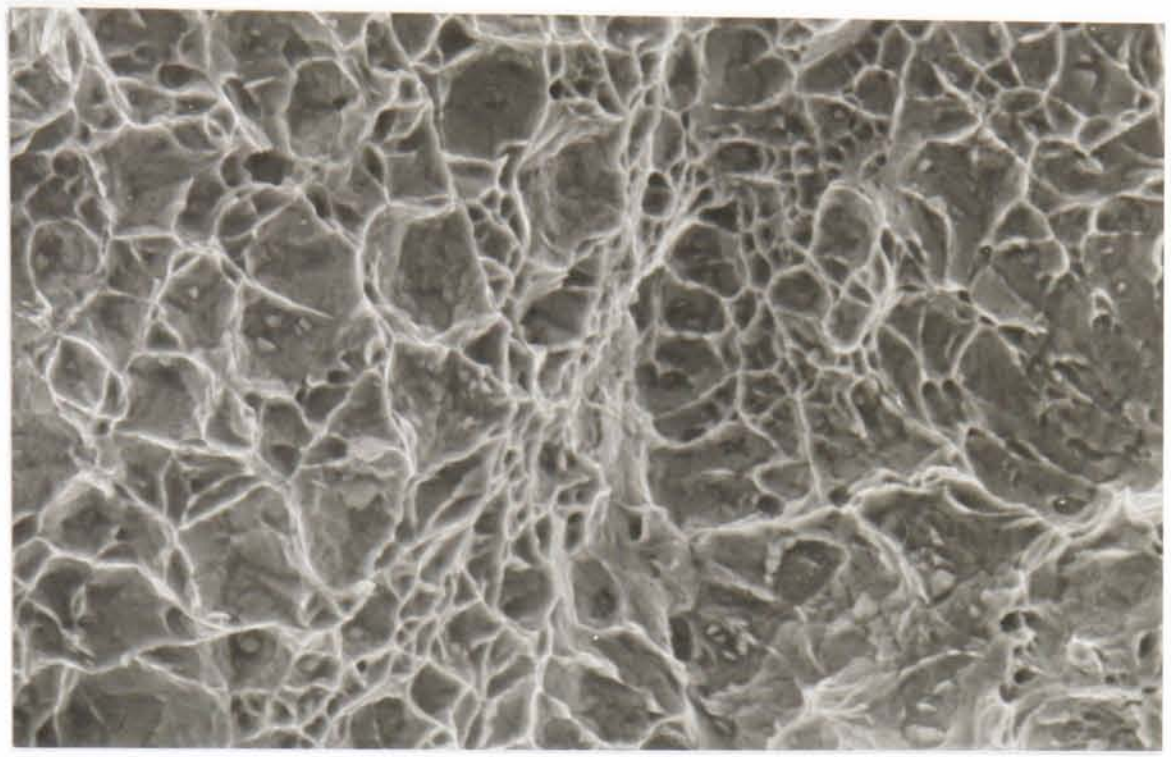

a) Microvoid coalescence of austenite and ferrite (X-Z, -20°C)

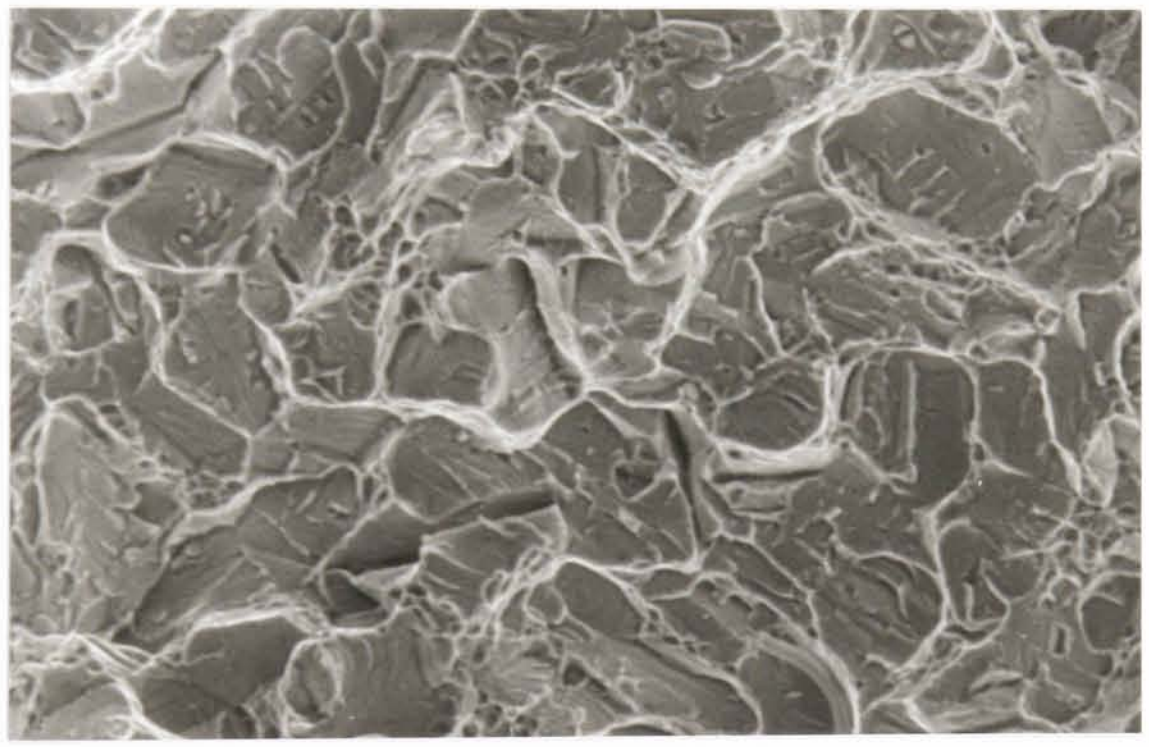

b) Cleavage failure of ferrite, ductile failure of austenite (X-Z, -140°C)

Figure 5.53 - Fracture surfaces of HIP'd powder material

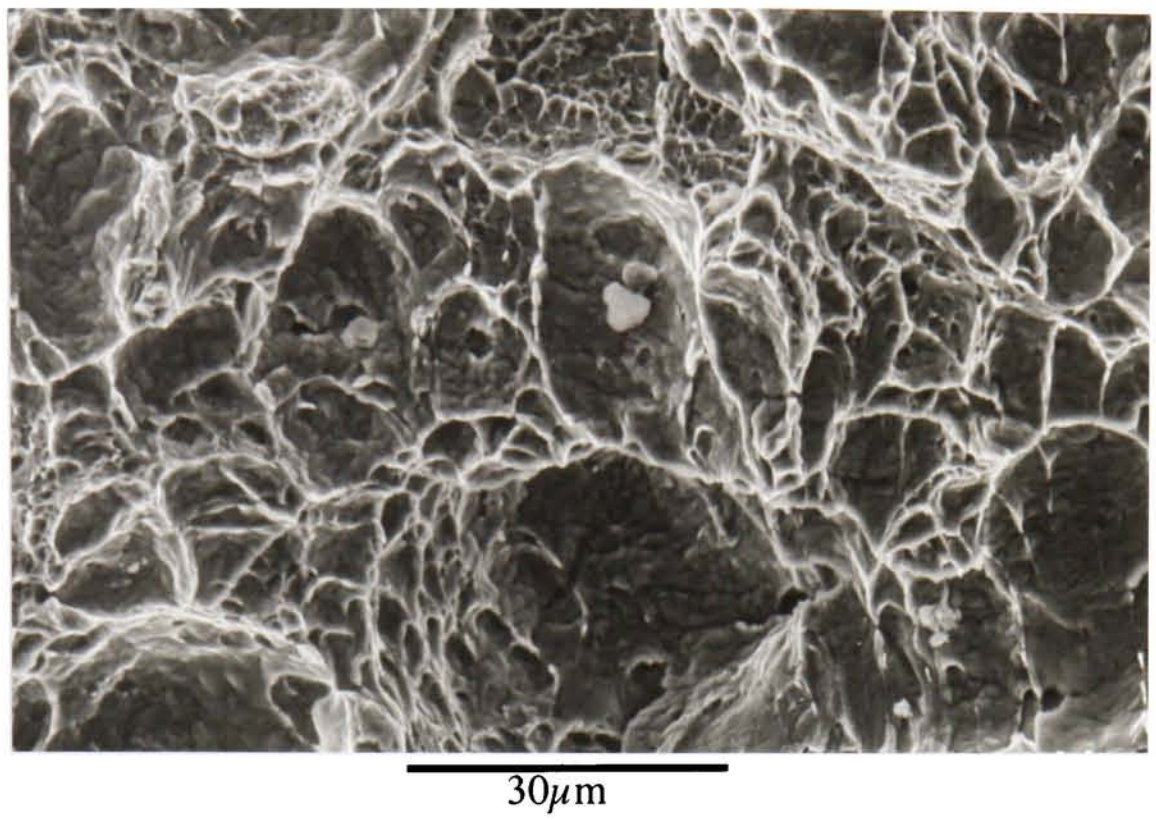

a) TIG weld (-40°C)

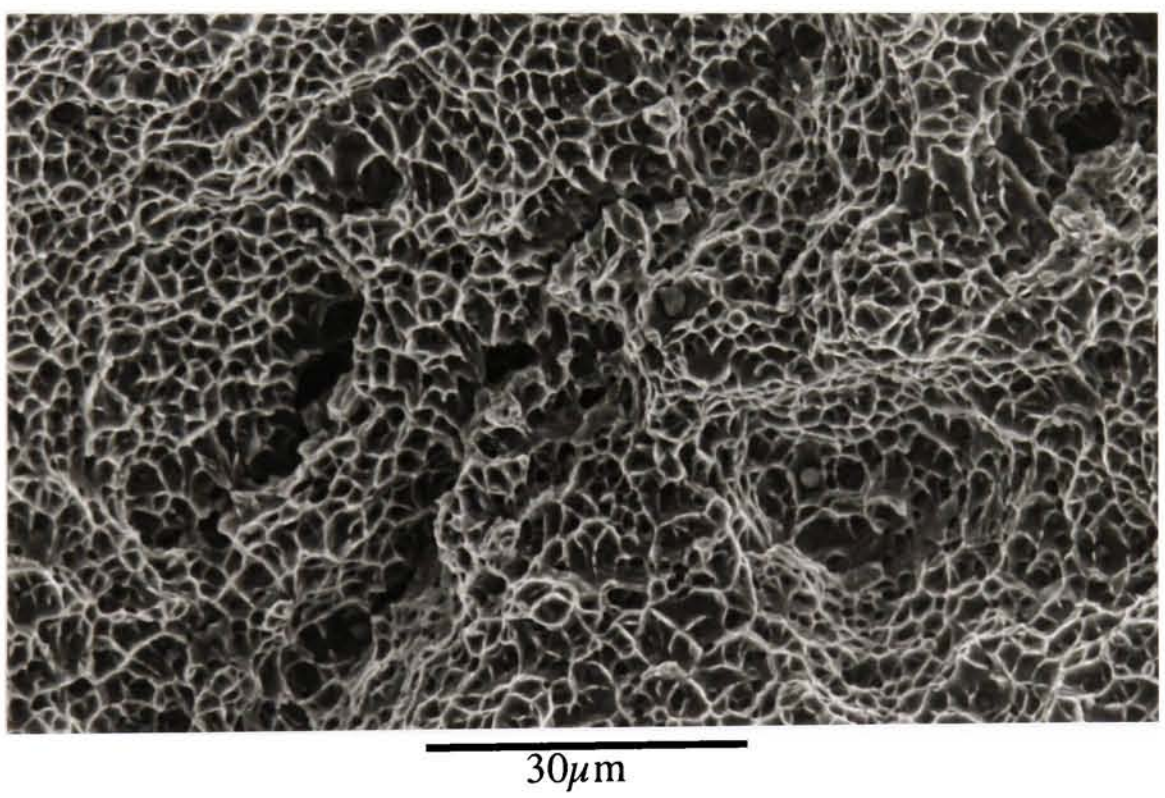

b) MMA weld (-40°C)

Figure 5.54 - Microvoid coalescence of austenite and ferrite (weld metals)

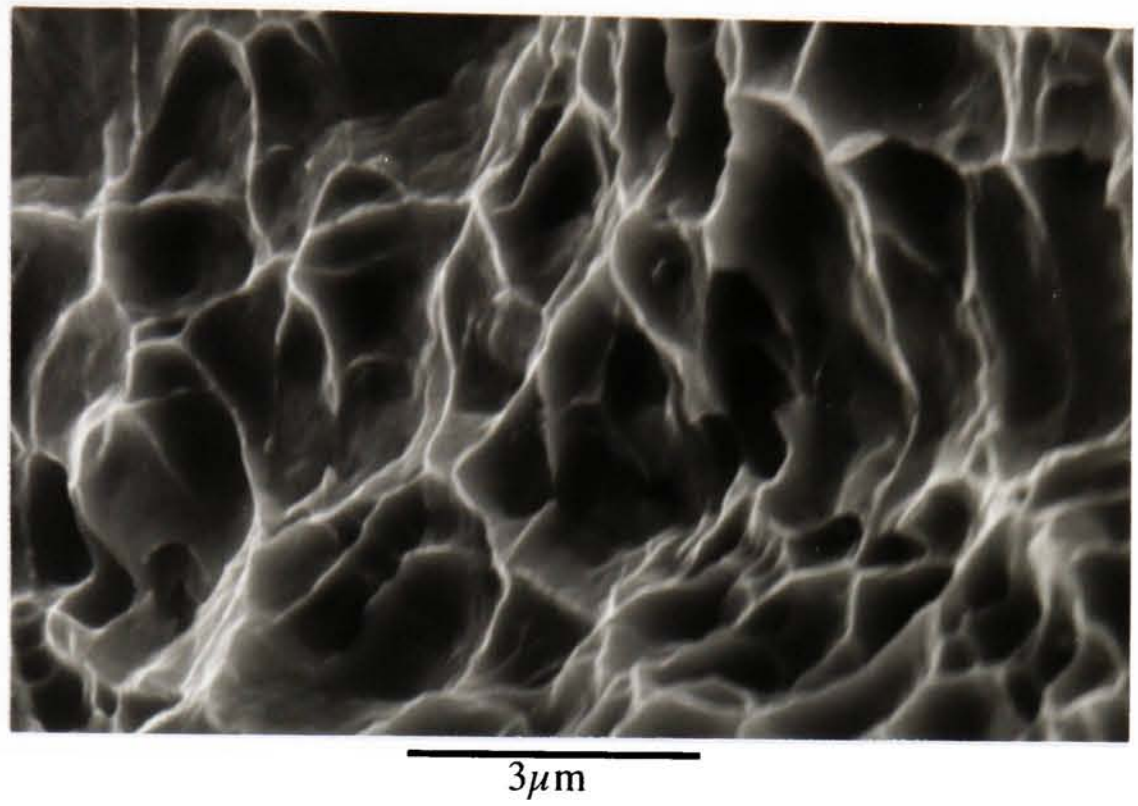

a) TIG weld (-40°C)

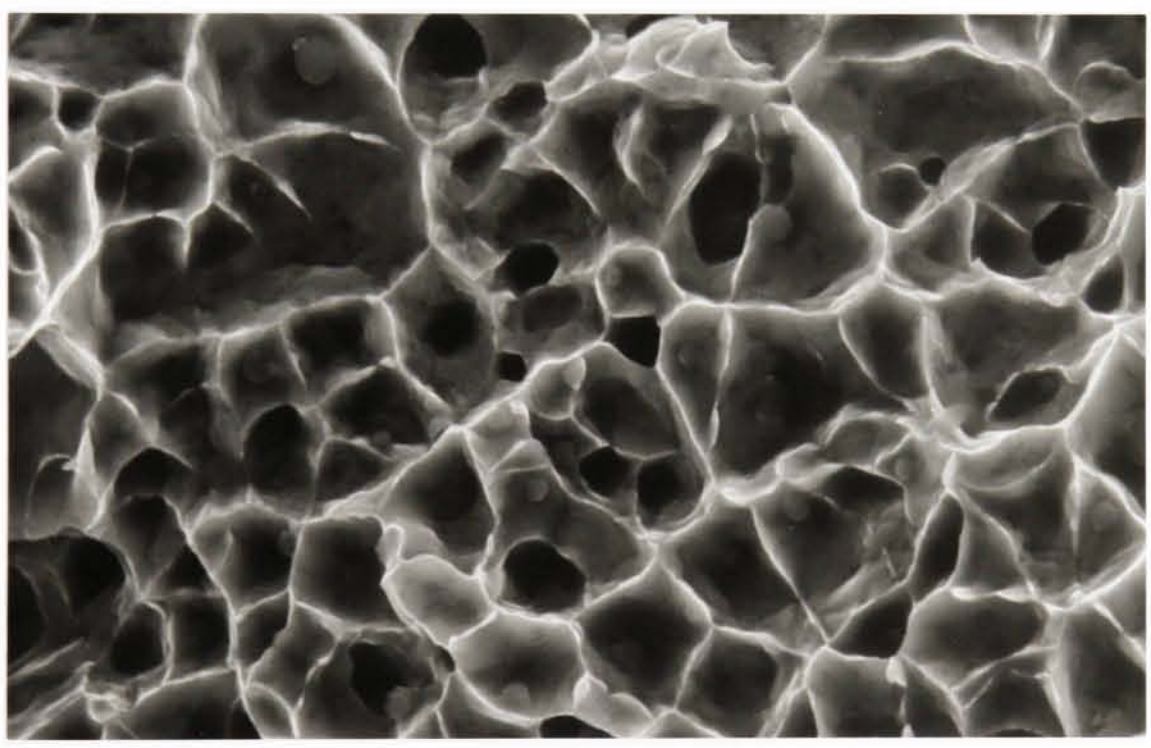

b) MMA weld (-40°C)

Figure 5.55 - Microvoids present in weld metals

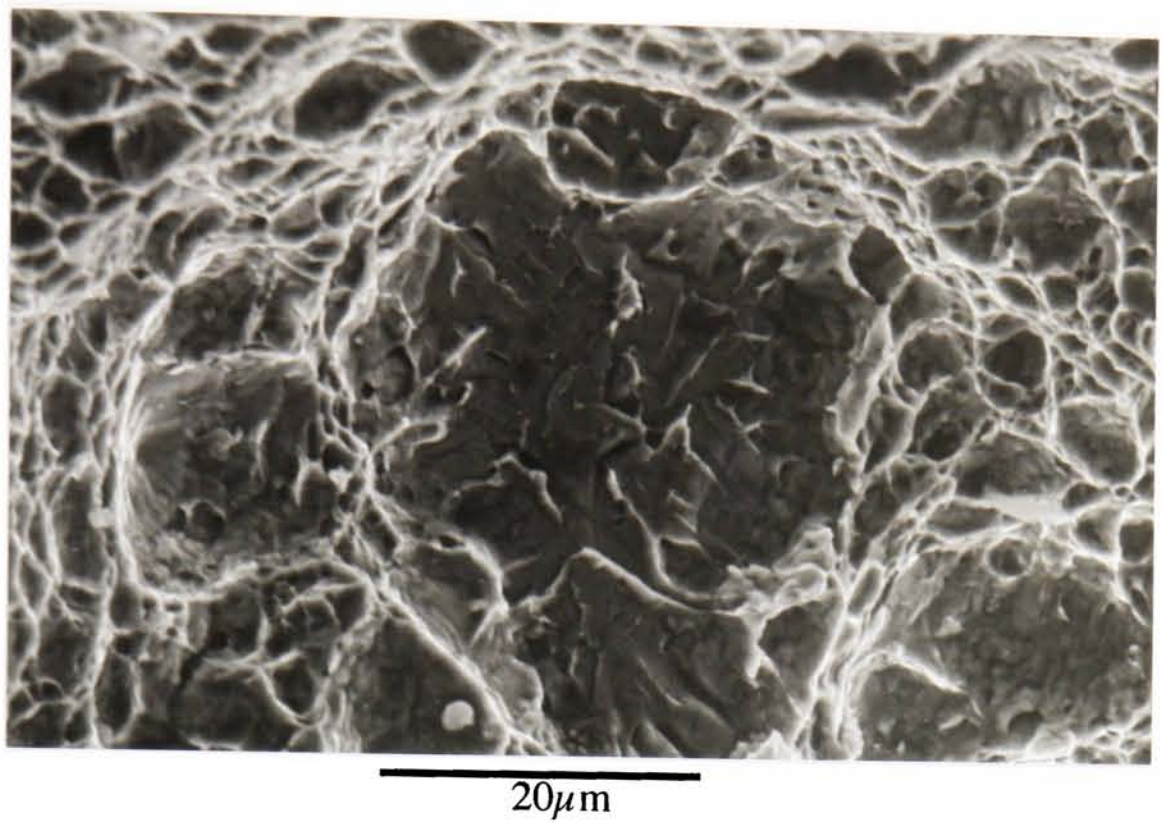

a) TIG weld (-50°C)

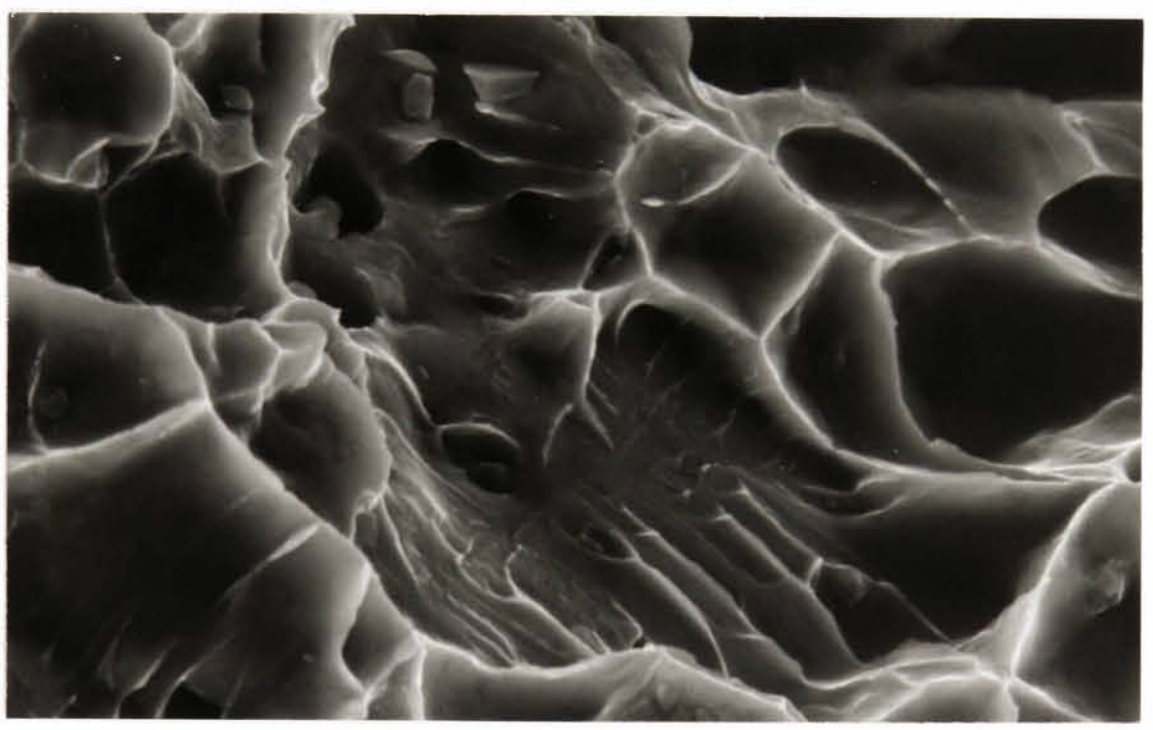

b) MMA weld (-70°C)

Figure 5.56 - Mixed-mode failure of ferrite, ductile failure of austenite (weld metals)

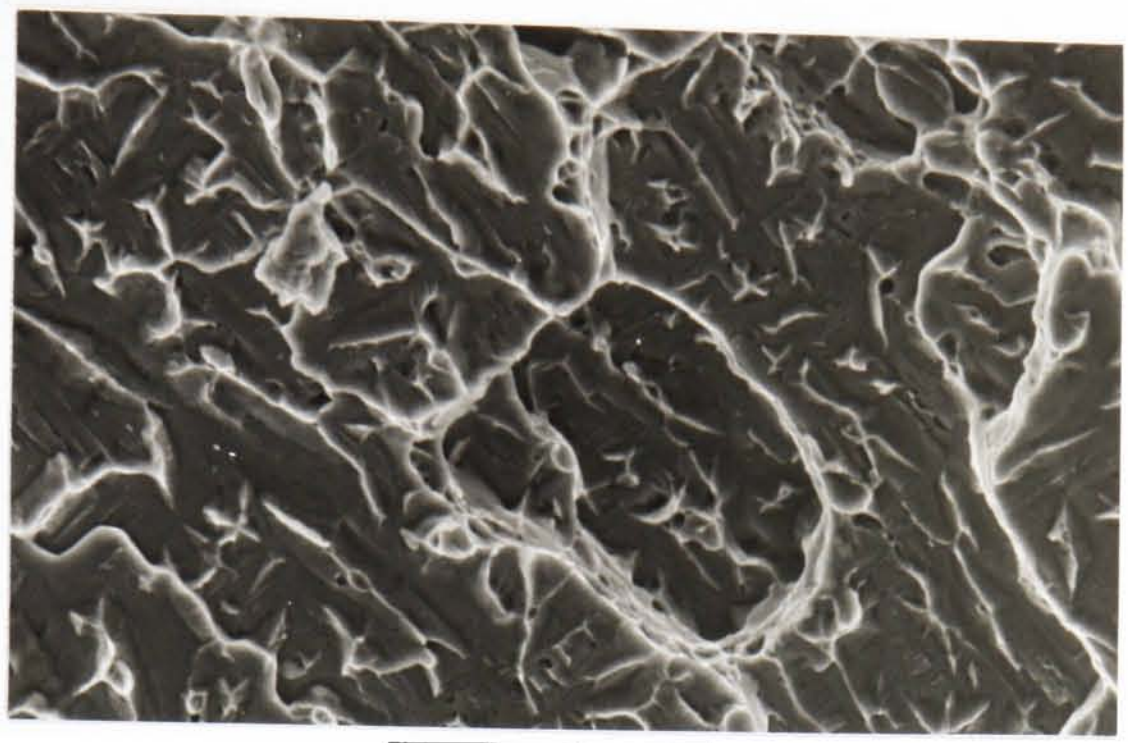

a) TIG weld (-150°C)

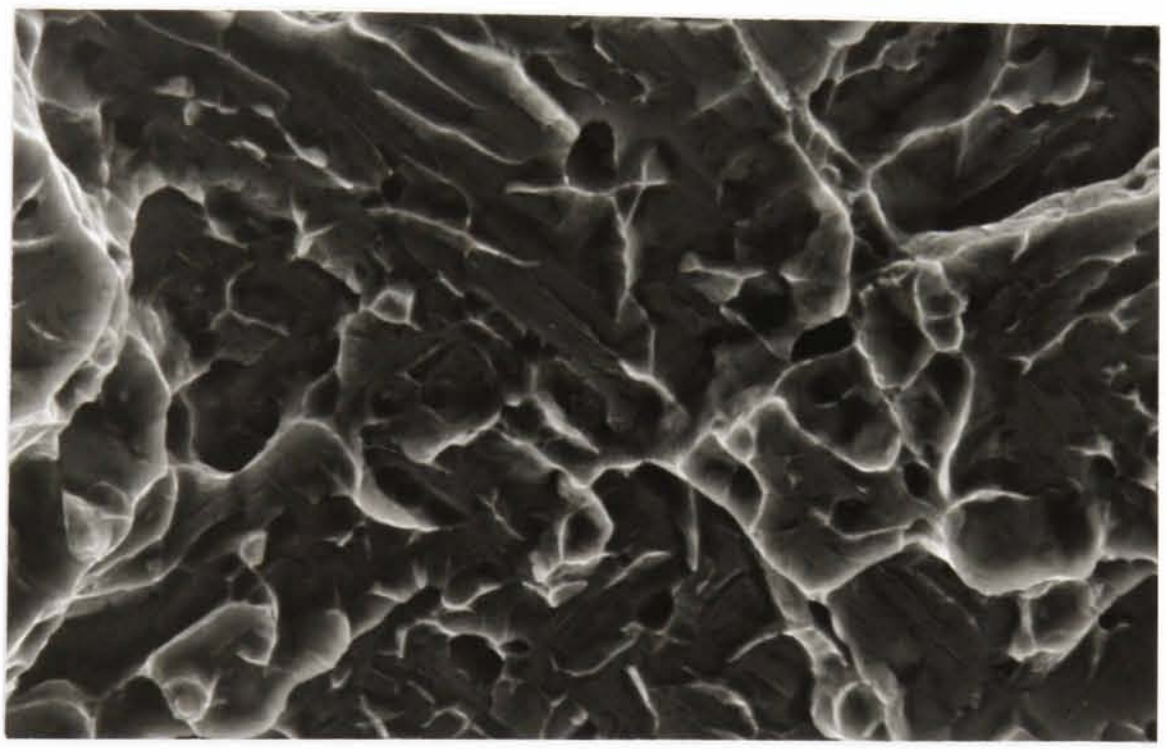

b) MMA weld (-150°C)
(note inclusion-initiated cleavage facet)

Figure 5.57 - Cleavage failure of ferrite, ductile failure of austenite (weld metals)

a) Area of pop-in (fatigue precrack on left)

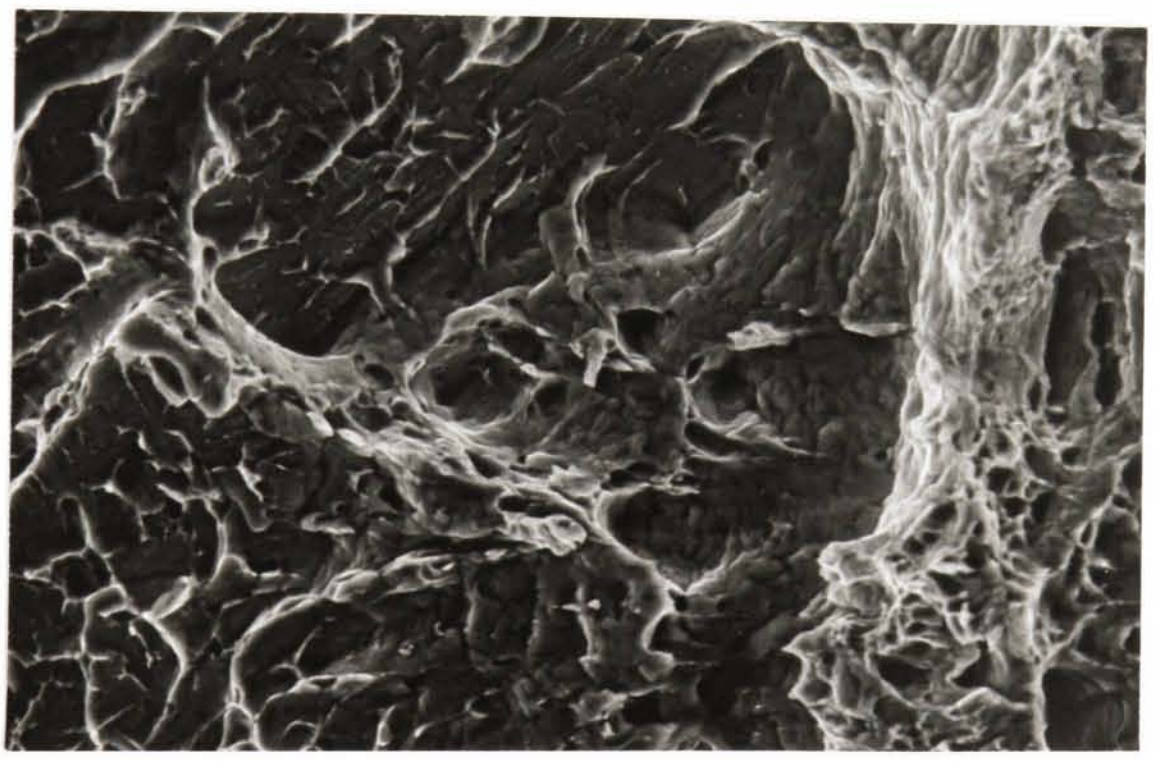

b) Arrest of brittle crack (cleaved pop-in on left)

Figure 5.58 - Pop-in failure of TIG specimen tested at a temperature of -50°C

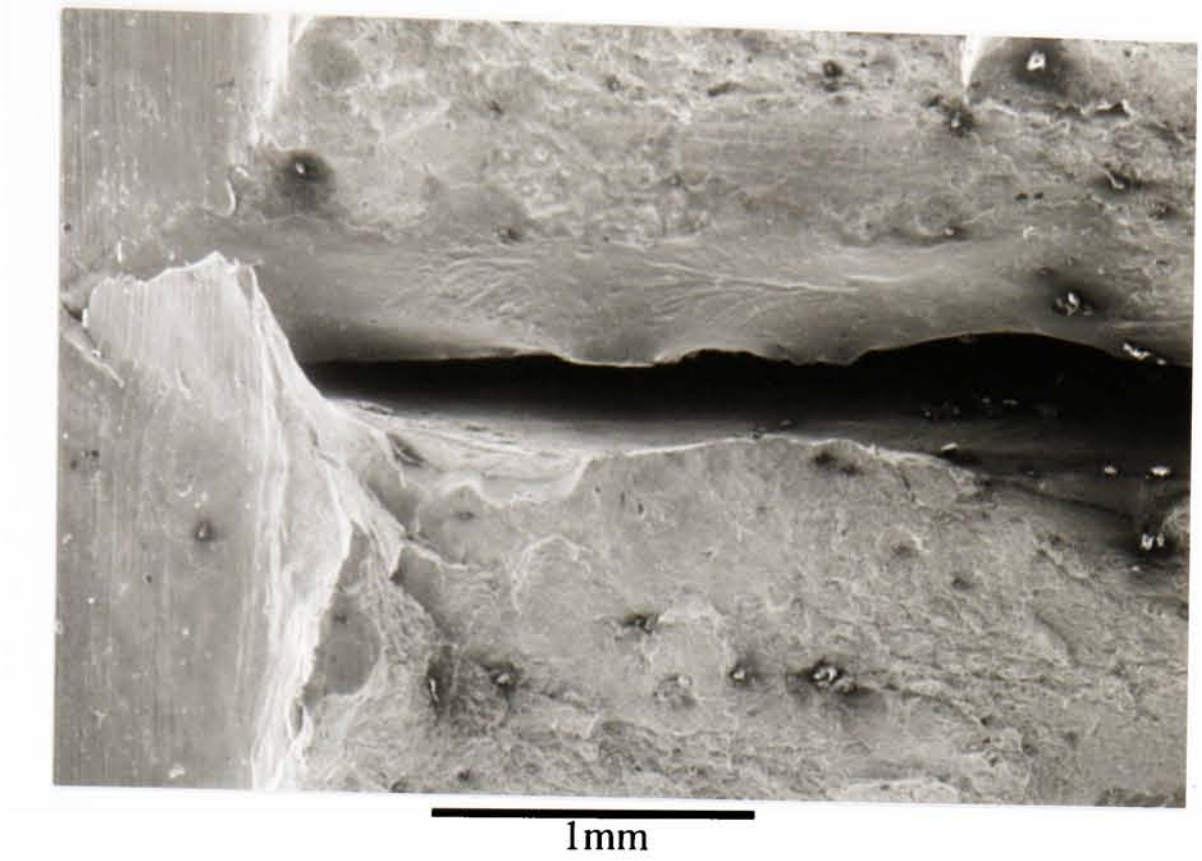

a) Crack formed at notch root (notch on left)

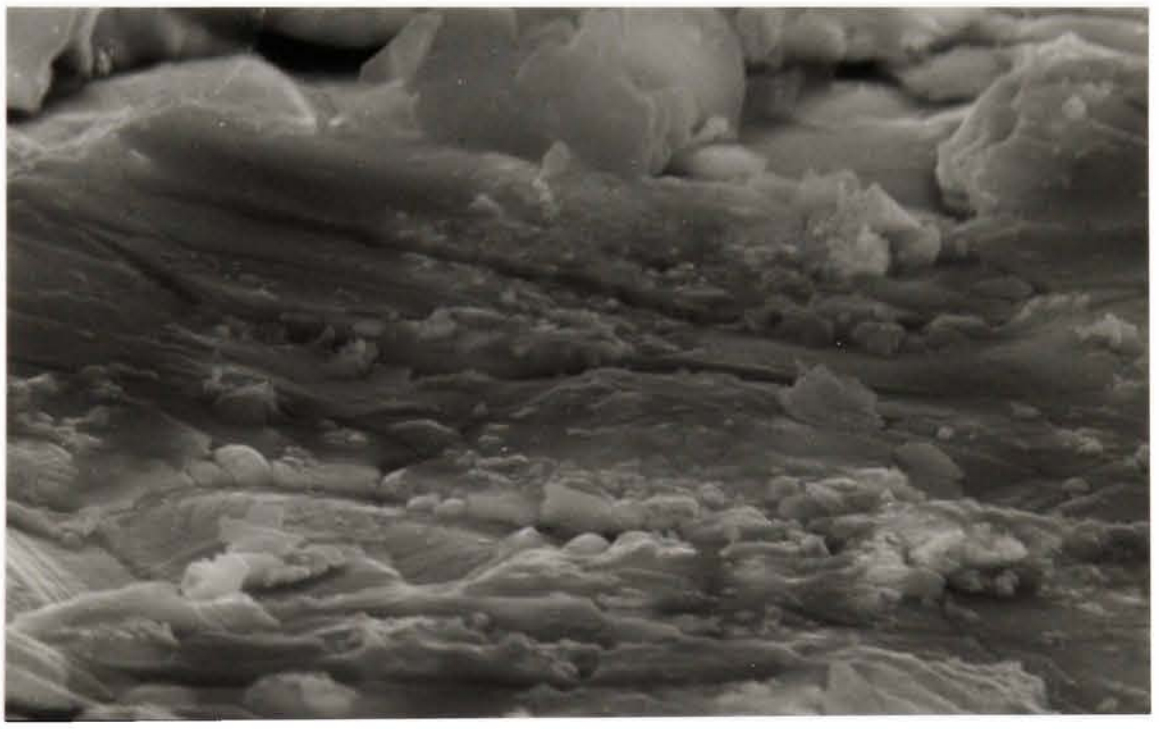

b) Crack surface

Figure 5.59 - Secondary crack formed in TIG Charpy specimen tested at a temperature of -100°C

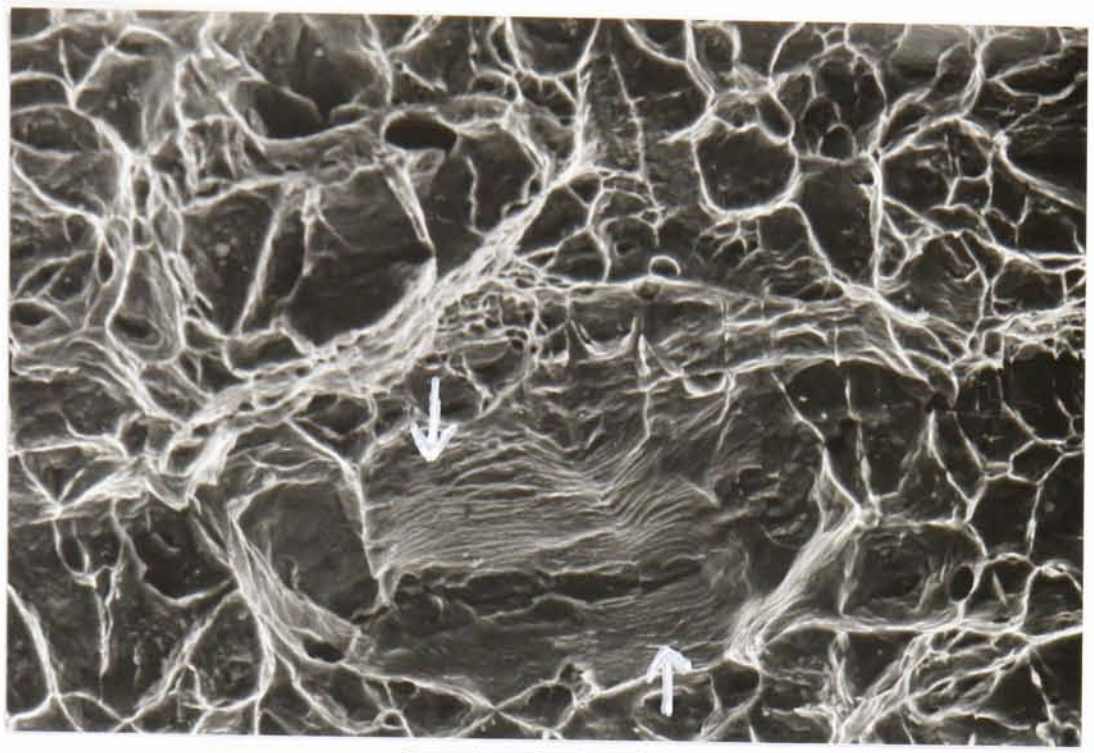

a) 5 minute anneal, showing areas of limited cleavage (arrowed)

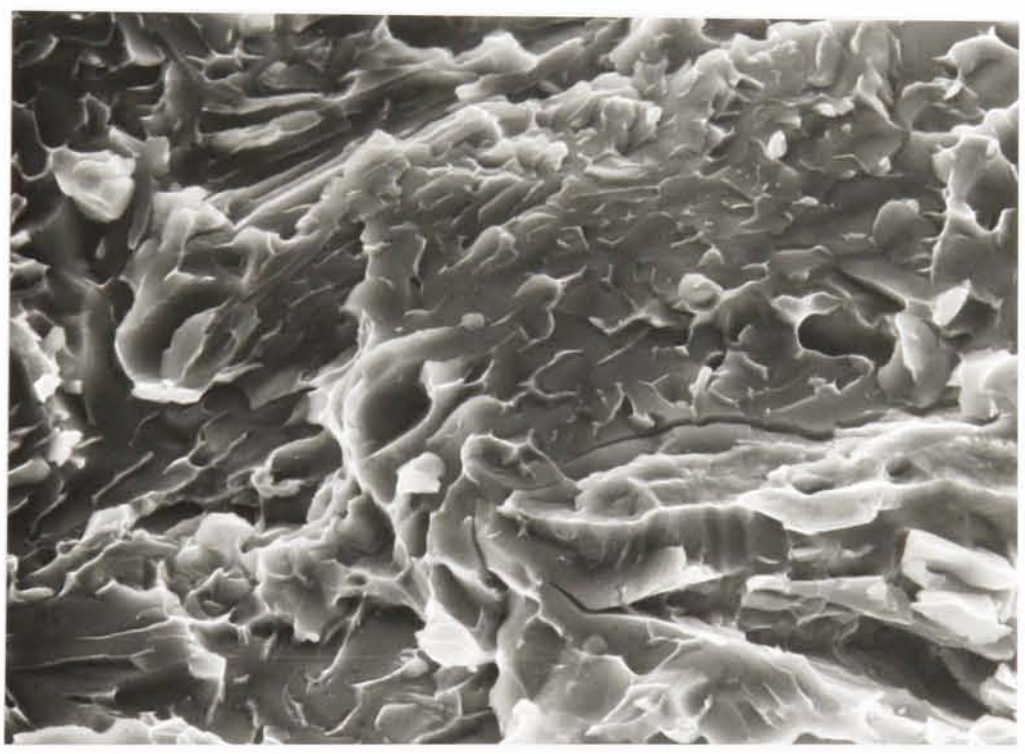

b) 45 minute anneal, showing total cleavage of fracture surface

Figure 5.60 - Fracture surfaces from tests at a temperature of -60°C of material annealed at a temperature of 850°C

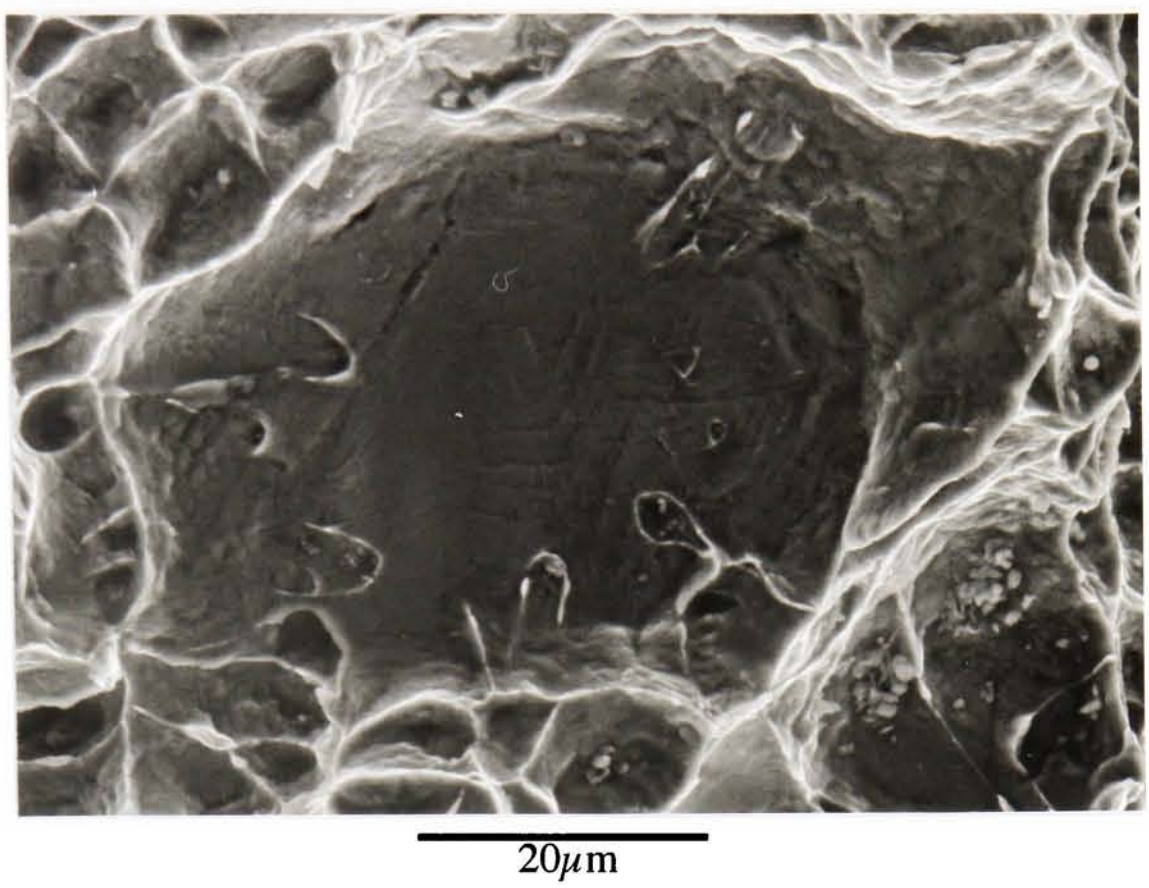

Figure 5.61 - Fracture surface from a room temperature test of material aged at a temperature of 425°C for 100 hours, showing limited ferrite cleavage

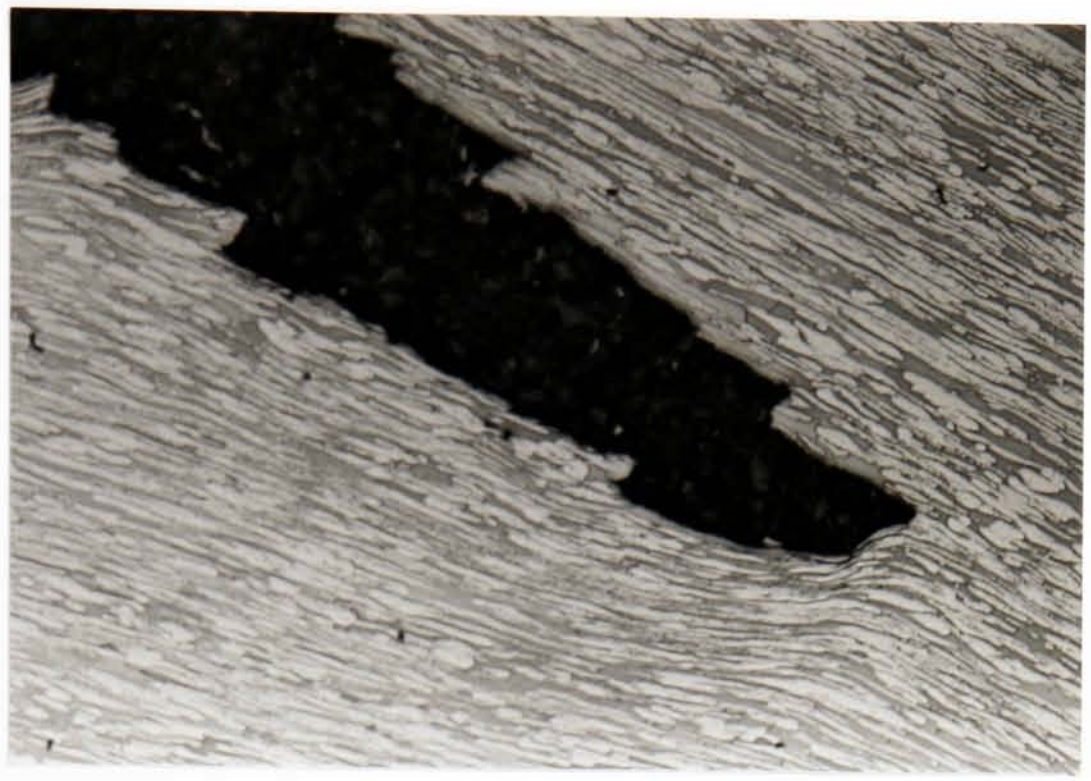

a) Transverse crack deviation along elongated grains

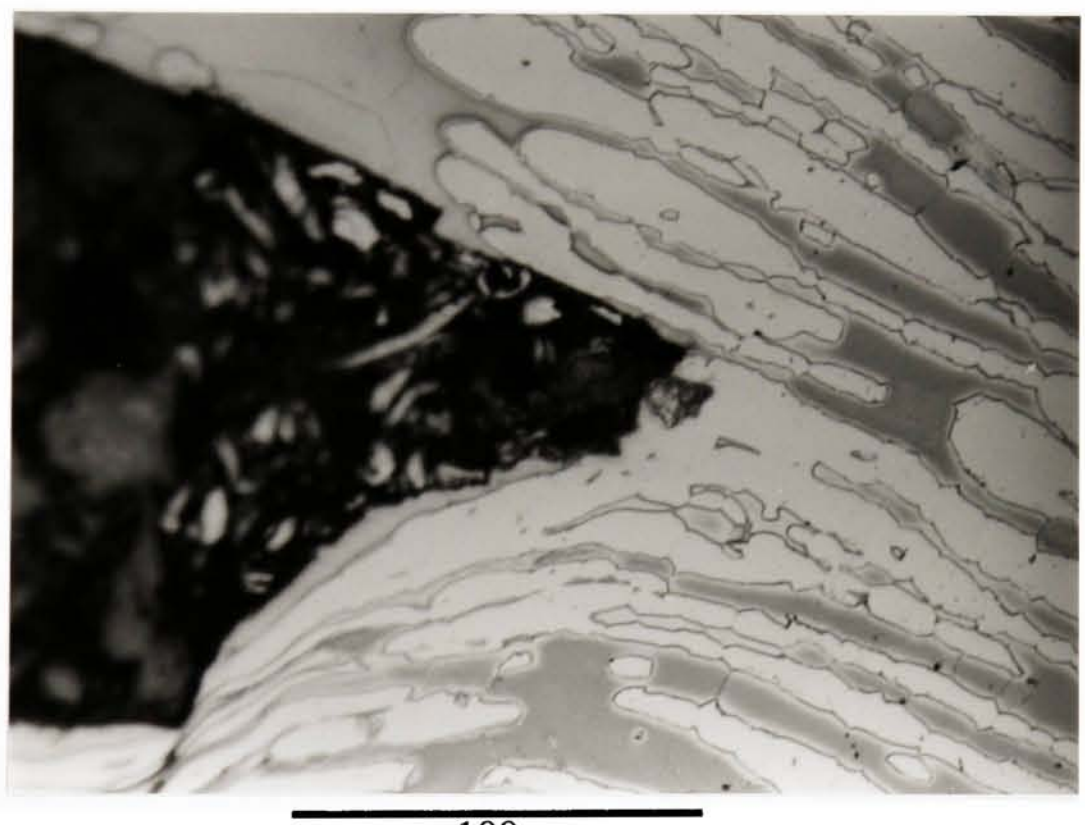

b) Crack tip, showing path preference for ferrite grains

Figure 5.62 - Crack advance in a specimen failing by plastic collapse (X-Z, -50°C)

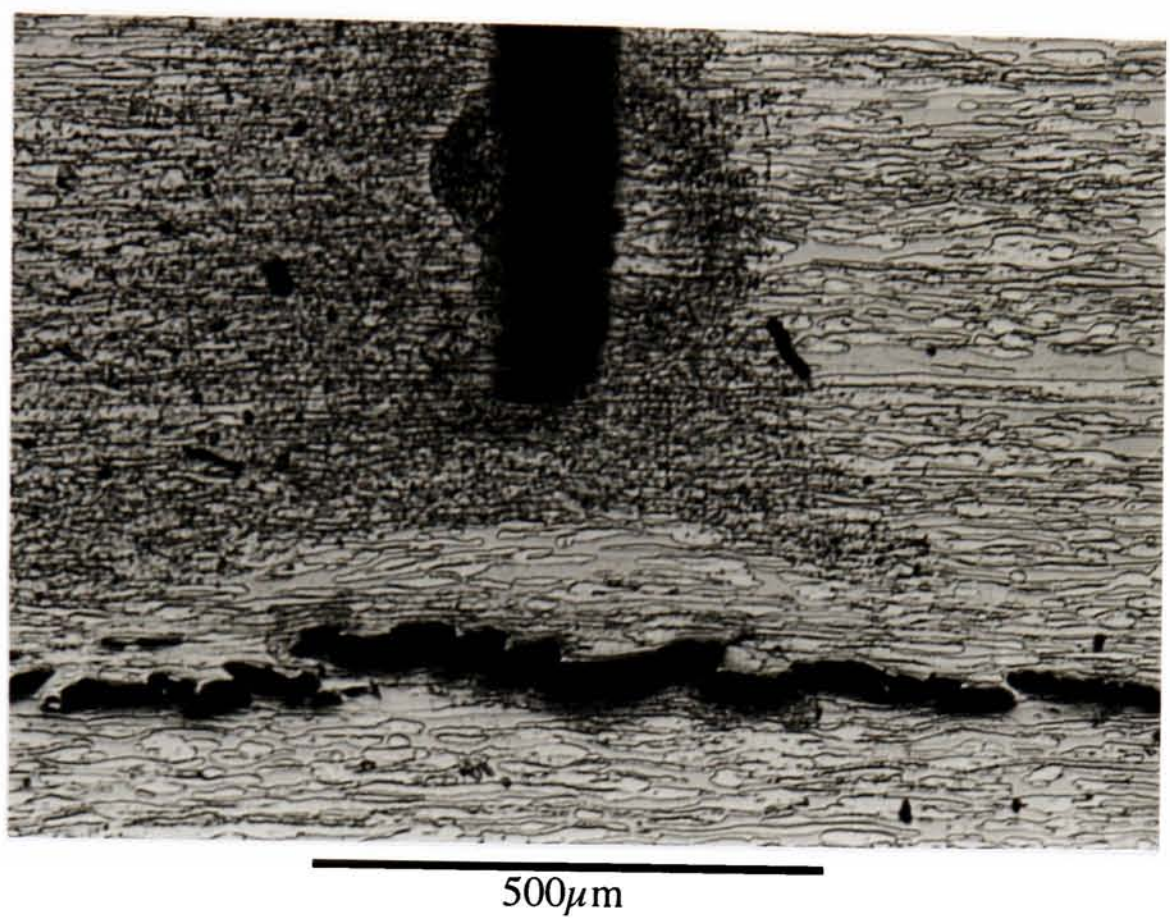

Figure 5.63 - Transverse crack ahead of fatigue precrack (X-Z, -110°C) (normal crack direction top to bottom)

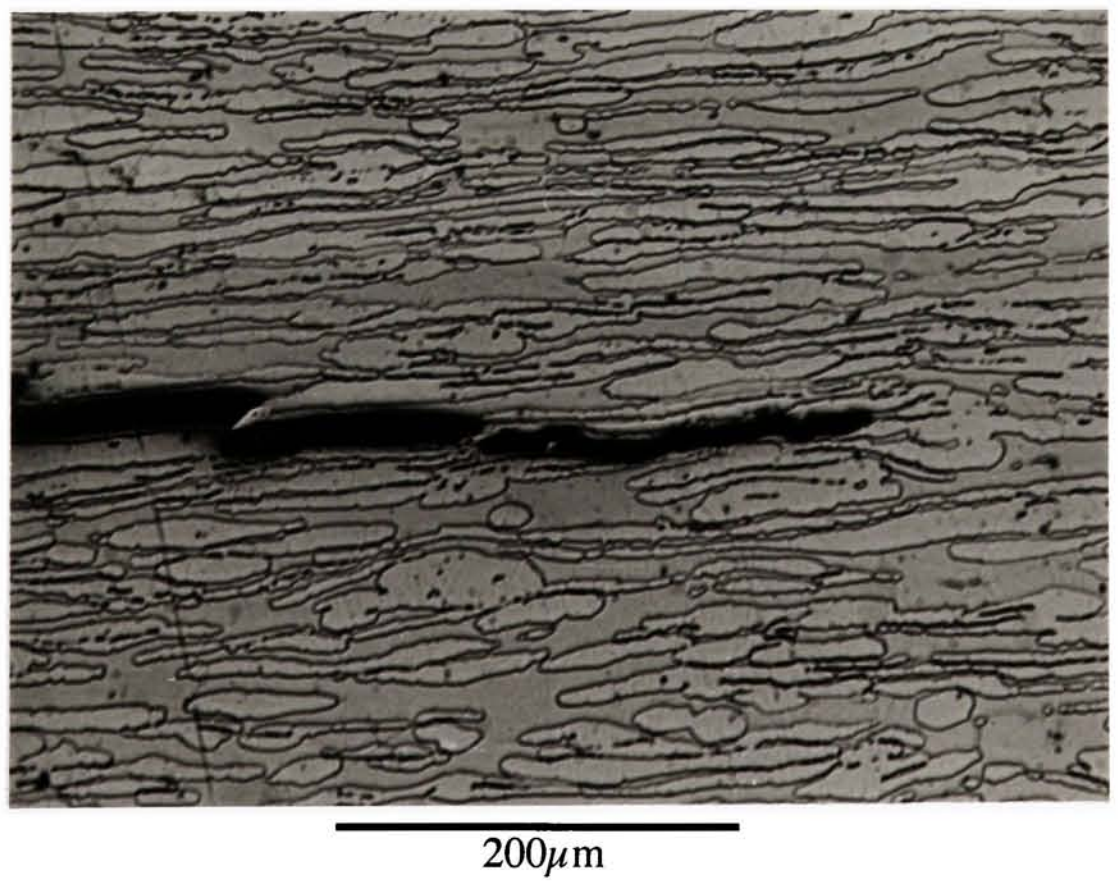

Figure 5.64 - Ferrite path preference of transverse crack (X-Z, -110°C)

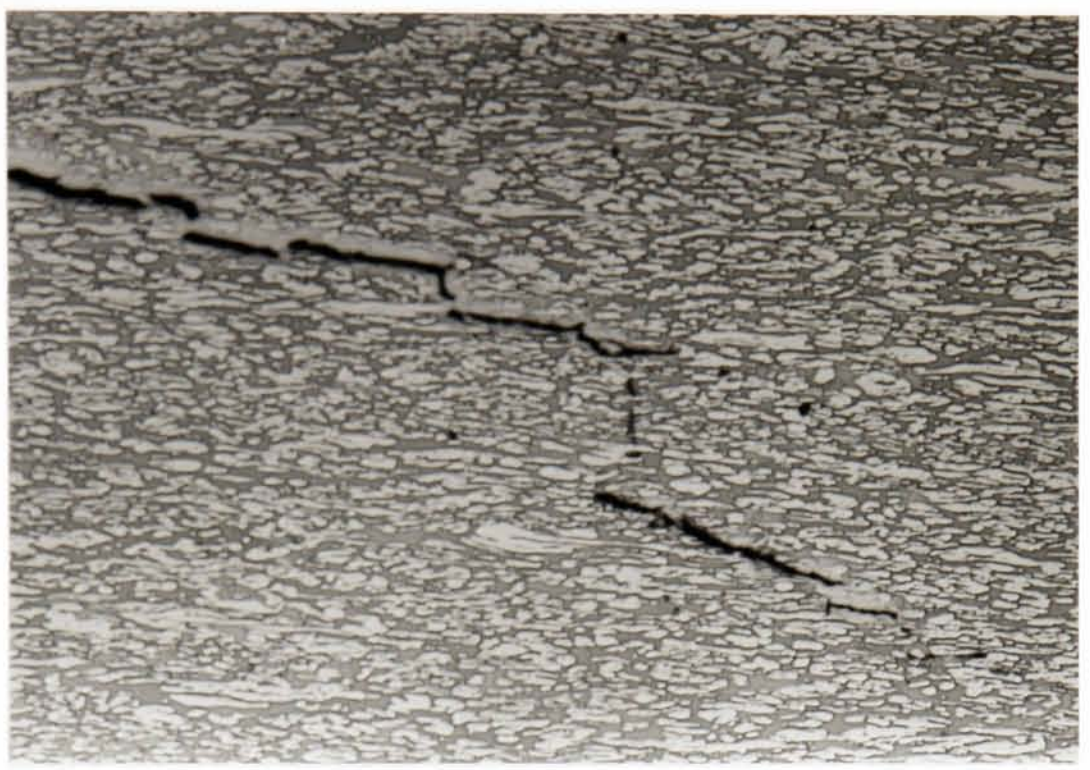

Figure 5.65 - Stepped transverse crack growth following bifurcation (X-Z -110°C) (normal crack direction top to botttom)

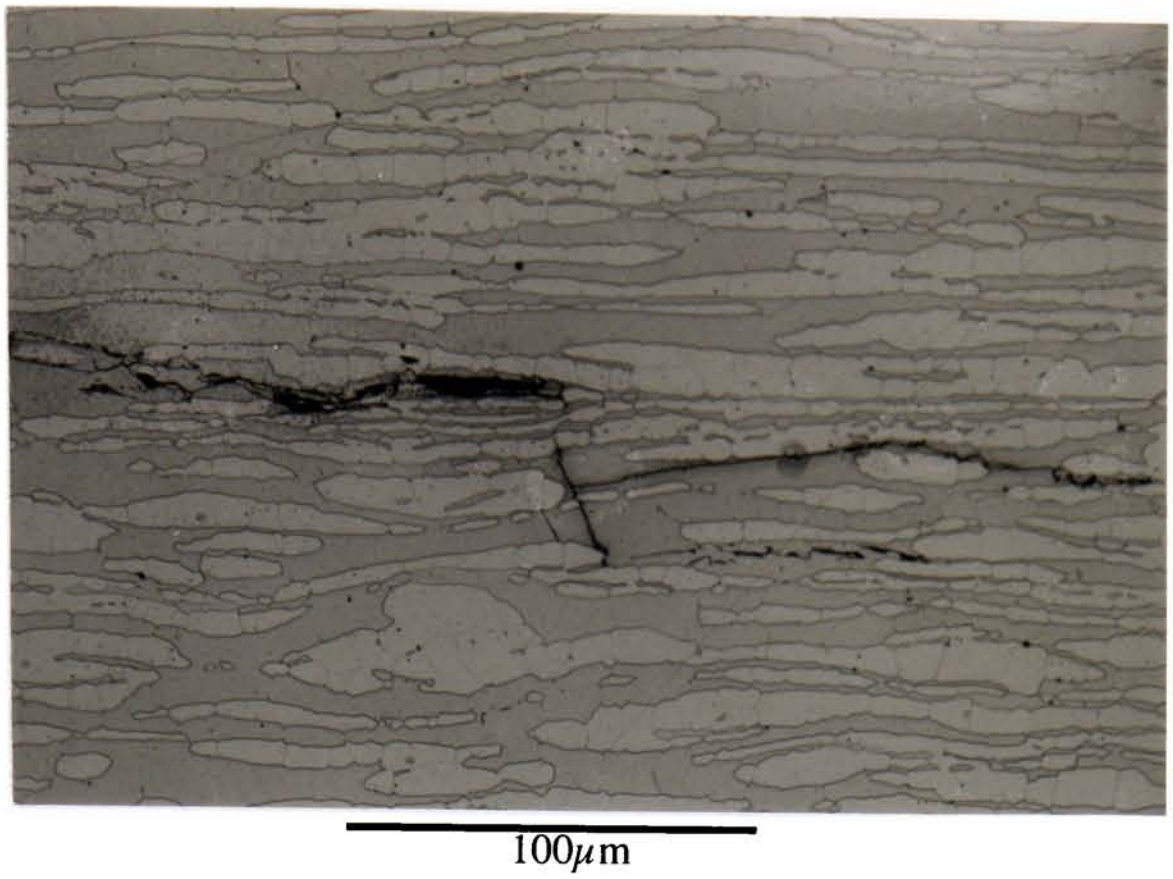

a) Test temperature -110°C

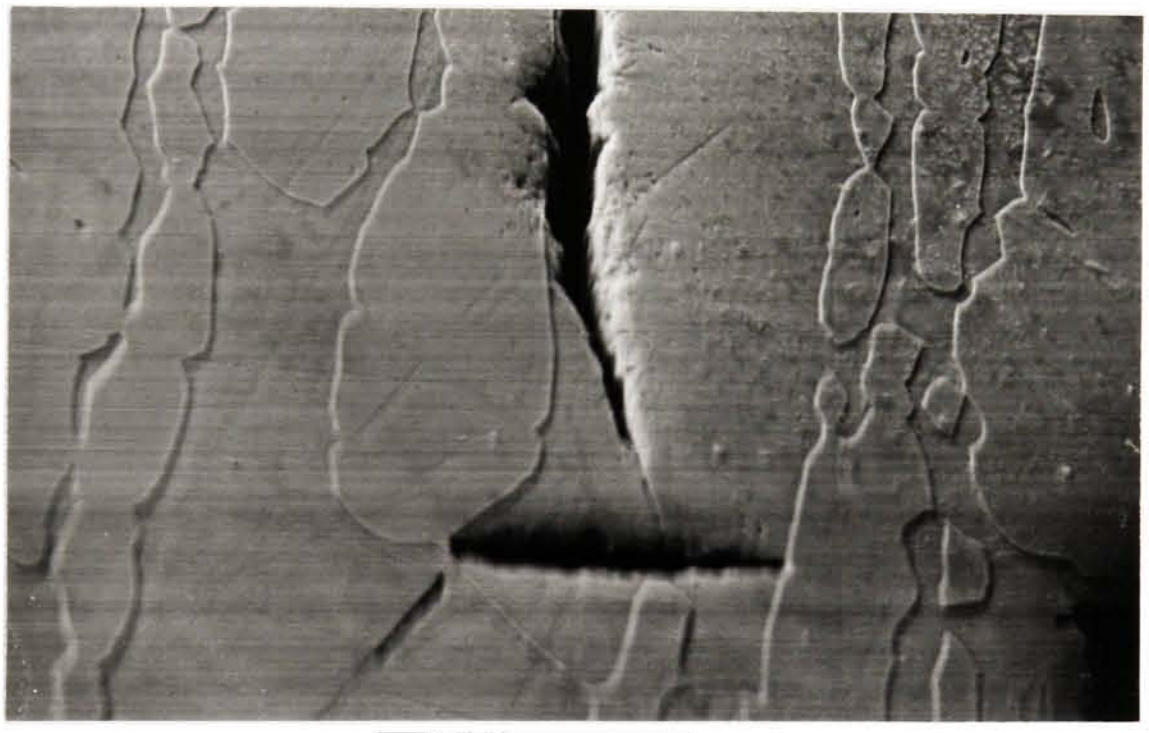

b) Test temperature -130°C

Figure 5.66 - Cracks showing path preference for ferrite grains (X-Z, -110°C)

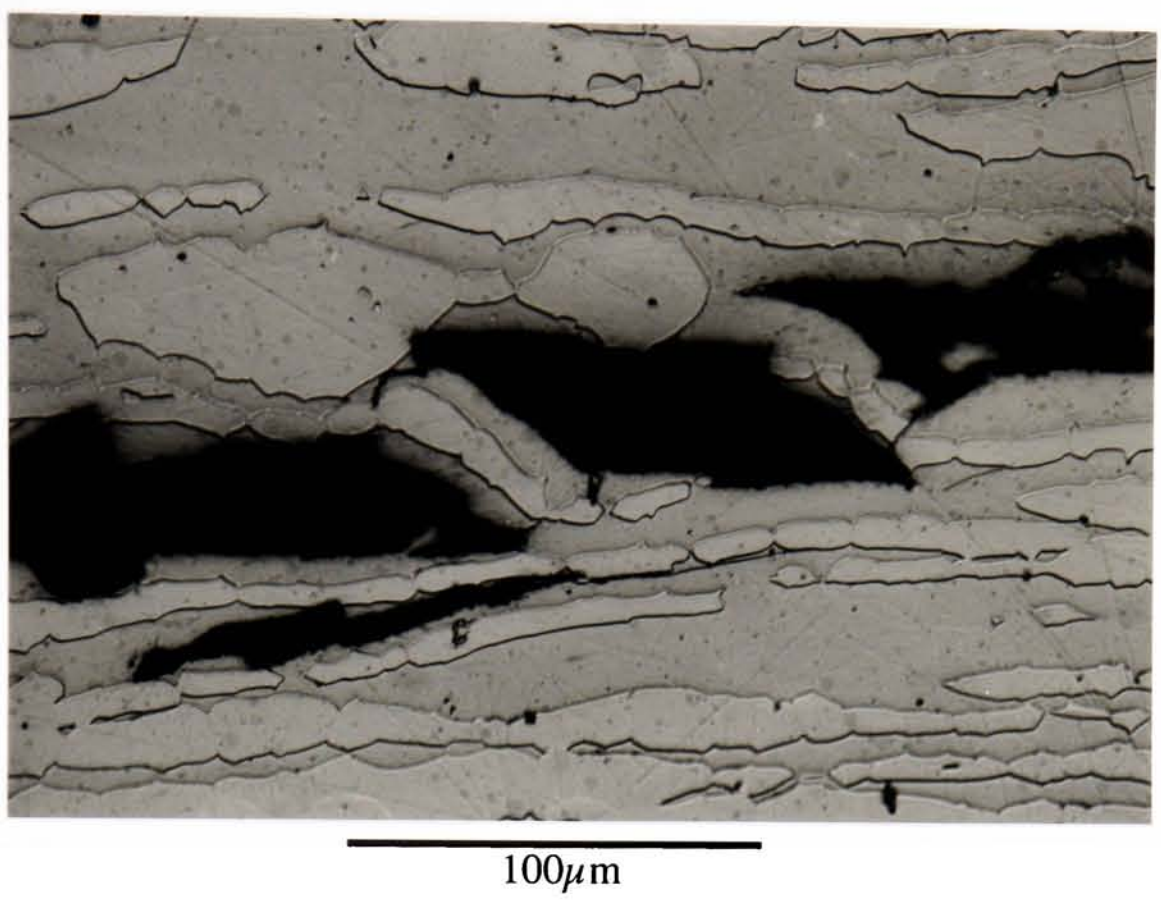

Figure 5.67 - Austenite colonies bridging ferrite crack (X-Z, -110°C)

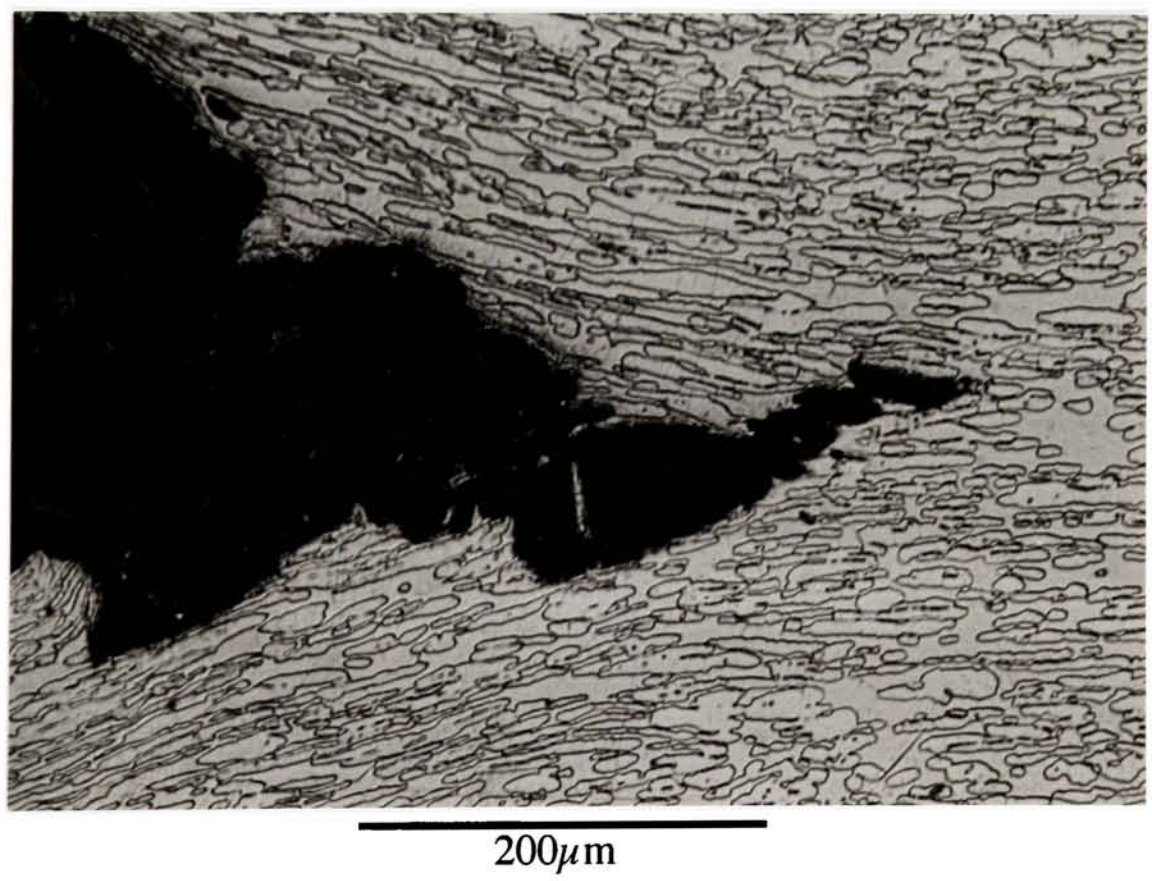

Figure 5.68 - Profile of secondary crack from X-Y orientated specimen (-150°C)

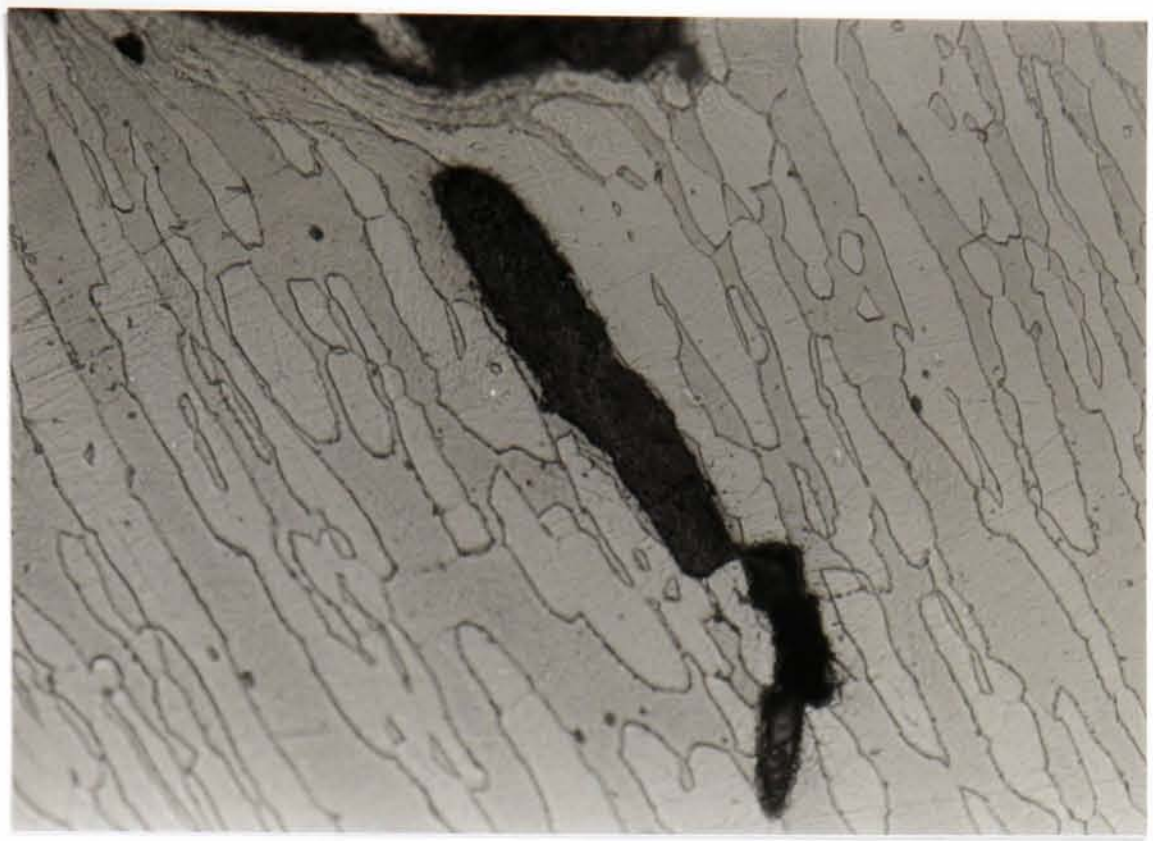

a) Test temperature -50°C

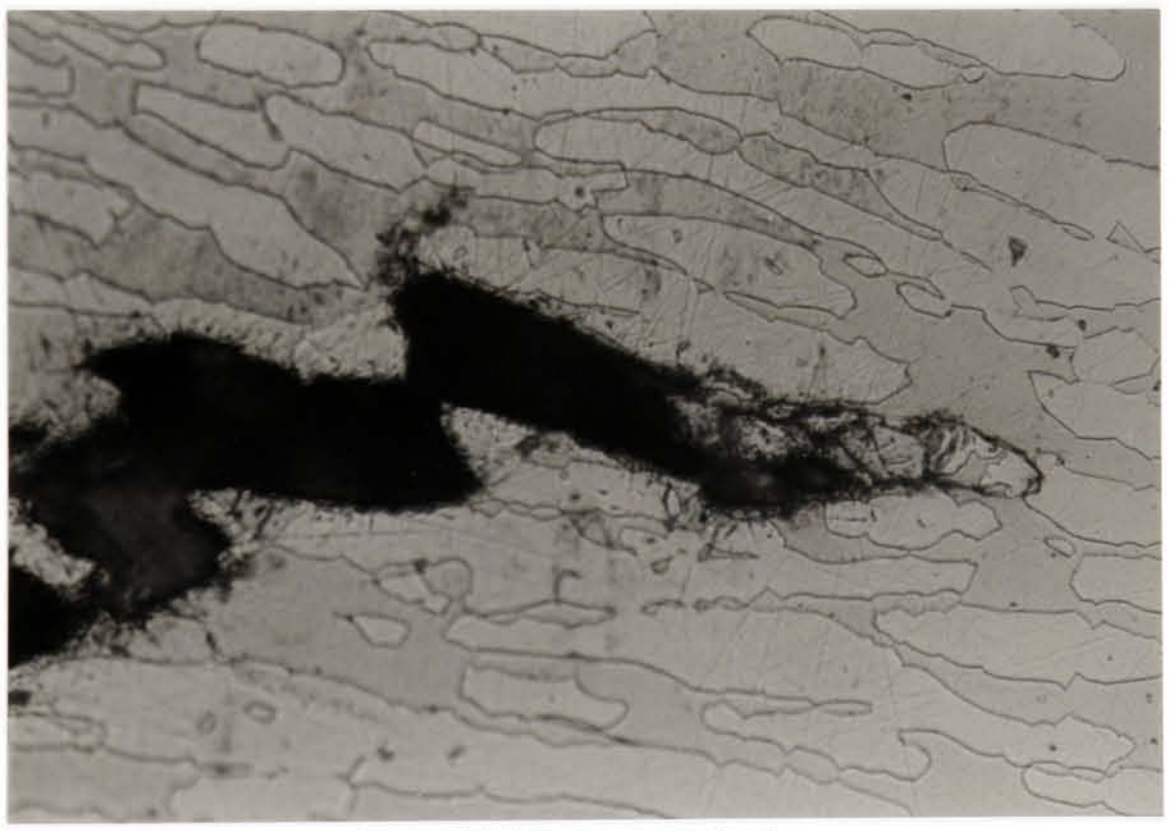

b)Test temperature -150°C

Figure 5.69 - Crack tips of splits from X-Y orientated specimens

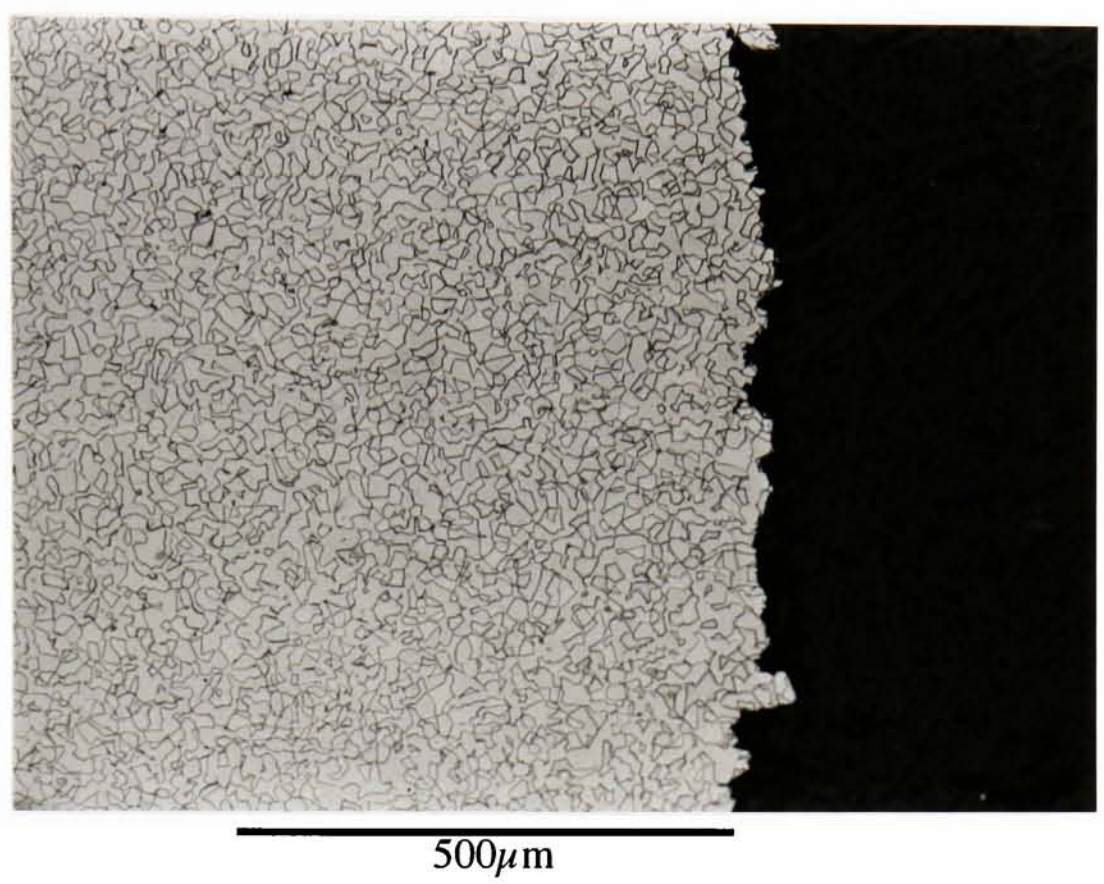

Figure 5.70 - Cross-section of HIP'd material fracture surface, showing crack deviation around austenite grains

a) Crack path following weld bead and (subsequently) HAZ interfaces

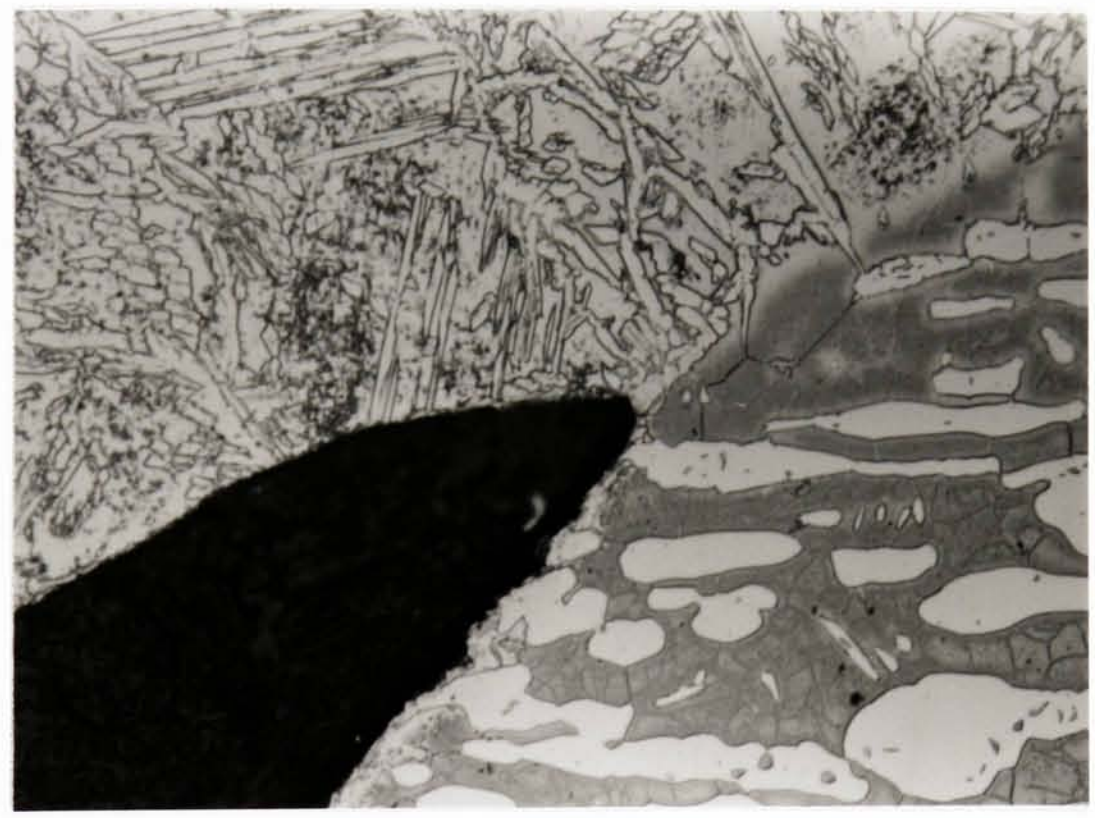

b) Crack tip at weld/HAZ interface

Figure 5.71 - Profile of a secondary crack in a Charpy tested TIG weld (-80°C)

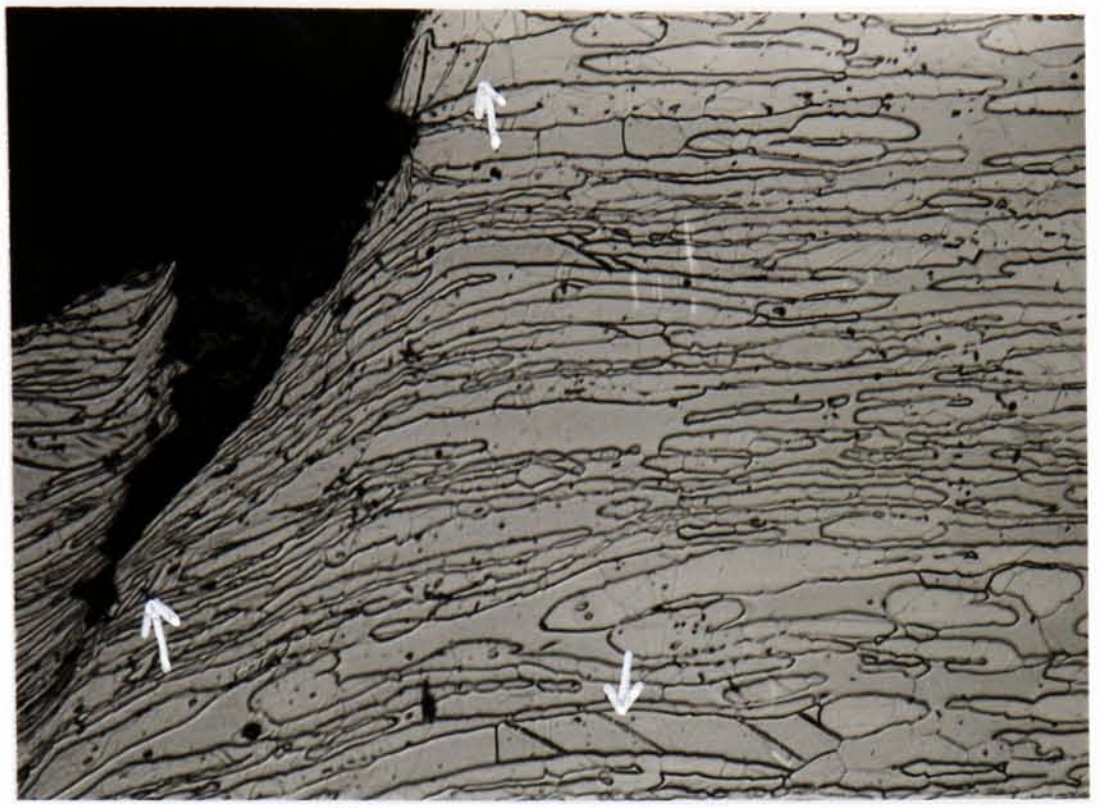

a) Section of fracture surface showing general planar defects (arrowed, notch tip on left)

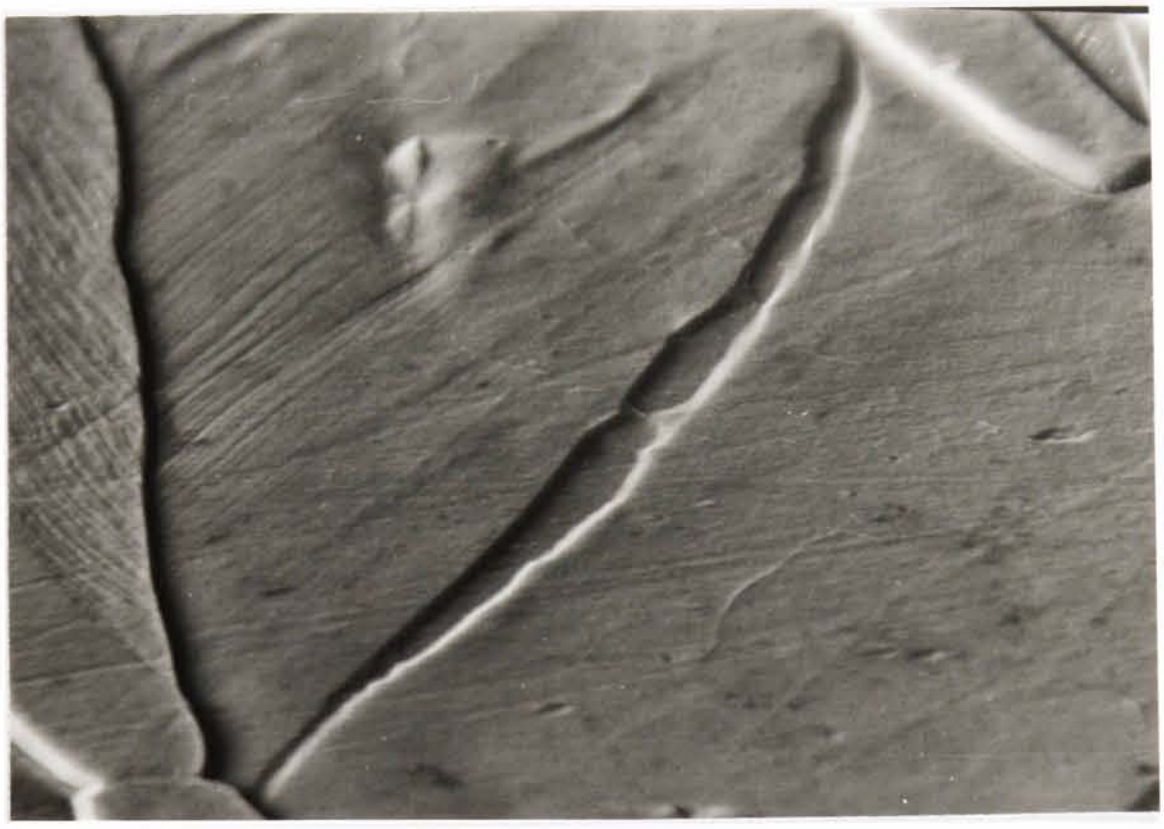

b) Planar defect subsequently identified as slip band by EBSP analysis

Figure 5.72 - Planar defects at a test temperature of -60°C

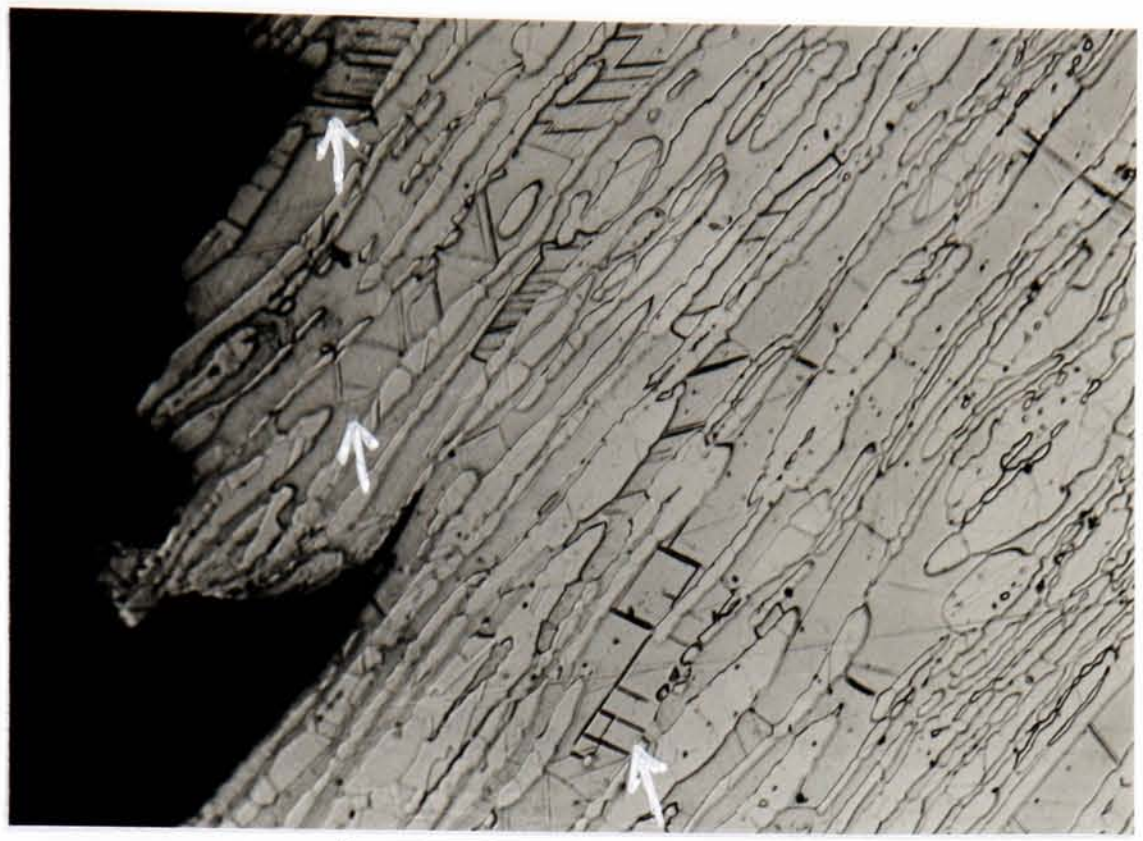

a) Section of fracture surface showing general planar defects (arrowed)

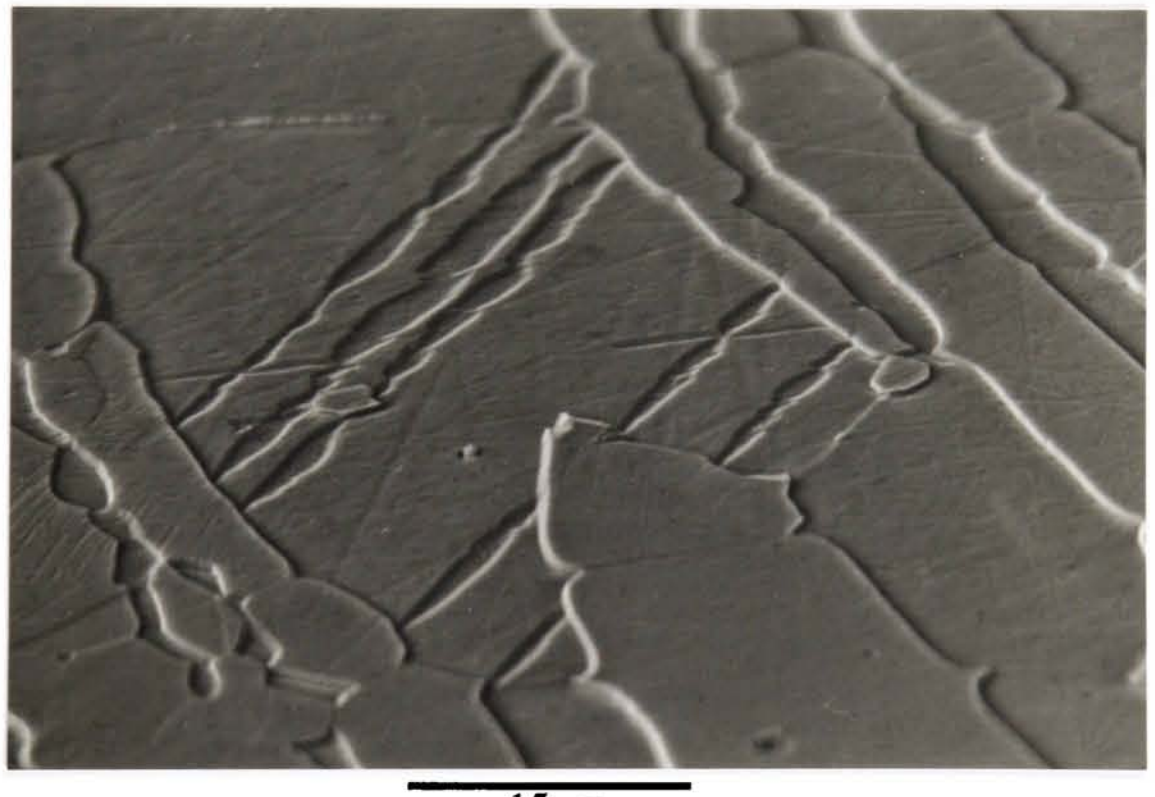

b) Planar defects subsequently identified as deformation twins by EBSP analysis

Figure 5.73 - Planar defects at a test temperature of -110°C

Figure 5.74 - Planar defects (arrowed) in ferrite phase below fracture surface of HIP'd material (X-Z, -80°C)

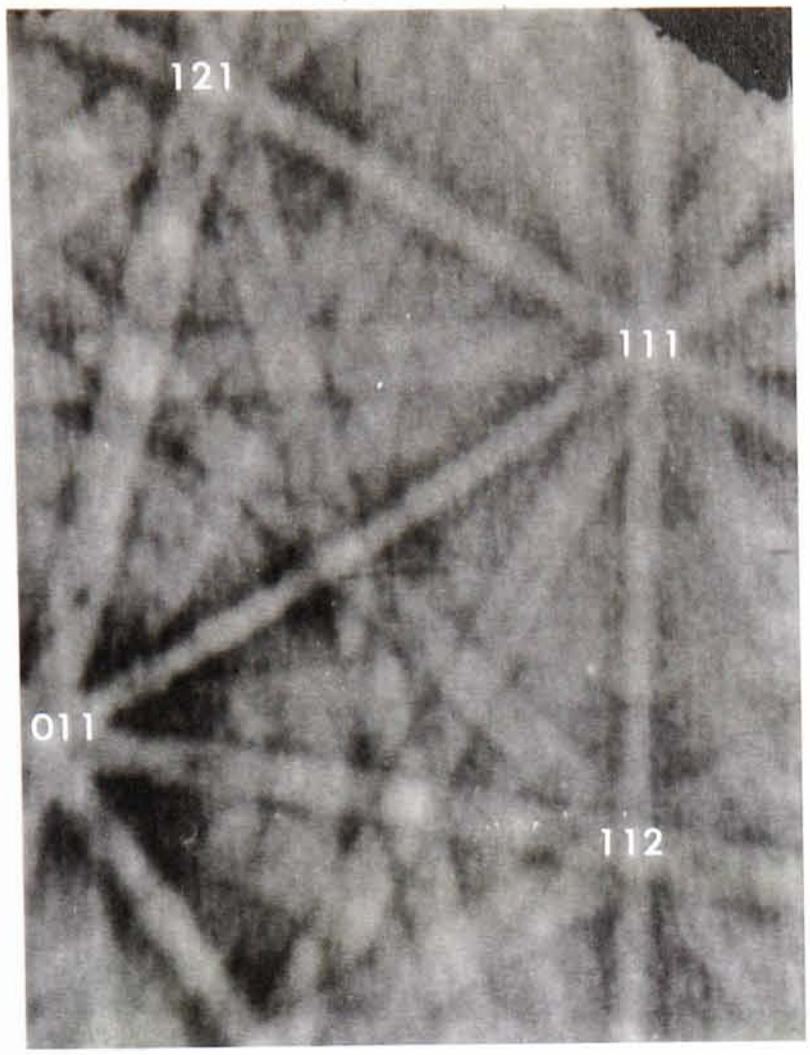

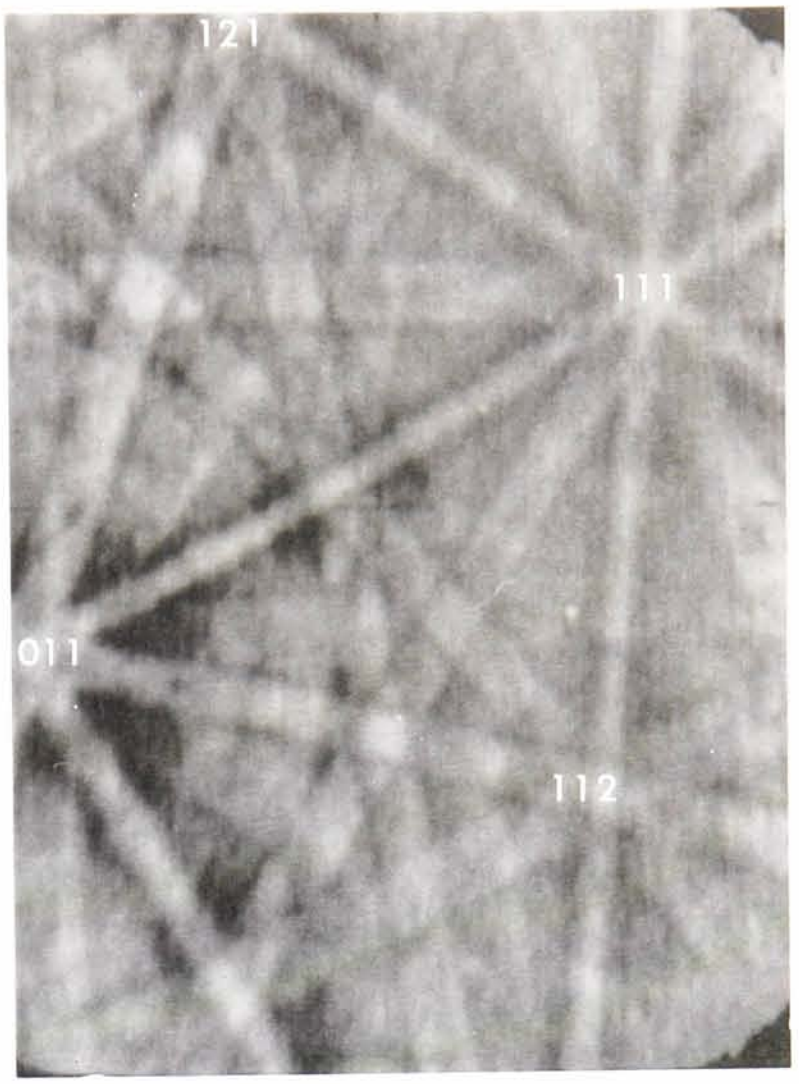

a) slip band misorientation

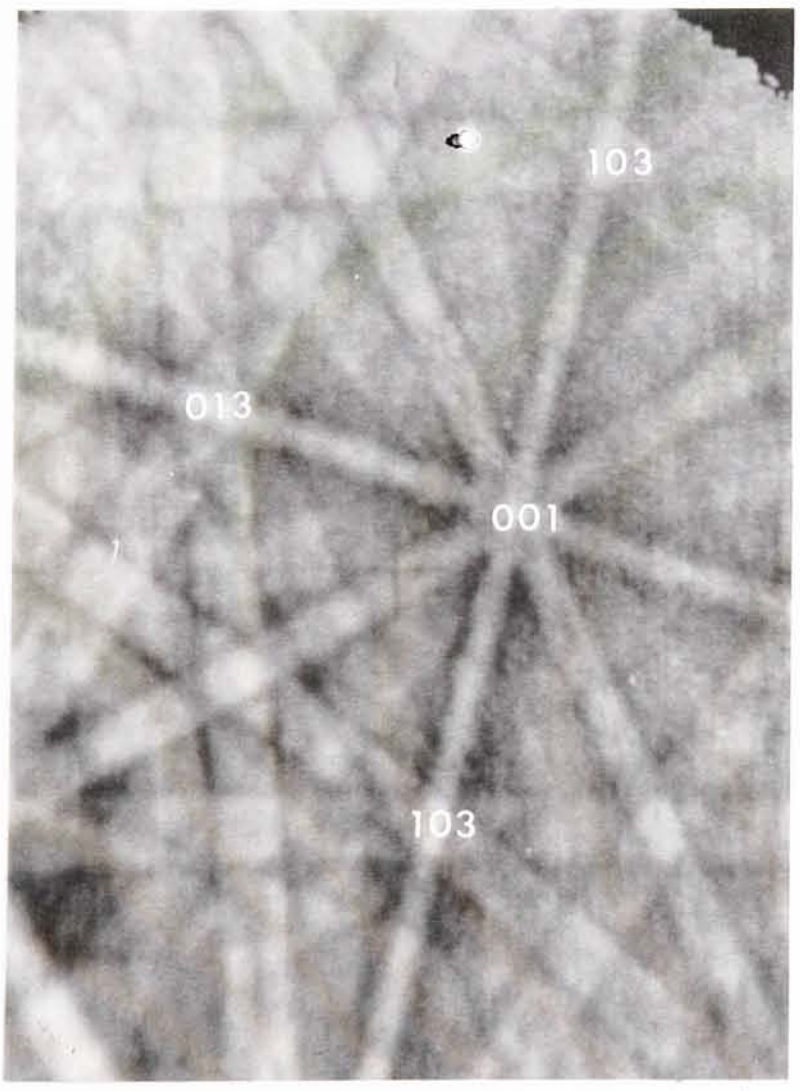

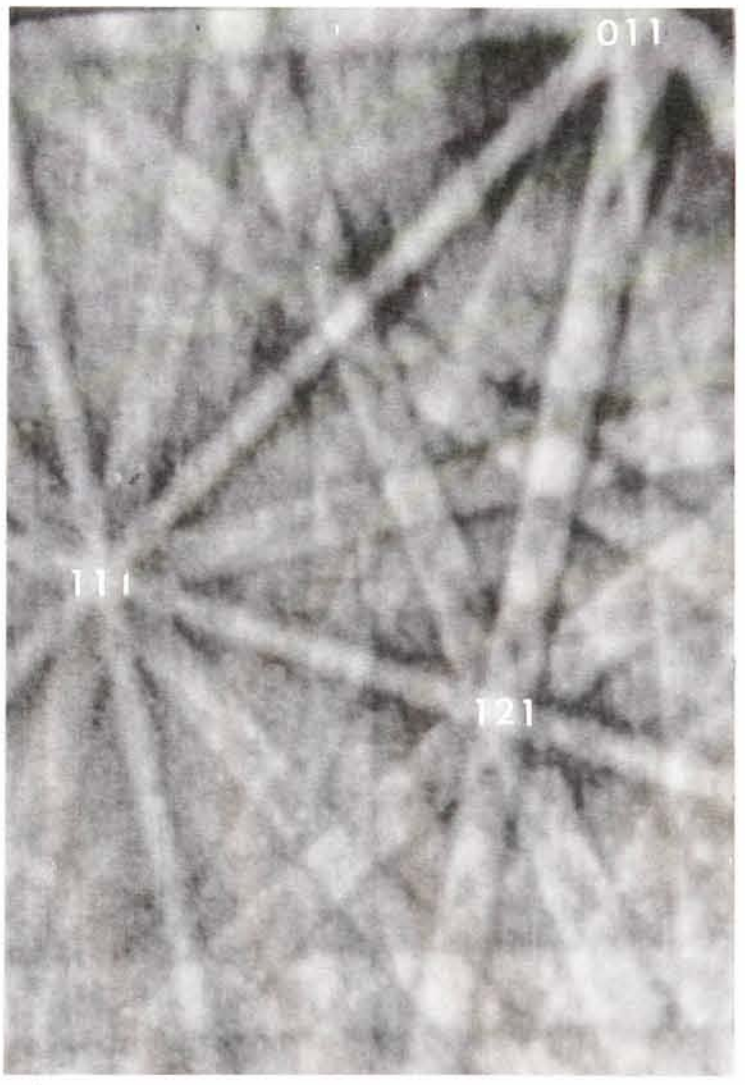

b) twin misorientation

Figure 5.75 - EBSP patterns recorded across planar defects

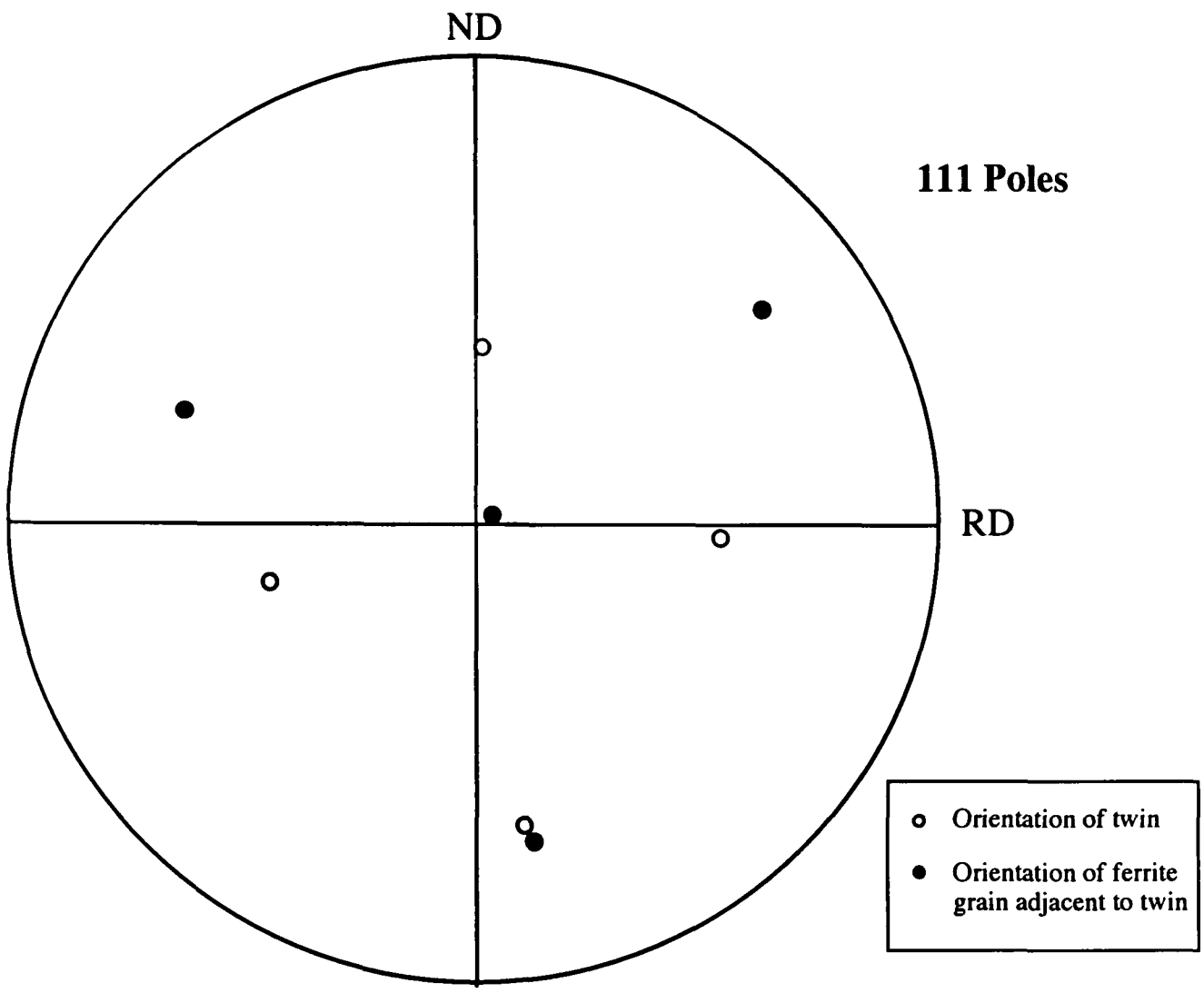

Misorientation across twin boundary is 60° about [1$\bar{1}\bar{1}$]

Figure 5.76 - Pole figure representation of misorientation across twin boundary from EBSP analysis

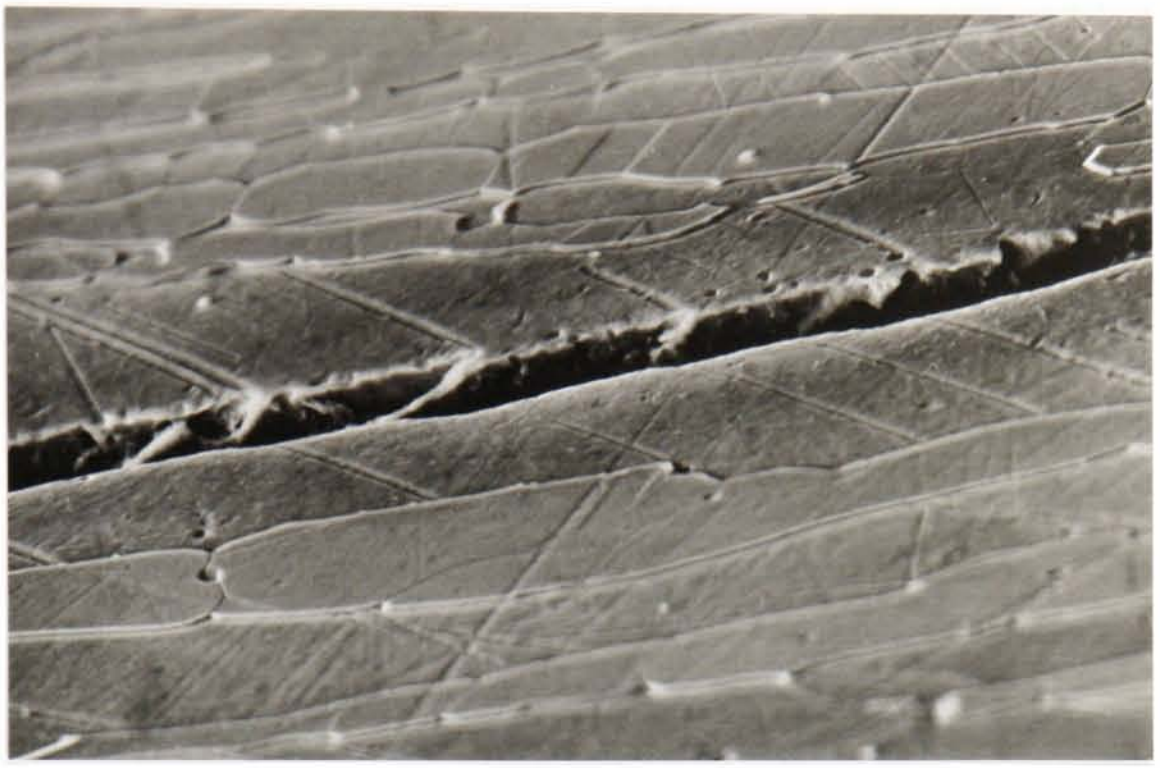

a) Rolled plate tested at a temperature of -110°C

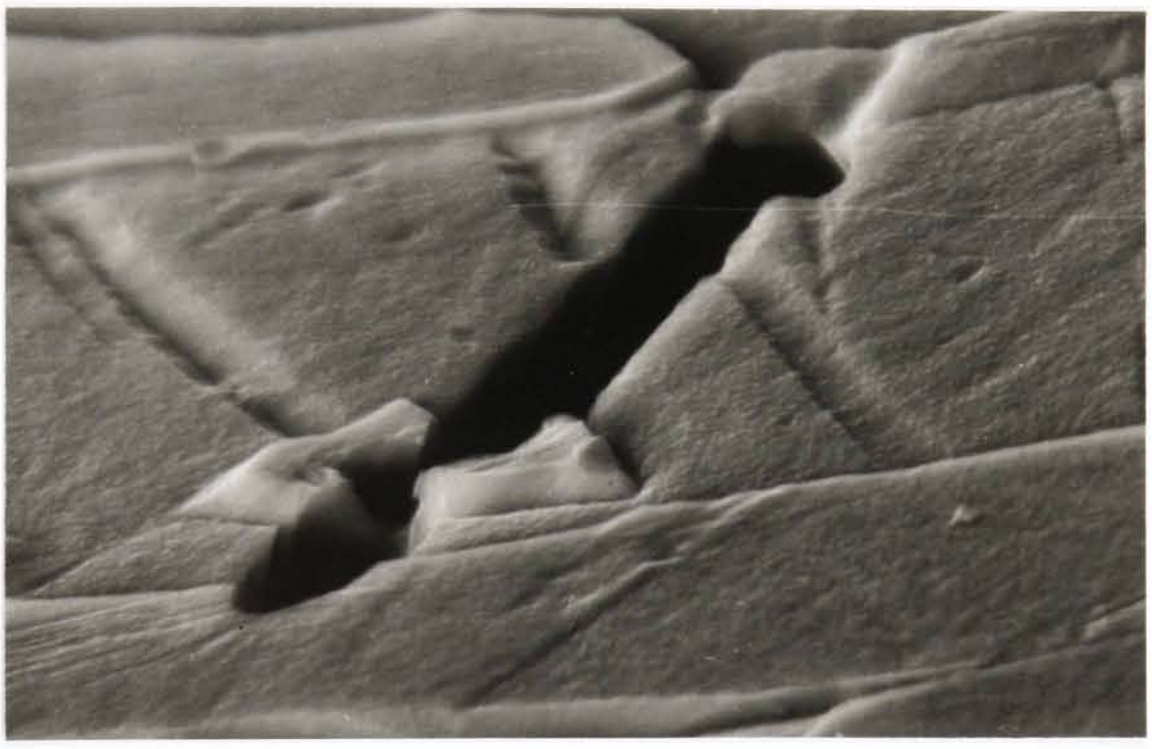

b) Rolled plate tested at a temperature of -130°C

Figure 5.77 - Twins bisecting ferrite microcracks

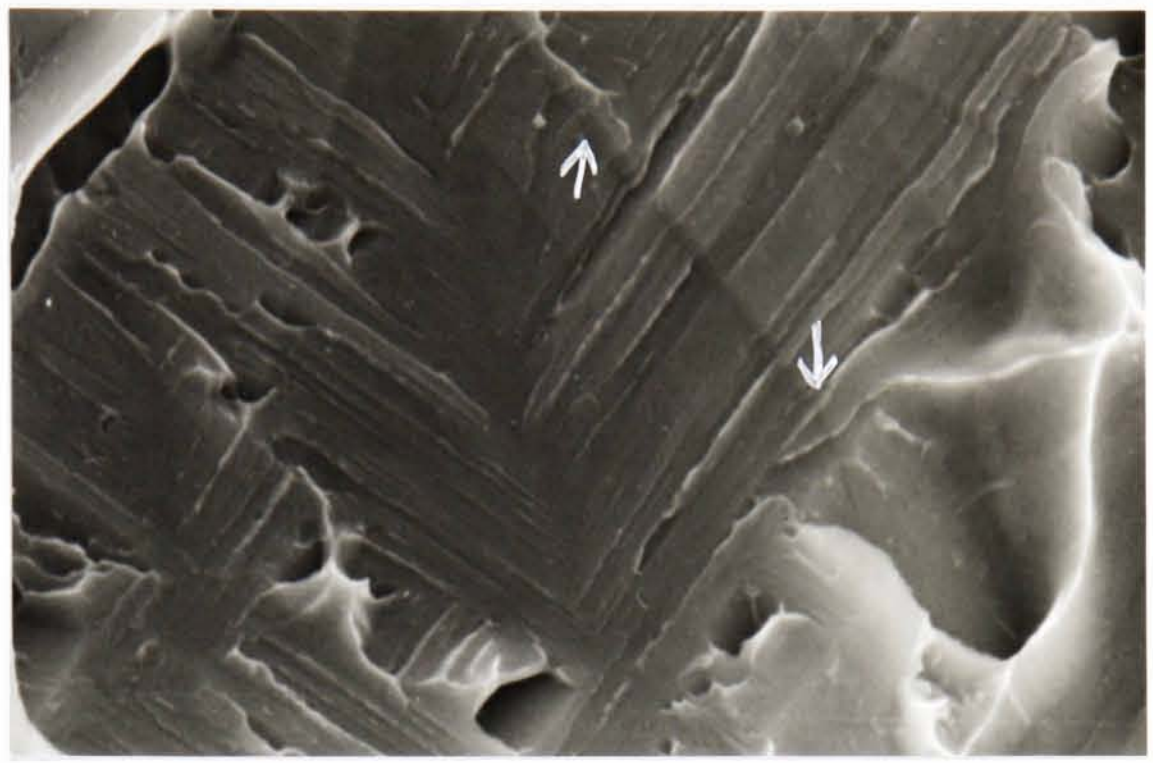

a) Rolled plate tested at a temperature of -110°C

b) Rolled plate tested at a temperature of -130°C

Figure 5.78 - Ferrite cleavage facets interrupted by twin boundaries (arrowed)

6 - DISCUSSION

6.1 FRACTURE BEHAVIOUR OF AS-RECEIVED PRODUCT FORMS

6.1.1 Crack Initiation

It has been seen that at test temperatures above -80°C, failure of the duplex stainless steel, Zeron 100 is characterised by highly ductile micromechanisms of sub-critical crack growth, followed by plastic collapse of the specimen (figure 5.39). Between test temperatures of -80 and -120°C, limited cleavage failure of the ferrite phase occurs, but microvoid coalescence is still the dominant failure mechanism (figure 5.40). However, as the test temperature is lowered below -100°C, the propensity for the ferrite phase to fail by cleavage increases (figure 5.41). At these low test temperatures, the austenite phase of course, still remains fully ductile.

No major differences in the fracture surfaces (for similar notch orientations and test temperatures) were observed between COD and Charpy tested specimens. In particular the micromechanisms of failure at specific test temperatures appeared to be identical. It is well known that the propensity for cleavage failure is increased by a high strain rate[1]. Therefore the ductile to brittle transition temperature of the Charpy test (which has a strain rate of approximately $1500s^{-1}$) would be expected be higher than that of COD test (which has a strain rate of approximately $0.0001s^{-1}$). However, the Charpy test employs a blunt notch whereas the COD test has a sharp fatigued precrack tip which generates a much higher maximum tensile stress ahead of the crack tip (which would in turn promote cleavage failure). Therefore for this material, the increase in strain rate from the COD to Charpy test appears to be almost exactly offset by the decrease in maximum tensile stress ahead of the notch. Note that no evidence could be found of martensitic transformations of the austenite phase, which had been observed by previous authors[2] to be triggered by the high strain rate of the Charpy test.

Where cleavage failure occurs, microcracks have been shown to form in the ferrite phase ahead of the crack tip (figure 5.66). It is presumed that these are non-critical as their propagation is prevented by neighbouring austenite grains (which remained fully ductile at all test temperatures). Deformation twins have also been observed adjacent to the fracture surface, both at the notch root and along the crack path (figures 5.72-5.74). Their density was much increased at test temperatures below -100°C. As expected, it was observed that more twins were produced in Charpy than COD test specimens, as their formation is favoured by a high strain rate. It is possible that these twins are nucleated by the high stress concentrations associated with cleavage failure and are not directly associated with the fracture process. However, some microcracks were observed to initiate from twin intersections (figure 5.77) as proposed in Hull's model of cleavage nucleation[3]. This, together with the absence of ferrite slip bands at low test temperatures suggests that these twins alone must be responsible for the nucleation of cleavage failure at low test temperatures in Zeron 100.

The test temperature for the onset of cleavage failure appeared to be similar for all product forms (-80°C). Therefore, it can be deduced that the ductile to brittle transition temperature was relatively independent of grain size, as the extruded powder material had a much finer microstructure than the other product forms. However, the twinning stress for ferritic steels has been shown to be decreased by increased levels of silicon[4]. The silicon content (shown in table 4.2) of the extruded ingot form (0.21wt.%) is half that of the extruded and HIP'd powder materials (0.4wt.%) suggesting that twin-nucleation and therefore cleavage could occur at higher test temperatures within the powder forms. Metallographic observations showed that the defect density was higher in these forms (figure 5.74) (although no detailed EBSP analysis could be undertaken to confirm this hypothesis as this equipment was only available for a limited period of time). No variation in transition temperature was detected between COD and Charpy tests, despite the greater density of twin defects in specimens from the latter test. Thus, the critical process for cleavage failure in these

materials appears to be the propagation of microcracks rather than their nucleation, in agreement with modern theories of cleavage fracture[5].

Previous observations made for aged duplex stainless steels[6] have found that the nucleation of microcracks is sensitive to the austenite crystallographic texture. Preferential nucleation was found to occur when the austenite grains were orientated close to the [011] pole. For the present study, it was also observed that the microcracks and twins were not homogeneously distributed through the ferrite phase, but tended to be grouped together in small clusters (figure 5.72). The austenite texture has been found to be virtually random for all product forms, thus assuming that fracture is indeed twin-nucleated, this supports the theory. However, no microtextural analysis was undertaken to confirm this type of relationship as it was considered beyond the scope of the present study.

6.1.2 Crack Propagation

It has been shown that both ductile and brittle cracks have a path preference for ferrite grains (figures 5.62-65). Indeed, it can often be seen within brittle cracks (which have grown a substantial length) that the crack tip runs close to the austenite/ferrite phase boundary (figure 5.66). However rather than following the actual phase interface, the crack is observed to run at a discrete distance from the boundary (~0.5-1μm). This suggests that preferential cracking is occurring in this 'near interfacial region'. Previous authors[7] have demonstrated the strong interaction between the crack tip and the interphase boundary, although in this instance the stress geometry was complicated because the cracks were produced in TEM thin foils. It has been shown[8,9] that cleavage is strongly promoted by both a prestrained microstructure and local residual stresses. Thus it is possible that residual stresses are present in this near interfacial region.

Residual stresses from the quenching process are thought to be present close to the interphase boundaries, due to the mismatch in thermal expansion coefficient and lattice parameter between the two phases. These stresses would alternate as compressive and tensile types across each interphase boundary, thus throughout the microstructure they would sum to no overall stress. Therefore, the blind hole drilling technique, which has a poor resolution, would fail to detect such stresses. It is thought that the residual stresses which were detected using this technique (table 5.4, figure 5.5) were macro-elastic stresses from the bulk of the quenched structure. Note that when the material is deformed, such interfacial stresses would be increased due to the higher yield stress of the ferrite phase and constraint across the interphase boundary.

TEM analysis of the near-interfacial microstructure failed to provide evidence of an area of high dislocation density within the ferrite phase (figure 5.4). This was possibly due to dislocation recovery during preparation of the thin foil. Thus the original dislocation structure was deduced by an ageing treatment at a temperature of 550°C for 5 hours. This promoted the formation of α'/nitride particles which are known to preferentially nucleate upon dislocation arrays, thus revealing the original substructure. The heat treatment revealed a band of precipitates adjacent to the interphase boundary (figure 5.15) which were largest at a distance of 0.2-1μm from the interface (figure 5.16). This suggested that preferential nucleation of these phases was occurring within this region. A parallel project[10] revealed that bands of R-phase precipitates were formed close to the interface upon further (20 hours) ageing (figure 5.16). These observations suggested that a near-interfacial band at a distance of up to 1μm from the interphase boundary contained a much higher dislocation density than the remainder of the ferrite phase, thus confirming the presence of residual stresses within the near-interfacial region. However, to fully characterise these stresses, it would be necessary to use X-ray diffraction or small-angle neutron scattering (SANS) techniques.

6.1.3 Crack Growth of Rolled Plate Material

Brittle fracture of the specimen occurred only at lower (<-80°C) test temperatures where the ferrite phase cleaved. At higher test temperatures, the ductile nature of both phases ensured that specimens failed by general plastic collapse with little crack extension (figure 5.42a).

The nature of crack propagation throughout the as-received materials was found to be highly anisotropic (figure 5.42). This was thought to be due to the crack path preference for ferrite grains. As ferrite is the matrix phase, the crack can often travel uninterrupted throughout these grains without intersecting the ductile austenite islands. However, the rolled plate material contained a microstructure highly elongated along the rolling direction (figure 5.1a), thus disrupting crack growth along the normal/transverse axes. This, coupled with the strong {001}<110> texture of the ferrite phase (which ensures that the {100} bcc cleavage planes are coincident with the rolling plane) provides an easy, uninterrupted crack path along the rolling plane. The effect of this texture is clearly demonstrated in figure 5.66a, where across the picture width, which incorporates many ferrite grains, the only cleavage cracks present are orthogonal to (which are subsequently arrested by the ductile austenite grains) or along the rolling direction (left to right). Therefore for notch orientations that are perpendicular to the elongated grains, there is a propensity for transverse crack growth to occur due to the uninterrupted cleavage path along the rolling plane. Note that the degree of transverse crack growth was probably affected by the 3-point loading nature of the test. Once a crack travels away from the central axis, the loading geometry results in a reduction of the stress field around the crack and mixed mode I/mode II loading conditions. These would both be expected to hinder crack propagation. For four-point bending or tensile tests, the off-axis load distribution could tend to facilitate further transverse crack growth.

It was found that the orientation of the crack front rather than the plane of the notch was the critical factor for crack path deviation. The strongest transverse crack growth occurred for X-Z orientated testpieces (figure 5.42b). For these specimens, the crack plane was perpendicular to the most highly orientated grain (rolling) direction, thus providing a driving force for transverse growth. The crack front was also coincident with the rolling plane, thus providing an uninterrupted transverse crack path across its width. The fracture surfaces for these orientations were composed of up to 90% ferrite (figure 5.41), indicating the dominance of the crack path within this phase. A lesser degree of transverse crack growth occurred in the Y-Z orientation, where the crack front was perpendicular to less highly elongated austenite grains. Sub-surface analysis of arrested test specimens revealed that crack growth in these specimens occurred in a stepped manner (figure 5.65). Transverse splits were produced ahead of the crack tip, and these were subsequently linked together by ductile rupture across the austenite grains (figure 5.61). This is somewhat similar to the lamellar tearing mechanism observed in the fracture of carbon-manganese welds[11], where transverse cleavage cracks are formed along stringers of sulphide inclusions. For duplex stainless steels, the transverse cleavage cracks are instead formed by the preferential cracking along the transverse-elongated near interfacial regions of the ferrite grains. These splits (which can result in crack bifurcation) are often evident in the form of brittle secondary cracks upon the fracture surfaces (figures 5.44-45). Note that the initial transverse splits formed (which often grew for up to 500μm in length due to their uninterrupted crack path) were associated with a pop-in failure along the loading curve for COD tests (figure 5.26b)

For specimens with X-Y and Y-X notch orientations, no major transverse deviation occurred during crack growth (figure 5.42c). Although the crack plane for these specimens is the same as those of the X-Z and Y-Z testpieces, the crack front is no longer orientated along the ferrite lamellae. Thus these testpiece orientations do not permit a continuous ferrite split to form across the width of the crack front, so any

transverse crack deviation that occurs is localised to a small fraction of the crack path. This explains the overall planar (mode I) crack growth of these specimens.

For X-Y and Y-X orientated specimens, although there is no crack path for continuous transverse deviation, the crack plane is perpendicular to the elongated microstructure, thus providing a driving force for some transverse growth to occur. This explains the formation of secondary cracks along the direction of crack growth (figure 5.46), which were thought to be nucleated by transverse tensile forces along the crack front. The extent of these cracks was seen to increase with decreasing test temperature due to the brittle nature of the ferrite grains at low test temperatures. Once these secondary cracks are initiated, the constraint of the fracture surface is reduced, effectively transforming the crack front into a series of plane stress specimens. This hypothesis is supported by the formation of highly ductile shear lips adjacent to some of the secondary cracks (figure 5.48). Previous authors who have observed these cracks in duplex stainless steels have suggested that their formation is due to delamination effects of the interphase boundaries[12]. However, no evidence of any such delamination could be found in the present work, and the surface of these cracks suggested that they were formed from ferrite cleavage (figure 5.47). Note that although these secondary cracks were of a brittle nature, they demonstrated a large crack tip opening due to extensive deformation of the austenite phase close to the primary fracture surface (figure 5.68-69).

Specimens tested in the Z-X and Z-Y orientations failed in a normal manner with no transverse crack deviation. As the notch plane was coincident with the ferrite lamella, there was no driving force for secondary crack growth to occur. However, the crack front orientation was found to affect the appearance of the fracture surface. Surfaces from Z-X orientated testpieces were composed almost exclusively of ferrite grains (figure 5.49), as the crack growth was along the direction of greatest grain elongation. This allowed the crack front to follow a ferrite path with virtually no

deviation or secondary cracking. However, for Z-Y orientated specimens, the crack path was along less-elongated grains, forcing the crack to encounter and thus deviate around more austenite grains This resulted in a slightly less planar (mixed mode I/mode II) fracture surface (figure 5.50).

6.1.4 Crack Growth of Other As-Received Product Forms

The crack growth behaviour of the other as-received product forms showed similar trends to that of the rolled plate. Growth was almost exclusively contained within the ferrite phase. Transverse crack deviation and secondary cracking were most pronounced in the product forms with highly elongated austenite grains, i.e. the rolled plate and extruded ingot materials (figures 5.51b,c, 5.51-53). The extruded powder form, which contained less elongated grains (figure 5.1d), fractured with only a small amount of crack path deviation. Note that this material contained the strongest ferrite texture, indicating that the elongation of the grains rather than the crystallographic texture strength was the most important variable for producing transverse crack growth. The HIP'd product form (which was composed of equiaxed grains) showed isotropic fracture behaviour, with planar fracture surfaces for all notch orientations. For this material, near interfacial cracking and transverse deviation still occurred locally around the equiaxed austenite grains (figure 5.70).

6.2 FRACTURE BEHAVIOUR OF WELDS

6.2.1 Micromechanisms of Failure

All weld specimens failed in a planar manner with no overall transverse crack growth. This is presumably because the elongated microstructure provides no significant driving force for transverse crack growth to occur as it is randomly elongated (figure 5.8). The micromechanisms of ductile failure were found to vary

between the TIG and MMA welds. For TIG fracture surfaces, the ferrite microvoids were substantially larger than those of the austenite (figure 5.54a). However, the MMA microvoids were much smaller and similarly sized for both phases (table 5.9 figure 5.54b). The density of inclusions was greater within the MMA weld (figure 5.9) and indeed the population of inclusions within microvoids was much greater upon these fracture surfaces (figure 5.55). Therefore, the high inclusion density of the MMA weld offered a greater number of void nucleation sites within the material, thus decreasing the void size. The high inclusion density of the MMA welds was deduced to be due to oxide particles imparted from the welding process[12] (which is less clean that the inert gas-shielded TIG technique).

In comparison to the parent material (rolled plate), the ductile to brittle transition temperature was raised, with evidence of cleavage failure at test temperatures of -50 and -70°C for the TIG and MMA welds respectively (figure 5.56). This increase in transition temperature (which is well documented[13]) is at least partly due to higher levels of oxygen and nitrogen present in the weld metals as a result of the welding processes. These interstitial alloying elements raise the yield stress of the ferrite matrix (figure 5.11) thus promoting cleavage failure.

At low test temperatures <-80°C the ferrite phase failed exclusively by cleavage (figure 5.57). However, the proportion of austenite and ferrite upon the fracture surface was similar, indicating that little or no crack deviation occurred around the ductile austenite grains. The austenite ligaments were much thinner than the as-received forms, thus facilitating their rupture during cleavage fracture. The fine grain size was also thought to reduce the stresses across the interphase boundary from thermal mis-match, thus reducing the propensity for cracking along the near interfacial region.

6.2.2 Central Embrittlement of the Weld

Hardness traces revealed that the weld central beads were strengthened compared to the outer layers (figure 5.11). Microstructural examination revealed that these areas contained a greater proportion of acicular austenite than the surrounding region (figure 5.8), thus increasing the yield strength via a Hall-Petch effect. These grains are thought to have formed during the repeated heating and cooling of this microstructure during the multilayer welding process, resulting in continued austenite dissolution/reprecipitation. This fine-grained microstructure is generally considered to improve the toughness properties of the weld[14]. However, it was found that this central region demonstrated a greater propensity for cleavage at intermediate test temperatures (-60 to -100°C) than the remainder of the weld (figure 5.58).

Examination of the root weld microstructure by SEM analysis could find no evidence of any intermetallic precipitation within the ferrite that could explain this embrittlement. This is to be expected, as the peak of the thermal cycle would dissolve any such precipitates. For carbon-manganese welds, it has been shown that the root bead has a reduced toughness due to strain ageing effects[15]. However, this is not possible for duplex steels, as the main interstitial element that embrittles the ferrite phase is nitrogen. Although the ferrite would be supersaturated with this element upon initial cooling, further annealing would simply partition this element to the austenite phase. Therefore the local embrittlement is thought to be caused simply by thermal cycling introducing prestrain into the ferrite matrix. This increase in strain, due to the thermal expansion mis-match across the interphase boundary, has been shown to increase during such cycling[16]. Thus subsequent to the welding process, the prestrained root bead microstructure would be susceptible to local cleavage in accordance with previous observations[9]. Note that if the ferrite matrix is highly deformed, the kinetics of spinodal decomposition are increased[17], thus it is possible that some alpha prime is formed during final cooling of the weld, further embrittling the microstructure. To prove this hypothesis, the weld microstructure should be examined

using nano-hardness techniques as well as comparing the kinetics of R-phase precipitation between the root and surface beads in order to elucidate the relative dislocation contents. Unfortunately due to time constraints, this work was considered beyond the scope of the present project.

The central embrittlement of the welds could be used to explain the pop-in behaviour and secondary crack formation upon the weld fracture surfaces (figures 5.58-59). For COD specimens (which were notched on top of the weld) tested at intermediate (-80 to -120°C) test temperatures, the fatigue precrack front was aligned within this embrittled region. This allowing unstable cleavage failure along the whole crack front length during initial growth. Once this crack entered a less reheated region (after around 1mm of growth), the propensity for cleavage failure was reduced, thus arresting unstable crack growth and causing the observed pop-in behaviour.

For the Charpy test specimens (notched 'end-on' to the weld), the crack front was orientated perpendicular to this central embrittled region, thus preventing cleavage failure along its length. However, the tensile stresses along the crack front allowed the formation of secondary cracks along the centrally embrittled region. This is a similar mechanism to the secondary crack formation of X-Y and Y-X orientated testpieces of the as-received product forms. Note that these cracks propagated in a brittle manner along the weld bead/HAZ interfaces which contained coarse grained ferrite, thus reducing the local resistance to crack propagation (figure 5.71)

6.3 EFFECTS OF HEAT TREATMENT UPON FRACTURE

6.3.1 Precipitation of Sigma Phase

Only limited investigations have been conducted of the effects of heat treatment upon fracture behaviour. Annealing at a temperature of 850°C results in the instantaneous nucleation and growth of sigma phase along ferrite/ferrite grain and interphase boundaries (figures 5.13-14). It appears that the critical volume fraction for significantly reducing the impact/fracture toughness is around 5vol% (5.34-35). This has been observed to form after as little as 5 minutes at temperature (figure 5.13), which is quicker than that previously observed for less highly alloyed duplex steels (10 minutes)[18]. The accelerated formation kinetics are thought to be due to the higher alloy content (particularly chromium and molybdenum) of Zeron 100, as described by Charles[19].

Sigma phase is a brittle intermetallic compound (with a complex ordered structure based upon a tetragonal unit cell) and thus cleaves preferentially to the failure of austenite and ferrite phases. Specimens were orientated in the X-Z direction, thus the untreated material showed extensive transverse crack growth. Specimens annealed at temperature for 45 minutes failed in a normal direction in an intergranular manner interspersed with planar regions of mixed mode failure (figure 5.60). Initial phase precipitation was as a thin layer upon the interphase boundary, thus allowing the crack path to deviate around the highly ductile (and untransformed) austenite grains by intergranular cracking along this boundary. This is demonstrated by the transgranular appearance of parts of the fracture surfaces. Note that this phase is surrounded by a layer of ductile secondary austenite, thus preventing any transverse splits from forming. The bulk of the ferrite phase was transformed to a very fine sigma/secondary austenite euctetoidal microstructure, through which the crack advanced in a normal direction. No crack deviation occurred here, due to the austenite ligaments being extremely thin (~1μm) and thus offering little resistance to crack extension.

6.3.2 Formation of Alpha Prime Phase

For specimens annealed at a temperature of 425°C, the α' that is formed via spinodal decomposition restricts the dislocation mobility within the ferrite phase. This results in an increase of the ferrite yield stress, thus reducing the effective plastic zone size ahead of the notch. Therefore the temperature at which position of the maximum tensile stress ahead of the notch exceeds the critical (RKR) distance (the effective ductile to brittle transition) is increased. This explains the appearance of cleavage facets in specimens tested at room temperature (figure 5.61).

6.4 IMPACT AND FRACTURE TOUGHNESS VALUES

6.4.1 As-Received Product Forms

It has been seen that for both COD and Charpy tests, the plate exhibits a broad ductile to brittle transition at test temperatures between -50 and -130°C (figures 5.25-5.30). Even below a test temperature of -130°C the austenite remains fully ductile (figure 5.41), thus allowing the material to retain a significant toughness. As was evident from the fractographic analysis (section 6.1.1) the upper to lower shelf transition was similar for both Charpy and COD tests due to a trade off between decreased strain rate and increased local crack tip stress.

Some notch orientations (X-Z and Y-Z) resulted in accentuated transverse crack growth by the formation of transverse splits ahead of the crack tip (figure 5.63). This increases the material's toughness as it effectively blunts the crack tip, thus limiting the concentration of stresses ahead of it. Note that this is somewhat similar to the fracture behaviour of a composite material. Once the crack has grown away from the central axis, the stress state is complicated to a mixed mode I/mode II type, and the off-axial stress is decreased due to the loading geometry of the specimen, thus further increasing

the apparent material toughness. Other notch orientations (X-Y and Y-Z) resulted in planar crack growth, with large secondary cracks along the crack path (figure 5.46). These cracks decrease the specimen constraint, thus increasing its ductility (figure 5.48) and thus raising the resistance to crack extension.

The fracture behaviour has been shown to be highly anisotropic. The plane of the notch is important for toughness values with toughness generally decreasing (figures 5.25-5.30) in the order of notch planes parallel to rolling direction (X-Z, and X-Z), transverse direction (Y-Z and Y-Z) and normal direction (Z-X and Z-Y). This is due to the crack front bisecting less orientated grains (figure 5.1), resulting in less transverse crack deviation or secondary cracking. The orientation of the crack front is also important, with toughness values decreasing in the order of crack fronts normal to the normal direction, transverse direction and rolling/extrusion direction respectively. This is because the crack front encounters less elongated austenite grains, thus reducing the amount of crack deviation required for failure.

For the various product forms, it was noted that the fracture toughness improved with increasing austenite grain aspect ratio (table 5.1, figures 5.28-30). As the extent of microstructural elongation increased, so did the extent of transverse crack growth or secondary cracking observed (depending on specimen orientation). This can be correlated with the preferential cracking in the near interfacial region discussed above. Note that the impact/fracture toughness of a fully ductile HIP'd specimen tested at a temperature of -20°C (140J/0.15mm) is less than that of an (X-Z orientated) extruded ingot specimen tested at -130°C (285J/0.18mm) which contained brittle transverse-deviated cracks. This shows that the crack path has a stronger influence upon the toughness values than the extent of cleavage upon the fracture surface.

Previous workers have found that a strong rolling texture can decrease the impact toughness of a bcc material[20]. However, this could not be correlated with the

results, as the powder extruded form had a pronounced texture, but a poor fracture toughness. Refining the grain size has also been found to improve toughness[9], but again the material with the smallest grain size (extruded powder) showed some of the lowest toughness results. Therefore, the crack path and thus extent of austenite grain elongation is the most important parameter for determining the material toughness.

6.4.2 Welds

The weld Charpy values had a higher transition temperature and lower upper shelf impact energy than the as-received forms. MMA weld specimens absorbed less energy during fracture. This was due to their higher inclusion content, resulting in a greater density of microvoids and therefore less deformation required to produce microvoid coalescence.

The COD values for the weld metals were very small, and there was little variation between the TIG and MMA welds (figures 5.31-32). This is contrary to the findings of previous authors[21]. The loading curves for these testpieces often exhibited large pop-in failures due to central embrittlement of the weld (figure 5.33a). These pop-ins were all defined to be critical events (from BS7448), and thus the COD had to be defined at this point. However, by calculating the maximum load COD from subsequent crack growth, a further comparison could be made between the weldments for behaviour on the upper shelf (figure 6.1). It can be seen that as expected, the TIG weld is much tougher than the MMA weld. Note that these pop-ins are caused as the specimens are notched from the top. Thus specimens notched 'end on' would be expected to show similar trends to the maximum load COD and Charpy results.

6.4.3 Heat Treated Materials

For materials heat treated at a temperature of 850°C, the presence of sigma precipitates drastically reduces the toughness (figures 5.34-35). This is partly due to the

brittle nature of the phase, but also the reduction of transverse crack deviation due to the formation of secondary austenite.

For materials aged to produce an α' dispersion, the transition temperature is increased as previously discussed, due to the smaller plastic zone of the hardened material. The upper shelf toughness values are also decreased due to the reduction of plasticity within this material (figures 5.36-37).

6.5 DESIGN CRITERIA FOR DUPLEX STAINLESS STEELS

One aim of the project was to provide a quantitative correlation between COD and Charpy values for Zeron 100, to allow industrial companies to predict fracture toughness from impact toughness values. However, as shown in figure 6.2 this correlation is affected by notch orientation as well as product form, thus is of little use. It is futile to try to model the relation between the two types of test as the COD values relate only to fracture initiation and stable crack growth prior to unstable failure, whereas the Charpy impact energy involves fracture of the complete specimen.

In recent years there has been a desire from producers of duplex stainless steels to format design criteria based upon these materials, rather than that of ferritic steels which are traditionally used. Their argument has been that the ductile to brittle transition is constrained by the ductile austenite grains. However, although the transition of toughness values is more gradual than that of ferritic steels, this is a result of the containment of ferrite-nucleated microcracks by austenite grains rather than prevention of any cracking. Thus the presence of these cracks demands that duplex stainless steels are only suitable for a ferritic steel design approach. Therefore, any design criteria for

duplex stainless steels must take account of the anisotropic nature of its fracture behaviour, and specify specific notch orientations for tests.

For structural applications, it is obvious that the fracture resistance will be limited by the performance of the weld rather than the base metal. A COD value of 0.18mm is often quoted as acceptable for welds in offshore applications[22]. This would relate to a Charpy impact energy of approximately 150J (for the TIG weld), suggesting that the current industry standard of 40J is rather optimistic. However, it is not reasonable to compare these values, as the COD value corresponds to a different notch orientation (top of weld) to that of the Charpy value (end on). Note that as such welds are often used in seam-welded pipes, which would reproduce the loading conditions of top-notched welds, it is important to use this worst orientation for formatting design criteria.

References:-

[1]DRAR H., 'On predicting the temperature and strain rate dependence of the fracture toughness of plain carbon steels', Mat.Char., 31, pp91-97, 1993.

[2]STRANGWOOD M. & DRUCE S.G., 'Ageing effects in welded cast CF3 stainless steel', Mat.Sci.Tech., 6, pp237-247, 1990.

[3]HULL D., 'Twinning and fracture of single crystals of 3% silicon iron', Acta Met., 8, pp11-18, 1960.

[4]LESLIE W.C., Met.Trans., 4, p379, 1973.

[5]KNOTT J.F., 'Microscopic aspects of crack extension', in "Advances in Elasto-Plastic Fracture Mechanics", Ed.Larsson, Applied Science Publ., London, pp21-41, 1980.

[6]JOLY P., COZAR R. & PINEAU A., 'Effect of crystallographic orientation of austenite on the formation of cleavage cracks in ferrite in an aged duplex stainless steel', Scripta Met., 24, pp2235-2240, 1990.

[7]YONG-TANG N, KE-FU Y., NAN-PING C. & PLUMTREE A., 'In-situ fracture experiment on a duplex stainless steel', Mat.Sci.Eng., A117, pp157-165, 1989.

[8]GROOM J.D.G., 'Effects of prestrain on fracture', PhD thesis, University of Cambridge, 1971.

[9]NYSTRÖM M., KARLSSON B. & WASÉN J., 'The influence of prestraining and 475°C annealing on the mechanical properties of a duplex stainless steel (SAF2205)', Proc.conf."Duplex Stainless Steels '90", Chiba, Japan, pub.ISIJ, pp738-745, 1991.

[10]LI X., 'Prediction and assessment of duplex stainless steel microstructures susceptible to low temperature cleavage failure', PhD thesis, University of Birmingham, 1997.

[11]FARRAR J.C.M. & DOLBY R.E., 'Lamellar tearing in welded steel fabrication', TWI, Cambridge, 1972.

[12]IRRISARRI A.M. & ERAUZKIN E., 'Effects of the heat treatment on the fracture toughness and corrosion embrittlement of a duplex stainless steel SAF2205', Proc.conf."Duplex Stainless Steels'91", Beaune, France, pub.Editions de Physique, pp779-785, 1991.

[13]LILJAS M., 'The welding metallurgy of duplex stainless steels', proc.conf."Duplex Stainless Steels '94", Glasgow, U.K., pub.TWI, paper KV, 1994.

[14]TWEED J.H. & KNOTT J.F., 'Effect of reheating on microstructure and toughness of C-Mn weld metal', Met.Sci., 17, pp45-54, 1983.

[15]McRobie D.E. & KNOTT J.F., 'Effects of strain ageing on fracture toughness of C-Mn weld metal', Mat.Sci.Tech., 1, pp357-365, 1985.

[16]SIEGMUND T., WERNER E. & FISCHER F.D., 'The irreversible deformation of a duplex stainless steel under thermal cycling', Mat.Sci.Eng., A169, pp125-134, 1993.

[17]CAHN J.W., 'On spinodal decomposition in cubic crystals', Acta Met., 10, pp179-183, 1962.

[18]SOUTHWICK P.D. & HONEYCOMBE R.W.K., 'Decomposition of ferrite to austenite in 26%Cr-5%Ni stainless steel', Met.Sci., pp253-261, 1980.

[19]CHARLES J., 'Structure and mechanical properties of duplex stainless steels', proc.conf."Duplex Stainless Steels '94", Glasgow, U.K., pub.TWI, paper KI, 1994.

[20]WELCH P.I. & DAVIES G.J., 'Texture and cleavage in molybdenum', Textures and Microstructures, 6, pp21-38, 1983.

[21]DHOOGE A. & DELEU E., 'Weldability and fracture behaviour of duplex and super-duplex stainless steels', proc.conf."Duplex Stainless Steels '94", Glasgow, U.K., pub.TWI, paper 77, 1994.

[22]BS4515, 'Welding of steel pipelines on land and offshore', British Standards Institute, London, 1984.

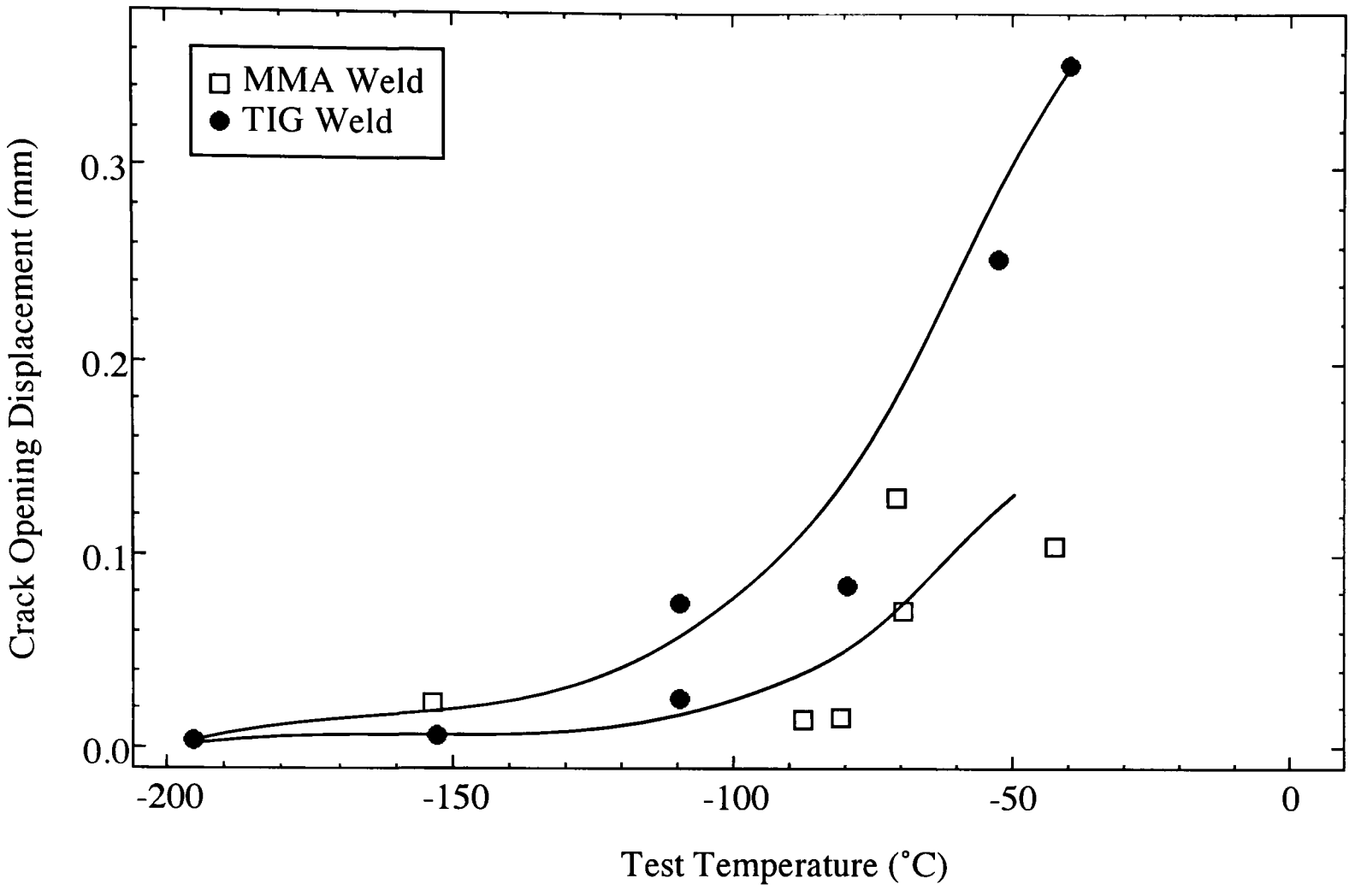

Figure 6.1 - Variation of maximum load COD with test temperature for weld metals

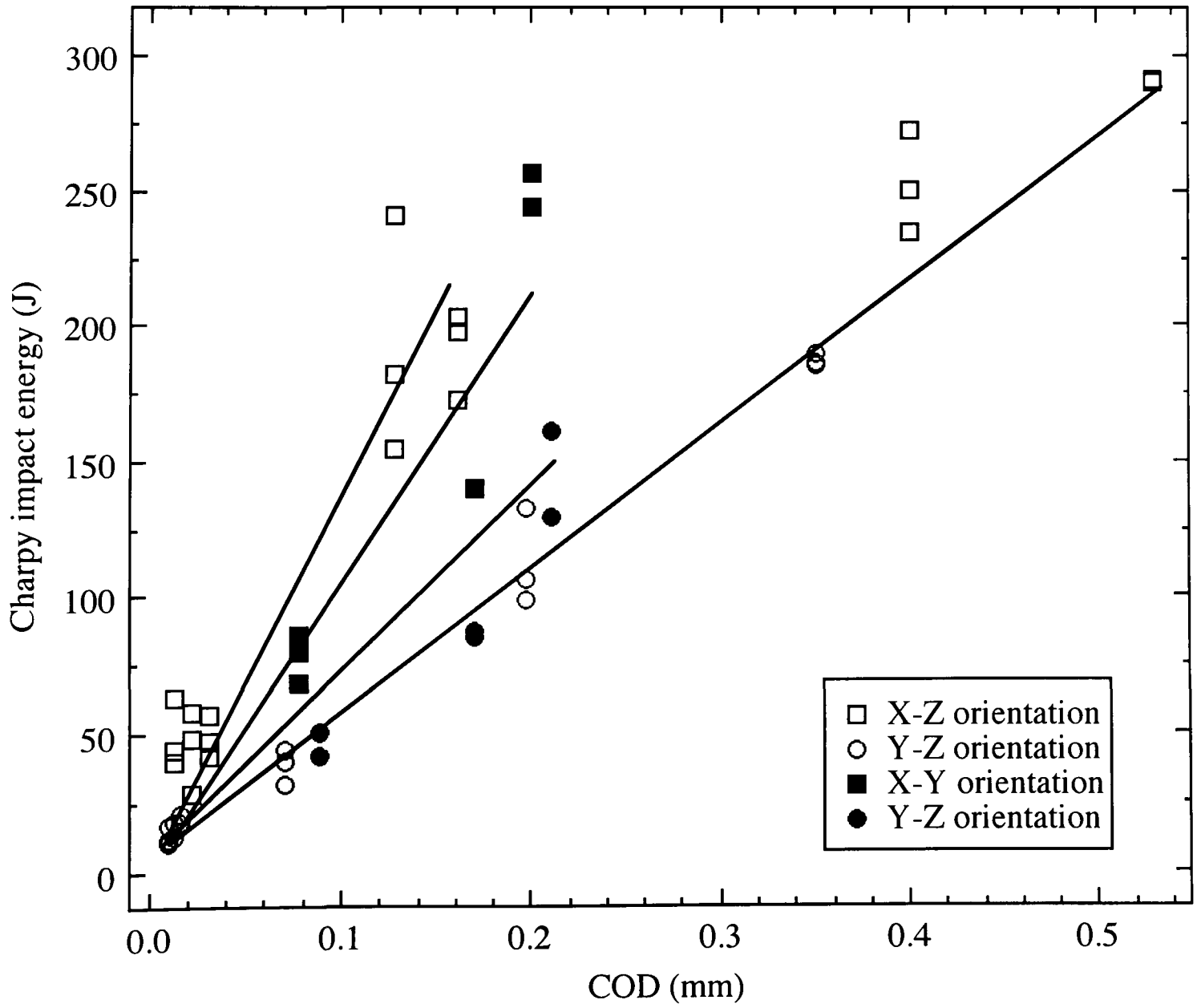

Figure 6.2 - Relationship between COD and Charpy values for as-received rolled plate material

7 - CONCLUSIONS

The super duplex stainless steel, Zeron 100 is extremely tough at test temperatures above -80°C for the as-received product forms, and fails in a ductile manner. Below this test temperature, the ferrite phase cleaves through a mechanism initiated by mechanical twin intersections. A highly strained region within the ferrite phase close to the interphase boundary results in preferential cleavage crack growth local to this region. The presence of the ductile austenite phase can lead to transverse crack growth or secondary cracking (depending upon notch orientation) in those product forms with an orientated microstructure (i.e. shape anisotropy). Grain size, minor compositional variations and crystallographic texture were found to have little influence on the fracture process and the controlling factor is the shape of the austenite grains. The crack path was found to have a greater influence upon the toughness values than the proportion of ductile/brittle micromechanisms of failure upon the fracture surface.

The ductile to brittle transition temperature was found to be similar for both COD and Charpy tests. Thus the increased propensity for cleavage failure due to the higher strain rate in the Charpy test is deduced to be almost exactly offset by a reduction in the maximum tensile stress ahead of the notch compared with that produced ahead of a fatigue precrack.

The welded microstructures showed a reduced toughness and increased transition temperature compared to the as-received forms. This was deduced to be due to their higher oxygen and nitrogen contents (compared to the parent plate material) as well as large inclusion content. The root bead of the weld was found to be further embrittled and it is thought that this is due to residual stresses from the thermal cycling of this region associated with the mis-match in thermal expansion coefficient across the

interphase boundary. The toughness of the TIG welded specimens was found to be significantly larger than those of the MMA material, due to the high inclusion content of the latter increasing the density of void nucleation. The COD values for the TIG welded microstructures were significantly reduced by large non-catastrophic pop-ins that occurred due to the central embrittlement of the weld.

Heat treatments at temperatures of 850 and 425°C both resulted in a severe reduction of fracture toughness, due to the formation of sigma phase and alpha prime respectively.

8 - FURTHER WORK

Although this project has provided a greater understanding of the general fracture behaviour of a duplex stainless steel, some areas of the project need to be investigated in more detail.

This project has strongly implicated that the nucleation of microcracks is caused by mechanical twin intersections. However, a detailed TEM study of the area ahead of the crack tip would be of further benefit to investigate the presence of twins/slip bands and their relation to the microstructure. Investigations should also be made of the effect of austenite grain orientation upon adjacent microcrack nucleation.

Further analysis (X-ray or neutron diffraction) of the near-interfacial region of the ferrite is needed to confirm the presence of residual stresses that cause the preferential cracking observed. In addition, finite element modelling should be undertaken to estimate the distribution of these stresses.

This project provided little understanding of the deformation micromechanisms prior to failure. In particular, the degree of constraint of austenite grains by the ferrite matrix is uncertain. A series of tensile tests interrupted at various strains prior to failure should be performed in order to elucidate the degree of austenite deformation. In addition, FEM modelling should be employed to calculate the stress distribution within the two phase microstructure ahead of the crack tip so that some attempt may be made to properly model the fracture behaviour.

The transverse crack deviation observed for the three-point loaded toughness tests may be partly due to the loading geometry. To investigate fully such crack path

behaviour, some double edged notched or centre cracked wide plate tests should be performed.

To confirm that the root bead of the weld is embrittled from residual stresses due to thermal cycling, an extensive nanohardness investigation of the region should be performed. The kinetics of R-phase precipitation (which nucleate preferentially upon dislocation arrays) should also be compared between surface and root beads.